SYNERGISTIC METHODS FOR THE PRODUCTION OF HIGH-STRENGTH AND LOW-COST BORON CARBIDE

A Thesis
Presented to
The Academic Faculty

by

Charles Schenck Wiley

In Partial Fulfillment
of the Requirements for the Degree
Doctor of Philosophy in
Materials Science and Engineering

School of Materials Science and Engineering
Georgia Institute of Technology
May 2011

SYNERGISTIC METHODS FOR THE PRODUCTION OF HIGH-STRENGTH AND LOW-COST BORON CARBIDE

Approved by:

Professor Robert F. Speyer, Advisor
School of Materials Science and Engineering
Georgia Institute of Technology

Professor Rosario A. Gerhardt
School of Materials Science and Engineering
Georgia Institute of Technology

Professor Robert L. Snyder
School of Materials Science and Engineering
Georgia Institute of Technology

Professor Sheldon M. Jeter
School of Mechanical Engineering
Georgia Institute of Technology

Professor Thomas H. Sanders, Jr.
School of Materials Science and Engineering
Georgia Institute of Technology

Dr. Jerry C. LaSalvia
Weapons and Materials Research Directorate
U.S. Army Research Laboratory

Professor Joe K. Cochran
School of Materials Science and Engineering
Georgia Institute of Technology

Date Approved: 10 December 2010

ACKNOWLEDGEMENTS

I would like to thank my friends and family who have supported me during this long intellectual journey. I could not have come this far without you. I would like to thank my advisor, Dr. Robert Speyer, who allowed me to pursue many challenging projects during my tenure at Georgia Tech. I would also like to recognize my friend and colleague, Dr. Beth Judson, who passed away this year. She was a bright light for all who knew her, and she was one my supporters who encouraged me to pursue this degree. Most of all, I would like to thank my mother, Tisha Wiley, and grandmother, Louise Wiley, who have always been my cheerleaders.

TABLE OF CONTENTS

LIST OF TABLES

LIST OF FIGURES

SUMMARY

Boron carbide (B_4C) is a non-oxide ceramic in the same class of nonmetallic hard materials as silicon carbide and diamond. The high hardness, high elastic modulus and low density of B_4C make it a nearly ideal material for personnel and vehicular armor. B_4C plates formed via hot-pressing are currently issued to U.S. soldiers and have exhibited excellent performance; however, hot-pressed articles contain inherent processing defects and are limited to simple geometries such as low-curvature plates. Recent advances in the pressureless sintering of B_4C have produced theoretically-dense and complex-shape articles that also exhibit superior ballistic performance. However, the cost of this material is currently high due to the powder shape, size, and size distribution that are required, which limits the economic feasibility of producing such a product. Additionally, the low fracture toughness of pure boron carbide may have resulted in historically lower transition velocities (the projectile velocity range at which armor begins to fail) than competing silicon carbide ceramics in high-velocity long-rod tungsten penetrator tests. Lower fracture toughness also limits multi-hit protection capability. Consequently, these requirements motivated research into methods for improving the densification and fracture toughness of inexpensive boron carbide composites that could result in the development of a superior armor material that would also be cost-competitive with other high-performance ceramics.

The primary objective of this research was to study the effect of titanium and carbon additives on the sintering and mechanical properties of inexpensive B_4C powders. The boron carbide powder examined in this study was a sub-micron (0.6 μm median particle size) boron carbide powder produced by H.C. Starck GmbH via a jet milling

process. A carbon source in the form of phenolic resin, and titanium additives in the form of 32 nm and 0.9 μm TiO_2 powders were selected. Parametric studies of sintering behavior were performed via high-temperature dilatometry in order to measure the *in-situ* sample contraction and thereby measure the influence of the additives and their amounts on the overall densification rate. Additionally, broad composition and sintering/post-HIPing studies followed by characterization and mechanical testing elucidated the effects of these additives on sample densification, microstructure development, and mechanical properties such as Vickers hardness and microindentation fracture toughness.

Based upon this research, a process has been developed for the sintering of boron carbide that yielded end products with high relative densities (i.e., 100%, or theoretical density), microstructures with a fine ($\sim$2-3 μm) grain size, and high Vickers microindentation hardness values. In addition to possessing these improved physical properties, the costs of producing this material were substantially lower (by a factor of 5 or more) than recently patented work on the pressureless sintering and post-HIPing of phase-pure boron carbide powder. This recently patented work developed out of our laboratory utilized an optimized powder distribution and yielded samples with high relative densities and high hardness values. The current work employed the use of titanium and carbon additives in specific ratios to activate the sintering of boron carbide powder possessing an approximately mono-modal particle size distribution. Upon heating to high temperatures, these additives produced fine-scale TiB_2 and graphite inclusions that served to hinder grain growth and substantially improve overall sintered and post-HIPed densities when added in sufficient concentrations. The fine boron carbide grain size manifested as a result of these second phase inclusions caused a substantial increase in hardness; the highest hardness specimen yielded

a hardness value (2884.5 kg/mm^2) approaching that of phase-pure and theoretically-dense boron carbide (2939 kg/mm^2). Additionally, the same high-hardness composition exhibited a noticeably higher fracture toughness (3.04 MPa·m$^{1/2}$) compared to phase-pure boron carbide (2.42 MPa·m$^{1/2}$), representing a 25.6% improvement. A potential consequence of this study would be the development of a superior armor material that is sufficiently affordable, allowing it to be incorporated into the general soldier's armor chassis.

CHAPTER I

INTRODUCTION

The recent wars in Afghanistan and Iraq have highlighted the importance of effective body armor on the success of military operations as well as the survivability of U.S. soldiers. The widespread availability of large caliber AK-47 rifles and the use of improvised explosive devices in these war zones pose serious threats to the safety of U.S. soldiers during these engagements. The renewed focus on Afghanistan as a strategic front has shifted the primary battlefield from the largely urban environments of Iraq to the mountainous regions of Afghanistan, resulting in soldiers having to carry substantial weight loads to remote outpost locations over difficult terrain. As a result, the development of new armor materials and systems that provide improved protection against ballistic or explosive threats while also lowering weight are being widely researched. Due to their high hardness, high elastic modulus and low density, non-oxide ceramics are highly effective armor materials. Of these non-oxide ceramics, boron carbide possesses the lowest density and thus provides the best ballistic protection for the least weight. Armor produced from boron carbide is three times lighter than similarly sized steel armor plating and also provides superior ballistic protection against armor piercing rounds.

Currently, boron carbide powders are densified into articles via hot-pressing or pressureless sintering with several weight percent (or more) of second-phase additives. Both of these methods produce near theoretically-dense parts; however, each method introduces defects or weaknesses within the material that ultimately limit its ballistic performance. In hot-pressing, the application of uniaxial pressure during heating to high temperatures results in $\sim$98% dense articles. However, the presence of residual

porosity results in a lower overall hardness and an increase in the number of sites for crack nucleation, thereby impairing the ballistic performance. Hot-pressing has the additional limitation of only allowing the formation of parts that can be stacked and pressed in series, so part geometry is restricted to simple shapes such as flat or low curvature plates. Boron carbide samples densified via pressureless sintering with second-phase additives such as graphite or alumina (Al_2O_3) have the advantage of being formed into dense complex shapes; however, the large amount of additives that has been added in prior work has reduced the hardness of the final product when compared to additive-free boron carbide of equivalent porosity.

Recent work by Lee, Cho, Bao and Speyer on the pressureless sintering and post-hot isostatic pressing (post-HIPing) of boron carbide has resulted in the production of theoretically-dense and additive-free boron carbide articles of complex geometry [1][2]. The improved hardness and complex shape capability could greatly improve soldier protection levels and thereby reduce war-related casualties. Despite these benefits, the material and manufacturing costs associated with the production of this boron carbide are currently high, which can limit the economic feasibility of manufacturing such a product. The prohibitive production costs are largely attributable to the high cost (nearly $200 per kg) of the HC Starck HS sinter-grade boron carbide powder, which limits the incorporation of this superior protection technology into a U.S. soldier's armor system. It is well established that producing a superior technology does not guarantee success in a market. Consequently, materials cost reductions would make pressureless-sintered boron carbide composites cost-competitive with other high-performance armor ceramics. Furthermore, the higher fracture toughness of boron carbide composites would be an added benefit that could potentially raise the ballistic effectiveness of the armor. The widespread availability of lightweight, theoretically-dense and body-contoured boron carbide composites would provide U.S. servicemen with greater armor coverage areas as well as greater freedom of motion,

thereby reducing casualties and improving tactical advantage. As a result, cost reductions in this material as well as methods for improving fracture toughness are highly desirable goals.

The introduction of small amounts (0-5 wt%) of specific additives may facilitate the sintering of inexpensive boron carbide powders with non-optimized particle size distributions via solid-state or liquid-phase sintering mechanisms. Additionally, intergranular metal boride reaction products that form during sintering may improve fracture toughness by facilitating energy absorption via microcracking or crack deflection. Several mechanisms for the improved densification, toughening and strengthening of boron carbide-additive systems have been suggested in previously published literature. However, most studies have been limited to large additive amounts ($\succ$10 vol%) and have not optimized the composition and processing parameters. Analysis of existing literature has indicated that out of the additives previously examined, Ti and C could yield promising results in the form of high sintered density and fracture toughness. Despite these beneficial attributes, certain areas of this system remain largely uninvestigated, such as the examination of the effect of Ti additive size, the effect of low Ti and C additions, the analysis of microstructural features depending on composition and sintering temperature, as well as the merits of incorporating recent boron carbide sintering technology. Consequently, the above reasons motivated further study in order to determine the effects of Ti and C additives on the sintering, microstructure, and mechanical properties of low cost boron carbide composites.

CHAPTER II

LITERATURE REVIEW

2.1 Boron Carbide

Boron carbide is a non-oxide ceramic that falls within the same class of nonmetallic hard materials such as silicon carbide, cubic boron nitride, and diamond. Boron-carbon materials were first produced in 1883 by Joly followed by Moissan in 1894. However, it was not until 1934 that Rigdway analyzed the composition of such boron-carbon compounds and designated B_4C as the chemical formula for stoichiometric boron carbide [3]. Boron carbide is distinguished by its high hardness (2950 kg/mm^2 on the Vickers scale), high elastic modulus (∼450-470 GPa) and low density (2.52 g/cm^3) [4].

The calculated boron-carbon covalent bond energy is 9.42 eV while the ionic bond energy is calculated to be 1.41 eV. These bond energies correspond to a bonding character that is almost 90% covalent [5]. This high covalent character explains the extreme hardness and elastic modulus associated with boron carbide. Despite the high hardness of boron carbide, its high bond strength, low coordination number (due to primarily covalent bonding), and lack of close packed slip systems contribute to signficant resistance to dislocation motion, resulting in brittle mechanical behavior. Consequently, the fracture toughness of boron carbide is typically low (∼2.9-3.7 MPa·m$^{1/2}$) [4].

The potential applications of sintered boron carbide articles range from machining/cutting bits and waterjet cutting nozzles to high-performance lightweight armor [4]. Additionally, boron carbide has a high neutron absorption cross-section due to the presence of ∼19.8% of the ^{10}B boron isotope. This property combined with its

refractoriness and low reactivity make boron carbide a useful material for nuclear reactor control rods or shielding panels [4]. It should be noted that with rising fossil fuel costs, nuclear reactors are an increasingly attractive form of power generation, which may lead to increased demand for boron carbide components.

2.2 Synthesis of Boron Carbide

Boron carbide is produced by the carbothermal reduction of boron oxide via the following reaction:

$$2B_2O_{3(l)} + 7C_{(s)} \rightarrow B_4C_{(s)} + 6CO_{(g)} \tag{1}$$

This reaction is highly endothermic, possessing a $\Delta\overline{H}^{o}_{rxn}$ of 1812 kJ/mol, and is typically performed in an electric furnace [4]. For a CO pressure equal to 1 atm, the above reaction exhibits a ΔG_{rxn} that is zero at 1561 °C and negative at higher temperatures. However, temperatures in excess of 2000 °C are required for the reaction to proceed at an acceptable rate [6]. It is important to note that certain gas-solid reactions may occur during boron carbide synthesis. At the high temperatures required for the production of boron carbide, B_2O_3 transitions into a liquid at ∼452 °C and boils at ∼1860 °C [7]. As a result, boron oxide has a significant vapor pressure at the reaction temperature, so the loss of boron via evaporation may be a production concern. The reduction of liquid B_2O_3 with carbon produces the volatile suboxide B_2O_2 starting at 1227 °C. The reaction of $B_2O_{2(g)}$ with excess carbon results in a gas-solid reaction mechanism for the production of boron carbide [7]. The two stated reactions are given below:

$$C_{(s)} + B_2O_{3(l)} \rightarrow B_2O_{2(g)} + CO_{(g)} \tag{2}$$

$$5C_{(s)} + 2B_2O_{2(g)} \rightarrow B_4C_{(s)} + 4CO_{(g)} \tag{3}$$

Following synthesis, large pieces of boron carbide are removed from the reactor and crushed and milled to produce a fine powder. The powder is then cleaned with HCl to remove any metal impurities imparted to the powder during mechanical processing [4].

2.3 Structure and Composition of Boron Carbide

Boron carbide possesses a rhombohedral unit cell whose lattice structure falls in the D^5_{3d}-R$\bar{3}$m space group. The unit cell contains 15 atoms whose arrangement produces eight icosahedra at the corners that are interconnected by inter-icosahedral three atom chains that lie along the *c*-axis of the rhombohedron (for a hexagonal unit cell interpretation) [4]. Emin stated that the structure of stoichiometric B_4C is best described as having $B_{11}C$ icosahedra connected by a body diagonal C-B-C inter-icosahedra chain [8]. An illustration of the boron carbide unit cell is provided in Figure 1.

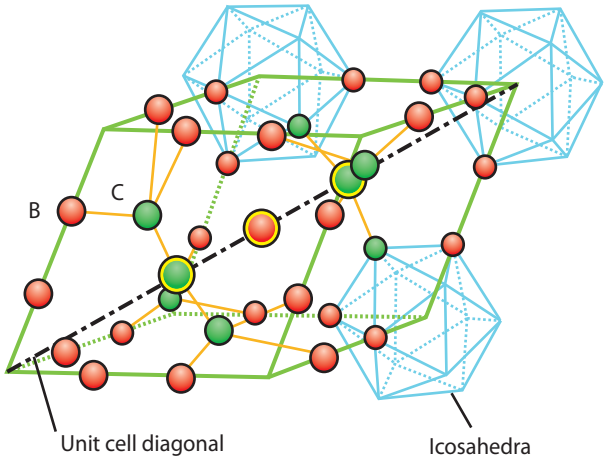

Figure 1: The B_4C unit cell with illustrated $B_{11}C$ icosahedra and C-B-C chain [5].

It is important to note that boron carbide exists as a solid solution over a composition range from 8.8 to 20 at% carbon, or $B_{10.4}C$ to B_4C [4]. Emin suggested that this composition range is explained by the exchange of carbon atoms and boron atoms at icosahedra or inter-icosahedra chain lattice sites. A carbon content exceeding 20

at% results in the formation of B_4C and free graphite (Figure 2). Decreasing carbon content from the stoichiometric composition results in the formation of boron-rich boron carbide in which carbon atoms are substituted by boron atoms [8].

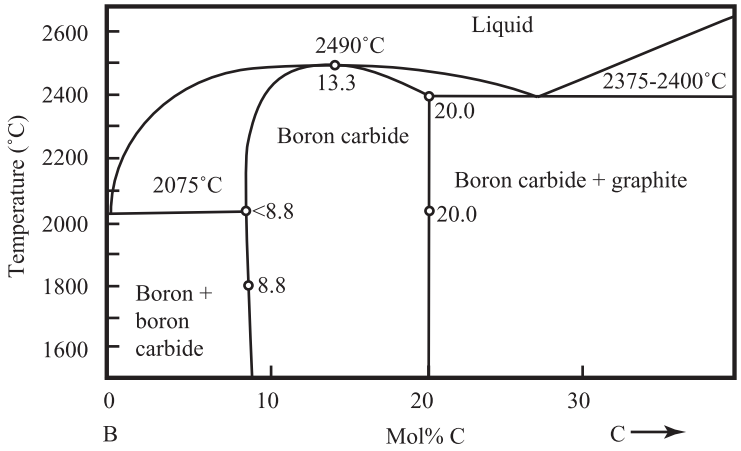

Figure 2: The boron-carbon phase diagram [4]

As the composition becomes increasingly boron-rich, one of the carbon atoms in the inter-icosahedral chains is replaced with boron, thereby producing C-B-B chains. At compositions with less than 13.3 mol% C ($B_{13}C_2$), the C-B-B chains remain, but the $B_{11}C$ icosahedra are transformed into B_{12} structures [8]. These changes in structure with composition necessarily result in a change in the lattice parameters and unit cell volume. The a lattice parameter decreases linearly with increasing carbon concentration. Interestingly, the hexagonal c lattice parameter also decreases with increasing carbon content, but it exhibits a change in slope at 13.3 mol% C which corresponds to the $B_{12} \rightarrow B_{11}C$ transformation mentioned above [9]. The decrease in the lattice parameters results in the linear decrease in unit cell volume with increasing carbon content. As a result, the theoretical density of boron carbide increases as a linear function of carbon content, from 2.465 g/cm^3 (for $B_{10.4}C$) to 2.52 g/cm^3 (for B_4C) [4]. A plot illustrating the behavior of the a and c lattice parameters as a function of boron carbide composition is provided in Figure 3.

In addition to density, the mechanical properties of boron carbide change with

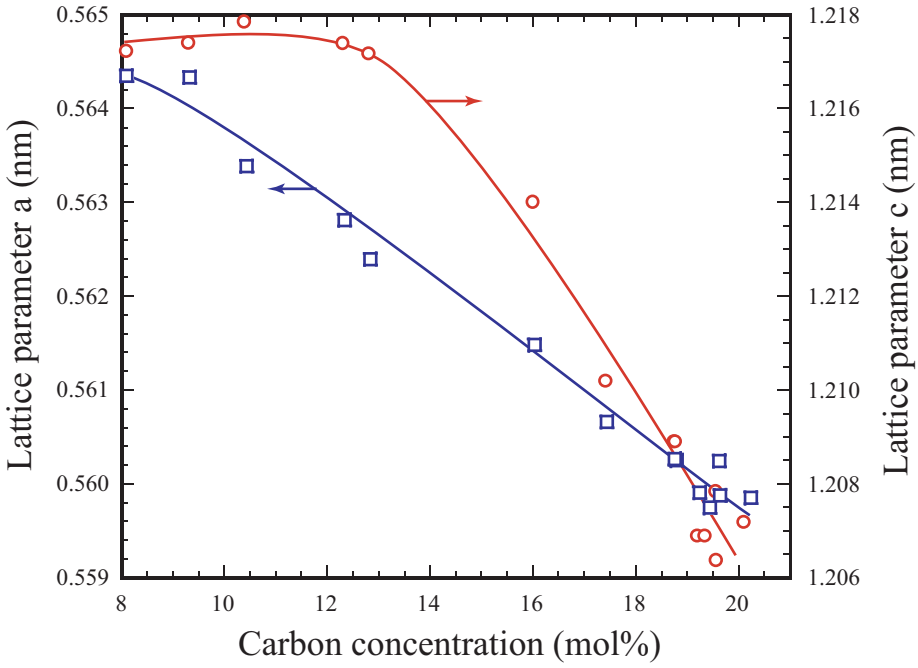

Figure 3: Influence of composition on boron carbide a and c lattice parameters [4]

composition. As cited in Thevenot, Aselage *et al.* observed a significant decrease in the elastic modulus of boron carbide for compositions containing less than 13.3 mol% C. This change is attributed to the reduction in the rigidity of the icosahedra resulting from the $B_{11}C \rightarrow B_{12}$ transformation [9]. Also, Niihara *et al.* determined that the highest values of hardness and microindentation fracture toughness for boron carbide occurred at the stoichiometric composition (B_4C), with hardness decreasing for increasingly boron-rich or carbon-rich compositions [10]. A plot illustrating the dependence of hardness upon the boron and carbon composition of boron carbide is given in Figure 4.

2.4 Sintering

Sintering is the process by which particulates in a compacted body consolidate via thermally activated mass transport mechanisms. The driving force for sintering is the reduction in the total free energy (ΔG_{tot}) as given by the equation

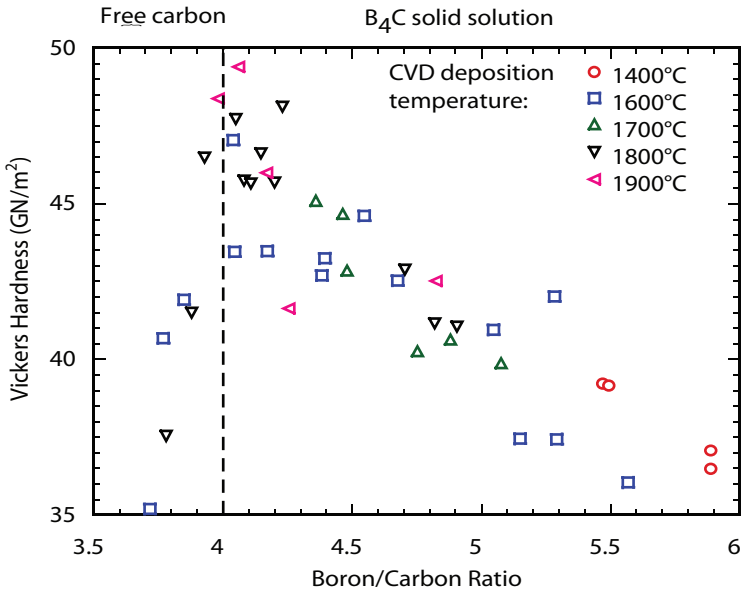

Figure 4: Effect on composition on the hardness of boron carbide [10]

$$\Delta G_{tot} = \Delta G_v + \Delta G_b + \Delta G_s \tag{4}$$

where ΔG_v, ΔG_b, and ΔG_s are the free energy changes for volume, boundaries, and surfaces, respectively. Reed states that the change in the surface free energy (ΔG_s) is typically the controlling factor in this equation and can be expressed as $\gamma_s \Delta A_s$ where γ_s represents the interfacial energy of the surface and ΔA_s represents the change in surface area [11]. Kang modified this interpretation of ΔG_s to account for the change in interfacial energy associated with different surfaces or interfaces. Accordingly, this equation, which is given below, is a more accurate model of the physical phenomena, because it takes into account both coarsening and sintering.

$$\Delta(\gamma A) = \gamma \Delta A + \Delta \gamma A \tag{5}$$

Coarsening involves the reduction in particulate surface area and does not lead to the creation of new interfaces, as given by the term $\gamma \Delta A$. Sintering involves the replacement of existing interfaces (e.g., grain-pore interfaces) with new interfaces (e.g., grain-grain interfaces), as given by the term $\Delta \gamma A$. Via this sintering process, grain

centers approach and grain geometry is altered to minimize the surface energy, which results in overall densification [12]. It is important to note that the change in interfacial energy ($\Delta\gamma$) depends on the sintering process that occurs for a particular system, of which there are two: solid-state sintering and liquid-phase sintering. The change in interfacial energy for a solid-state sintering process is the difference between the solid-solid interfacial energy (the surface energy of particles that are physically bonded at a grain boundary) and the solid-vapor interfacial energy (the surface energy of isolated and non-sintered particles). For liquid-phase sintering, the change in interfacial energy is the difference between the solid-liquid interfacial energy (the surface energy associated with the interface between solid particles and a liquid) and the liquid-vapor interfacial energy (the surface energy associated with a liquid-pore interface) [12].

2.4.1 Solid-State Sintering

Solid-state sintering involves the densification of a solid via mass transport between adjacent particles and is characterized by an absence of a wetting liquid phase. There are several models that seek to explain this sintering process. The first model is a stress-based explanation that takes into account the effect of surface energy over a curved surface. This explanation provides a model for the driving force that results from surface free energy; however, more rigorous models are available which encompass the multiple influences of surface energy on mass transport mechanisms.

As a powder compact is heated to a sufficiently high temperature to initiate diffusion, adjacent particles locally fuse at the contact point to form a neck. The change in surface curvature resulting from the creation of a neck between two particles gives rise to a sintering stress, which is modeled by the Laplace equation [13].

$$\sigma = \gamma \left(\frac{1}{R_1} + \frac{1}{R_2} \right) \tag{6}$$

In the above equation, γ represents the surface energy and R_1 and R_2 represent the principal radii of curvature for a given particle surface [13]. It is important to note that a convex surface results in a positive radius of curvature and thus a positive or tensile stress. Conversely, a concave surface results in a negative radius of curvature and results in a negative or compressive stress. A flat surface exhibits no curvature and thus is stress free, so it can be considered to be the most stable geometric state. As a result, any surface irregularities will tend to flatten in order to eliminate stress. A simple illustration of the initial sintering of two spheres meeting at a neck is given in Figure 5.

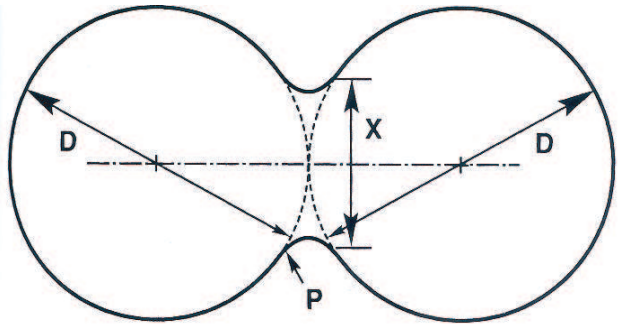

Figure 5: Illustration of two spheres undergoing neck formation via solid-state sintering [13].

Using the Laplace equation, the stress of the area away from the neck is $\sigma = 4\gamma/D$, where D is the particle diameter. The stress at the neck is given by $\sigma = \gamma((2/X) - 4D/(X^2))$, where X is the neck diameter. The transition from the convex particle surface (under tensile stress) to the concave neck surface (under compressive stress) results in a substantial stress gradient. This stress gradient provides the driving force for mass transport mechanisms to the neck. However, as mass progressively flows to the neck, the radius of the neck increases. This process subsequently decreases the stress gradient, so the driving force decreases and the sintering process decelerates [13]. The concept of a sintering stress is a relatively simple model that seeks to explain the role of surface energy in influencing mass transport during the sintering process.

Surface free energy results from the broken bonds of atoms located at a solid-vapor interface. In a simple energy model, the driving force for mass transport is the elimination of these higher energy solid-vapor interfaces by the creation of lower energy solid-solid interfaces. In a more detailed model, the driving force for sintering can be explained as originating from the difference in bulk pressure (ΔP), vacancy concentration (ΔC_v), and vapor pressure (ΔP_{vap}). The bulk pressure difference is given by the equation

$$\Delta P = \gamma_{sv}\left(\frac{2}{a} + \frac{1}{r} - \frac{1}{x}\right) \cong \frac{\gamma_{sv}}{r} \tag{7}$$

where a is the particle radius, r is the neck radius of curvature, x is the neck radius, and γ_{sv} is the solid-vapor interfacial energy [12]. The difference in vacancy concentration is given by

$$\Delta C_v = C_{v,\infty}\frac{V_m^{'}\gamma_{sv}}{RTr} \tag{8}$$

where $C_{v,\infty}$ is the concentration of vacancies for a perfectly flat surface and $V_m^{'}$ is the molar volume of vacancies [12]. The difference in the concentration of vacancies originates from the phenomenon that concave surfaces exhibit a higher vacancy concentration than the equilibrium state, while convex surfaces have a lower vacancy concentration than equilibrium. The vacancy concentration for a curved surface is given by the equation

$$C = C_o\left[1 - \frac{\gamma\Omega}{kT}\left(\frac{1}{R_1} + \frac{1}{R_2}\right)\right] \tag{9}$$

where C_o is the equilibrium vacancy concentration (which increases exponentially with temperature), γ is the surface energy, Ω is the atomic volume, k is Boltzmann's constant, T is the temperature, and R_1 and R_2 are the principal radii of curvature. For a spherical particle approximation, the particle possesses a convex surface; however,

a neck formed between two particles has a concave surface. The vacancy concentration gradient (from the high vacancy concentration at the neck to the lower vacancy concentration at the particle surface) leads to mass transport into the neck [13]. The vapor pressure difference is given by

$$\Delta P_{vap} = P_{vap,\infty} \frac{V_m \gamma_{sv}}{RTr} \tag{10}$$

where $P_{vap,\infty}$ is the vapor pressure over a perfectly flat surface, and V_m is the molar volume of the solid [12]. The difference in vapor pressure originates from the Gibbs-Thomson equation, $\mu_r = \mu_\infty + \gamma \mathrm{K} \mathrm{V}_m$, where μ_r is the chemical potential of a particle of radius r, μ_∞ is the chemical potential of an infinitely flat surface, and K is the average curvature of the interface. With the assumption of local equilibrium at the solid(α)-vapor(β) interface ($d\mu^\alpha = d\mu^\beta$), the vapor pressure over a curved surface can be determined:

$$P_r^\beta = P_\infty \left(1 + \frac{2\gamma V_m^\alpha}{RTr}\right) \tag{11}$$

where P_r^β is the vapor pressure of the solid α phase. It is worth noting that the vacancy concentration can be viewed as a dispersed vacuum phase, so the effect of curvature on vacancy concentration is opposite of the effect on vapor pressure (i.e., vacancy concentration is highest at a concave surface while vapor pressure is lowest) [12]. An illustration of the Gibbs-Thomson effect on vapor pressure as well as on vacancy concentration is given in Figure 6.

These three contributions of bulk pressure, vacancy concentration, and vapor pressure result in the mass transport phenomena that lead to coarsening and densification [12]. These mechanisms along with their diffusion paths and overall effects are given in Table 1.

Viscous flow is the process by which glass and polymeric solids densify via a

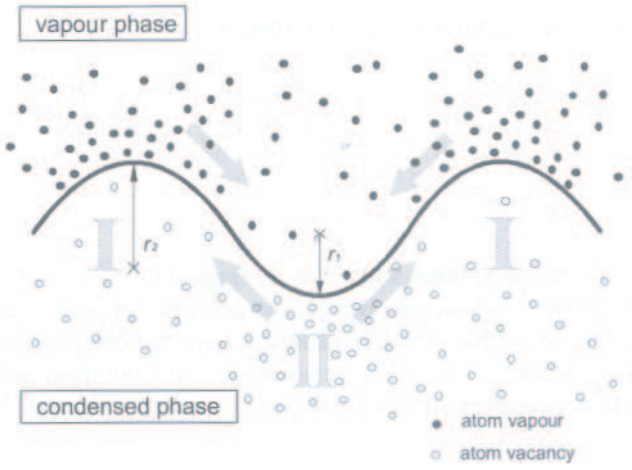

Figure 6: Illustration of the effect of surface curvature on vacancy concentration and vapor pressure [12].

Table 1: Solid-State Sintering Densification and Coarsening Mechanisms [11][13][14]

Mechanism	Path of Atoms	Result
Viscous Flow	Lattice → Neck	Densification
Plastic Flow	Dislocation → Neck	Densification
Evaporation-Condensation	Surface → Vapor → Neck	Coarsening
Volume/Lattice Diffusion	Boundary → Lattice → Neck	Densification
Grain Boundary Diffusion	Boundary → Neck	Densification
Surface Diffusion	Surface → Neck	Coarsening

decrease in viscosity with increasing temperature. This process applies only to amorphous materials, because the neck formed between two sintered particles is distinguished by the lack of a grain boundary. Consequently, viscous flow is not observed during the solid-state sintering of crystalline materials [13].

Plastic flow contributes to mass transport during solid-state sintering via two potential mechanisms:

1. Nonconservative dislocation motion (dislocation climb) due to vacancy diffusion

   or

2. Dislocation glide

Dislocation climb facilitates densification by annihilating vacancies originating

from surrounding pores. This process is accelerated by higher temperatures that increase lattice vibrations and result in larger equilibrium vacancy concentrations. Accordingly, a higher prevalence of dislocations would necessarily accelerate this vacancy annihilation process. As an example, experiments with cold-worked iron powders have shown that a higher dislocation density can raise the sintering rate by 10 to 100 times. However, this dislocation climb process occurs early in the sintering process and ultimately ceases as dislocation density is reduced. Dislocation glide also occurs early in the sintering process due to the high sintering shear stresses (which promote dislocation glide) observed at the outer surface of a newly formed neck between two particles [13].

Evaporation-condensation is the process whereby material evaporates from a particle surface, is transported across a pore, and condenses on a neighboring surface. This process results in the reduction in total surface free energy via the reduction in particle surface area; however, particle centers do not approach and no densification occurs. Evaporation-condensation results in the reduction of surface area due to mass transport from convex surfaces to concave surfaces [14]. The resulting coarsening effect can dramatically reduce sinterability, and this problem is exacerbated by the higher vapor pressure associated with small powders. This effect is pronounced for materials that exhibit sintering-related weight loss, such as boron nitride and boron carbide. Mass transport to the inter-particle neck via evaporation-condensation is ultimately limited by the balance of the solid-solid free energy (γ_{ss}) and the solid-vapor free energy (γ_{sv}) at the equilibrium dihedral angle ϕ according to the equation

$$\gamma_{ss} = 2\gamma_{sv} \cos\frac{\phi}{2} \tag{12}$$

which can be further approximated by the equation

$$X = G \sin\frac{\phi}{2} \tag{13}$$

where X is neck diameter and G is grain size. Continued neck growth beyond this point depends on grain growth, in which grain size, G, usually follows a power law relationship with time ($G \approx t^n$ where n=1/2 to 1/4, with n=1/3 being a typical value). An illustration of two solid-state sintered particles with labeled dimensions is provided in Figure 7 [13].

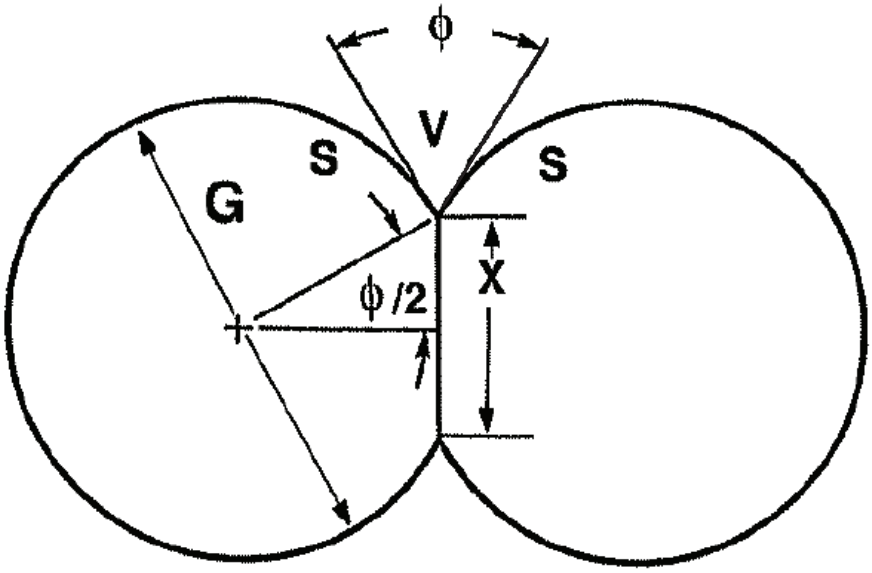

Figure 7: Illustration of solid-state sintered particles with labeled dimensions [13]

Volume diffusion (also referred to as lattice diffusion) is the result of vacancy diffusion through a crystalline lattice. The kinetics of volume diffusion are affected by three separate parameters [13]:

1. Temperature
2. Composition
3. Curvature

Temperature influences the rate of volume diffusion due to the exponential increase in equilibrium vacancy concentration, C_v, with increasing temperature, which follows the Arrhenius relationship

$$C_v = \exp\left(-\frac{Q_v}{RT}\right) \tag{14}$$

where Q_v is the activation energy required for vacancy formation, R is the ideal gas constant, and T is temperature.

Composition influences volume diffusion by altering the vacancy concentration from that observed at the stoichiometric composition. This effect is observed primarily for ionic compounds, because ionic materials with non-stoichiometric compositions must contain excess vacancies in order to maintain charge neutrality. For example, the addition of TiO_2 to Al_2O_3 facilitates sintering via the creation of excess vacancies [14]:

$$3\mathrm{Ti}_{\mathrm{Al}} + \frac{3}{4}\mathrm{O}_2(\mathrm{g}) = 3\mathrm{Ti}_{\mathrm{Al}}^{\cdot} + \mathrm{V}_{\mathrm{Al}}^{'''} + \frac{3}{2}\mathrm{O}_{\mathrm{o}} \tag{15}$$

Curvature affects volume diffusion via the previously mentioned Gibbs-Thomson relationship which describes the effect of particle surface curvature on vacancy concentration. Concave surfaces exhibit vacancy concentrations higher than equilibrium, while convex surfaces exhibit lower vacancy concentrations than equilibrium.

The effects of temperature, composition, and curvature on sinterability are sufficiently described by Fick's first law:

$$J = -D_v \frac{dC}{dx} \tag{16}$$

where J is the atomic or vacancy flux, D_v is the vacancy diffusion coefficient, and $\frac{dC}{dx}$ is the vacancy concentration gradient. Greater mass transport (i.e., larger flux) can be expected from enhanced vacancy diffusivity (from higher temperatures and/or composition variation) and a larger vacancy concentration gradient (from smaller particles that possess higher radii of curvature).

There are three pathways through which vacancy transport occurs via volume diffusion. The first pathway is the diffusion of vacancies from the grain boundary

between two grains to an adjacent pore (or neck surface). This process results in mass transport from particle interiors to the interparticle region, resulting in densification. The second path is the diffusion of vacancies from the particle interior to the interparticle grain boundary via dislocation climb, which was discussed previously. This process also results in densification. The third pathway is a theoretical concept which involves mass transport from the particle surface, through the inside of the particle, to the neck surface between two particles. This mass transport mechanism, termed volume diffusion adhesion, would ultimately result in surface-to-surface transport, which would not cause densification. Currently, there is no significant data indicating the predominance of this adhesion process during sintering. It is important to note that volume diffusion typically only becomes a dominant mass transport mechanism at high temperatures. Competing mechanisms, such as grain boundary diffusion and surface diffusion, which possess lower activation energies, are more commonly observed. An illustration of the volume diffusion pathways is provided in Figure 8 [13].

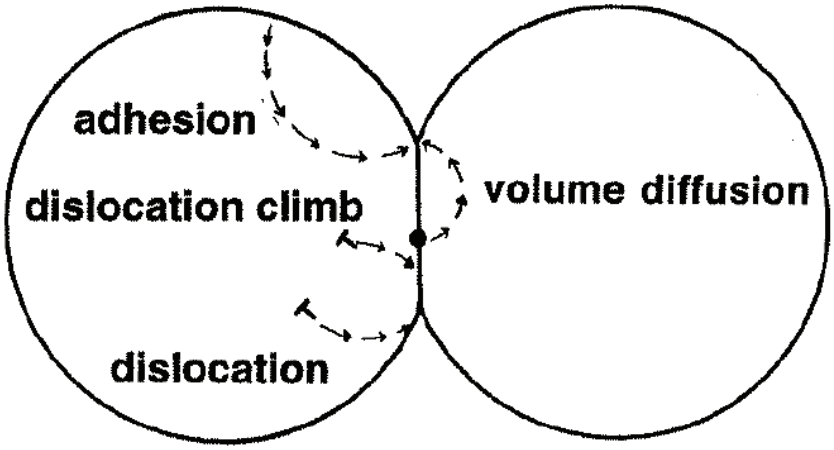

Figure 8: Illustration of volume diffusion pathways [13]

Volume diffusion can also contribute to the coarsening of pores near the end of the sintering process. This Ostwald ripening process results from the difference in

equilibrium vacancy concentrations associated with pores of differing sizes/radii of curvature; smaller pores (with higher vacancy concentrations) are vacancy sources while larger pores (with lower vacancy concentrations) are vacancy sinks. The diffusion of vacancies along grain boundaries from the smaller pores to the larger pores results in overall pore coarsening. An illustration of pore coarsening is provided in Figure 9 [13].

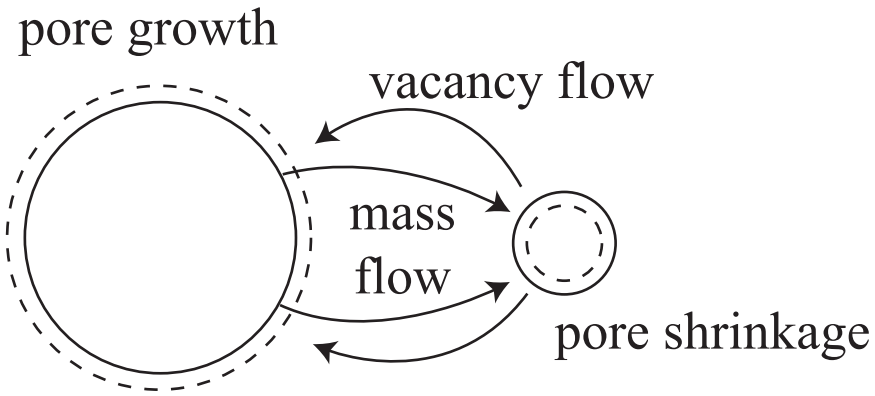

Figure 9: Illustration of pore coarsening [13]

Grain boundary diffusion involves the transport of material along the highly defective region between two sintered particles that accommodates misaligned crystallographic orientations. It should be noted that diffusion along a grain boundary requires more activation energy than surface diffusion but less energy than volume diffusion. Additionally, grain boundary diffusion requires the formation of sintered bonds between adjacent particles, so the elimination of free surfaces via surface diffusion or evaporation-condensation processes are prerequisite. Grain boundaries act as vacancy sinks via particle rotation and slip, allowing mass to be transported to the bond between particles. As sintering progresses and densification increases, the larger number of inter-particle bonds sufficiently increases the compact strength so as to preclude particle movement, making grain boundaries ineffective vacancy sinks (because grain boundary movement is required to accomodate vacancy buildup).

The grain boundary energy is a significant factor determining sintering behavior. A low grain boundary energy results in increased sinterability and densification, because the replacement of free surfaces with grain boundaries is more energetically favorable. A low grain boundary energy is characterized by a high dihedral angle between sintered particles. Conversely, a high grain boundary energy results in reduced sinterability and is characterized by a low dihedral angle. Additionally, a high grain boundary energy can result in significant grain growth as a system seeks to reduce overall free energy via the reduction in total grain boundary area. Grain growth can be reduced via the presence of porosity or second-phase additions that preferentially segregate at the grain boundaries and thereby reduce the grain boundary energy by acting as diffusion barriers [13]. This grain boundary pinning effect is illustrated in Figure 10 [13].

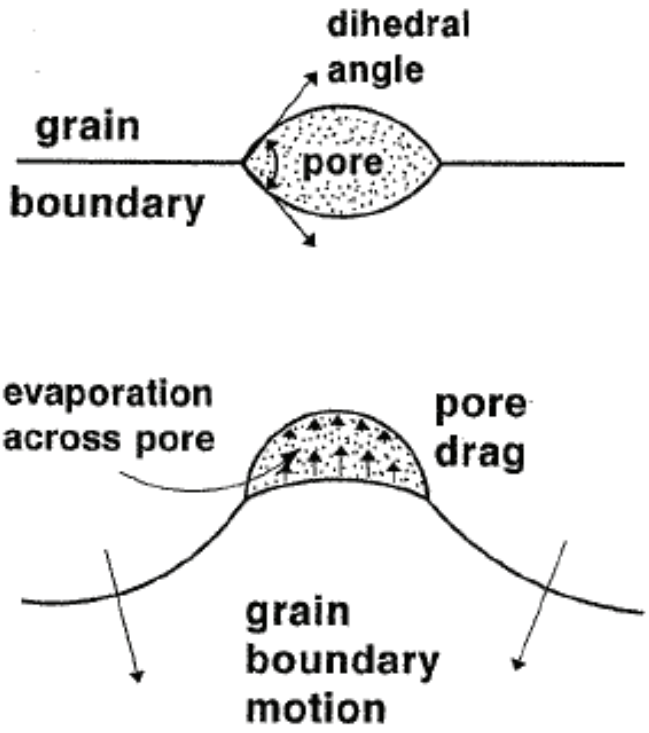

Figure 10: Illustration of grain boundary pinning due to a pore or second-phase particle [13]

Surface diffusion results from the movement of atoms along the defects present on a particle surface. Surface diffusion is enhanced by the larger concentration of surface defects made possible by higher temperatures and increased surface curvature (i.e., small particles). Additionally, certain crystallographic orientations may also increase the surface defect concentration and thus facilitate surface diffusion. Surface diffusion involves the breaking of a bond at the surface, transport of an atom along the surface, and the formation of a new bond at another surface site. The activation energy required for surface diffusion is typically less than that required for other transport mechanisms; therefore, surface diffusion is typically observed at lower temperatures early in the sintering process. Surface diffusion ceases as free surfaces are consumed via the creation of sintered bonds between particles. It is important to note that surface diffusion does not result in densification due to the surface-to-surface transport path. Fast heating rates can be used to heat to temperatures at which densifying mass transport mechanisms (e.g., volume diffusion) would overcome the coarsening effect of surface diffusion [13]. An illustration of the diffusion pathways active during solid-state sintering is provided in Figure 11.

Solid-state sintering has been described as taking place in three stages during which the different mass transport mechanisms discussed above dominate. During the initial stage of sintering, surface diffusion and evaporation/condensation are the dominant mass transport mechanisms and result in neck formation between adjacent particles. Particle rearrangement occurs and curvature gradients between particles are reduced. Densification does not occur during this initial state. During the intermediate stage of sintering, grain boundary and volume/lattice diffusion dominate and result in the movement of atoms from particle interiors to the neck and surrounding pores. Pores become rounded and adopt cylindrical geometries along grain edges. The preponderance of densification occurs during this intermediate stage. An illustration of the porosity geometry observed during this intermediate stage of sintering

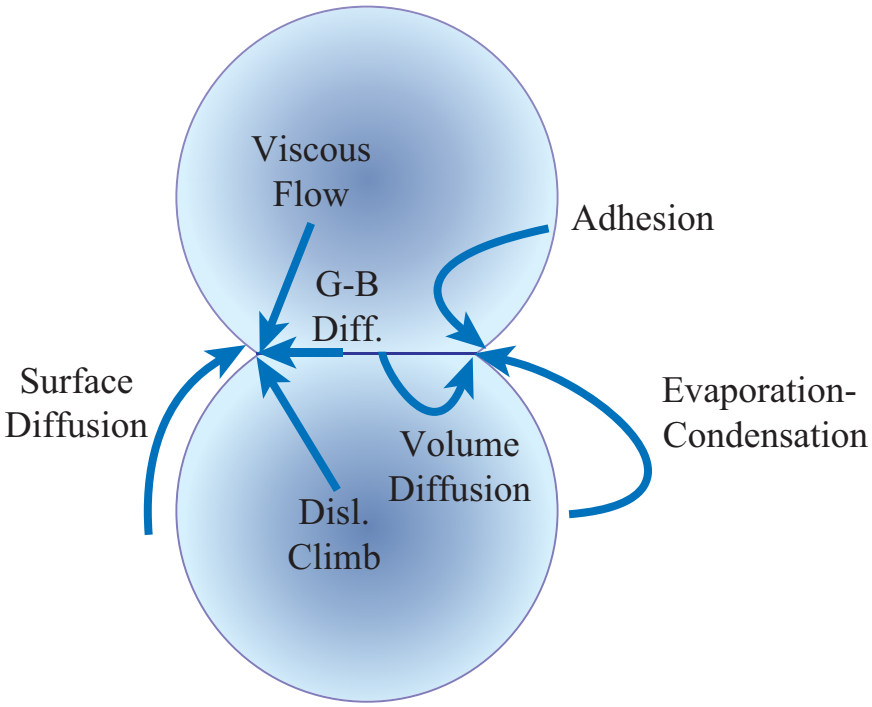

Figure 11: Summary illustration of solid-state sintering diffusion pathways [13]

is provided in Figure 12.

During the final stage of sintering, pores shrink and become isolated at grain triple points and are no longer effective for pinning grain boundaries. It is important to note that pore shrinkage will occur for pores with diameters less than one half the average grain size, large dihedral angles, and low coordination numbers. As a result, pore removal can be assisted via improved particle packing. Grain boundary diffusion results in grain growth, which reduces the grain boundary area and thus reduces total grain boundary energy. Further grain growth may lead to exaggerated grain growth, where larger grains grow at the expense of smaller grains. Exaggerated grain growth may lead to pore entrapment, in which grain boundary migration causes pores to become permanently trapped within grain interiors [13][14].

Several models have been proposed to describe the kinetics of solid-state sintering. An isothermal kinetic model for the shrinkage ($\Delta L/L_o$) of particles of a given diameter (D) during solid-state sintering is given by the equation [13]:

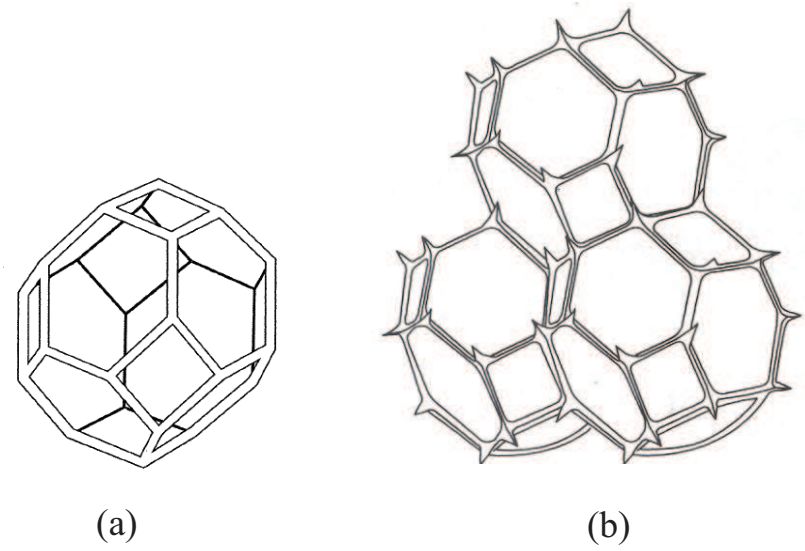

Figure 12: Illustration of the intermediate stage interconnected pore structure for (a) a single grain and (b) several grains [13]

Table 2: Solid-State Sintering Model Variables [13]

Mechanism	n	m	B
Viscous Flow	2	1	$3\gamma\eta$
Plastic Flow	2	1	$9\pi\gamma b D_v/kT$
Evaporation-Condensation	3	2	$(3P\gamma/\rho^2)(\pi/2)^{1/2}(M/kT)^{3/2}$
Volume/Lattice Diffusion	5	3	$80D_v\gamma\Omega/kT$
Grain Boundary Diffusion	6	4	$20\delta D_b\gamma\Omega/kT$
Surface Diffusion	7	4	$56D_s\gamma\Omega^{4/3}/kT$

$$\left(\frac{\Delta L}{L_o}\right)^{n/2} = \frac{Bt}{2^n D^m} \tag{17}$$

The variables n, m, and m can be altered in order to more appropriately describe the multitude of mass transport mechanisms described in Table 1. Typical values for these variables are provided in Table 2.

Variable Descriptions:

γ=surface energy	D_v=volume diffusivity
η=viscosity	D_s=surface diffusivity
b=Burgers vector	D_b=grain boundary diffusivity
k=Boltsmann's constant	P=vapor pressure
T=absolute temperature	M=molecular weight
ρ=theoretical density	Ω=atomic volume
δ=grain boundary width	

2.4.2 Liquid-Phase Sintering

The sintering of powders in the presence of a wetting liquid phase is termed liquid-phase sintering. This liquid formation during the sintering process typically results in an increase in the densification rate when compared to solid-state sintering. The driving force for liquid-phase sintering remains the reduction in surface free energy as in solid-state sintering [13]. Liquid-phase sintering is sometimes preferred over solid-state sintering, because the melting of a secondary or eutectic phase can allow for lower process temperatures that may reduce the occurrence of grain growth in the primary particulate phase [11]. An early model for liquid-phase sintering developed by Cannon and Lenel occurred in three stages: 1) liquid flow, 2) solution/precipitation, and 3) solid-state sintering [15].

In the liquid flow stage, additive particles melt into a liquid that surrounds adjacent solid particles. The contact angle between a solid particle and a wetting liquid represents the balance of the interfacial energies, as illustrated by the equation

$$\gamma_{sv} = \gamma_{sl} + \gamma_{lv}\cos(\theta) \tag{18}$$

where γ_{sv} is the solid-vapor interfacial energy, γ_{sl} is the solid-liquid interfacial energy, γ_{lv} is the liquid-vapor interfacial energy, and θ is the wetting angle. In order for a

liquid to completely wet a solid, it is required that $\gamma_{sv} > \gamma_{sl} + \gamma_{lv}$ [13]. A wetting liquid on the surface of solid particles will tend to flow into smaller sized pores. This is an important experimental concern, because larger solid particles that melt upon heating to form a liquid will leave behind large pores as the liquid flows into surrounding smaller pores. Consequently, smaller-sized second-phase particles are desirable, because the smaller pores they leave behind after liquid flow are more easily removed during sintering [13]. The capillarity effect resulting from a wetting liquid between two particles results in a pressure difference across the surface of the liquid. In a similar application of the Laplace equation used in solid-state sintering, the difference in pressure (ΔP) across a curved liquid surface is given by the equation

$$\Delta P = \gamma_{lv} \left(\frac{1}{R_1} + \frac{1}{R_2} \right) \tag{19}$$

where γ_{lv} is the liquid-vapor interfacial energy, and R_1 and R_2 are the radii of curvature [13]. This pressure difference across the liquid surface results in a compressive force that brings the particles closer together. Additionally, this force is responsible for the particle rearrangement, densification, and contact flattening associated with liquid-phase sintering. This force is described by the equation

$$F = \frac{\pi}{4} X^2 \Delta P + \pi X \gamma_{lv} \cos(\psi) \tag{20}$$

where ΔP is the pressure difference due to the surface curvature of the liquid, and ψ is the angle illustrated in Figure 13.

Particles that are connected by a liquid meniscus as illustrated in Figure 13 are drawn together towards the equilibrium state of zero separation distance for a completely wetting liquid. This attractive force increases as the separation distance decreases. For incompletely wetting liquids, the equilibrium state is a non-zero separation distance, in which a liquid meniscus connects the two particles. As liquids become increasingly non-wetting on the solid particles, the attractive force between

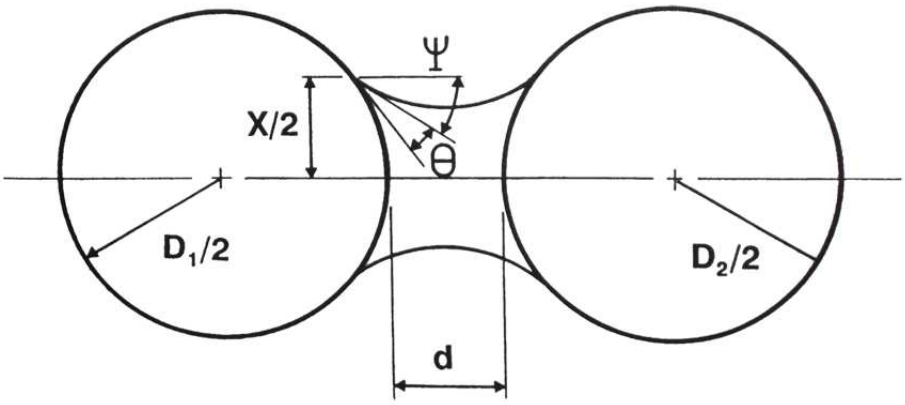

Figure 13: Illustration of the two-sphere model with interparticle liquid [13].

the two particles transitions into a repulsive force. This repulsion is typically observed in systems with contact angles of 60° or more and results in expansion of the part as the liquid phase forms [13].

For systems in which the liquid sufficiently wets the solid particles, the capillary force results in the compression of the inter-particle contact areas. This compressive force can be substantial. For example, a 1 μm particle with a surface free energy of 1 J/m^2 results in a compressive stress of approximately 10 MPa. This compressive stress results in particle rearrangement, which allows particles to reorient and achieve higher packing densities [13].

In the second stage of the Cannon and Lenel liquid-phase sintering model, densification occurs via a solution/precipitation process. For this stage, the solubility of the solid within the liquid, and the liquid within the solid are of experimental concern. A high solubility of the liquid within the solid is not desirable, because it may lead to part bloating during heating. However, a solubility of the solid within the liquid in the range of 1 to 20 vol% is desirable, because densification is facilitated by the solution/precipitation mass transport mechanism that results in mass transport from smaller particles to larger particles [13]. This 'Ostwald ripening' phenomenon is described by the Lifshitz-Slyozov-Wagner (LSW) theory and results from the increased

solubility of the solid within the liquid that is observed as particle size decreases [12]. The effect of particle size on solubility is given by the equation

$$\ln\left(\frac{C}{C_o}\right) = \frac{4\gamma_{sl}\Omega}{DkT} \tag{21}$$

where C is the solubility of the particle, C_o is the equilibrium solubility of an infinitely flat surface, γ_{sl} is the solid-liquid interfacial energy, Ω is the atomic volume, D is the particle diameter, k is Boltzmann's constant, and T is absolute temperature. Consequently, smaller particles have a higher solubility in the liquid than larger particles, which causes larger particles to grow at the expense of smaller particles [13].

It is important to note that Kingery provided a different theory for the second stage of liquid-phase sintering. Kingery's theory postulates that the phenomenon of 'contact flattening' (the flattening of particles near contact areas with adjacent particles) predominates during this second stage. For this theory, Kingery assumed a two particle model in which grain growth did not occur and in which the solid was soluble in the liquid film between the two particles. The theory states that the inter-particle compressive force resulting from the capillary pressure causes sufficient compressive stress at the inter-particle contact points to increase the chemical potential of the atoms located near those points. Consequently, the higher chemical potential atoms near the contact points dissolve more readily into the surrounding liquid and precipitate at off-contact locations where the contact pressure is lower (thus the chemical potential is lower). As a result of this mass transport, particles tend to flatten where they contact their neighbors [16].

In the final stage of the Cannon and Lenel model as well as in the theory of Kingery, the effect of solution/precipitation is said to be insignificant and densification is said to occur via a solid-state sintering mechanism. However, no details on the kinetics of this stage of the model are provided. Furthermore, the slower kinetics associated with mass transport in solid-state sintering do not agree with the faster liquid-phase

sintering densification kinetics [12].

While the Kingery adaptation of the Cannon-Lenel model is typically designated the classical model for liquid phase sintering, it does have a few deficiencies. The Kingery model predicts the continual decrease in pore size as sintering time increases; however, in real systems, the incidence of small pores tends to decrease while that of large pores does not change until densification is complete [12]. The assumption that grain growth does not occur is also problematic, because achieving equilibrium grain geometry would require both the phenomena of contact flattening and grain growth [17]. As a result of the deficiencies of the Kingery model, Kang suggested that contact flattening is a mechanism that only takes place early in the sintering process and assists in the development of equilibrium grain geometry [12].

Other liquid-phase sintering models have been developed based on the theory of pore filling. Kwon and Yoon proposed a model composed of three stages: 1) liquid coagulation, 2) liquid redistribution, and 3) liquid filling of pores. In the initial stage, liquid coagulation results in the reduction of the liquid-vapor interfacial energy via liquid flow. In the second stage, liquid redistribution results in a more uniform microstructure via the creation of a homogeneous distribution of pores [18][19]. These first two stages occur very quickly during the initial heating process, so the liquid filling of pores is the dominant densification mechanism [20]. An illustration depicting the pore filling process is provided in Figure 14.

The overall driving force for the pore filling stage is the capillary pressure resulting from the liquid wetting the particle surfaces [21]. Initially, if the gas pressure within the pore is equal to the pressure of the surrounding atmosphere, then the pressure acting on the wetting liquid is everywhere uniform. As grain coarsening occurs, the radius of the liquid meniscus increases linearly with grain size [22]. With continued grain growth, the radius of the liquid meniscus eventually becomes equal to the pore radius and the liquid completely wets the pore. Any further grain growth beyond this

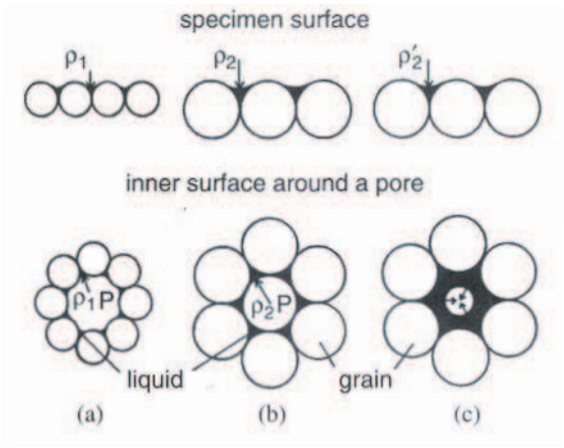

Figure 14: Illustration of the pore-filling model: (a) initial particles and liquid around a pore, (b) the critical point at which liquid meniscus radius is equal to the pore radius, and (c) liquid filling of the pore following continued grain growth. ρ is the radius of the liquid meniscus, where $\rho_1 < \rho_2 < \rho_2'$ [12].

critical pore wetting results in a difference in liquid pressure between the compact surface and the pore interior. This pressure difference occurs, because the radius of the liquid meniscus at the surface of the pore is limited by the radius of pore, but the liquid meniscus at the surface of the part has no such limitation. As a result, any further grain growth results in the liquid filling of the pore [21].

This model of pore filling was further developed by Kang [23]. Kang stated that the process of pore filling described above results in a corresponding decrease in the pressure of the liquid surrounding grains throughout the compact. This pressure decrease in the liquid results in a higher capillary pressure between grains and causes grains to adopt space-filling geometries as they grow. Additionally, the newly liquid-filled pores are homogenized into the microstructure via growth of the surrounding grains [23].

The pore filling model is fundamentally different from the classical Kingery model. The contact flattening mechanism of Kingery requires high capillary pressure (which in turn requires small particles) to facilitate the dissolution and reprecipitation of solid

particles from the high-pressure contact points to regions of lower pressure. Additionally, the Kingery model is deficient in explaining several experimental phenomena in liquid-phase sintering. Conversely, the pore filling model involves the grain-growth-driven difference in liquid pressure to drive densification. Also, since the point of critical pore filling is proportional to the pore size, this model implies that pores are filled in the order of smallest to largest, which concurs with experiment [21][24]. Given that pore filling is a process driven by grain growth (i.e., the larger grains become, the larger the number of filled pores), a system with a given pore size distribution is more easily densified by a coarser grained powder [25]. It is important to note that the potential use of a coarser powder has economic implications since powder cost drops dramatically with increasing particle size.

2.5 Sintering of B_4C

Boron carbide has historically been difficult to sinter to high densities without the application of pressure or the introduction of additives. Hot-pressing is currently the most common method for the densification of boron carbide small arms protective insert (SAPI) plates that are issued to U.S. servicemen. Hot pressing densifies boron carbide powders via the simultaneous application of heat (∼2100 °C) and pressure (30-40 MPa) and results in articles that are approximately 98% of theoretical density [26][27].

Explanation for the poor sintering behavior of boron carbide without the application of pressure or the introduction of additives was established only recently. Dole *et al.* found that boron carbide samples exhibited strong evidence of particle coarsening following the sintering of additive-free boron carbide samples at 2000 °C. Conversely, boron carbide samples to which carbon had been added did not exhibit coarsening. It was postulated that liquid boron oxide coatings may have facilitated the rapid surface diffusion of boron carbide and resulted in the observed coarsening

[28][29][30]. Lee and Speyer described two additional coarsening mechanisms. The first mechanism involved the evaporation and condensation of boron oxide and the second involved the evaporation and condensation of boron carbide at higher temperatures [1].

In order to research these coarsening phenomena and their effect on the densification of boron carbide, Lee and Speyer performed a systematic study using a high-temperature graphite resistance furnace coupled with a differential dilatometer. The study examined the sintering behavior of boron carbide powder (HS, H. C. Starck GmbH, Goslar, Germany) with a specific surface area of 18.8 m^2/g. Early analysis showed that boron carbide densification began at ∼1800 °C and that significant densification occurred from 1870 °C to 2010 °C. This initial densification was attributed to the physical contact of boron carbide surfaces following the vaporization of boron oxide coatings. Between 2010 °C and 2140 °C, densification continued but was slowed by a simultaneous coarsening process that was perceived to be the result of high-temperature evaporation-condensation mass transport. Above 2140 °C, the rate of densification increased via the formation of a eutectic grain boundary liquid or an activated sintering process (due to the increased grain boundary diffusivity made possible by residual carbon remaining after the preferential vaporization of boron). Continued work by Lee and Speyer indicated that densification was improved by the introduction of approximately 10% H_2 gas into a flowing He gas atmosphere and holding for 30 minutes at 1350 °C before heating to higher sintering temperatures. They suggested that a hydrogen-containing atmosphere facilitates the volatilization of boron oxide coatings on particle surfaces via the reaction

$$H_2(g) + B_2O_3(l) \leftrightarrow H_2O(g) + B_2O_2(g) \tag{22}$$

In addition to the boron oxide removal, rapid heating through the previously mentioned coarsening temperature regimes greatly improved densification and allowed

the production of 94.7% dense samples [1].

Cho, Bao, and Speyer studied the effect of soaking temperature on the microstructure and hardness of sintered boron carbide samples. The time required to reach the extent of sintering was determined by holding at the soak temperature until the shrinkage rate approached a value of 0.005%/min. They observed that continued heat treatment beyond the determined extent time resulted in significant grain growth. Additionally, higher temperatures resulted in abnormal grain growth in samples sintered at temperatures above 2298 °C. A sintering temperature of 2317 °C resulted in a bimodal grain size distribution. Samples sintered at 2336 °C exhibited large grains of similar size containing porosity trapped within grain interiors. Additionally, x-ray analysis indicated an increase in graphite concentration in boron carbide samples processed at temperatures of 2317 °C and above. X-ray diffraction peak splitting also suggested the decomposition of boron carbide for sintering temperatures at and above 2336 °C. Higher process temperatures resulted in ultimately poor material properties; samples sintered at temperatures in excess of 2300 °C exhibited reduced density and hardness values. For temperatures below 2300 °C, experiments in which samples were sintered only to extent indicated that relative density and Vickers hardness increased with sintering temperature, reaching a maximum for samples sintered at ∼2250 °C to 2300 °C. Post-hot isostatic pressing (post-HIPing) of samples with entirely closed porosity (i.e., samples with relative densities $\geq$ 93%) resulted in theoretically-dense articles with improved hardness values compared to hot-pressed boron carbide. A plot illustrating the hardnesses and relative densities associated with different process temperatures is given in Figure 15. Additionally, a comparison of non-HIPed and HIPed boron carbide microstructures is provided in Figure 16 [2].

Prior to the work of Lee, Cho, Bao and Speyer, the pressureless sintering of boron carbide was achieved via the introduction of second-phase additives. Carbon is the most commonly known sintering aid for boron carbide. Carbon is typically added in

the form of phenolic resin (which decomposes at high temperatures to yield ∼50 wt% carbon) and permits the pressureless densification of boron carbide at 2150 °C to 98% of theoretical density [31]. Carbon permits the removal of boron oxide coatings at lower process temperatures (∼1350 °C) via the reaction

$$6C + 2B_2O_3 \leftrightarrow B_4C + 6CO \tag{23}$$

Furthermore, it has been suggested that free carbon may facilitate activated solid-state sintering by increasing diffusion along grain boundaries. Another explanation for improved densification due to carbon addition is the formation of a eutectic liquid at the grain boundaries [32]. A eutectic is observed in the B_4C-C system beginning at 2245 °C [33]. This eutectic temperature may be reduced for systems with sub-micron particles of higher surface free energy. Additionally, carbon may also function as a sintering aid via grain boundary pinning, whereby the segregation of carbon between grains limits grain growth.

It should be noted that sintering aids may also be used to facilitate hot-pressing. EDS and x-ray diffraction analysis by Cho [34] and Vargas [35] have revealed the presence of graphite and alumina in hot-pressed samples from two manufacturers. These hot-pressed samples exhibited reduced hardness values (∼2450 kg/mm^2 for the hot-pressed sample containing graphite and ∼2625 kg/mm^2 for the hot-pressed sample containing alumina) when compared to the hardness of theoretically-dense and additive-free boron carbide (∼2950 kg/mm^2).

While carbon is the most commonly used additive, other materials have also been used to facilitate the densification of boron carbide and the improvement in mechanical properties. These additives are best organized by the mechanisms through which they facilitate boron carbide densification or improve the mechanical properties.

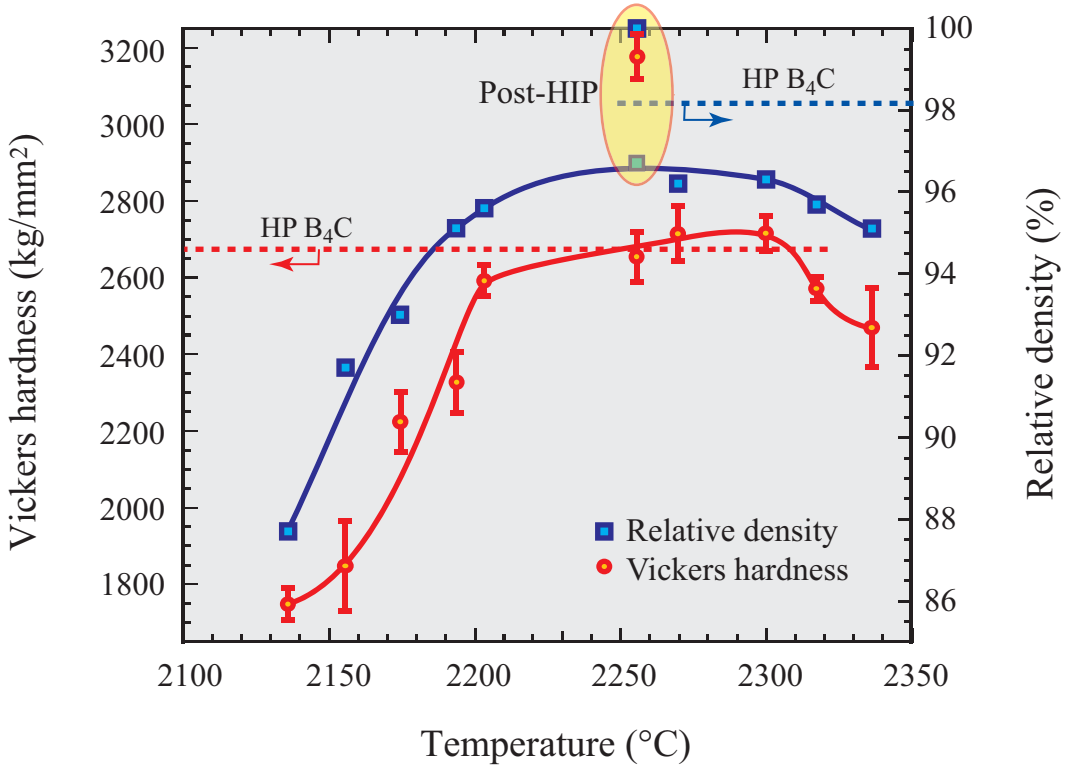

Figure 15: Effect of process temperature on the Vickers hardness and relative density of boron carbide [2].

2.5.1 Grain Size Refinement

Kanno *et al.* performed studies on the effect of Al, TiB_2, SiC, and AlF_3 additions on the densification of B_4C. They determined that the addition of Al produced the highest density ($\sim$ 95%) by sintering at 2200 °C in a flowing argon atmosphere for 30 min. Kanno *et al.* also observed that all of the additives except SiC resulted in reduced grain and pore growth, and proposed that this observation was caused by the additive-induced reduction in surface transport [36].

Ekbom *et al.* found that grain growth in boron carbide could be inhibited by the addition of small amounts (1-5 at%) of silicon or aluminum, resulting in a flexural strength increase [37]. Telle and Petzow proposed that the reduction in grain growth due to the addition of Si was the formation of a B_4C-Si solution that subsequently

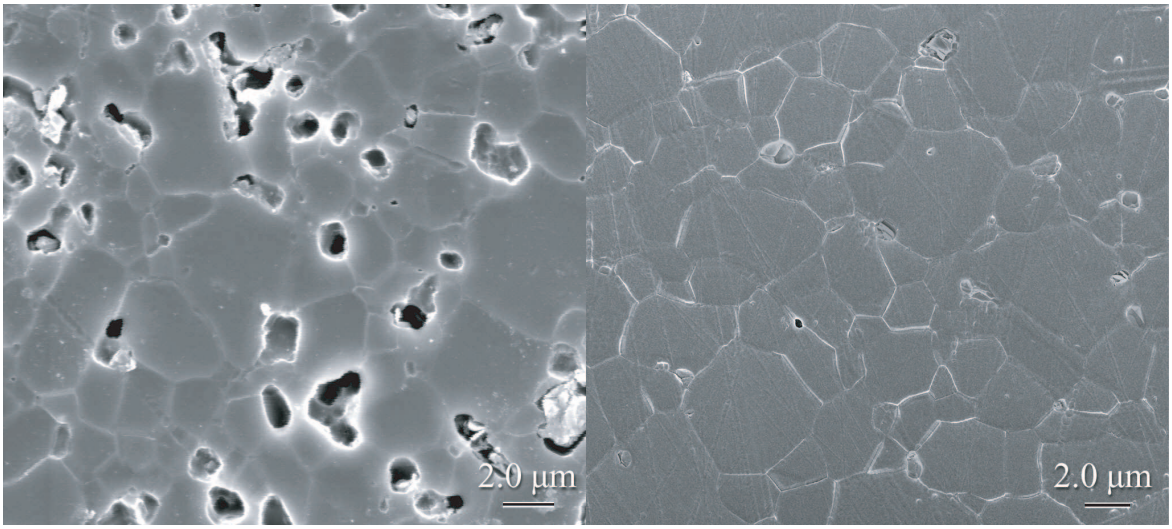

Figure 16: Left: Microstructure of pressureless-sintered boron carbide ($\rho_{rel} \approx 93\%$), Right: Microstructure of pressureless-sintered and post-HIPed boron carbide ($\rho_{rel} = 100\%$) [2].

precipitated a 100-200 nm layer of SiC on the surrounding B_4C particles. They postulated that the mobility of the grain boundaries may have been reduced by this thin SiC layer and resulted in minimal B_4C grain growth [38]. Lorcher *et al.* investigated the effect of polysilane additives on the formation of B_4C-SiC composites. They observed that the metallorganic polysilane precursor resulted in the uniform dispersion of SiC throughout the microstructure following pyrolysis at 1000 °C. As with Telle and Petzow, the researchers noted that the presence of the SiC at the boron carbide grain boundaries inhibited grain growth and resulted in a finer microstructure [39]. It is noted that the results of Ekbom *et al.*, Telle and Petzow, and Lorcher *et al.* disagree with the findings of Kanno *et al.*. MgO is another effective additive. MgO inhibits particle growth during the magnesiothermal reduction method of boron carbide formation, resulting in very fine (specific surface area ≈ 21 m^2/g) particles [4].

It should be noted that in addition to assisting sintering, grain size refinement via the addition of second-phase compounds may substantially increase the flexural strength of boron carbide. Sasaki *et al.* reported flexural strengths as high as 820

MPa for boron carbide containing 10 vol% TiC that was hot-pressed at 2150 °C [40]. Additionally, Telle and Petzow reported flexural strength values approaching 1100 MPa for HIPed boron carbide containing dispersed TiB_2 and W_2B_5 additives [41].

2.5.2 Toughening

Skorokhod *et al.* analyzed the mechanical properties of fully dense B_4C-TiB_2 composites formed via the pressureless sintering of submicron B_4C, TiO_2, and carbon powders at 2050-2100 °C. They observed maximum values of flexural strength (500 MPa) and fracture toughness (4.6 MPa·$m^{1/2}$) for the sample containing 15 vol% TiB_2. The increases in flexural strength and fracture toughness were attributed to the thermal mismatch between the TiB_2 grains and the surrounding B_4C matrix. Crack branching and cracking around the circumference of TiB_2 grains were observed and interpreted as the primary toughening mechanisms [42].

Sigl *et al.* also performed a detailed analysis on the effects of microcracking in B_4C-TiB_2 composites. They formed these composites via the processing of mixed B_4C and TiB_2 powders that included phenolic resin as a carbon source. The samples were sintered at 2175 °C in an argon atmosphere for 2 hours and post-HIPed at 2050 °C under 200 MPa of argon for 30 minutes. Mechanical testing of pre-notched bars revealed that the fracture toughness of the composites increased from 2.2 MPa·$m^{1/2}$ for pure boron carbide to 3.0 MPa·$m^{1/2}$ and 3.6 MPa·$m^{1/2}$ for composites with 20 wt% and 40 wt% TiB_2, respectively. Increased microcracking and a higher toughness were observed in samples where carbon segregated to the B_4C-TiB_2 grain boundaries; fracture toughness values near 6 MPa·$m^{1/2}$ were observed for samples containing 4.78 wt% carbon. Sigl *et al.* proposed that the presence of carbon resulted in a weak interface that promoted microcracking and consequently resulted in increased toughness [43]. A microstructure image of circumferential cracking around TiB_2 grains in the B_4C-TiB_2 composites produced by Sigl *et al.* is provided in Figure 17.

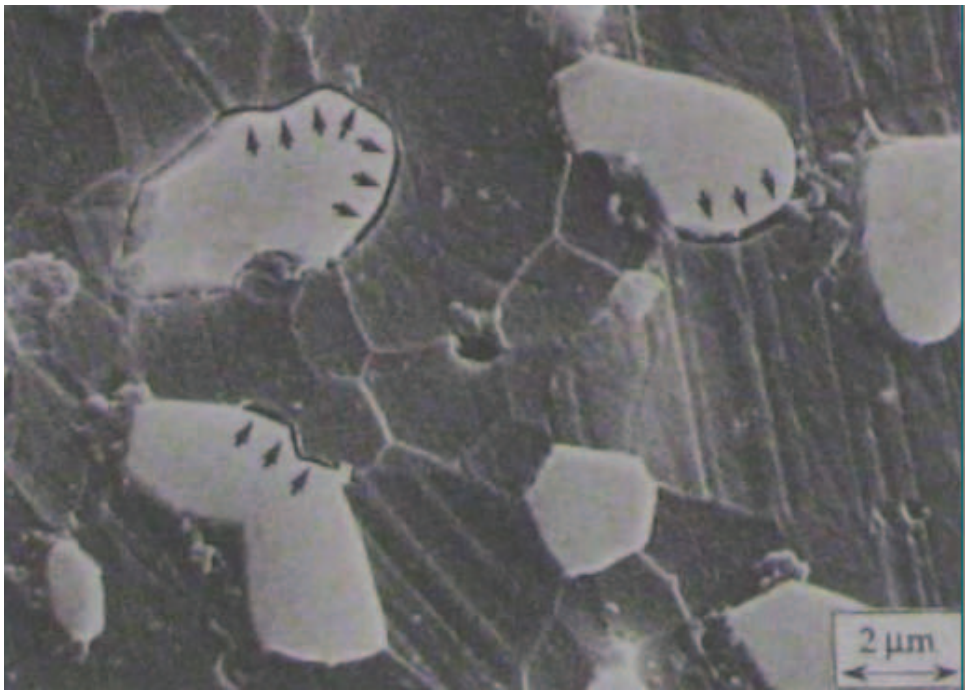

Figure 17: Microstructure of B_4C-TiB_2 composites containing microcracks (indicated by arrows) [43].

Wen *et al.* observed that the hot-pressing of boron carbide powders with 20 to 40 vol% tungsten carbide resulted in significant densification as well as improvements in flexural strength and fracture toughness. Hot-pressing at 1900 °C and 35 MPa of pressure for 30 minutes resulted in fracture toughness values of 6.98 MPa·$m^{1/2}$ and 8.70 MPa·$m^{1/2}$ for the 20 vol% and 40 vol% tungsten carbide compositions, respectively. Wen *et al.* attributed the increased fracture toughness to the formation of tungsten boride via the following reaction:

$$5B_4C + 8WC \leftrightarrow 4W_2B_5 + 13C \tag{24}$$

The formation of W_2B_5 resulted in weak bonding between grains, which enhanced microcracking [44]. Telle and Petzow recommended that fracture toughness can be increased by the mixture of a low thermal expansion matrix such as B_4C with a high thermal expansion additive such as TiC, TiB_2 or W_2B_5. They stated that in such systems, the operational toughening mechanisms are crack deflection and crack

branching [45].

2.5.3 Lattice Distortion

Skorokhod *et al.* studied the pressureless sintering of B_4C-TiB_2 composites formed via the reaction of B_4C, TiO_2, and carbon [46]:

$$B_4C + 2TiO_2 + 3C \rightarrow 2TiB_2 + 4CO \tag{25}$$

This reaction resulted in fully dense compacts, a decreased sintering temperature (1900-2100 °C) and also led to a significant increase in fracture strength and fracture toughness [46]. They determined that the TiB_2 reaction product resulted in a lowering of the sintering activation energy from 717 kJ/mol (for 0 vol% TiB_2) to 266 kJ/mol (for 25 vol% TiB_2) [47]. In a similar statement, Levin *et al.* suggested that the sinterability of boron carbide may increase as the content of the TiO_2 additive increases. Levin *et al.* also proposed that the *in situ* reaction between boron carbide and the additive oxide may facilitate sintering more than the addition of a pre-reacted metal-boride powder. Levin stated that the reaction stoichiometry preferentially resulted in the formation of boron-rich boron carbide: B_4C_{1-x}, where $x \approx 0.6$. As discussed earlier, the boron carbide unit cell distorts and the unit cell volume increases with increasing boron content. Levin proposed that carbon atoms located on the boron carbide C-B-C chains are preferentially removed by the reaction with the metal oxide additive. Consequently, diffusion and sinterability are enhanced by the greater unit cell volume [48]. As an example, Ekbom and Amundin demonstrated that $B_{13}C_2$ is more easily sintered than B_4C [37].

After examining the work of Levin, Kakazey *et al.* performed a detailed study of the reaction between B_4C and TiO_2 and proposed the following reaction between the two materials:

$$B_4C_{(s)} + 5TiO_{2(s)} \rightarrow 5TiB_{2(s)} + 4CO_{(g)} + 6BO_{(g)} \quad (26)$$

Via x-ray diffraction and electron paramagnetic resonance (EPR) methods, they observed that the reaction between B_4C and TiO_2 began at ∼1173 K and was comprised of two separate mechanisms: (1) gas-transport exchange reactions, and (2) diffusion of Ti into the lattice of B_4C. Their work suggested that boron carbide serves as a reducing agent for TiO_2. Following heat-treatment under low vacuum (1 Pa) of a 95 wt% B_4C and 5 wt% TiO_2 mixture at 1873 K, the primary titanium-containing phase was Ti_2O_3, whereas an identical heat-treatment of pure TiO_2 powder yielded only trace amounts of Ti_2O_3. Interestingly, the formation of TiB_2 in B_4C samples containing TiO_2 was not observed until temperatures approached 1973 K.

The EPR line width data for the pure B_4C powders followed a decreasing trend with increasing sintering temperature. Kakazey *et al.* indicated that this trend was caused by the presence of free carbon found as an impurity in the boron carbide. The combined effects of oxidative removal (carbon reacting with boron oxide) and the donor center role that carbon atoms serve for adjacent boron carbide surfaces resulted in a decreasing EPR line width with increasing sintering temperature. The EPR line width data for B_4C powders containing 5 wt% TiO_2 followed a sharply increasing trend with sintering temperature starting at ∼1373 K. The researchers explained that increasing line width was the result of the diffusion of titanium atoms into the highly defected surfaces of boron carbide particles, whereby the impurity atoms served as additional donor centers. A plot of the EPR line width data is provided in Figure 18 [50].

Goldstein *et al.* observed that the reactions of B_4C with additive metal oxides such as TiO_2, V_2O_5, ZrO_2, and Cr_2O_3 begin at ∼1000 °C and are all complete by 1600 °C [49]. These are important experimental observations, because the completion of the reaction between boron carbide and the additive may exclude liquid-phase sintering

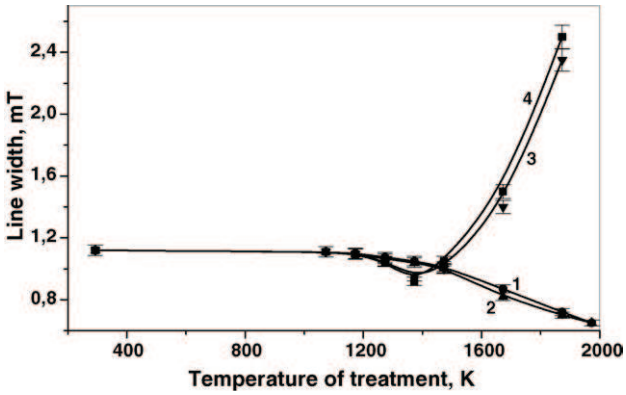

Figure 18: EPR signal line width versus sintering temperature of pure B_4C (curves 1 and 2) and B_4C containing 5 wt% TiO_2 (curves 3 and 4) [50]

at lower temperatures due to the high melting temperature of the oxide additives (e.g., TiO_2 melts at 1843 °C). However, the process may differ for lower melting temperature oxides.

It is important to note that the addition of non-oxide additives may have different effects on the boron carbide lattice. Radev and Zakhariev performed measurements of the *c* lattice parameter of boron carbide doped with varying amounts of transition metal carbide additives and observed an overall contraction of the *c* lattice parameter for compositions in which the additive composed less than 20 wt% of the total mixture. Interestingly, the *c* lattice parameter expanded for compositions containing more than 20 wt% of the carbide additives. Radev and Zakhariev attributed this lattice expansion to the solubility of the transition metal additive within the boron carbide lattice. A graph of the *c* lattice parameter changes with additive amount are given in Figure 19 [51].

The effect of strengthening via the dissolution of additive atoms within the boron carbide lattice is an important phenomenon. Portnoy *et al.* observed a higher hardness in boron carbide sintered in the presence of TiB_2 and suggested that this observation resulted from the solubility of TiB_2 in boron carbide [52]. Lipp and Roder suggested that a similar solubility strengthening mechanism occurred for the addition

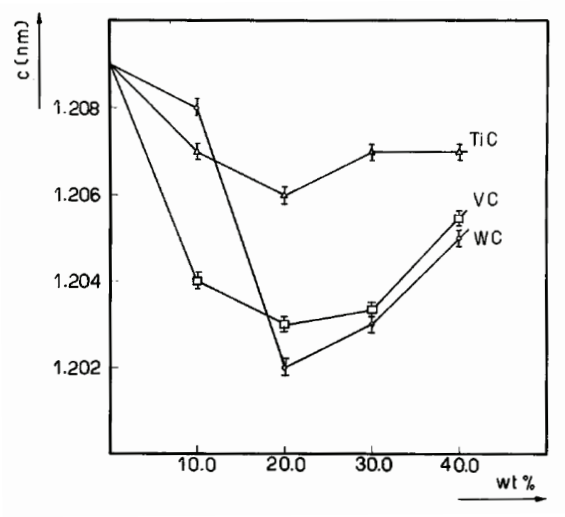

Figure 19: Change in the c lattice parameter of boron carbide due to sintering in the presence of additives [51]

of Al to B_4C [53].

Additionally, Radev and Zakhariev performed structural analysis of boron carbide via Raman spectroscopy. They determined that metal cations (originating from transition metal carbide additions) preferentially replace boron atoms located in the icosahedra of the boron carbide unit cell. The substitution of a small boron atom by a large metal cation necessarily distorts the lattice. The macroscopic expression of this effect is an increase in hardness [54].

Recent computer modeling research has also indicated that the hardness of boron carbide could be improved via the presence of additive atoms within the lattice. Fanchini *et al.* examined the energetic stability of certain boron carbide polytypes (e.g., $(B_{11}C)CBC$ and $(B_{12})CCC$) in order to explain why boron carbide exhibited a sudden glass-like (i.e., low elasticity and plasticity) strength loss under high pressures. They found that several boron carbide polytypes are stable at ambient pressure. Of these polytypes, $(B_{12})CCC$ possesses the lowest activation energy for shock amorphization, or the pressure-induced transformation of boron carbide into segregated boron and carbon phases. Modeling indicated that the $(B_{12})CCC$ polytype collapsed under a

hydrostatic pressure of 6 GPa, which is significantly lower than the elastic limit of 20 GPa expected for boron carbide. This shock amorphization resulted in the formation of 2-3 nm bands of segregated B_{12} and amorphous carbon along the (113) plane. These modeling results agreed with TEM analysis of boron carbide fragments collected after ballistic testing [55]. A TEM image of the observed amorphous bands is provided in Figure 20. Fanchini *et al.* indicated that the introduction of impurity atoms into the boron carbide lattice might significantly reduce the formation of the $(B_{12})CCC$ polytype and thus improve the high-pressure strength of boron carbide [57].

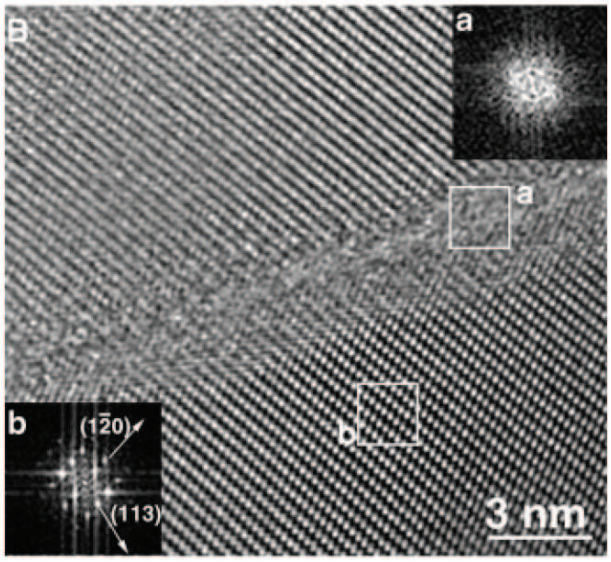

Figure 20: TEM image of shock amorphization band observed in boron carbide [56].

2.5.4 Liquid-Phase Sintering

Vasilos and Dutta observed that alumina acted as a sintering aid for boron carbide above 1950 °C via liquid-phase interactions [27]. Lee and Kim also studied the effect of alumina on the sintering of boron carbide. They prepared B_4C (HS grade powder from H. C. Starck) samples with 0-5 wt% alumina and observed the effect of different sintering temperatures (2075-2150 °C). They determined that the highest density (96%) was achieved with an alumina content of 3 wt% and a sintering temperature

of 2150 °C. A graph illustrating the effect of both sintering temperature and alumina content on the final relative density is provided in Figure 21.

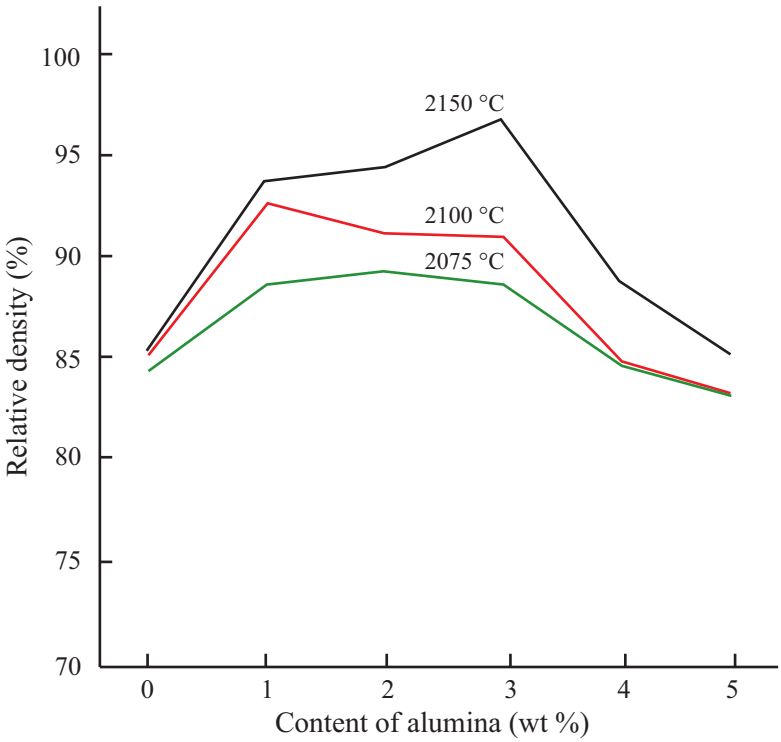

Figure 21: Effect of temperature and alumina content on the sintering of boron carbide [58].

Alumina contents higher than 3 wt% resulted in abnormal grain growth due to the presence of excess liquid. Lee and Kim also noted the presence of the phase $AlB_{12}C_2$ resulting from the reaction of B_4C and Al_2O_3 [58]. Lange *et al.* suggested that $AlB_{12}C_2$ facilitates diffusion via reduction of the energy barrier for mass transport [59].

Yamada *et al.* investigated the liquid-phase sintering of boron carbide via the addition of CrB_2. They cited the presence of a eutectic at 2150 °C in the B_4C-CrB_2 phase diagram as the motivation for this study. For this study, B_4C powder (with an average particle size of 0.43 μm) was mixed with 10-25 mol% of CrB_2 powder (with an average particle size of 3.5 μm). The powders were ball milled and pressureless sintered at 1850-2030 °C for 1 hour. The highest post-sintered Archimedes density

(∼98%, based on a theoretical density of 2.92 g/cm^3 calculated via rule of mixtures) was observed for the 20 mol% CrB_2 sample. The flexural strength and fracture toughness of this sample were determined to be 525 MPa and 3.7 MPa·m$^{1/2}$, respectively. Despite these relatively high mechanical properties, no values of hardness were reported [60].

Silicon carbide may also be a potential liquid-phase sintering additive. Recent observations in our laboratory have confirmed that the presence of silicon carbide significantly reduces the melting temperature of boron carbide to below 2200 °C. These results agree with the observed eutectic reaction between SiC and B_4C. A phase diagram of the B_4C-SiC system is given in Figure 22 [61].

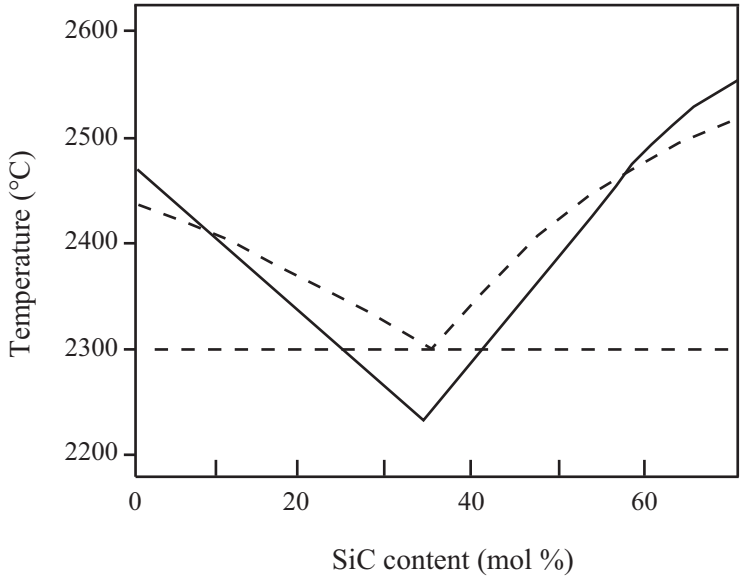

Figure 22: Phase diagram of B_4C-SiC system (dashed and solid lines represent two different sources) [61].

Thevenot cited the work of Grabchuk in which boride compounds were suggested to activate the sintering of boron carbide via reduction in melting temperature [4][62]. Rogl and Bittermann calculated phase diagrams for B_4C-M systems, with M = Hf, Ti, V, W, and Zr. From their calculations, the presence of liquid at elevated temperatures implies that the liquid phase sintering or activated/reaction sintering of boron carbide

Table 3: Calculated Eutectic Temperatures for Pseudo-Binary B_4C-M Systems [63]

System	Eutectic Temperature (°C)	Composition Range
B_4C-Hf	2318	$\leq \sim$27 at% Hf
B_4C-Ti	2267	$\leq \sim$28 at% Ti
B_4C-V	2209	$\leq \sim$26 at% V
B_4C-W	2187	$\leq \sim$24 at% W
B_4C-Zr	2189	$\leq \sim$26 at% Zr

may be facilitated by the addition of these transition metals (Table 3)[63].

Radev and Zakhariev performed detailed experiments on B_4C-Me_xB_y composites, where Me represents Cr, V, and W. They carried out these experiments in order to overcome the difficulties related to the pressureless sintering of boron carbide at that time [51]. This research was driven by findings that transition metal (group IV-VI) carbides were discovered to facilitate the sintering of boron carbide [64][65]. Submicron powders of transition metal carbides (Cr_3C_2, VC, and WC) were ball milled with boron carbide powders and pressureless sintered at 2150-2250 °C in flowing argon. During sintering, the transition metal carbides reacted with the boron carbide via the following proposed reaction:

$$B_4C + Me_x^{IV-VI}C_y = Me_x^{IV-VI}B_y + C \tag{27}$$

This reaction resulted in the production of metal borides such as CrB_2, VB_2, and W_2B_5. Via the above reaction, the boron content in the boron carbide unit cell decreased with the creation of the metal boride reaction products. Radev and Zakhariev observed a decrease in the c lattice parameter of B_4C with increasing additive content, which is explained by the removal of boron via reaction with the transition metal carbides [51]. Following synthesis, the sample compositions producing the densest microstructures were selected for microstructure analysis and Vickers microindentation hardness measurement. Grains as large as 20 μm were observed and attributed to

the increase is mass transport made possible by liquid-phase sintering. For hardness measurements using a loading force of 1 N, the hardness values were determined to be ∼56 GPa (or 5710 kg/mm^2) for B_4C-10 wt% CrB_2, ∼45 GPa (or 4588 kg/mm^2) for B_4C-10 wt% W_2B_5, ∼43 GPa (or 4384 kg/mm^2) for B_4C-10 wt% VB_2, and ∼30 GPa (or 3059 kg/mm^2) for hot-pressed B_4C [51]. It should be noted that these hardness values are artificially high due to the very low loading force of 1 N as compared to the force of 9.81 N required by the ASTM C 1327 standard for microindentation hardness. However, these hardness values do give useful information when compared to the hardness of the hot-pressed sample. A plot comparing the hardness measurements performed by Radev and Zakhariev is given in Figure 23.

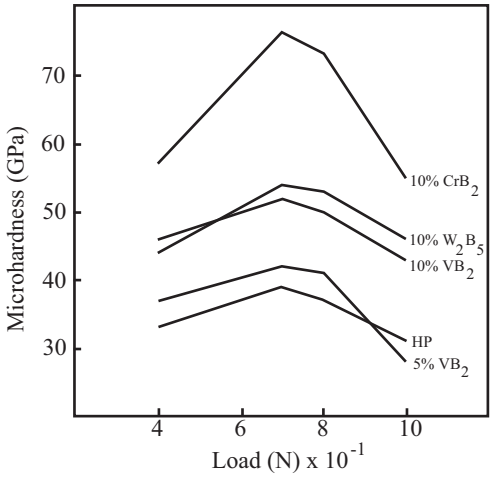

Figure 23: Effect of several additives on hardness of boron carbide with hot-pressed (HP) sample for comparison [51]

2.5.5 Benefits of Titanium Additive

Of the elemental additives examined in prior studies, titanium appears to possess several beneficial properties as a sintering additive. Titanium is available in an inexpensive and low-toxicity chemical source in the form of TiO_2, and the TiB_2 that results from the reaction with boron carbide has a significantly higher hardness than

Table 4: Properties of B_4C, TiB_2 and Other Additives [67]

	B_4C	TiB_2	SiC	Al_2O_3	W_2B_5	VB_2	CrB_2
Density (g/cm^3)	2.52	4.50	3.22	3.98	13.03	5.05	5.58
Hardness (GPa)	40	30	26	21	27	21	22
Elastic Modulus (GPa)	450	560	480	400	770	510	540
Coefficient of Thermal Expansion (10^{-6} K^{-1})	5.0	7.8	5.3	8.4	7.8	7.6	10.5
Melting Temperature (°C)	2450	3225	2760	2047	2365	2747	2188

other metal borides potentially used as sintered additives in boron carbide. Compared to B_4C, TiB_2 adopts a more simplistic hexagonal unit cell. For reference, an illustration of the hexagonal close-packed unit cell of TiB_2 is provided in Figure 24.

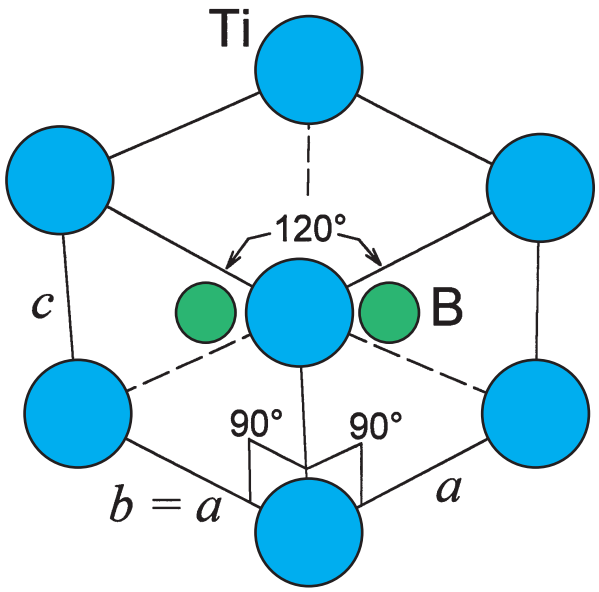

Figure 24: TiB_2 crystal structure [66]

A comparison of several important mechanical and thermal properties for B_4C, TiB_2, and other additives is provided in Table 4.

This high hardness suggests that small TiB_2 amounts should not significantly reduce the hardness of the composite when compared to theoretically dense pure boron carbide. Additionally, TiB_2 possesses a 56% higher coefficient of thermal expansion than boron carbide, which can ultimately result in a stressed or broken interface and lead to the previously described toughening effect via crack blunting and crack deflection. The equation describing the stress field at the interface between a particle and matrix with differing coefficients of thermal expansion is given by

$$\sigma_{radial} = -2\sigma_{tangential} = (\alpha_m - \alpha_p)\Delta T \left[\frac{1+\nu_m}{2E_m} + \frac{1-2\nu_p}{E_p}\right]^{-1} \left(\frac{R_p}{r+R_p}\right)^3 \quad (28)$$

where the m and p subscripts correspond to the matrix and particle, respectively [68]. α represents the coefficient of thermal expansion, ν represents the Poisson's ratio, E represents the elastic modulus, ΔT is the temperature differential from processing temperature to ambient temperature, R_p is the diameter of the particle, and r is the radial distance extending from the outer surface of the particle into the matrix. For this equation, maximum stress occurs for $r = 0$. An illustration and typical B_4C-TiB_2 interfacial stress values resulting from thermal mismatch are provided in Figure 25.

This thermal mismatch results in a local tensile stress field at the interface between the TiB_2 particle and the surrounding matrix and can result in crack deflection as shown in the micrograph in Figure 26. Interestingly, the stress field is maximum at the interface, but the distance over which this stress dissipates into the matrix shows strong dependence on the size (R_p) of the particle or inclusion. A larger particle would cause the stress to dissipate over a longer distance, while a very small particle would cause a very sharp drop in stress with distance, which indicates a more stable (and potentially crack/defect free) mechanical condition. As a result, controlling the size of TiB_2 particles within a B_4C matrix may yield interesting mechanical behavior.

Most importantly, TiB_2 may function as a sintering additive by promoting liquid phase sintering at high process temperatures (~2270-2310°C) or enhancing solid state

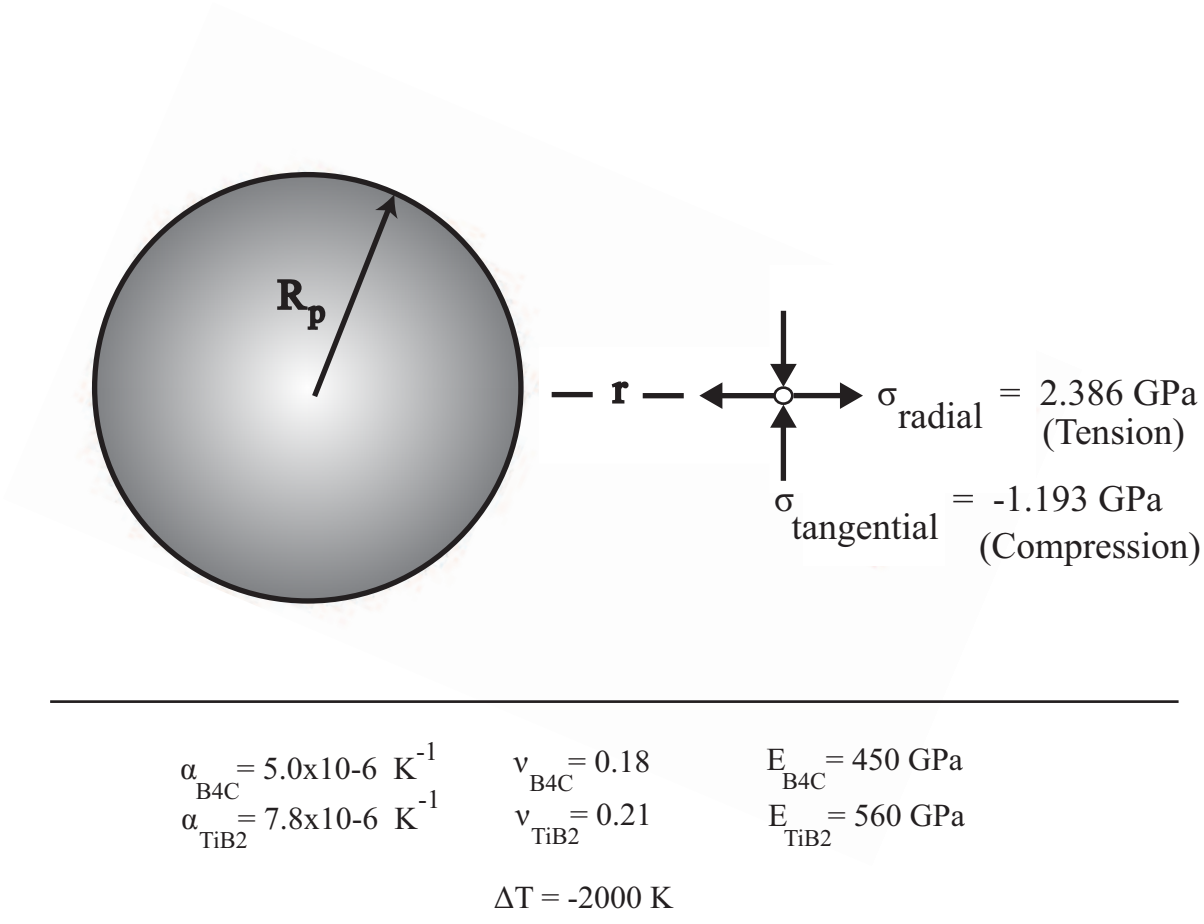

Figure 25: Illustration and typical B_4C-TiB_2 interfacial stress due to thermal mismatch

sintering at lower temperatures. Liquid phase sintering may occur due to the eutectic behavior of boron carbide and TiB_2 mixtures at high temperatures. This relationship suggests that small additions of TiB_2 to boron carbide could promote the formation of a controllable volume of liquid that could in turn improve densification rates. It should be noted that the high eutectic temperature observed for this system (∼2272-2310±15°C) may result in rapid grain growth. A ternary Ti-B-C phase diagram calculated by Gusev using a subregular solution model is provided in Figure 27. This phase diagram indicates a eutectic temperature of 2272°C for the pseudobinary system of $B_{4.5}C$-TiB_2, and that at this eutectic temperature, $B_{4.5}C$ dissolves 1.5 mol% TiB_2. Based on this diagram, the eutectic temperature of the boron carbide-TiB_2

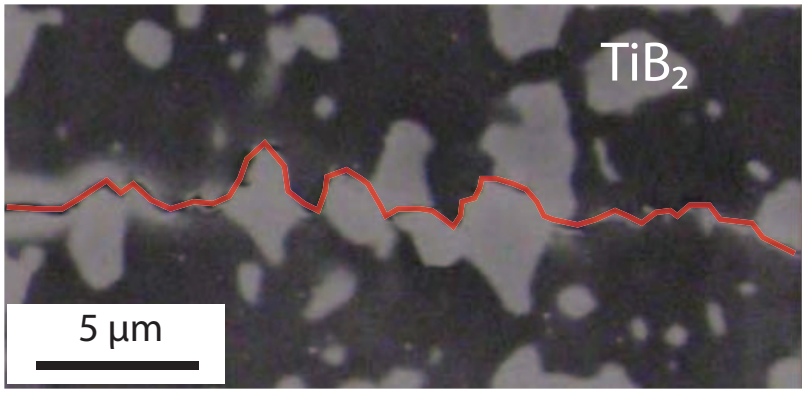

Figure 26: Crack deflection in TiB_2 composite [45]

pseudo-binary join decreases with both increasing and decreasing carbon content from the slightly boron-rich $B_{4.5}C$ composition. Similarly, a pseudo-binary phase diagram produced by Schouler *et. al* illustrating the same eutectic relationship—albeit with a higher eutectic temperature of 2310°C—between TiB_2 and $B_{4.5}C$ is provided in Figure 28.

This eutectic behavior may also permit the activated sintering of B_4C-Ti compositions at temperatures below the eutectic temperature. Although such phenomena would occur below the melting temperature, the increase in vacancy concentration as the eutectic temperature is approached may yield improved densification. Additionally, at these lower temperatures where solid-state sintering would occur, hard TiB_2 particles may inhibit grain growth/coarsening by impeding grain boundary mobility. A refined grain size can significantly improve the flexural strength and hardness of the final product due to the Petch relationship, which states that the fracture strength should increase with decreasing grain size, d (more specifically, $\sigma_{fracture}\ \alpha\ \mathrm{d}^{-1/2}$). This phenomenon occurs in brittle materials, because the high stresses required for plastic flow in ceramics causes stress to accumulate at the grain boundaries until the bond strength is exceeded. Once the bond strength is exceeded, one would expect the flaws initiated at the grain boundaries of fine-grained ceramics to be smaller and more distributed than coarser-grained ceramics, because the accumulating internal stresses

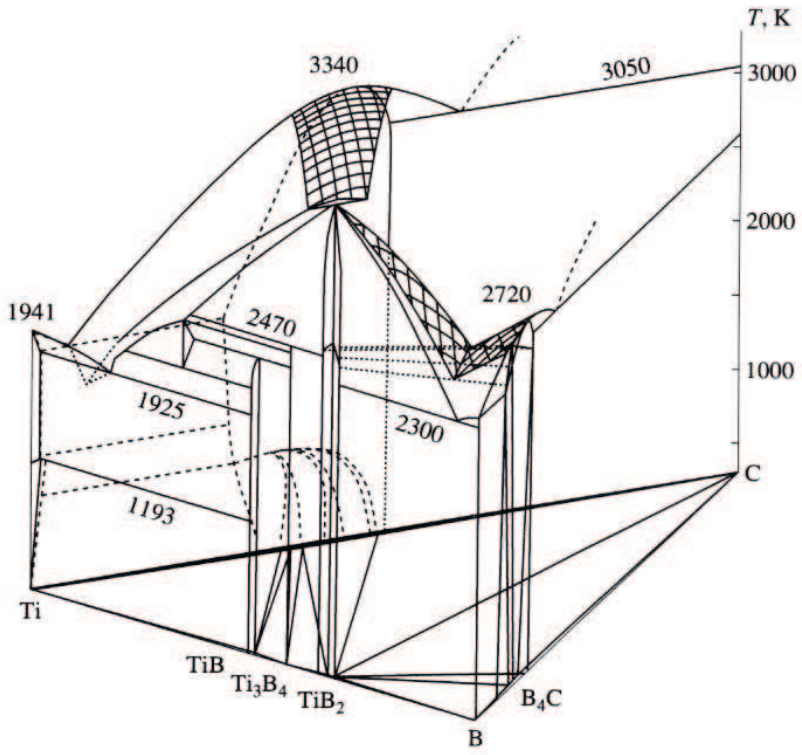

Figure 27: Ti-B-C ternary phase diagram in the temperature range of 300-3500 K [69]

can be shared over a greater grain boundary area. This phenomenon is manifested as increased bulk hardness and fracture strength [14].

Further study of the B_4C-Ti materials system is warranted, because previous work has focused on the effect of large amounts of added Ti (in the form of submicron TiO_2 or TiB_2) on the sintering and/or mechanical properties of B_4C, and these past studies did not take advantage of recent boron carbide sintering advancements developed in our lab. Additionally, previous work did not perform detailed dilatometry or investigate the effect of the Ti source size on sintering behavior. Consequently, investigating the influence of small amounts of nanoscale TiO_2 and submicron TiO_2, as well as the effect of carbon concentration would provide a more complete characterization of the relationship between the composition and mechanical properties of B_4C-TiB_2 composites.

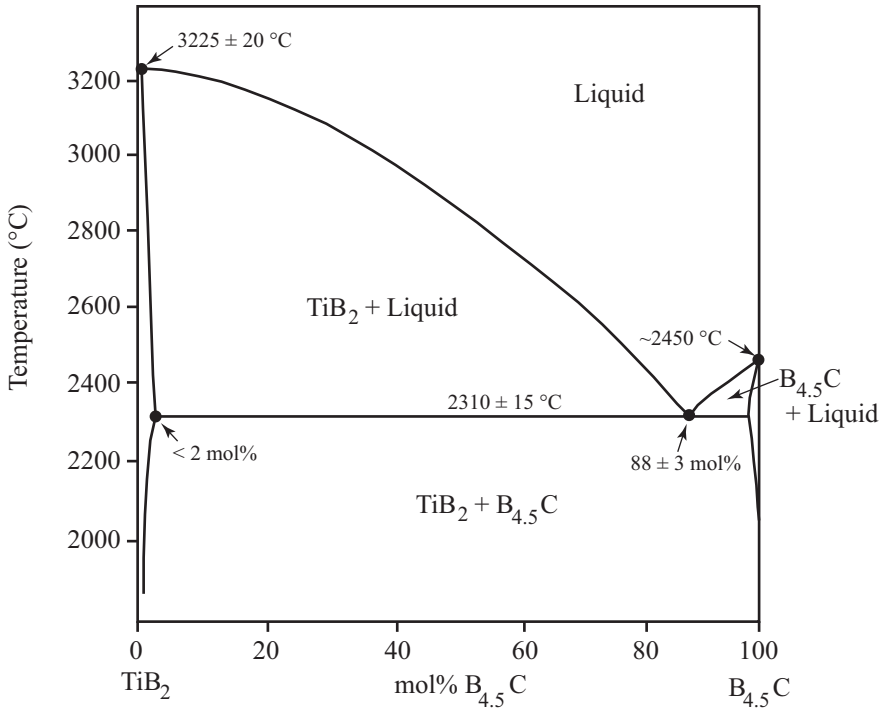

Figure 28: TiB_2-$B_{4.5}C$ phase diagram [61]

CHAPTER III

EXPERIMENTAL PROCEDURE

3.1 High Temperature Differential Dilatometer

3.1.1 Dilatometer Construction

A high temperature differential dilatometer was constructed for analyzing the sintering behavior of the boron carbide studied in this work. A graphite resistance furnace (1000-2560-FP, Thermal Technology Inc., Santa Rosa, CA) was obtained and mounted to a custom-manufactured support frame. The furnace was composed of a water-cooled cylindrical aluminum shell that contained a centrally positioned graphite heating element surrounded by a hard graphite containment tube and fibrous graphite insulation. A water-cooled steel cap affixed to a hard graphite hearth covered the bottom of the furnace hot-zone while a graphite-felt-lined and water-cooled steel access port covered the top of the furnace, allowing the sample casing tube to be raised and lowered out of the furnace. All power feed-throughs, power cables, top and bottom cover plates as well as the vacuum pump access port were water-cooled. The furnace was designed for a maximum safe operating temperature of 2900°C in flowing He gas, and the 5 cm sample hot-zone region was rated to a temperature uniformity of ±3°C at 1750°C as specified by Thermal Technology, Inc. The furnace was capable of atmospheric conditions ranging from high vacuum to 15 psig of dry inert gas. For this work, ultra-high purity Helium gas (99.999% HE-UHP300, Airgas, Atlanta, GA) was used exclusively. Helium flow through the furnace was controlled via a mass flow controller (Aalborg Inc., Orangeburg, NY) that permitted a maximum flow rate of 1 liter per minute. After passing through the furnace, the exhaust gas was flowed through a two-flask bubbler setup to prevent air back flow.

The temperature within the furnace was monitored using an infrared pyrometer (Model RAYMM1MHVF1L, Raytek Co., Santa Cruz, CA) measuring at a wavelength of 1 μm. The pyrometer was mounted to the outer shell of the furnace via a threaded cylindrical assembly that also contained a fused silica viewing window under a compressive o-ring seal. The pyrometer focal point was set to the minimum allowed value of 300 mm.

A custom hardware-computer interface was fabricated that allowed furnace power to be feedback-controlled via a PID algorithm programmed using Microsoft Visual Basic 4.0. The operational temperature range of the pyrometer was 600°C to 3000°C, so initial heating of the furnace was set to start at 30% control power and linearly increase with time until 600°C when PID furnace control would begin. This linearly increasing power mode resulted in an initial heating rate of ∼63°C/min up to 600°C.

Sample contraction during sintering was measured with a differential dilatometer (Theta Industries Inc., Port Washington, NY) containing two pushrods and a linearly variable differential transformer (LVDT). The dilatometer was mounted to a sliding fixture above the furnace to allow samples to be entered into and removed from the furnace hot-zone with relative ease. Samples were placed on the bottom of a partly closed end custom-fabricated graphite sample tube (Poco Graphite Inc., Decatur, TX) that was oriented vertically. Two graphite pushrods with steel thread screws (Poco Graphite Inc., Decatur, TX) were located inside the sample tube and individually screwed into the reference and sample pushrod mounts on the dilatometer. The sample pushrod was connected directly to the floating magnetic core of the LVDT, while the reference pushrod was connected to the LVDT itself. As a result, any dimensional change resulting from the graphite sample tube and pushrods could be eliminated, because any expansion of those components causing a shift in the magnet core would be offset by an equal shift in the LVDT unit. A counterweight connected to the LVDT core-sample pushrod assembly reduced the applied force on test specimens

during data acquisition, thereby preventing any hot-pressing effect resulting from the weight of the pushrod. Sample displacement was measured relative to a graphite reference of equal height (effectively the end of the reference pushrod). The thermal expansion polynomial equation of the reference graphite sample was provided by the manufacturer and this value was continually calculated with changing temperature and added to the sample displacement in order to offset the shift in LVDT position with increasing temperature. The thermal expansion polynomial equation used for graphite is provided in the following equation [70]:

$$\alpha_{PocoGraphite} = \frac{-177.361 + 8.989T - 6.253 * 10^{-3}T^2 + 1.011 * 10^{-5}T^3 - 6.665 * 10^{-9}T^4 + 1.697 * 10^{-12}T^5}{1000000} \quad (29)$$

where T is the temperature in °C. As a result of these measures, all displacement data could be attributed only to the sample.

To ensure safe operation, a water chiller system was installed to maintain the flow of cool (∼18°C) water through the system. Additionally, a backup water system connected to city-provided water was set to activate upon power failure of the chiller system or if the water temperature exceeded 80°C.

3.1.2 Dilatometer and Pyrometer Calibration

The LVDT was calibrated using an analog micrometer with 1 mm graduations that was affixed to the LVDT assembly. The LVDT output voltage (measured using a multi-meter) was recorded for micrometer positions of 0 and 1 mm. This process was repeated 20 times to ensure accuracy. Following measurement, a regression line equation was produced that allowed LVDT voltage data to be translated into dimensional data.

The infrared pyrometer was calibrated using a 6.41 mm diameter pellet pressed out of pure iron powder (99.99+%, Sigma-Aldrich, St. Louis, MO), whereby the dimensional changes associated with the allotropic phase transitions of α-iron $\rightarrow$ γ-iron

Figure 29: Image of graphite differential dilatometer with water cooling tower and secondary backup water system

and γ-iron $\rightarrow$ δ-iron were detected. The iron pellet was pressed at a pressing pressure of 150 MPa using a tool steel die. Thin alumina fragments were placed on the top and bottom of the iron sample to prevent contact and potential reaction with the graphite pushrod and casing of the dilatometer. The transition from BCC α-iron to FCC γ-iron occurs at 912°C, while the transition from FCC γ-iron to BCC δ-iron occurs at 1394°C [71]. During heating, the iron sample was observed to contract/sinter rapidly with heating, which made direct observation of the phase changes (particularly the transition of $\alpha \rightarrow \gamma$-iron) difficult when based solely on dimensional change data. Plotting the dimensional change rate facilitated deconvoluting the phase transitions from the overall sintering contraction of the sample. The calibration experiment indicated that the pyrometer was within 1°C of the allotropic transition temperatures cited in literature by showing sharp dimensional rate changes that completed at 911°C and 1393°C. Additional confirmation that these are indeed the allotropic

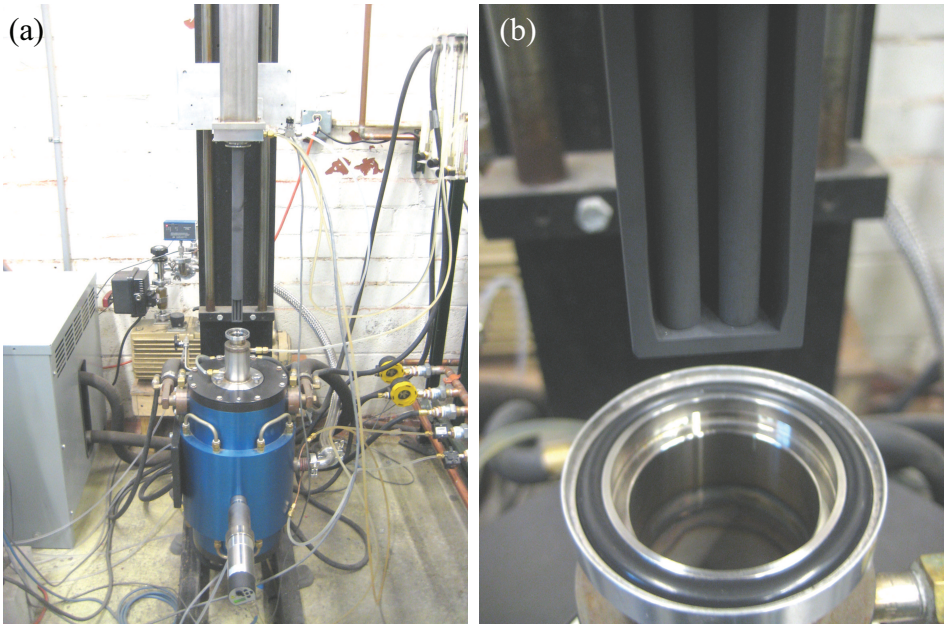

Figure 30: Images of (a) differential dilatometer and (b) graphite casing and pushrod assembly

phase changes of iron is provided by the sign of the dimension change rate; an abrupt sample contraction at ~912°C is consistent with the net volumetric contraction of a BCC→FCC transition, and an abrupt expansion at ~1394°C is consistent with a FCC→BCC transition. A plot of the dimensional rate of change versus the measured pyrometer temperature is provided in Figure 31. As a result of this calibration test, no corrective algorithm was deemed necessary for the infrared pyrometer.

3.2 Initial Compositional Parametric Study

The primary goal of this research was to identify the titanium and carbon additive compositions that yielded optimal sintering characteristics (high relative density) and mechanical properties (high hardness and indentation fracture toughness) while also lowering overall material costs. Boron carbide powder (HD15, H. C. Starck GmbH, Goslar, Germany) costing less than one fifth the price (based on bulk quantities) of current high-quality sinter grade boron carbide powders was used in this study. Specific powder characteristics provided by the manufacturer, such as particle size,

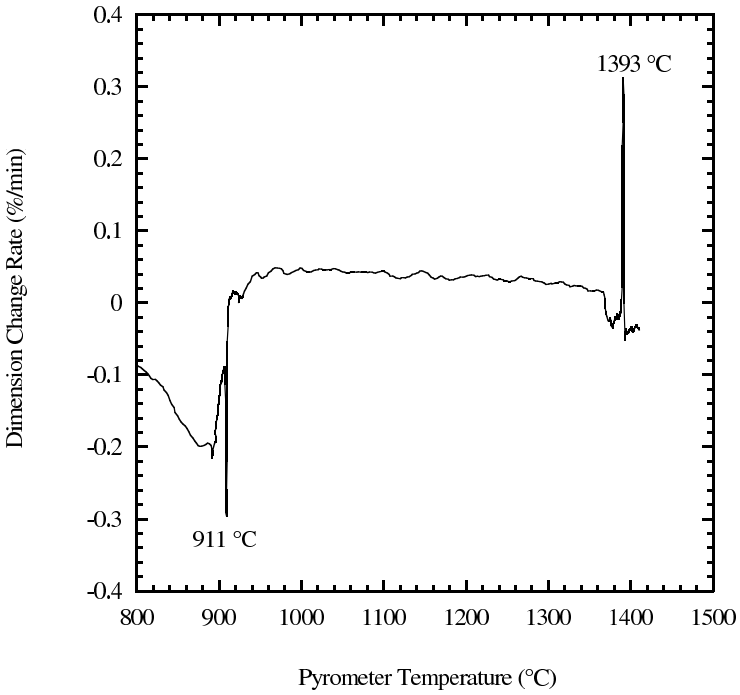

Figure 31: Dimensional rate of change versus measured temperature for calibration of pyrometer using pure iron

boron-carbon stoichiometry, as well as impurity levels are provided in Table 5.

The B_4C powder was mixed with incremental additions of titanium and carbon. In order to investigate the effect of titanium additive size, two different titanium sources were used: 32 nm anatase TiO_2 (45 m^2/g APS, Alfa Aesar, Ward Hill, MA) and 0.9-1.6 μm rutile TiO_2 (3.3-6.1 m^2/g APS, Alfa Aesar, Ward Hill, MA). The carbon source selected for addition was a water-soluble phenolic resin (SP-6877, SI Group, Schenectady, NY). Prior experiments indicated that this resin contained 63 wt% solids after convection oven drying, which in turn produced 48.02 wt% carbon char following pyrolysis at 1000°C. A binder system composed of 1 wt% polyvinyl alcohol (PVA), 0.5 wt% polyethylene glycol (PEG) plasticizer, and 1 wt% Darvan 821A dispersant (R.T. Vanderbilt Company, Norwalk, CT) was used for all experimental compositions. The prepared compositions are provided in Table 6.

Batches containing 200 grams of boron carbide HD15 powder were mixed with the respective TiO_2 powders, deionized water, the binder components, phenolic resin

Table 5: HD15 B_4C Powder Characteristics

Specific Surface area	19 m^2/g
Particle size	$d_{90} = 1.5$ μm
	$d_{50} = 0.6$ μm
	$d_{10} = 0.2$ μm
Impurity Content	1.7 wt% O
	0.2 wt% N
	0.09 wt% Si
	0.0 wt% Fe
	0.02 wt% Al
Carbon Content	21.8 wt%
B:C Ratio	3.9

Table 6: Experimental Compositions

Ti Source Additive	Ti (wt%)	C (wt%)
32nm TiO_2	0.5	0, 1, 3
(anatase)	1	0, 1, 3
	3	0, 1, 3
	5	0, 1, 3
0.9-1.6 μm TiO_2	0.5	0, 1, 3
(rutile)	1	0, 1, 3
	3	0, 1, 3
	5	0, 1, 3

(when required), and 10 drops of a concentrated defoaming agent (Hercules Inc., Wilmington, DE) in 2 liter high-density polyethylene (HDPE) mixing barrels. The solids loading of the slurries was maintained at 17-22 vol% in order to produce a low viscosity mixture capable of easily flowing through small diameter plastic tubing. Boron carbide milling media equal to approximately half the volume of the slurry components was placed inside the barrels and the compositions were ball-milled for 24 hours to ensure that all components were homogeneously mixed. Following ball milling, all sample compositions were spray dried using a pilot plant-scale Bowen 'Nozzle Tower' spray dryer (GEA Process Engineering, Columbia, MD, USA) in conjunction with an ultra-sonicating nozzle (Sono-Tek Corporation, Milton, NY). An illustration of the spray dryer during operation is provided in Figure 32. During operation, the inlet and outlet temperatures of the spray dryer were maintained at 260-270°C and 50-70°C, respectively.

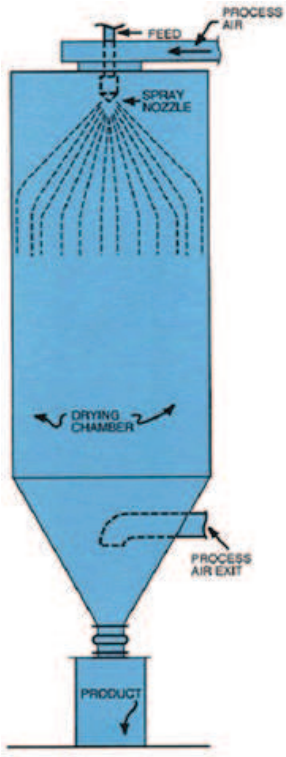

Figure 32: Illustration of a Bowen 'Nozzle Tower' pilot plant scale spray dryer (Image courtesy of GEA Process Engineering)

After spray drying, the granulated powders were characterized to determine the size and shape of the spray-dried granules via optical microscopy (Olympus BX40, Olympus America, Inc., Center Valley, PA). The powders were then analyzed via X-ray diffraction (XRD) in order to determine the phases present prior to sintering (X'Pert PRO Alpha-1, PANalytical, Almelo, The Netherlands). X-ray diffraction patterns were generated with a 0.084 °/s scan speed, a step size of 0.017°, and 2θ range of 10° to 85°. Soller slits (0.04 radians) were installed in the incident and diffracted x-ray beam pathways. A 10 mm mask was installed in the incident beam pathway, and a 5 mm mask was installed in the diffracted beam pathway. In order to determine how the phases in high TiO_2-content powder of varying carbon contents changed with temperature, several samples (in loose powder form) of the 5 wt% Ti, 0 wt% C, 0.9 μm TiO_2 composition as well as the 5 wt% Ti, 3 wt% C, 0.9 μm TiO_2 composition were placed into graphite crucibles and heated in the dilatometer furnace at a fast heating rate (50°C/min) to 1300, 1600, and 1900°C in flowing He. After reaching the set temperature, the samples were immediately cooled at 100°C/min in order to limit continued reaction. Additionally, a lower temperature of 1000°C was investigated for the 5 wt% Ti, 0 wt% C, 0.9 μm TiO_2 composition using an identical procedure. Following heat-treatment, the powders were removed from the furnace and analyzed for phase composition via XRD. The XRD parameters used were identical to those followed for analysis of the as-spray-dried powders discussed above.

Following characterization of the powders, each composition was pressed into pellets measuring 6.41 mm in diameter and approximately 5 mm in height using a tool steel die under 304 MPa of pressure applied via a hand-actuated hydraulic press (Carver Inc., Wabash, IN). Pellets containing no phenolic resin were debound in-situ during sintering. However, pellets containing phenolic resin were placed in tiered graphite crucibles and thermally debound in a vacuum furnace (BREW, Thermal Technology Inc., Santa Rosa, CA) under continuous mechanical vacuum pumping

(via heating at 0.5°C/min to 500°C, holding for 7 hours, and then heating at 3°C/min to 1350°C, and holding for 4 hours) in order to avoid any potential resin deposition on the pyrometer view window.

The sintering characteristics of pellets corresponding to each composition were analyzed in the high-temperature dilatometer. An identical startup procedure was followed for all sintering experiments. Following sample placement in the furnace, all gas valves to the furnace were closed and the chamber was pumped down to a pressure of less than 80 mTorr (measured via a Convectron gauge) using a mechanical vacuum pump. After reaching the desired vacuum level, the vacuum valve was closed, the main body gas valve was opened, and the furnace was backfilled with He gas flowing at 1 lpm until the pressure exceeded 760 Torr. At that point, gas inlet valves flowing into the pyrometer port and the dilatometer measuring head were opened in order to avoid disturbing the position of the sample under the pushrods. Initial experiments followed a standard sintering test profile. Samples were heated at 15°C/min to the sintering temperature and held for 30 min. Two different sintering temperatures (2200°C and 2300°C) were selected for this initial evaluation. After holding at the sintering temperature, the samples were quenched by cooling at 100°C/min to room temperature. It should be noted that 30 minutes was selected for the sintering hold time, because prior literature indicated such a short time was sufficient to reach the end of sintering for process temperatures approaching 2300°C [2]. Sintering time was kept constant throughout this work in order to keep the number of variables and scope of the study manageable. After sintering, the Archimedes density of each pellet was measured.

Following dilatometry analysis, slightly larger samples were prepared for compositional and temperature optimization studies. Each powder composition was pressed into cylindrical disks measuring 12.7 mm in diameter and approximately 3 mm in height using a tool steel die under 150 MPa of pressure via a hand-actuated hydraulic

press (Carver Inc., Wabash, IN). All disks were then placed into latex bags, pulled under vacuum, and cold isostatically pressed (CIPed) at 345 MPa for 2 minutes (CIP, American Isostatic Presses, Inc., Columbus, OH) in order to improve green density and to remove any density gradients resulting from pressing. After CIPing, the weight and caliper dimensions of the height and diameter were measured. The disks were then placed in tiered graphite crucibles and thermally debound in a vacuum furnace (BREW, Thermal Technology Inc., Santa Rosa, CA) under continuous mechanical vacuum pumping (via heating at 0.5°C/min to 500°C, holding for 7 hours, and then heating at 3°C/min to 1350°C, and holding for 4 hours). After debinding, the weight of each disk was measured to determine the weight loss resulting from the debind process. The disks were then sintered in the dilatometer furnace with the measuring head replaced by a top cap composed of a water-cooled steel sealing surface attached to an insulating graphite hearth. The simultaneous firing of numerous larger volume disks necessitated the incorporation of a 2-hour deoxidation hold at 1300°C. Prior research showed that sufficiently removing the oxide coating on boron carbide particles dramatically improved sintering behavior [1][2]. The samples were heated at 15°C/min up to 1300°C, held for 2 hours, and then heated at 15°C/min up to the final sintering temperature and held for 30 minutes. Four different sintering temperatures (2240°C, 2260°C, 2280°C, and 2300°C) were selected for each of the 24 compositions in this study. After holding at the sintering temperature, the samples were rapidly quenched at 100°C/min to 30°C in order to prevent grain growth that could occur if a slower cooling rate were used. Following sintering, the Archimedes densities of all the samples were measured. The weight loss resulting from sintering was also recorded. All of the samples were then hot isostatically pressed (HIPed) at 2050 °C and 206 MPa of argon pressure for 1 hour. After HIPing, the Archimedes density was measured.

The theoretical density values used to calculate the relative densities of the samples were determined via the Rule of Mixtures:

$$\rho_{composite} = \rho_{B_4C} V_{B_4C} + \rho_{TiB_2} V_{TiB_2} + \rho_C V_C \tag{30}$$

where ρ and V represent the theoretical density and volume fraction of each component (B_4C, TiB_2, and graphite) in the composite, respectively. The theoretical density values used for B_4C, TiB_2, and graphite were 2.52 g/cm^3, 4.50 g/cm^3, and 2.16 g/cm^3, respectively. The volume fraction of graphite was estimated by calculating the amount of residual carbon remaining following reaction with the B_2O_3 and TiO_2 present in the samples. For simplicity, perfect stoichiometric reduction was assumed (i.e., the carbon was assumed to react with the available oxygen to produce only CO_2). This assumption results in a higher calculated residual carbon content, which is reasonable given that some oxide may be removed by evaporation—not reaction with carbon—prior to the 1350°C hold of the debinding heat treatment. The data sheet provided by the boron carbide powder manufacturer indicated an oxygen content of 1.7 wt% (presumably in the form of boron oxide). The molar amount of carbon reacting with the pre-existing boron oxide and the added TiO_2 was subtracted from the molar amount of added carbon to determine the residual carbon remaining in the composites, which is given by the following equation:

$$m_{ResidualC} = \left\{ \frac{m_C}{M(C)} - \frac{m_{Ti}}{M(Ti)} - \frac{1}{2}\left(\frac{1.7\% * m_{B_4C}}{M(O)} \right) \right\} * M(C) \tag{31}$$

where m represents the mass of the component added to the composite, and M represents the molar mass. The molar mass values used for C, Ti, and O were 12.0107 g/mol, 47.8671 g/mol, and 15.9994 g/mol, respectively. The theoretical density values calculated using the above equations are provided in Table 7.

Table 7: Theoretical Density Values Calculated from the Rule of Mixtures

Additive	Ti Amount Added (wt%)	Carbon Amount Added (wt%)	Calculated Theoretical Density (g/cm^3)
32 nm TiO_2	0.5	0	2.5256
32 nm TiO_2	1	0	2.5311
32 nm TiO_2	3	0	2.5537
32 nm TiO_2	5	0	2.5767
0.9 μm TiO_2	0.5	0	2.5256
0.9 μm TiO_2	1	0	2.5311
0.9 μm TiO_2	3	0	2.5537
0.9 μm TiO_2	5	0	2.5767
32 nm TiO_2	0.5	1	2.5246
32 nm TiO_2	1	1	2.5307
32 nm TiO_2	3	1	2.5541
32 nm TiO_2	5	1	2.5773
0.9 μm TiO_2	0.5	1	2.5246
0.9 μm TiO_2	1	1	2.5307
0.9 μm TiO_2	3	1	2.5541
0.9 μm TiO_2	5	1	2.5773
32 nm TiO_2	0.5	3	2.5160
32 nm TiO_2	1	3	2.5221
32 nm TiO_2	3	3	2.5470
32 nm TiO_2	5	3	2.5726
0.9 μm TiO_2	0.5	3	2.5160
0.9 μm TiO_2	1	3	2.5221
0.9 μm TiO_2	3	3	2.5470
0.9 μm TiO_2	5	3	2.5726

Table 8: Grinding and Polishing Procedure

Step	Finish	Surface	RPM	Rotation Direction	Time (min)
1	220 Grit	Struers MD Piano 220	300	Opposite	60
2	45 μm	Beuhler Apex B	300	Concurrent	5
3	15 μm	Beuhler Apex B	150	Concurrent	15
4	9 μm	Beuhler Apex B	150	Concurrent	15
5	9 μm	Beuhler Texmet-P	150	Concurrent	45
6	3 μm	Struers MD Pan	150	Concurrent	60
7	1 μm	Struers MD Dur	150	Concurrent	60

3.3 Characterization

After HIPing, the disks were encapsulated in SpeciFix resin (Struers, Inc., Westlake, OH) and prepared for characterization by grinding away the outer graphite-rich surface using a 220 grit diamond-coated grinding plate, as well as metal-bonded diamond plates combined with 45, 15, and 9 μm diamond suspensions (Struers Piano, Struers, Inc., Westlake, OH)(Apex B and Metadi Supreme, Buehler, Lake Bluff, IL). Samples were washed with water following each grinding step. After grinding to flat surfaces, the samples were polished on specialized cloths with 9, 3, and 1 μm polycrystalline diamond suspensions (Struers MD, Struers, Inc., Westlake, OH)(Texmet and Metadi Supreme, Buehler, Lake Bluff, IL). After all 9, 3, and 1 μm polishing steps, the samples were washed and placed in an ultrasonicating bath to remove residual diamonds from the polished surface. The grinding and polishing procedure is detailed in Table 8.

After polishing, microindentation hardness and fracture toughness measurements were performed. Microindentation measurements were calibrated using the SRM 2831 tungsten carbide standard reference disk obtained from NIST (SRM-2831, National Institute for Standards and Technology, Gaithersburg, MD). Samples were indented at arbitrary and unbiased microstructure locations using a Vickers diamond indenter

(Duramin-2, Struers, Westlake, OH, USA) under an applied load of 1 kg for 15 seconds in order to measure the microindentation hardness values. The diagonal lengths of ten acceptable indentations (as determined by the ASTM C 1327-99 "Standard Test Method for Vickers Indentation Hardness of Advanced Ceramics") were measured and hardness values (in units of kg/mm^2) were calculated using the equation

$$HV = (0.102)(1.8544)\left(\frac{P}{d^2}\right) \tag{32}$$

where P is the load (N) and d is the average indentation diagonal length (mm). The same acceptable indentations used for the hardness measurements were also used for fracture toughness measurement. The length of the cracks emanating from the corners of the Vickers indentations were measured and this data was used to calculate the microindentation fracture toughness values of the materials using the Miyoshi equation:

$$K_{IC} = 0.018P\sqrt{\frac{E}{c^3 HV}} \tag{33}$$

where HV is the Vickers hardness (GPa) E is Young's modulus (GPa), P is the applied load (N), and $2c$ is the average crack length (m) [72]. A Young's modulus value of 450 GPa was used in the fracture toughness calculations.

The phases contained within several spray dried powder samples, reaction study specimens, and the HIPed disk samples were identified via X-ray diffraction (X'Pert PRO Alpha-1, PANalytical, Almelo, The Netherlands). X-ray diffraction patterns were generated with a 0.084 °/s scan speed, a step size of 0.017°, and 2θ range of 10° to 85°. Soller slits corresponding to 0.04 radians were installed in the incident and diffracted x-ray beam pathways in order to produce scans with minimal background interference relative to the intensities of the diffraction peaks. Additionally, a 10 mm mask was installed in the incident beam pathway, and a 5 mm mask was installed in the diffracted beam pathway.

Following x-ray diffraction, the disks were electrolytically etched in order to reveal the location of the grain boundaries. Samples were etched for ∼20-30 seconds in a dilute aqueous solution of KOH (1 g of KOH in 100 mL of deionized water) using a current of 20 mA at 21 VDC applied through a thin Pt foil cathode. The microstructures of the HIPed samples were examined using optical microscopy (Olympus BX40, Olympus America, Inc., Center Valley, PA) and scanning electron microscopy (SEM, Model 1530 SEM, LEO Electron Microscopy, Inc., Oberkochen, Germany). Energy-dispersive X-ray spectroscopy (EDS, Oxford Pentafet Detector, Oxford Instruments, Oxfordshire, UK) was performed during SEM in order to identify the chemical composition of specific microstructure locations. The optical micrographs were analyzed using the linear intercept quantitative characterization method to determine the cumulative percent finer grain size distribution and median (d_{50}) grain size for select samples based upon 50 grain measurements across four separate microstructure images for a total of 200 measurements.

CHAPTER IV

RESULTS

4.1 Analysis of Prepared Powders

The spray dried powders produced for this study exhibited substantially improved flow and die fill characteristics when compared to the as-received, non-spray-dried boron carbide powder. Examination of the spray dried granules via optical microscopy indicated an approximate agglomerate size of 50-80 μm and a roughly spherical morphology. A characteristic optical microscopy image of one of the spray dried powder batches from this study is provided in Figure 33.

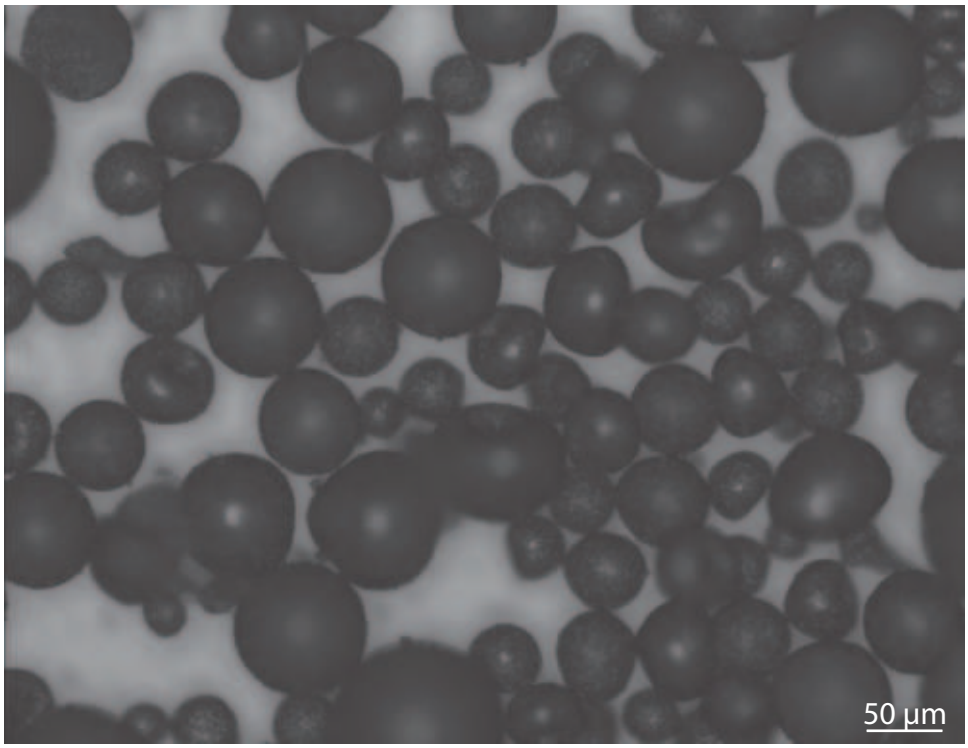

Figure 33: Optical microscope image of spray dried boron carbide powder containing TiO_2 and carbon additives

XRD was performed on the as-received HD15 B_4C powder and several spray dried

compositions in order to determine the phases present prior to sintering. The XRD traces of these green samples are provided in Figure 34.

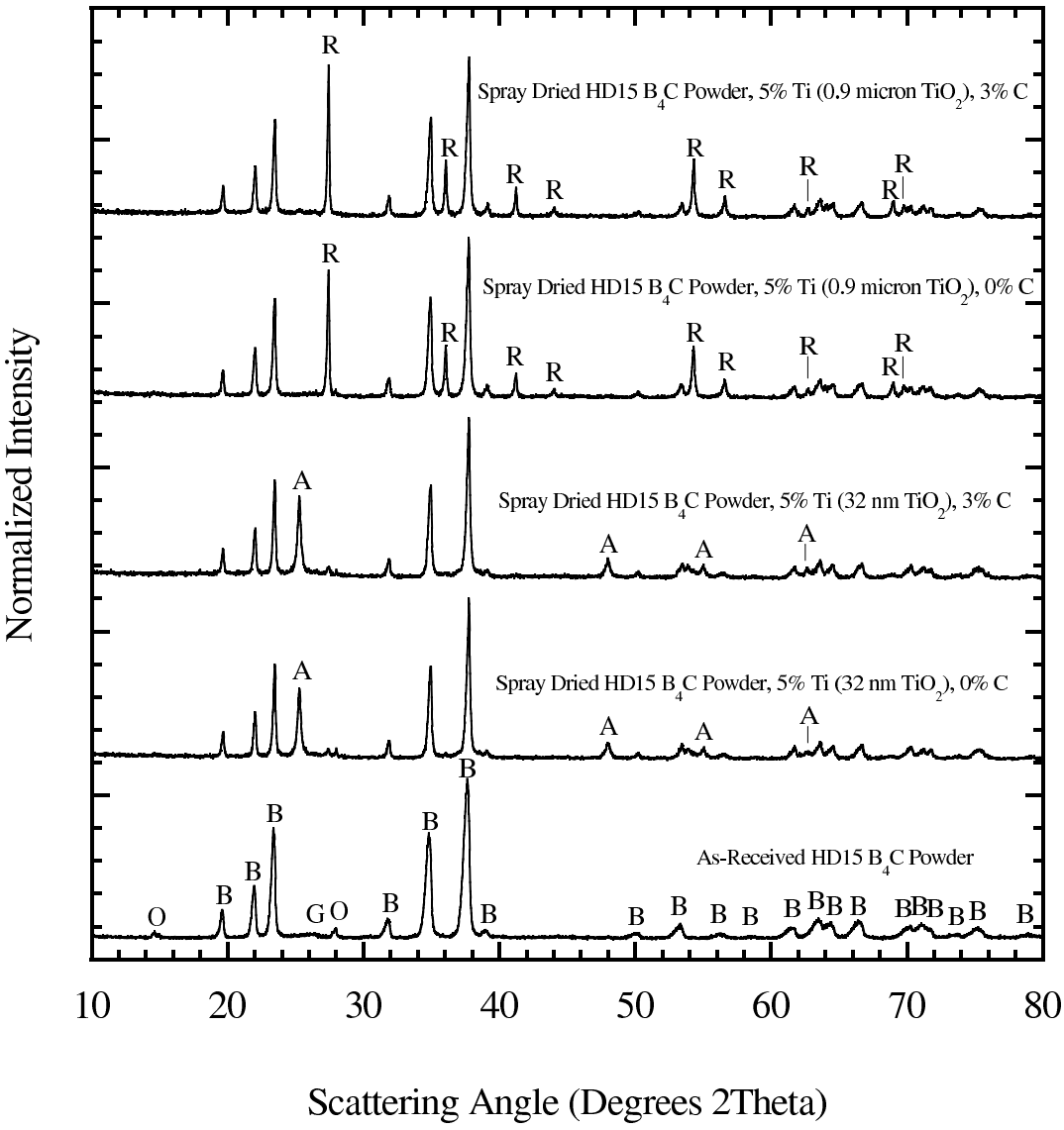

Figure 34: XRD traces of as-received HD15 B_4C powder and various high-additive content spray dried compositions. The diffraction patterns were normalized based upon the most intense peak in each scan. Labeling corresponds to the following: B(B_4C solid solution), O(B_2O_3), G(graphite), R(rutile TiO_2), and A(anatase TiO_2).

The XRD traces reveal the presence of graphite and boron oxide impurities in the as-received powder. Each of the analyzed spray dried compositions show slightly

reduced integrated intensities corresponding to the most intense peak of boron oxide at 27.769 °2θ, which suggests that ball-milling of the powders in water prior to spray drying may have assisted in impurity removal. XRD traces for both of the 32 nm TiO_2 samples show clear evidence of the anatase TiO_2 phase, which is expected. A small impurity content of rutile TiO_2 was also detected in these two samples, which could have resulted from residual deposits of previously spray dried compositions containing 0.9 μm TiO_2 that were not entirely cleaned from the spray dryer piping. XRD traces for the 0.9 μm TiO_2 compositions indicate the presence of rutile TiO_2 as anticipated. Comparison of differences between the 0%C and 3%C samples across the various TiO_2 types reveals no indication of phenolic resin addition.

XRD was also performed on the series of 5 wt% Ti, 0.9 μm TiO_2 compositions containing 0 and 3 wt% C that were analyzed in the reaction progression study. Loose powders of these compositions were heated at 50°C/min to 1000 (only for the 0 wt% C sample), 1300, 1600, and 1900°C in flowing He, and then immediately cooled at 100°C/min. The XRD traces of these samples are provided in Figures 35 through 36. The XRD traces of the reaction progression for the 0 wt% C powder composition indicate that TiO_2 had started to react with the surrounding boron carbide and carbon by 1000°C. It should also be noted that some of the initial stoichiometric boron carbide (i.e., B_4C) was converted into boron-rich boron carbide ($B_{13}C_2$) after heating to this temperature. Several new Ti-O phases emerged from the reaction, such as Ti_2O_3 and $TiBO_3$. Small peaks corresponding to those of TiB_2 were also detected. The most intense peak of rutile TiO_2 at 27.38 °2θ was convoluted with a similar peak in the XRD pattern of the newly formed Ti metal boride phase, TiB_2. The full-width half-maximum (FWHM) values of the most intense XRD peaks for the Ti-O phases and TiB_2 are significantly broadened, indicating a distribution of fine reaction products from the reduction of TiO_2. With increasing temperature to 1300°C, the powder sample exhibited graphite, boron oxide, and TiB_2. The presence

of TiO_2 was suggested, but the peak overlap with TiB_2 made identification difficult. The most intense TiB_2 peak for this temperature displayed decreased broadening compared to that observed in the 1000°C heat-treatment sample. For the 0 wt% C powder heat-treated at 1600°C, boron oxide was no longer present, the integrated intensity of the graphite peak decreased, and the TiB_2 peak narrowed. As the heat-treatment temperature was raised to 1900°C, the only detectable phases were boron carbide and TiB_2.

The XRD traces of the reaction progression for the 5 wt% Ti, 0.9 μm TiO_2 powder composition containing 3 wt% C indicate the formation of $B_{13}C_2$ and TiB_2 by 1300°C. As observed in the 0 wt% C samples, the most intense TiB_2 peak at 44.393 °2θ shows significant broadening compared to the same peak for the samples heat-treated at higher temperatures. After heating the 3 wt% C powder to both 1600 and 1900°C, the only phases present were boron carbide, graphite, and TiB_2.

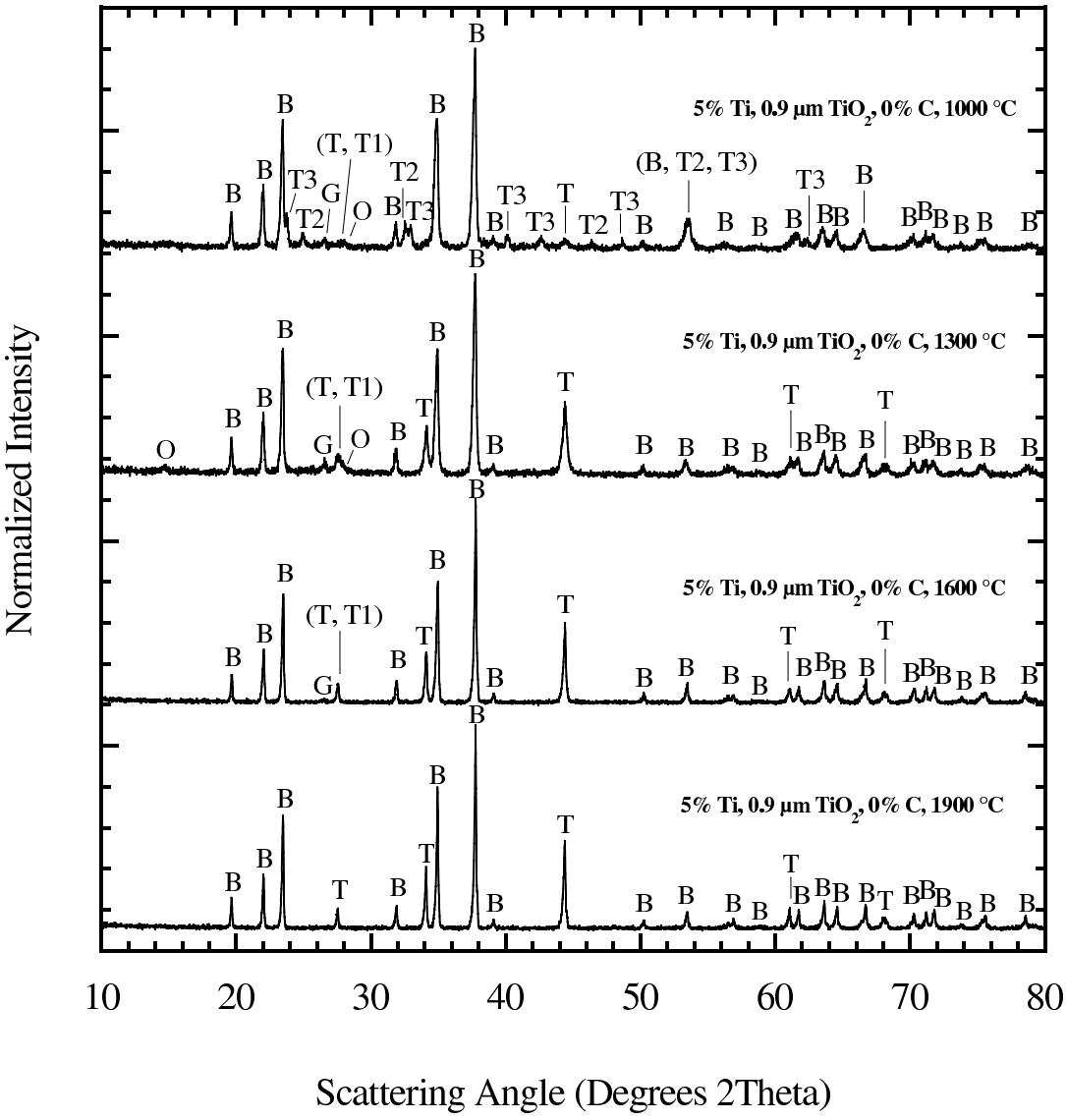

Figure 35: XRD traces of 5 wt% Ti, 0 wt% C, 0.9 μm TiO_2 powder composition heated at 50°C/min to 1000, 1300, 1600, and 1900°C. The diffraction patterns were normalized based upon the most intense peak in each scan. Labeling corresponds to the following: B($B_{13}C_2$), O(B_2O_3), G(graphite), T(TiB_2), T1(TiO_2), T2($TiBO_3$), and T3(Ti_2O_3).

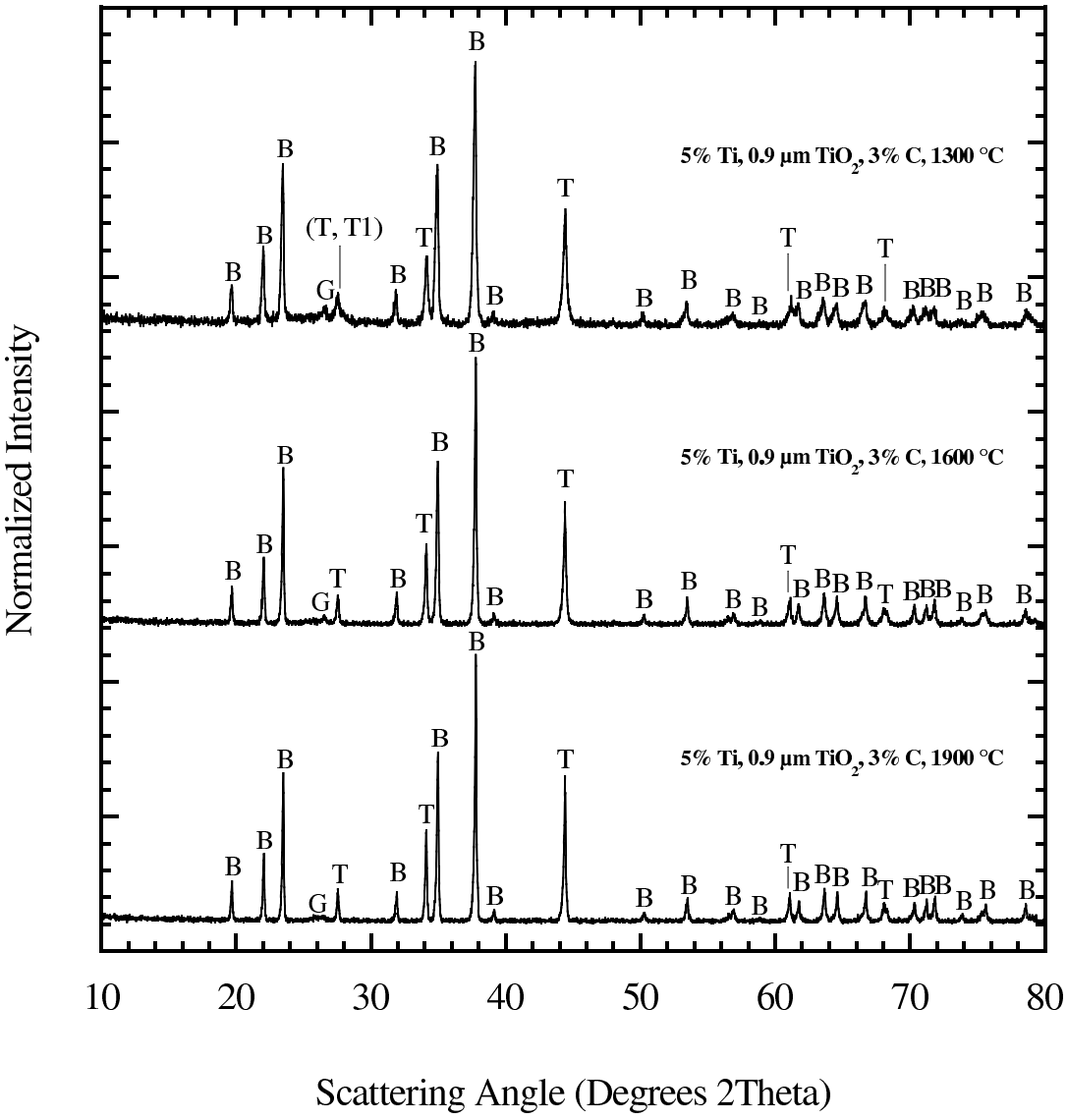

Figure 36: XRD traces of 5 wt% Ti, 3 wt% C, 0.9 μm TiO_2 powder composition heated at 50°C/min to 1300, 1600, and 1900°C. The diffraction patterns were normalized based upon the most intense peak in each scan. Labeling corresponds to the following: B($B_{13}C_2$), G(graphite), T(TiB_2), and T1(TiO_2).

4.2 Dilatometry Evaluation of Sintering Behavior

The green and post-sintered relative density data as well as the dilatometry traces for the pellets of each composition sintered at 2200°C and 2300°C are provided in the following tables and figures. Plots of the dimension change rate (i.e., the derivative of the dilatometry traces) for the 2300°C dilatometry traces are also included in order to illustrate the varying sintering rate behaviors of the different compositions. The relative green density and sintered density for the 0 wt% C, 32 nm TiO_2 dilatometry pellets sintered at 2200 and 2300°C are provided in Table 9. The dilatometry data for the 0% carbon 32 nm TiO_2 samples are provided in Figures 37 to 39. The green densities of these samples were in the range of 57% and did not display any observable dependence on the Ti content. The relative densities of the 0 wt% C, 32 nm TiO_2 samples sintered at 2200°C increased by 0.78% as the Ti content increased from 0.5 wt% to 1 wt%; however, the sintered relative densities decreased substantially by 8.91% and 14.22% with continued increases in Ti content up to 3 wt% and 5 wt%, respectively. The dilatometry traces for the 2200°C samples showed final dimension change values that were mostly consistent with the sintered relative densities; however, the 1 wt% Ti sample possessed the highest relative density, but showed slightly less dilatometric sintering shrinkage than the 0.5 wt% Ti sample, which had a marginally lower sintered relative density. This result could be explained by small caliper error during green density calculation prior to sintering.

The sintered relative densities of the 0 wt% C, 32 nm TiO_2 samples increased from ∼61-75% up to ∼70-92% by raising the sintering temperature from 2200°C to 2300°C. The sintered relative densities followed the trend of decreasing with increasing Ti content. For the samples sintered at 2300°C, the final contraction percentages were consistent with the measured sintered density results; however, the 0.5 wt% Ti sample, which possessed the highest sintered relative density, exhibited a marginally lower dilatometric sintering contraction than the 1 wt% Ti sample, which had a

slightly lower relative density.

The dimension change rate traces for the 0 wt% C, 32 nm TiO_2 dilatometry pellets sintered at 2300°C showed the onset of sintering for the 0.5, 1, 3, and 5 wt% Ti samples to occur at approximately 1731°C, 1737°C, 1725°C, and 1691°C, respectively. The sintering onset temperature for these samples initially increased and then decreased with increasing Ti content. As the temperature increased, the traces exhibited a slowing in the sintering rate. The temperature range of this initial deceleration region was strongly dependent upon the Ti content. For the 0.5, 1, 3, and 5 wt% Ti samples, the initial deceleration temperature ranges (with extents provided in parentheses) were 1923-2077°C (154°C), 1934-2076°C (142°C), 1872-2034°C (162°C), and 1869-1962°C (93°C), respectively. The onset temperature of this deceleration followed the general trend of shifting to lower temperatures with increasing Ti content. Additionally, the extent of this deceleration maintained a temperature range of 150-160°C, but shortened significantly to 93°C as the Ti content increased to 5 wt%.

Following the initial deceleration region, the sintering rate increased significantly with increasing temperature. The 0.5 and 1 wt% Ti samples exhibited slowing in the range of ∼2185 to 2242°C, but the higher Ti content samples did not display this behavior. With increasing temperature, the sintering rate increased to the maximum value for each sample. The magnitude of the sintering rate decreased substantially with increasing Ti content. After reaching the sintering temperature, the sintering rate slowed dramatically, and the samples exhibited varying times required to reach the end of sintering; for the 0.5, 1, 3, and 5 wt% Ti samples, the times to reach the end of sintering were 14.06, 14.07, 30, and 30 minutes, respectively. It should be noted that the 3 and 5 wt% Ti samples did not reach the end of sintering within the 30 minute sintering time prescribed in the experimental procedure. Based on these data, the sintering time increased by more than 200% as the Ti content (added in the form of TiO_2) exceeded 1 wt% for these 0 wt% C compositions.

Table 9: Relative Green Density and Sintered Density for 0 wt% C, 32 nm TiO_2 Samples Sintered at 2200 and 2300°C

Additive	Ti (wt%)	Sintering Temperature (°C)	Relative Green Density	Relative Sintered Density
32 nm TiO_2	0.5	2200	57.59%	74.80%
32 nm TiO_2	1	2200	57.23%	75.58%
32 nm TiO_2	3	2200	56.97%	66.67%
32 nm TiO_2	5	2200	57.76%	61.36%
32 nm TiO_2	0.5	2300	56.68%	92.10%
32 nm TiO_2	1	2300	57.12%	91.87%
32 nm TiO_2	3	2300	56.99%	82.78%
32 nm TiO_2	5			70.64%

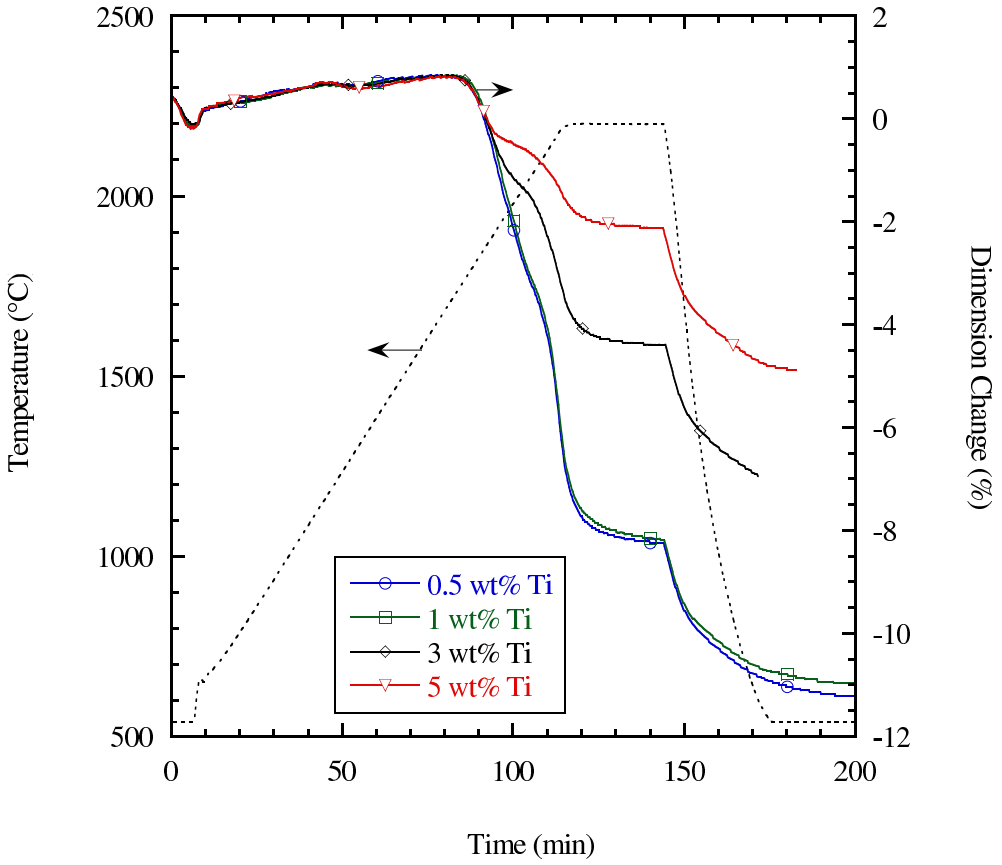

Figure 37: Dilatometry traces for all 0 wt% carbon 32 nm TiO_2 samples sintered at 2200°C

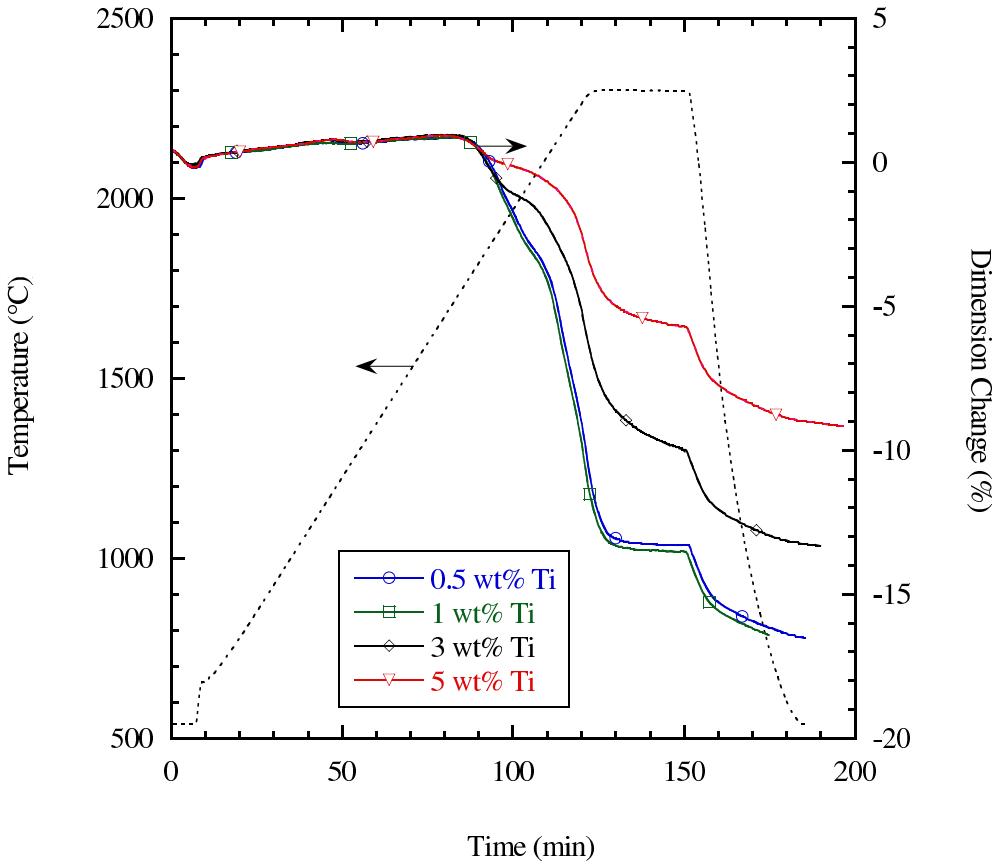

Figure 38: Dilatometry traces for all 0 wt% carbon 32 nm TiO_2 samples sintered at 2300°C

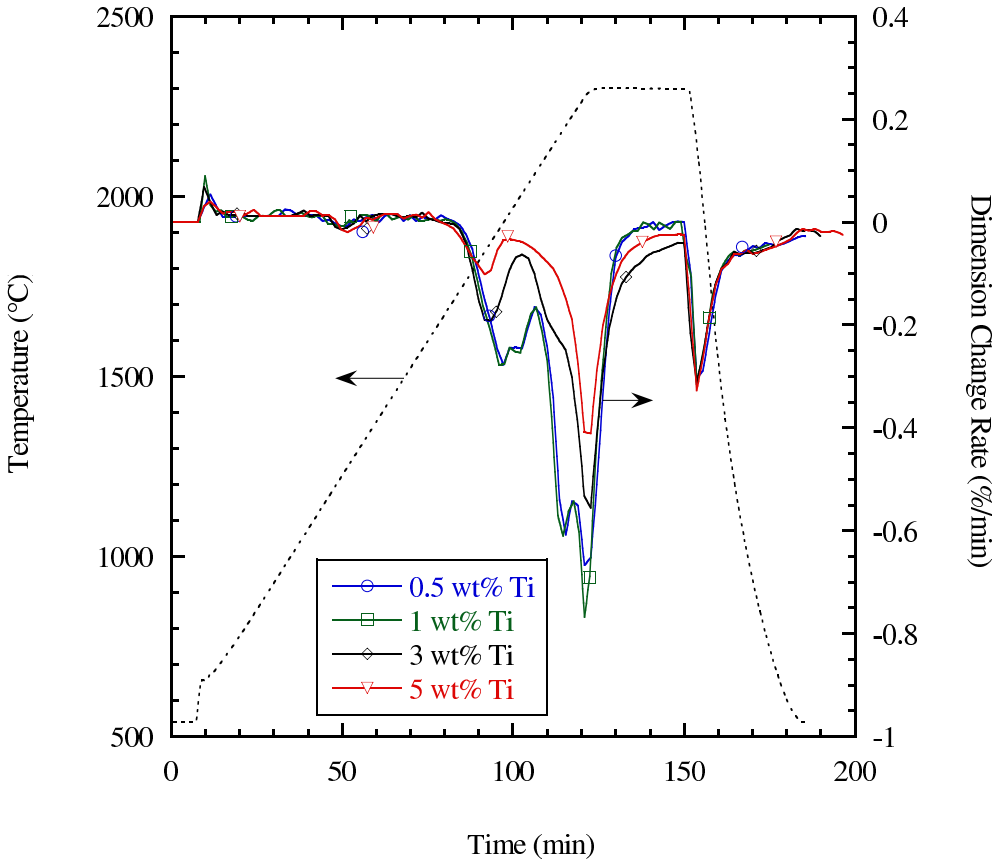

Figure 39: Dilatometry dimension change rate plots for all 0 wt% carbon 32 nm TiO_2 samples sintered at 2300°C

The relative green density and sintered density for the 1 wt% C, 32 nm TiO_2 dilatometry pellets sintered at 2200 and 2300°C are provided in Table 10. The dilatometry data for the 1 wt% carbon 32 nm TiO_2 samples are provided in Figures 40 to 42. The green densities of these samples were in the range of 51-53% and did not display any observable dependence on the Ti content. The relative densities of the 1 wt% C, 32 nm TiO_2 samples sintered at 2200°C decreased with increasing Ti content; the relative density decreased by 21.33% as the Ti content increased from 0.5 wt% to 5 wt%. The dilatometry traces for the 2200°C samples showed final dimension change values that were consistent with the sintered relative densities; samples with lower sintered relative densities exhibited lower sintering shrinkage.

The sintered relative densities of the 1 wt% C, 32 nm TiO_2 samples increased from ∼66-76% up to ∼77-92% by raising the sintering temperature from 2200°C to 2300°C. The sintered relative densities followed the trend of decreasing with increasing Ti content; however, as Ti content increased from 0.5 wt% to 1 wt%, the samples exhibited a slight increase (1.39%) in relative density. For the samples sintered at 2300°C, the final contraction percentages were mostly consistent with the measured sintered density results; however, the 1 wt% Ti sample, which possessed the highest sintered relative density, exhibited a marginally lower dilatometric sintering contraction than the 0.5 wt% Ti sample, which had a slightly lower relative density. This aberration could be the result of caliper error.

The dimension change rate traces for the 1 wt% C, 32 nm TiO_2 dilatometry pellets sintered at 2300°C showed the onset of sintering for the 0.5, 1, 3, and 5 wt% Ti samples to occur at approximately 1625°C, 1719°C, 1546°C, and 1631°C, respectively. These samples displayed no clear trend for the sintering onset temperature. It should be noted that the 3 wt% Ti sample displayed a substantially lower sintering onset temperature. A second pellet of this composition displayed identical shrinkage rate behavior when sintered under matching conditions. As the temperature increased,

the traces exhibited a slowing in the sintering rate. The temperature range of this initial deceleration region was strongly dependent upon the Ti content. For the 0.5, 1, 3, and 5 wt% Ti samples, the initial deceleration temperature ranges (with extents provided in parentheses) were 1924-2093°C (169°C), 1931-2079°C (148°C), 1876-2045°C (169°C), and 1888-1955°C (67°C), respectively. The onset temperature of this deceleration followed the overall trend of shifting to lower temperatures with increasing Ti content. Displaying behavior similar to the 0%C 32 nm TiO_2 samples, the extent of this deceleration maintained a temperature range of 150-170°C, but shortened significantly to 67°C as the Ti content increased to 5 wt%.

Following the initial deceleration region, the sintering rate increased significantly with increasing temperature. The 0.5 and 1 wt% Ti samples exhibited slowing in the range of ∼2180 to 2243°C, but the higher Ti content samples did not display this behavior. With increasing temperature, the sintering rate increased to the maximum value for each sample. The magnitude of the sintering rate decreased substantially with increasing Ti content. After reaching the sintering temperature, the sintering rate slowed dramatically, and the samples exhibited varying times required to reach the end of sintering; for the 0.5, 1, 3, and 5 wt% Ti samples, the times to reach the end of sintering were 15.53, 16.4, 30, and 30 minutes, respectively. It should be noted that the 3 and 5 wt% Ti samples did not reach the end of sintering within the 30 minute sintering time prescribed in the experimental procedure. Like the 0%C samples, the sintering time increased significantly as the Ti content exceeded 1 wt%.

Table 10: Relative Green Density and Sintered Density for 1 wt% C 32 nm TiO_2 Samples Sintered at 2200 and 2300°C

Additive	Ti (wt%)	Sintering Temperature (°C)	Relative Green Density	Relative Sintered Density
32 nm TiO_2	0.5	2200	53.35%	76.16%
32 nm TiO_2	1	2200	53.74%	75.46%
32 nm TiO_2	3	2200	52.52%	70.22%
32 nm TiO_2	5	2200	51.69%	66.00%
32 nm TiO_2	0.5	2300	52.81%	91.29%
32 nm TiO_2	1	2300	52.07%	92.68%
32 nm TiO_2	3	2300	53.04%	87.80%
32 nm TiO_2	5	2300	52.75%	79.91%

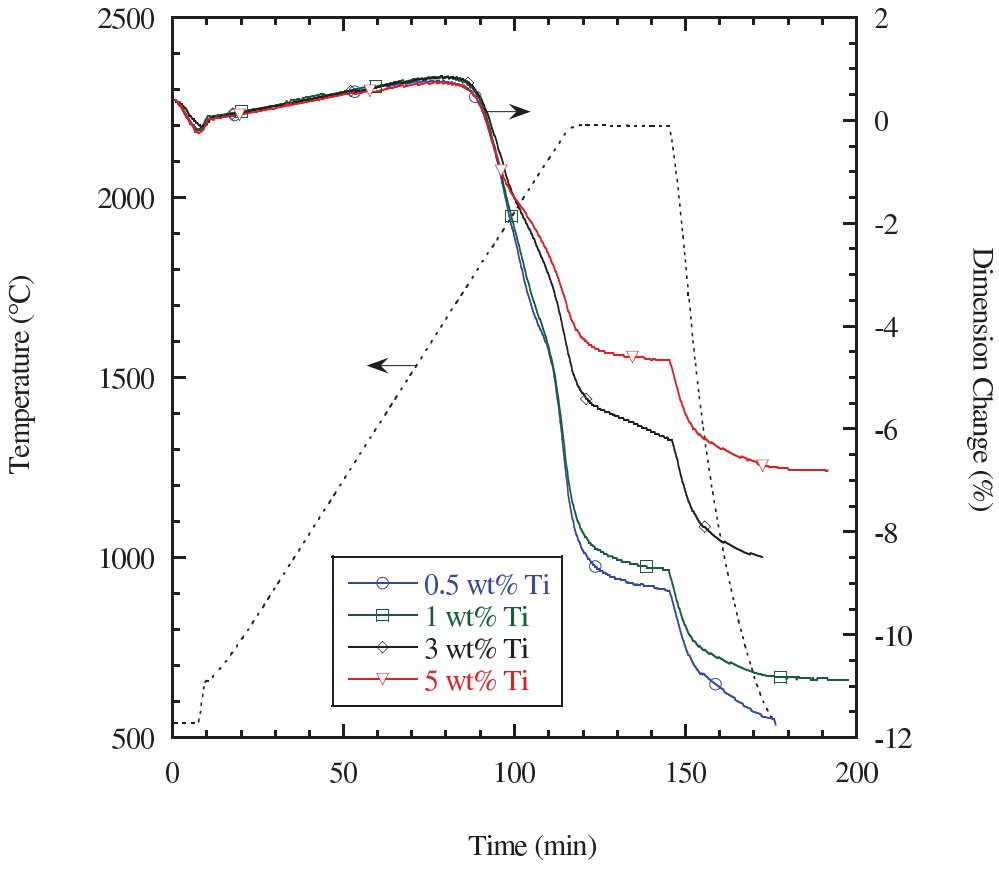

Figure 40: Dilatometry traces for all 1 wt% carbon 32 nm TiO_2 samples sintered at 2200°C

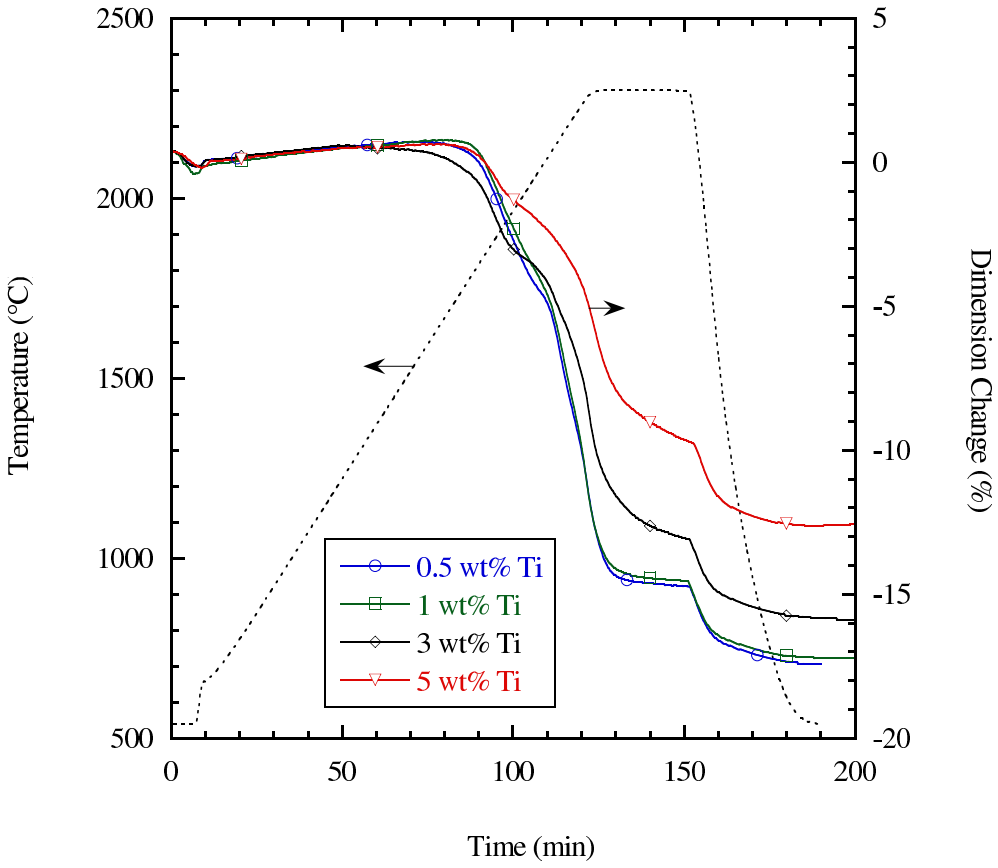

Figure 41: Dilatometry traces for all 1 wt% carbon 32 nm TiO_2 samples sintered at 2300°C

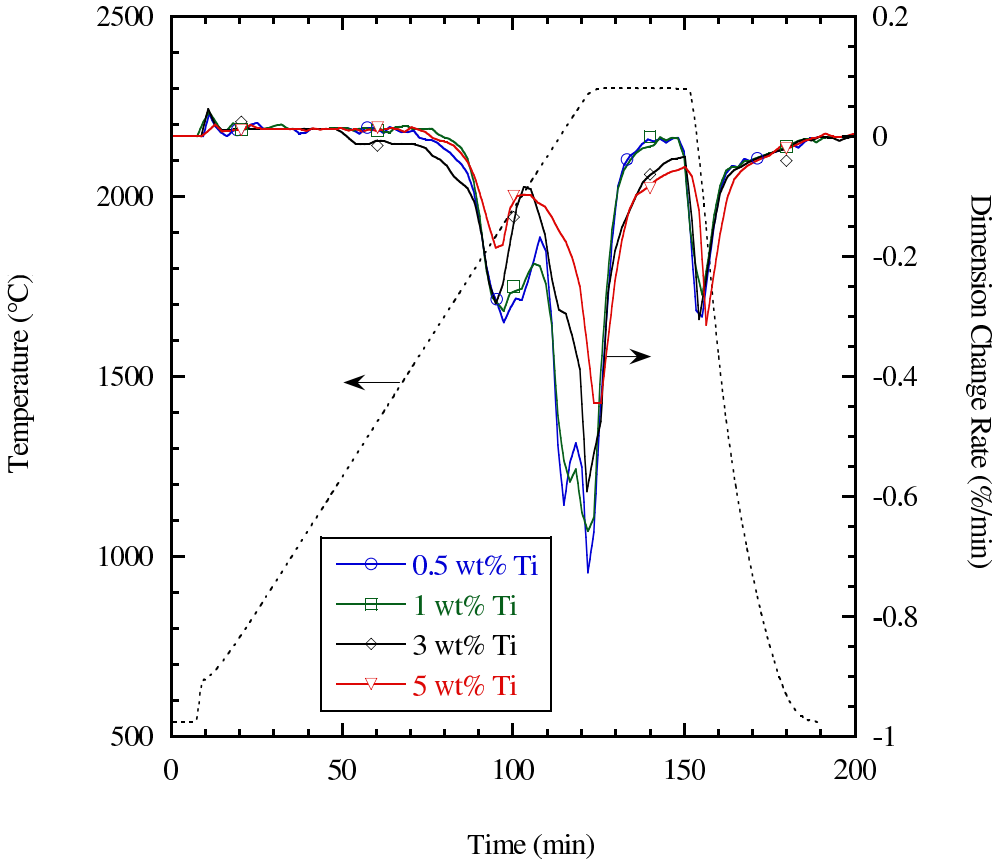

Figure 42: Dilatometry dimension change rate plots for all 1 wt% carbon 32 nm TiO_2 samples sintered at 2300°C

The relative green density and sintered density for the 3 wt% C, 32 nm TiO_2 dilatometry pellets sintered at 2200 and 2300°C are provided in Table 11. The dilatometry data for the 3% carbon 32 nm TiO_2 samples are provided in Figures 43 to 45. The green densities of these samples were in the range of 54-55% and did not display any observable dependence on the Ti content. The relative densities of the 3 wt% C, 32 nm TiO_2 samples sintered at 2200°C increased as the Ti content increased from 0.5 wt% to 1 wt%. The relative density then decreased by 5.02% as the Ti content increased from 1 wt% to 5 wt%. The dilatometry traces for the 2200°C samples showed final dimension change values that were very similar; however, these sintering shrinkage values were inconsistent with the sintered relative densities. The error associated with green body dimensional measurements using calipers could be the result of these inconsistencies.

The sintered relative densities of the 3 wt% C, 32 nm TiO_2 samples increased from ∼79-84% up to ∼94-96% by raising the sintering temperature from 2200°C to 2300°C. The sintered relative densities followed the trend of decreasing with increasing Ti content. For the samples sintered at 2300°C, the final contraction percentages were not consistent with the measured sintered density results; the sample containing 3 wt% Ti had the second lowest relative density, yet it displayed the greatest sintering shrinkage. Additionally, the 0.5 wt% Ti sample had the highest relative density, but exhibited a noticeably lower sintering shrinkage than the other samples. These discrepancies could be explained by the higher green density measured for the 0.5 wt% Ti sample, and the low green density measured for the 3 wt% Ti sample. For similar final sintered relative densities, one would expect lower green density samples to incur more sintering-related shrinkage and the converse for samples with higher green densities.

The dimension change rate traces for the 3 wt% C, 32 nm TiO_2 dilatometry pellets sintered at 2300°C showed the onset of sintering for the 0.5, 1, 3, and 5 wt% Ti samples

to occur at approximately 1656°C, 1672°C, 1690°C, and 1701°C, respectively. For these samples, the sintering onset temperature increased with increasing Ti content. As the temperature increased, the traces exhibited a slowing in the sintering rate. The temperature range of this initial deceleration region was strongly dependent upon the Ti content. For the 0.5, 1, 3, and 5 wt% Ti samples, the initial deceleration temperature ranges (with extents provided in parentheses) were 1938-1981°C (43°C), 1932-1983°C (51°C), 1931-1983°C (52°C), and 1940-1982°C (42°C), respectively. The onset temperature of this deceleration did not significantly change with increasing Ti content. Compared to the 0 and 1%C 32 nm TiO_2 samples, the extent of this deceleration shortened significantly to 40-50°C as the carbon content increased to 3 wt%.

Following the initial deceleration region, the sintering rate increased significantly with increasing temperature. None of the samples exhibited deceleration in the range of ∼2180 to 2243°C. With increasing temperature, the sintering rate increased to the maximum value for each sample. The magnitude of the sintering rate did not change substantially with increasing Ti content. After reaching the sintering temperature, the sintering rate slowed dramatically, and the samples exhibited similar times to reach the end of sintering; for the 0.5, 1, 3, and 5 wt% Ti samples, the times required to reach the end of sintering were 9.96, 10.25, 11.13, and 10.54 minutes, respectively. Compared to the 0 and 1%C samples, the sintering time decreased significantly (by $\sim$ 40%) as the carbon content increased to 3 wt%. Additionally, the 3 and 5 wt% Ti samples containing 3 wt% C did not exhibit the exceedingly long sintering times observed for the 0 and 1 wt% C samples containing identical amounts of Ti.

Table 11: Relative Green Density and Sintered Density for 3 wt% C, 32 nm TiO_2 Samples Sintered at 2200 and 2300°C

Additive	Ti (wt%)	Sintering Temperature (°C)	Relative Green Density	Relative Sintered Density
32 nm TiO_2	0.5	2200	54.95%	83.99%
32 nm TiO_2	1	2200	55.03%	84.31%
32 nm TiO_2	3	2200	54.80%	82.49%
32 nm TiO_2	5	2200	54.04%	79.29%
32 nm TiO_2	0.5	2300	55.83%	96.12%
32 nm TiO_2	1	2300	54.86%	95.99%
32 nm TiO_2	3	2300	54.60%	95.13%
32 nm TiO_2	5	2300	54.90%	94.81%

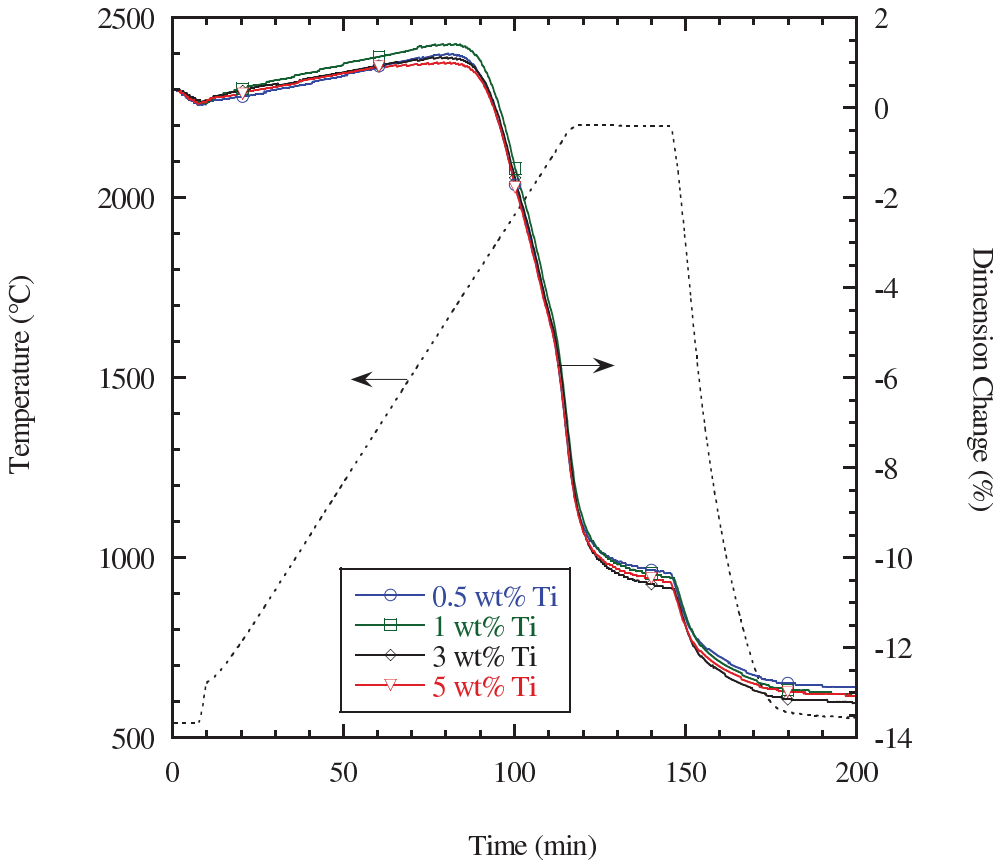

Figure 43: Dilatometry traces for all 3 wt% carbon 32 nm TiO_2 samples sintered at 2200°C

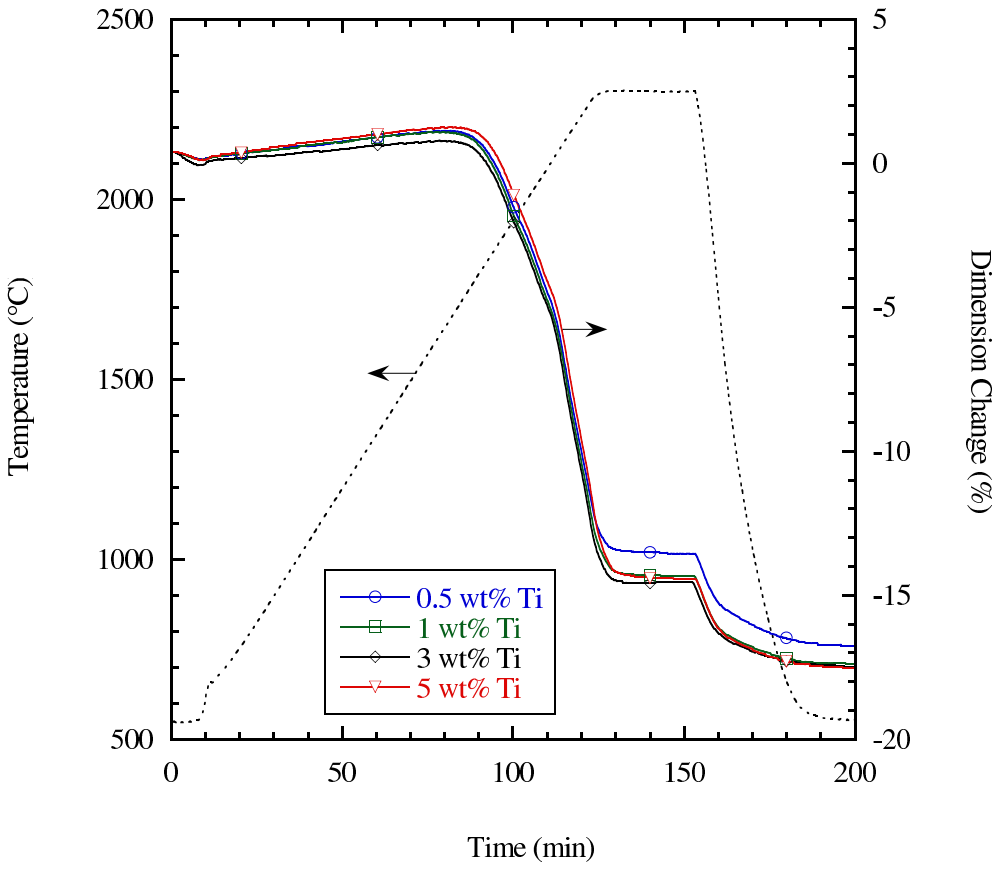

Figure 44: Dilatometry traces for all 3 wt% carbon 32 nm TiO_2 samples sintered at 2300°C

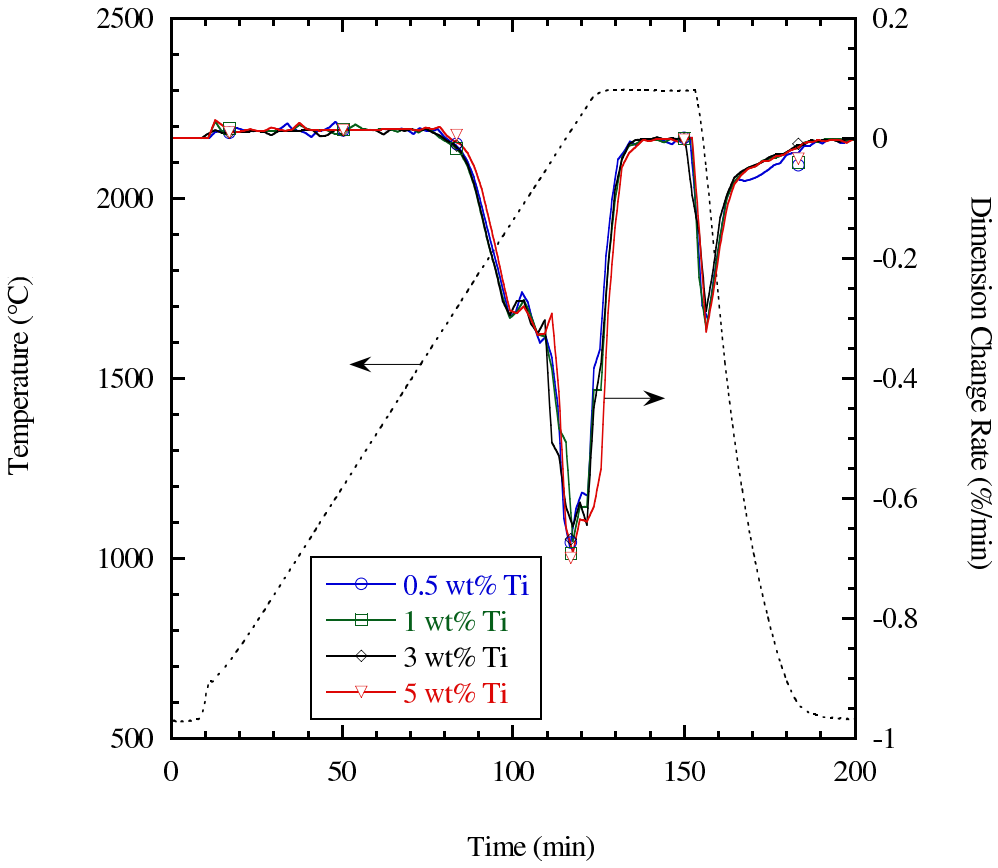

Figure 45: Dilatometry dimension change rate plots for all 3 wt% carbon 32 nm TiO_2 samples sintered at 2300°C

The relative green density and sintered density for the 0 wt% C, 0.9 μm TiO_2 dilatometry pellets sintered at 2200 and 2300°C are provided in Table 12. The dilatometry data for the 0% carbon 0.9 μm TiO_2 samples are provided in Figures 46 to 48. The green densities of these samples were in the range of 57-58% and did not display any dependence on the Ti content. The relative densities of the 0 wt% C, 0.9 μm TiO_2 samples sintered at 2200°C decreased by 15.36% as the Ti content increased from 0.5 wt% to 5 wt%. The dilatometry traces for the 2200°C samples showed final dimension change values that were consistent with the sintered relative densities.

The sintered relative densities of the 0 wt% C, 0.9 μm TiO_2 samples increased from ∼62-77% up to ∼71-92% by raising the sintering temperature from 2200°C to 2300°C. The sintered relative densities followed the trend of decreasing with increasing Ti content. For the samples sintered at 2300°C, the final contraction percentages were mostly consistent with the measured sintered density results. The sample containing 1 wt% Ti had the second highest relative density, yet it displayed the greatest sintering shrinkage, and the 0.5 wt% Ti sample had the highest relative density, but exhibited a lower sintering shrinkage than the 1 wt% Ti sample. The green densities of the samples did not explain this behavior, so the aberration could be the result of measurement error.

The dimension change rate traces for the 0 wt% C, 0.9 μm TiO_2 dilatometry pellets sintered at 2300°C showed the onset of sintering for the 0.5, 1, 3, and 5 wt% Ti samples to occur at approximately 1733°C, 1732°C, 1719°C, and 1710°C, respectively. For these samples, the sintering onset temperature decreased with increasing Ti content. As the temperature increased, the traces exhibited a slowing in the sintering rate. The temperature range of this initial deceleration region was strongly dependent upon the Ti content. For the 0.5, 1, 3, and 5 wt% Ti samples, the initial deceleration temperature ranges (with extents provided in parentheses) were 1924-2066°C (142°C),

Table 12: Relative Green Density and Sintered Density for 0 wt% C, 0.9 μm TiO_2 Samples Sintered at 2200 and 2300°C

Additive	Ti (wt%)	Sintering Temperature (°C)	Relative Green Density	Relative Sintered Density
0.9 μm TiO_2	0.5	2200	57.88%	77.57%
0.9 μm TiO_2	1	2200	57.97%	76.12%
0.9 μm TiO_2	3	2200	57.76%	66.18%
0.9 μm TiO_2	5	2200	58.60%	62.21%
0.9 μm TiO_2	0.5	2300	57.90%	92.79%
0.9 μm TiO_2	1	2300	58.54%	92.03%
0.9 μm TiO_2	3	2300	57.88%	83.05%
0.9 μm TiO_2	5	2300	58.51%	71.73%

1930-2076°C (146°C), 1910-2009°C (99°C), and 1884-1991°C (107°C), respectively. The onset temperature of this deceleration initially increased and then decreased with increasing Ti content. Additionally, the extent of this deceleration range shortened by 35°C as the Ti content increased from 0.5 wt% to 5 wt%.

Following the initial deceleration region, the sintering rate increased significantly with increasing temperature. None of these 0.9 μm TiO_2 samples exhibited deceleration in the range of ~2180 to 2240°C that had been observed in several of the 32 nm TiO_2 samples. With increasing temperature, the sintering rate increased to the maximum value for each sample. The magnitude of the sintering rate decreased substantially with increasing Ti content. After reaching the sintering temperature, the sintering rate slowed dramatically, and the samples exhibited increasing times to reach the end of sintering with increasing Ti content; for the 0.5, 1, 3, and 5 wt% Ti samples, the times required to reach the end of sintering were 10.54, 13.8, 30, and 30 minutes, respectively. It should be noted that the 3 wt% and 5 wt% Ti samples did not reach the end of sintering within the 30 minute hold at the sintering temperature.

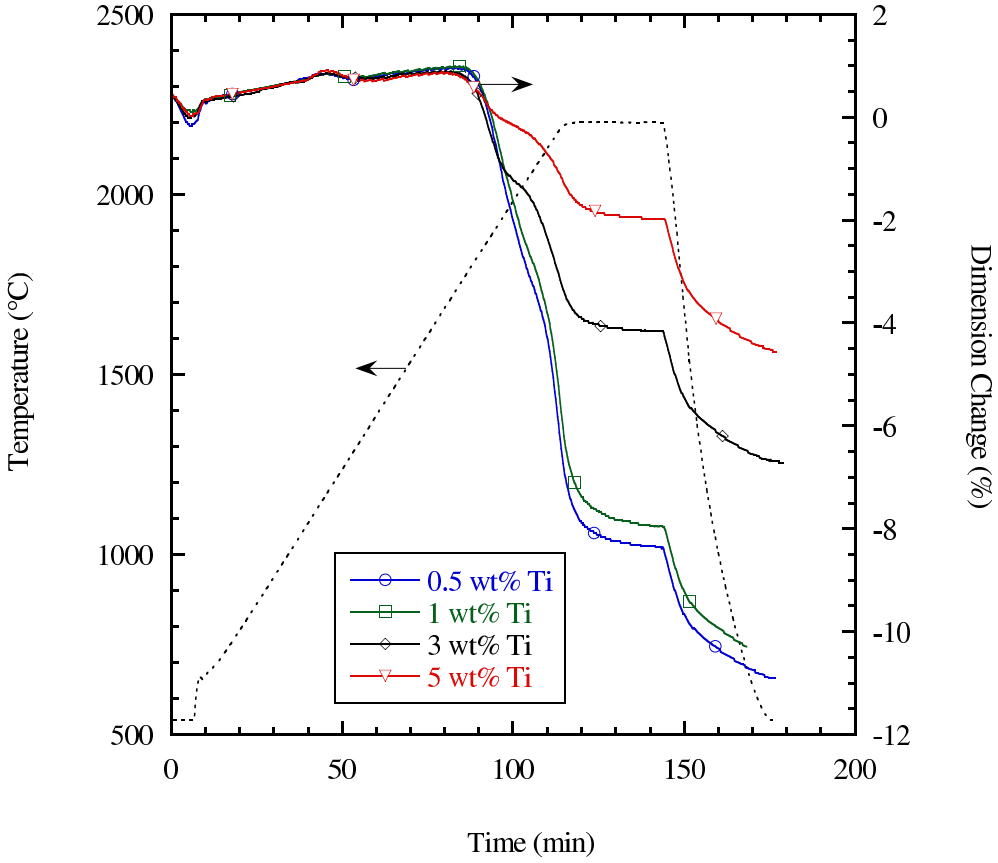

Figure 46: Dilatometry traces for all 0 wt% carbon 0.9 μm TiO_2 samples sintered at 2200°C

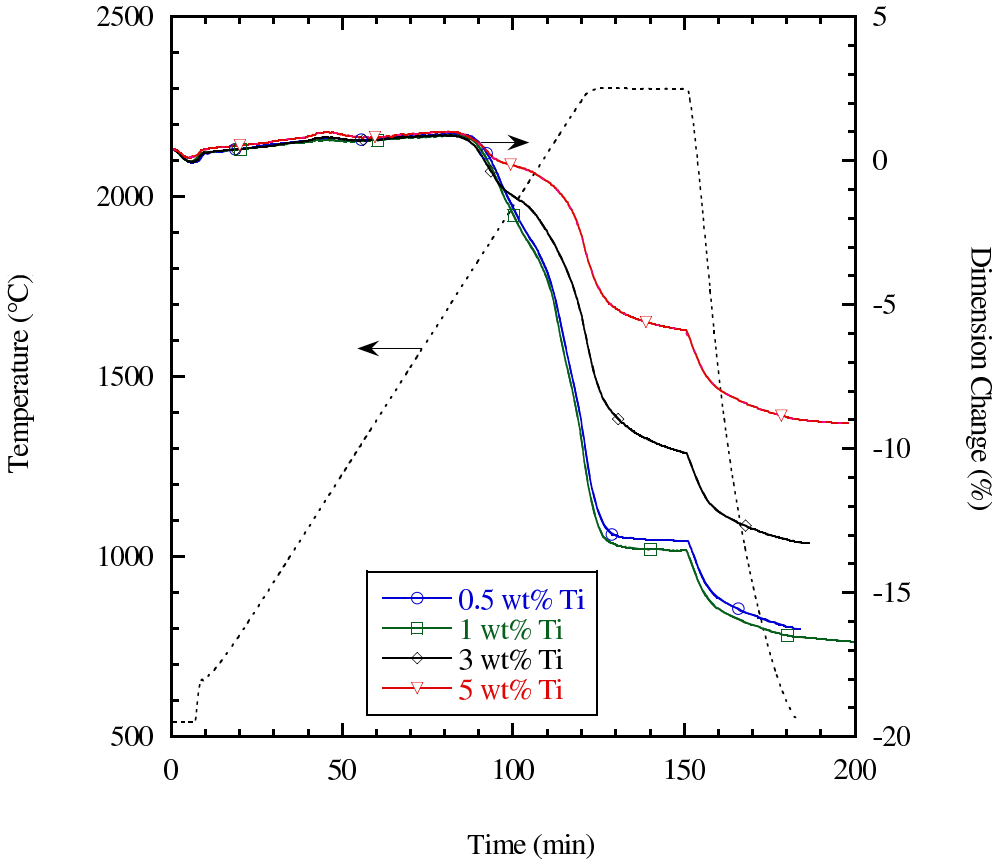

Figure 47: Dilatometry traces for all 0 wt% carbon 0.9 μm TiO_2 samples sintered at 2300°C

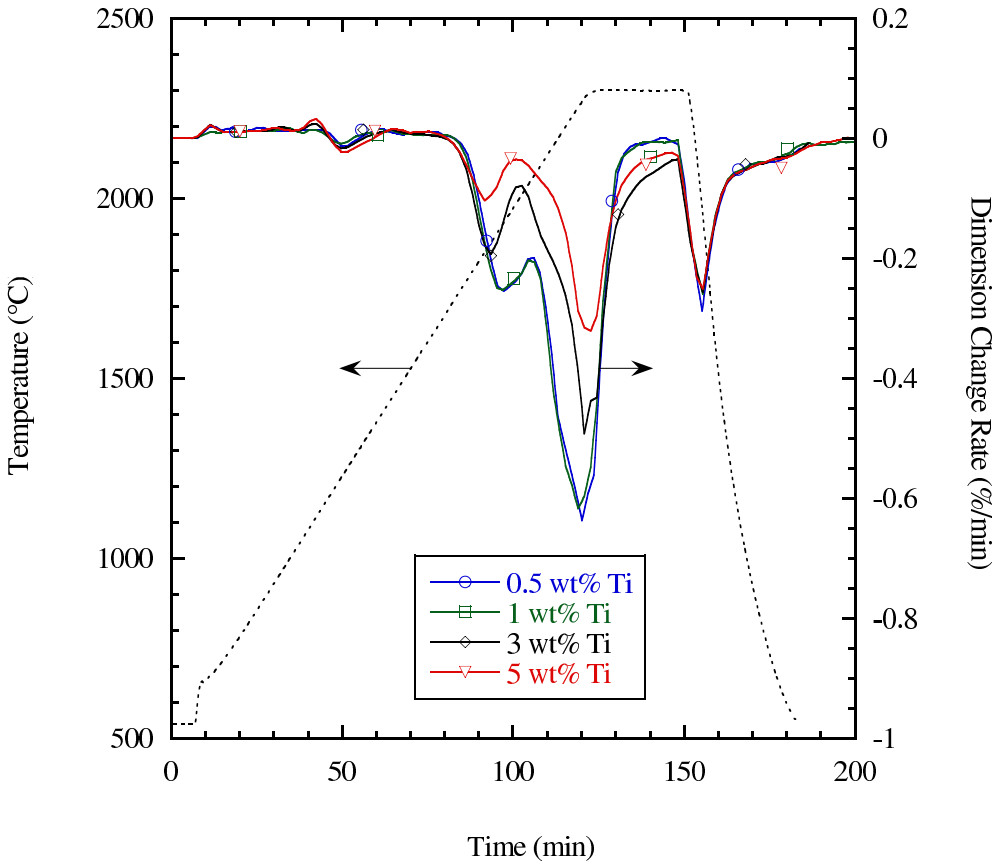

Figure 48: Dilatometry dimension change rate plots for all 0 wt% carbon 0.9 μm TiO_2 samples sintered at 2300°C

The relative green density and sintered density for the 1 wt% C 0.9 μm TiO_2 dilatometry pellets sintered at 2200 and 2300°C are provided in Table 13. The dilatometry data for the 1% carbon 0.9 μm TiO_2 samples are provided in Figures 49 to 51. The green densities of these samples were in the range of 51-53% and decreased with increasing Ti content. The relative densities of the 1%C 0.9 μm TiO_2 samples sintered at 2200°C increased as the Ti content increased from 0.5 wt% to 1 wt% Ti, but the relative density then decreased as the Ti content continued to increase. The relative density decreased by 8.61% as the Ti content increased from 1 wt% to 5 wt%. The dilatometry traces for the 2200°C samples showed final dimension change values that were mostly consistent with the sintered relative densities. While the ordering of the sintering contractions were in agreement with the sintered densities, the dimensional change of the 1 wt% Ti sample appeared to be disproportionately larger than warranted by the marginally high relative density.

The sintered relative densities of the 1%C 0.9 μm TiO_2 samples increased from ∼68-77% up to ∼82-92% by raising the sintering temperature from 2200°C to 2300°C. The sintered relative densities followed the trend of decreasing with increasing Ti content. For the samples sintered at 2300°C, the final contraction percentages were mostly consistent with the measured sintered density results. The sample containing 1 wt% Ti had the second highest relative density, yet it displayed the greatest sintering shrinkage, and the 0.5 wt% Ti sample had the highest relative density, but exhibited a lower sintering shrinkage than the 1 wt% Ti sample. The lower green density of the 1 wt% Ti sample could explain the greater observed sintering contraction.

The dimension change rate traces for the 1%C 0.9 μm TiO_2 dilatometry pellets sintered at 2300°C showed the onset of sintering for the 0.5, 1, 3, and 5 wt% Ti samples to occur at approximately 1685°C, 1649°C, 1642°C, and 1603°C, respectively. For these samples, the sintering onset temperature decreased with increasing Ti content. As the temperature increased, the traces exhibited a slowing in the sintering rate.

The temperature range of this initial deceleration region was strongly dependent upon the Ti content. For the 0.5, 1, 3, and 5 wt% Ti samples, the initial deceleration temperature ranges (with extents provided in parentheses) were 1928-2093°C (165°C), 1925-2062°C (137°C), 1919-2008°C (89°C), and 1895-2008°C (113°C), respectively. The onset temperature of this deceleration decreased with increasing Ti content, and the extent of this deceleration range shortened by 76°C as the Ti content increased from 0.5 wt% to 3 wt%. The deceleration region extent then lengthened by 24°C as the Ti content increased from 3 to 5 wt%.

Following the initial deceleration region, the sintering rate increased significantly with increasing temperature. None of these 0.9 μm TiO_2 samples exhibited deceleration in the range of ~2180 to 2240°C that had been observed in several of the 32 nm TiO_2 samples. With increasing temperature, the sintering rate increased to the maximum value for each sample. The magnitude of the sintering rate decreased substantially with increasing Ti content. After reaching the sintering temperature, the sintering rate slowed dramatically, and the samples exhibited increasing times to reach the end of sintering with increasing Ti content; for the 0.5, 1, 3, and 5 wt% Ti samples, the times required to reach the end of sintering were 10.67, 12.76, 30, and 30 minutes, respectively. It should be noted that the 3 wt% and 5 wt% Ti samples did not reach the end of sintering within the 30 minute hold at the sintering temperature.

Table 13: Relative Green Density and Sintered Density for 1 wt% C 0.9 μm TiO_2 Samples Sintered at 2200 and 2300°C

Additive	Ti (wt%)	Sintering Temperature (°C)	Relative Green Density	Relative Sintered Density
0.9 μm TiO_2	0.5	2200	53.19%	76.73%
0.9 μm TiO_2	1	2200	52.98%	77.02%
0.9 μm TiO_2	3	2200	51.83%	71.17%
0.9 μm TiO_2	5	2200	51.20%	68.41%
0.9 μm TiO_2	0.5	2300	53.57%	92.00%
0.9 μm TiO_2	1	2300	53.45%	91.72%
0.9 μm TiO_2	3	2300	52.70%	88.09%
0.9 μm TiO_2	5	2300	51.32%	82.65%

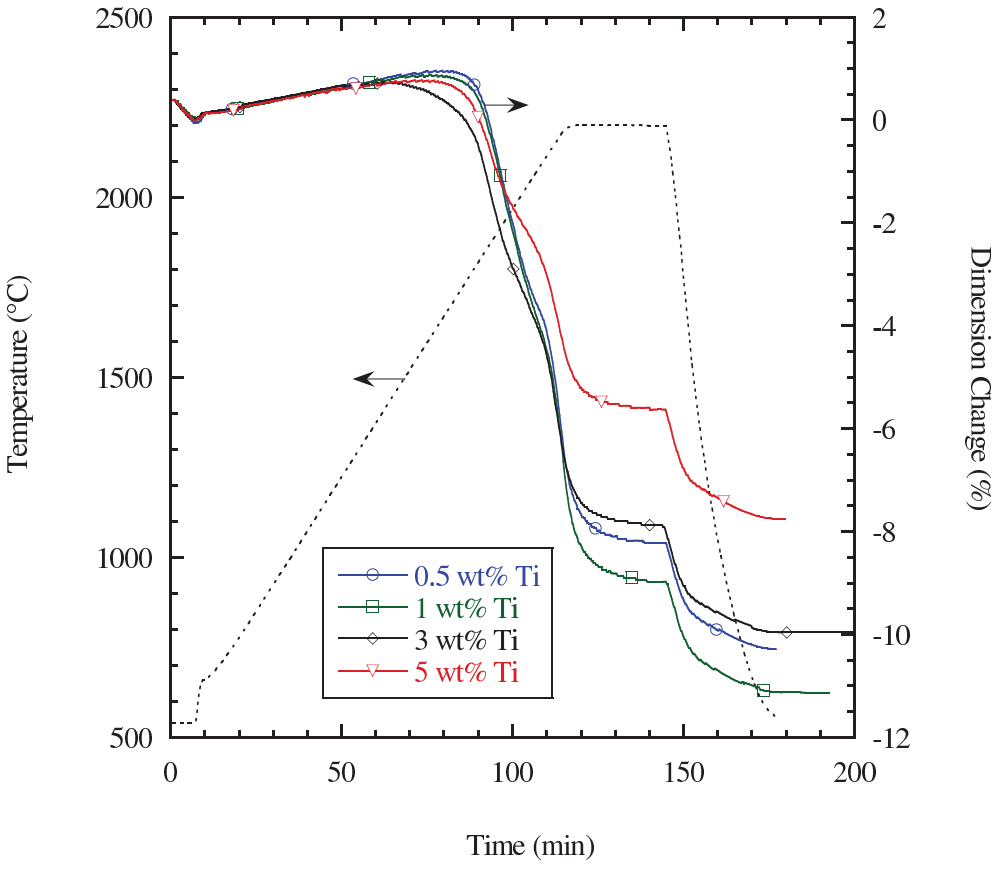

Figure 49: Dilatometry traces for all 1 wt% carbon 0.9 μm TiO_2 samples sintered at 2200°C

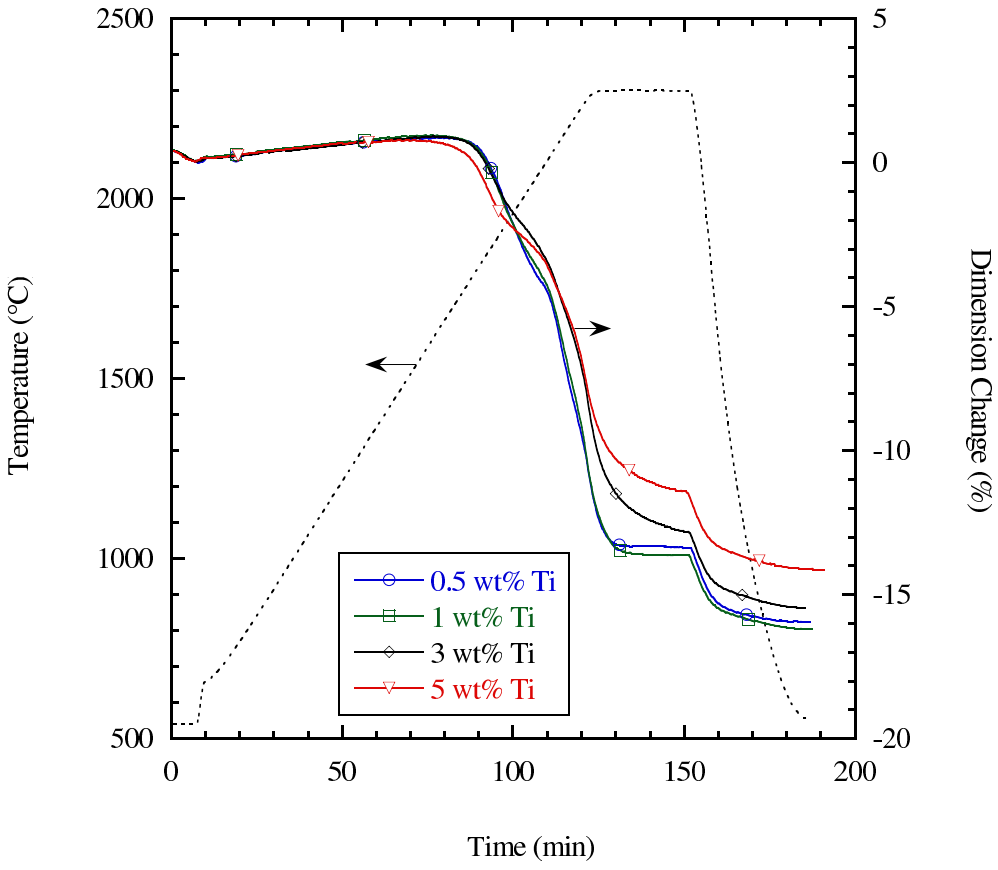

Figure 50: Dilatometry traces for all 1 wt% carbon 0.9 μm TiO_2 samples sintered at 2300°C

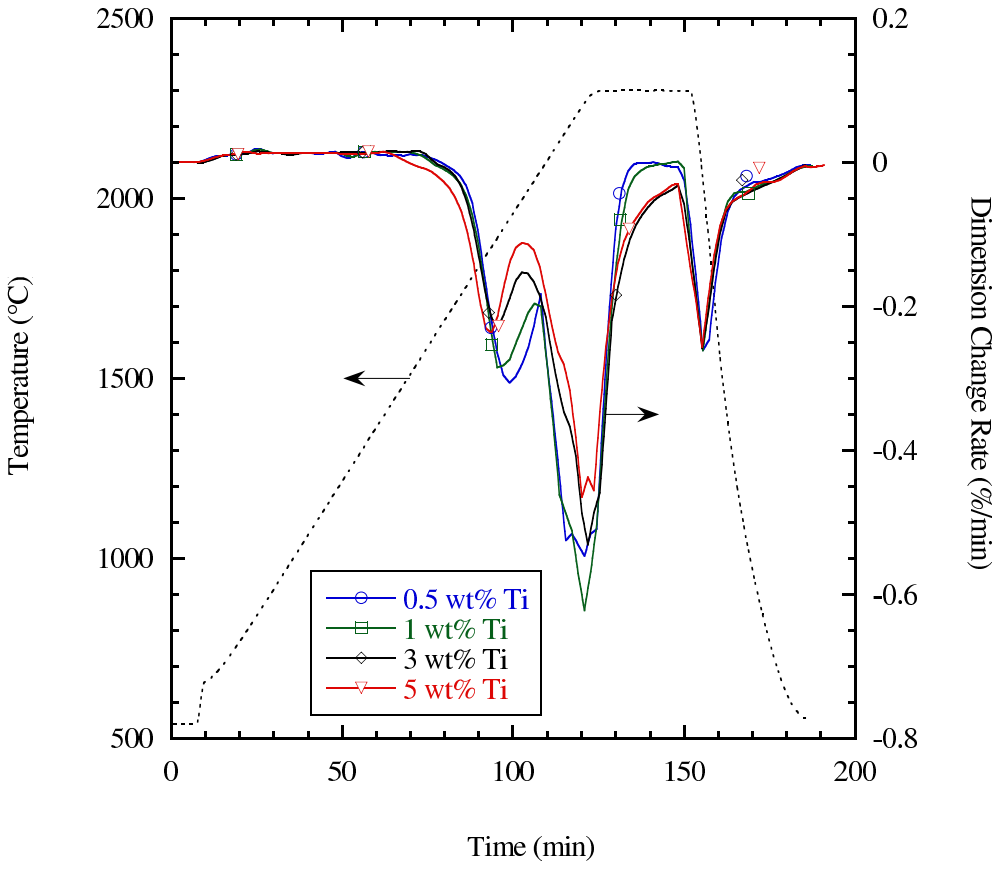

Figure 51: Dilatometry dimension change rate plots for all 1 wt% carbon 0.9 μm TiO_2 samples sintered at 2300°C

The relative green density and sintered density for the 3% C 0.9 μm TiO_2 dilatometry pellets sintered at 2200 and 2300°C are provided in Table 14. The dilatometry data for the 3% carbon 0.9 μm TiO_2 samples are provided in Figures 52 to 54. The green densities of these samples were in the range of 54-55% and decreased with increasing Ti content. The relative densities of the 3%C 0.9 μm TiO_2 samples sintered at 2200°C decreased as the Ti content increased. The relative density decreased by 3.16% as the Ti content increased from 0.5 wt% to 5 wt%. The dilatometry traces for the 2200°C samples showed final dimension change values that were very similar despite the varying final relative sintered densities. The lower green density with increasing Ti content could explain the behavior of the sintering contraction data.

The sintered relative densities of the 3%C 0.9 μm TiO_2 samples increased from ∼80-83% up to ∼95-96% by raising the sintering temperature from 2200°C to 2300°C. The sintered relative densities decreased as the Ti content increased from 0.5 wt% to 3 wt%; however, the relative density then increased as the Ti content increased to 5 wt%. For the samples sintered at 2300°C, the final contraction percentages were inconsistent with the measured sintered density results. The sample containing 5 wt% Ti had the second highest relative density, yet it displayed the greatest sintering shrinkage, and the 3 wt% Ti sample had the lowest relative density, but exhibited the second highest sintering shrinkage. The ordering of the sintering contraction for these samples could be explained by the differences in green density; as the green density decreased with increasing Ti content, greater sintering contraction was required to reach a given relative density.

The dimension change rate traces for the 3%C 0.9 μm TiO_2 dilatometry pellets sintered at 2300°C showed the onset of sintering for the 0.5, 1, 3, and 5 wt% Ti samples to occur at approximately 1674°C, 1653°C, 1663°C, and 1667°C, respectively. For these samples, the sintering onset temperature decreased as the Ti content increased from 0.5 wt% to 1 wt% and then increased slightly as the Ti content further increased.

As the temperature increased, the traces exhibited no deceleration in the sintering rate within the temperature range of 1920-2090°C. The behavior of these higher carbon content samples differed significantly from the sintering characteristics observed for the 0 and 1%C 0.9 μm TiO_2 samples, which displayed noticeable deceleration in the aforementioned temperature range.

With increasing temperature, the sintering rate increased significantly, and none of the 3%C samples exhibited deceleration in the range of ∼2180 to 2240°C. As the temperature approached the sintering hold temperature, the sintering rate increased to the maximum value for each sample. All of the samples displayed very similar sintering shrinkage magnitudes that had no detectable dependence on Ti content. After reaching the sintering temperature, the sintering rate slowed dramatically, and the samples exhibited increasing times to reach the end of sintering with increasing Ti content; for the 0.5, 1, 3, and 5 wt% Ti samples, the times required to reach the end of sintering were 7.62, 8.2, 10.25, and 11.72 minutes, respectively. Compared to the 0 and 1%C samples, the sintering time decreased significantly as the carbon content increased to 3 wt%. Additionally, the 3 and 5 wt% Ti samples containing 3 wt% C did not exhibit the exceedingly long sintering times observed for the 0 and 1 wt% C samples containing identical amounts of Ti.

Table 14: Relative Green Density and Sintered Density for 3 wt% C, 0.9 μm TiO_2 Samples Sintered at 2200 and 2300°C

Additive	Ti (wt%)	Sintering Temperature (°C)	Relative Green Density	Relative Sintered Density
0.9 μm TiO_2	0.5	2200	55.51%	83.55%
0.9 μm TiO_2	1	2200	54.82%	83.47%
0.9 μm TiO_2	3	2200	54.33%	81.75%
0.9 μm TiO_2	5	2200	54.11%	80.39%
0.9 μm TiO_2	0.5	2300	55.50%	95.94%
0.9 μm TiO_2	1	2300	55.40%	95.37%
0.9 μm TiO_2	3	2300	54.51%	94.94%
0.9 μm TiO_2	5	2300	53.98%	95.70%

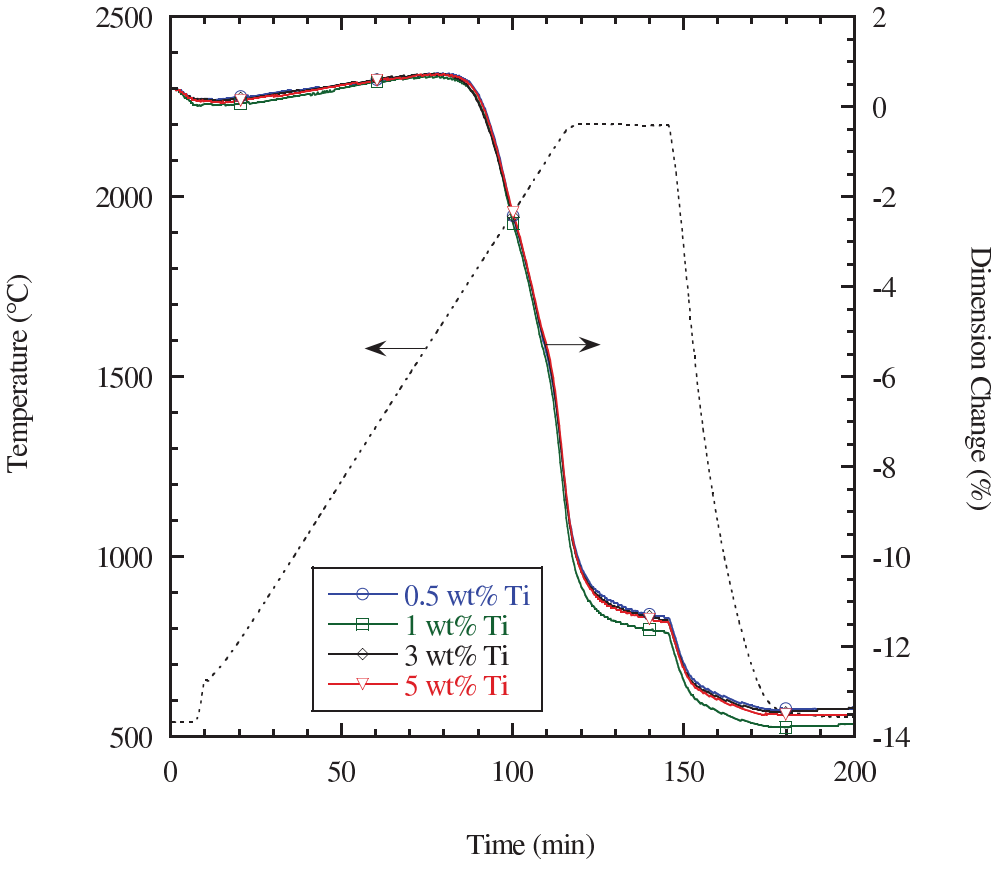

Figure 52: Dilatometry traces for all 3 wt% carbon, 0.9 μm TiO_2 samples sintered at 2200°C

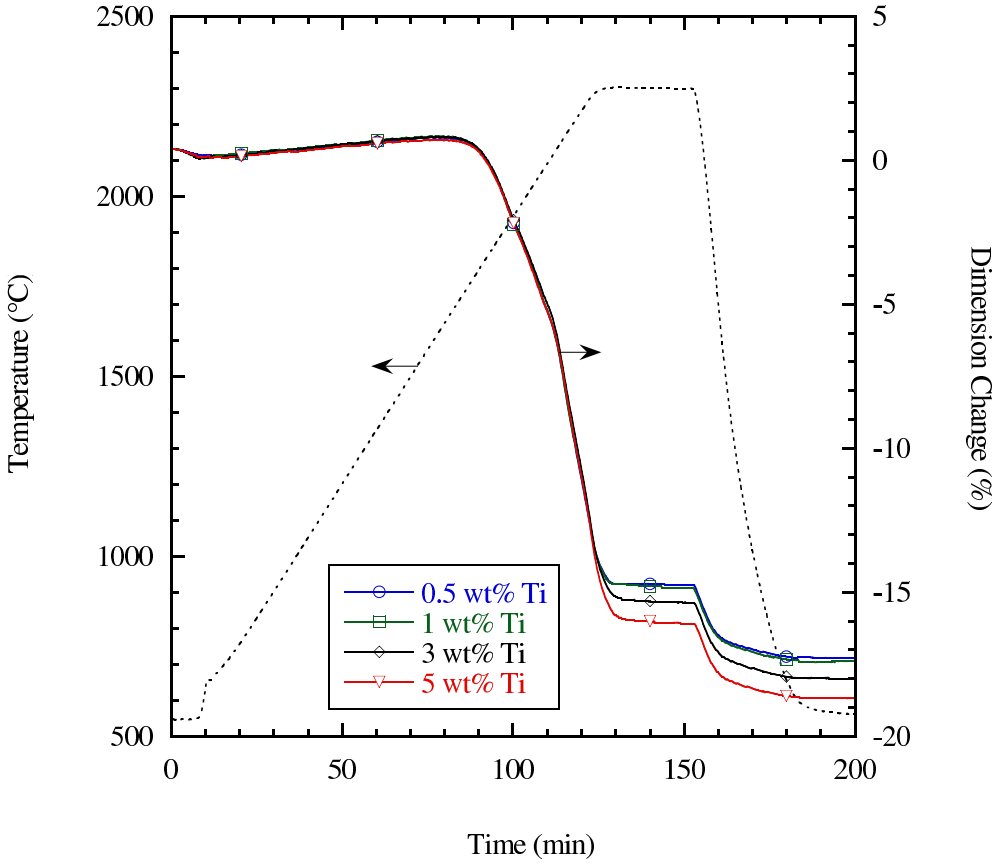

Figure 53: Dilatometry traces for all 3 wt% carbon, 0.9 μm TiO_2 samples sintered at 2300°C

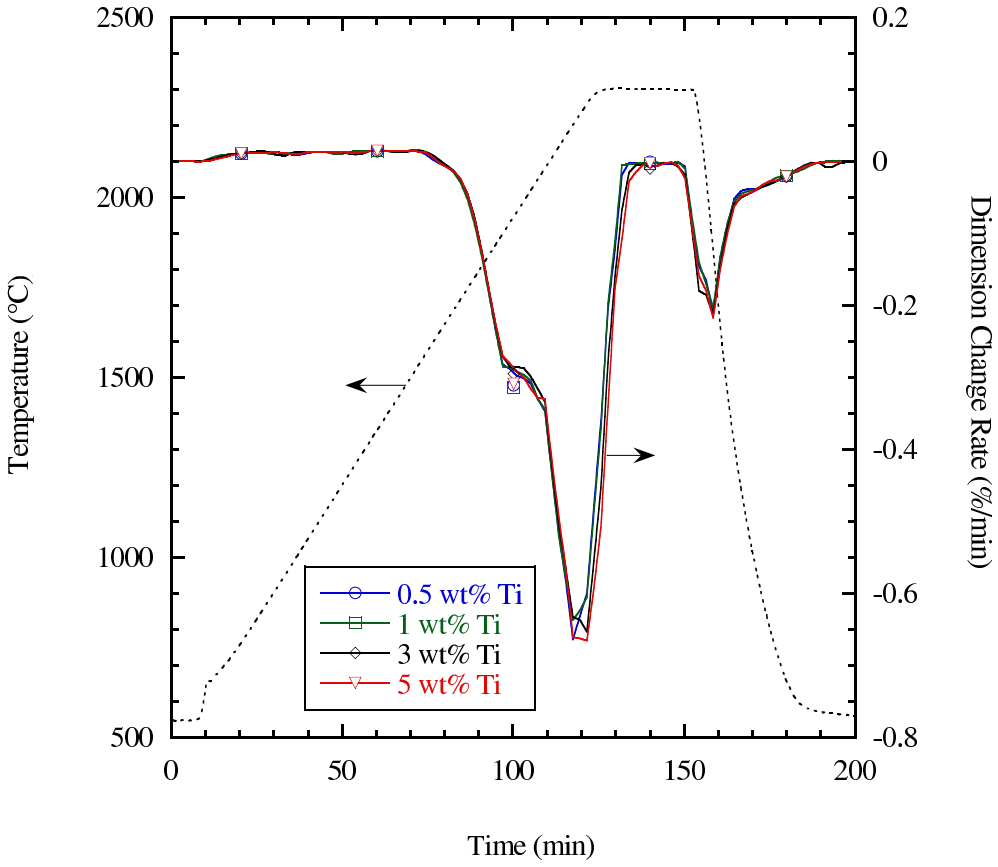

Figure 54: Dilatometry dimension change rate plots for all 3 wt% carbon, 0.9 μm TiO_2 samples sintered at 2300°C

4.3 Compositional and Sintering Parametric Study

4.3.1 Analysis of Green Parts

For this compositional and sintering parametric study, larger cylindrical disk samples were produced that possessed ∼2.5 times the mass of powder in the small dilatometry pellets. Four cylindrical disks were pressed from each of the 24 spray-dried powder compositions previously analyzed via high-temperature dilatometry. These parts were subsequently CIPed under high pressure in order to further increase the green density via improved particle packing and to remove density gradients within the sample interiors. It should be noted that the CIPing step was an addition to this section of the study resulting from the lower pressing pressure employed (∼150 MPa); CIPing was not deemed necessary for the small dilatometry pellets that were pressed under exceedingly high uniaxial pressure (∼304 MPa). Following CIPing, these parts were thermally debound using a slow heating schedule to remove binder and other species that might evolve at high temperatures. No damage or cracking was apparent in the parts following post-debind examination. The average relative green density, post-debinding density, and debinding-related weight loss with their respective standard deviations calculated based on measurements of the 4 disks pressed from each composition are provided in Table 15.

The relative green density data were quite consistent for compositions containing the same amount of added carbon; compositions with 0 wt% C showed densities of ∼57%; compositions with 1 wt% C showed densities of ∼58%; and compositions with 3 wt% C showed densities of ∼60%. The green density appeared to increase with the amount of added carbon. The post-debind relative density data exhibited more variation than the green density data, and certain trends were evident. Like the green samples, the debound samples showed an increase in density with increasing carbon addition. Additionally, there appeared to be a general trend of decreasing post-debind

Table 15: Relative Green Density, Post-Debind Density, and Debind Weight Loss

Additive	Ti (wt%)	Carbon (wt%)	Relative Green Density	Relative Post-Debind Density	Debind Weight Loss
32 nm TiO_2	0.5	0	57.63±0.27%	53.23±0.40%	7.63±0.76%
32 nm TiO_2	1	0	57.54±0.29%	53.27±0.68%	7.42±0.75%
32 nm TiO_2	3	0	57.64±0.32%	52.59±0.48%	8.77±0.67%
32 nm TiO_2	5	0	57.56±0.35%	51.49±0.68%	10.55±0.70%
0.9 μm TiO_2	0.5	0	57.76±0.33%	53.64±0.47%	7.85±0.79%
0.9 μm TiO_2	1	0	57.55±0.18%	52.98±0.48%	7.84±0.75%
0.9 μm TiO_2	3	0	57.70±0.60%	52.26±0.76%	8.98±0.64%
0.9 μm TiO_2	5	0	58.34±0.56%	52.26±0.95%	10.02±0.69%
32 nm TiO_2	0.5	1	58.77±0.45%	54.28±0.37%	7.63±0.70%
32 nm TiO_2	1	1	58.54±0.25%	53.95±0.26%	7.84±0.73%
32 nm TiO_2	3	1	58.54±0.34%	53.09±0.36%	9.31±0.59%
32 nm TiO_2	5	1	58.99±0.17%	52.44±0.41%	11.11±0.78%
0.9 μm TiO_2	0.5	1	58.23±0.42%	53.83±0.65%	7.54±0.74%
0.9 μm TiO_2	1	1	58.52±0.52%	53.84±0.71%	8.01±0.71%
0.9 μm TiO_2	3	1	58.26±0.36%	52.64±0.71%	9.65±0.71%
0.9 μm TiO_2	5	1	58.79±0.18%	52.14±0.33%	11.31±0.71%
32 nm TiO_2	0.5	3	60.53±0.31%	55.28±0.33%	8.68±0.93%
32 nm TiO_2	1	3	59.97±0.22%	54.75±0.44%	8.69±0.90%
32 nm TiO_2	3	3	60.07±0.45%	54.02±0.81%	10.07±0.92%
32 nm TiO_2	5	3	60.40±0.19%	53.10±0.60%	12.08±0.82%
0.9 μm TiO_2	0.5	3	60.30±0.08%	54.85±0.48%	9.04±0.88%
0.9 μm TiO_2	1	3	60.33±0.38%	54.94±0.58%	8.93±0.96%
0.9 μm TiO_2	3	3	60.06±0.31%	53.88±0.62%	10.29±0.87%
0.9 μm TiO_2	5	3	60.15±0.35%	52.94±0.71%	11.98±0.79%

density with increasing Ti content for the 32 nm and 0.9 μm TiO_2 compositions. The decrease in density from the CIPed green state to the post-debind state appeared to show strong correlation to the weight loss from debinding. In general, the weight loss from debinding increased with increasing Ti content as well as with increasing phenolic resin addition.

4.3.2 Sintering Data

The debound 12.7 mm disks of each composition were sintered at four different temperatures: 2300°C, 2280°C, 2260°C, and 2240°C. Graphs illustrating the influence of Ti and C content as well as sintering temperature on the sintered relative densities of the sample disks are provided in the following figures.

The sintered density data for the 0, 1, and 3 wt% carbon 32 nm TiO_2 samples sintered at 2240°C to 2300°C are provided in Figures 55 to 57. The 0 wt% C, 32 nm TiO_2 samples showed sintered relative densities in range of 88.64-92.93%. The samples sintered at 2300°C displayed sintered relative density values in the range of 91.35-92.93%, and these values followed noticeably different behavior with increasing Ti content compared to identical composition samples sintered at lower temperatures. For these 2300°C samples, the relative density decreased as the Ti content increased from 0.5 wt% to 1 wt% and then increased with increasing Ti content, while the lower sintering temperature samples exhibited sharp drops in relative sintered densities as the Ti content increased from 1 to 5 wt%. This trend difference indicates that at this higher temperature the added Ti may have resulted in a shift to a composition- and temperature-dependent reaction, causing a change in the functionality of the Ti species. For the 2280°C samples series, the sintered relative densities were in the range of 89.02-91.78%. These specimens showed an increase in relative density values as the Ti content increased from 0.5 to 1 wt%; however, the relative densities decreased dramatically with further increases in Ti. For the 0 wt% C samples sintered

at 2260°C, the 0.5 and 1 wt% Ti compositions exhibited the highest sintered relative densities. However, the remaining samples also sintered at 2260°C exhibited the same decrease in density as the Ti content increased to 5 wt% as observed for the 2280°C specimens. As a result, these 2260°C samples had sintered relative densities over the broad range of 88.94-92.93%. The samples sintered at 2240°C showed sintered relative densities in the range of 88.64-91.94%, and these values followed a similar trend as that observed for the 2260°C and 2280°C sample series.

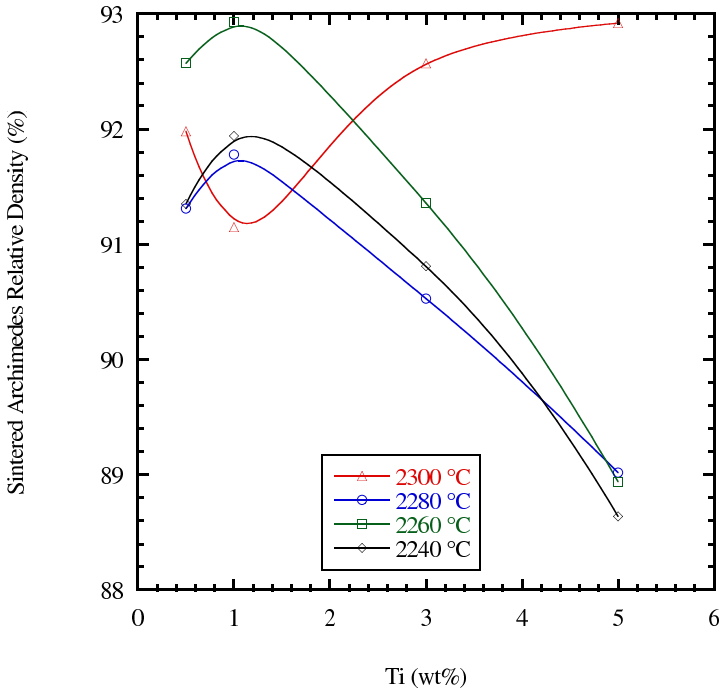

Figure 55: Sintered densities for all 0 wt% carbon 32 nm TiO_2 samples sintered at 2240-2300°C

The 1 wt% C, 32 nm TiO_2 samples displayed sintered relative densities in the range of 88.4-93.33%, which was a broader range than observed for the 0 wt% C, 32 nm TiO_2 series. The samples sintered at 2300°C displayed relative densities in the range of 91.57-93.33%. The relative density of these samples slightly decreased as the Ti content increased from 0.5 to 1 wt%, then increased as the Ti content reached 3

wt%, and finally decreased sharply as the Ti content increased to 5 wt%. The 2280°C samples showed sintered relative densities in the range of 90.44-92.92%. These samples exhibited steadily decreasing relative density with increasing Ti content. The 2260°C samples followed a trend nearly identical to that observed for the 2280°C samples and had relative densities in the range of 89.76-93.22%. The 2240°C series of samples exhibited the lowest relative densities out of the 1 wt% C series, showing values in the range of 88.4-91.63%. These lower temperature samples also showed steadily decreasing density values with increasing Ti content.

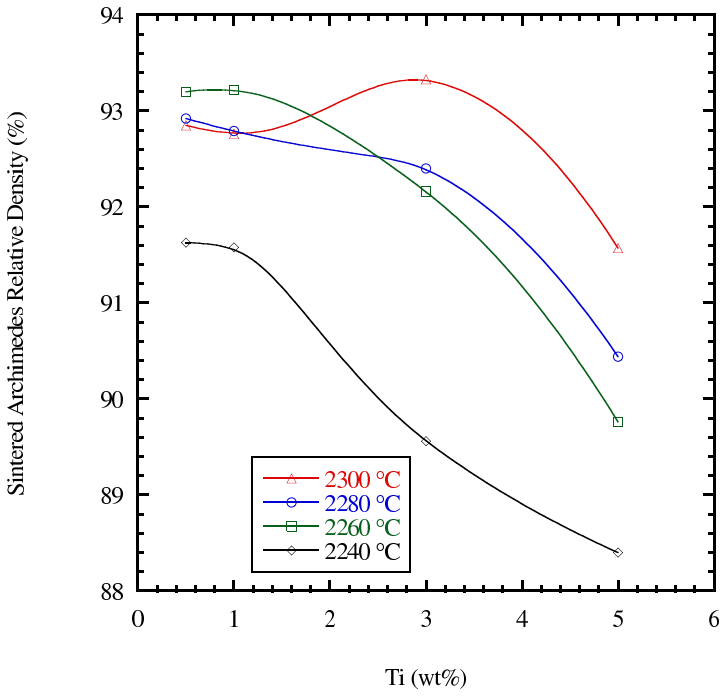

Figure 56: Sintered densities for all 1 wt% carbon 32 nm TiO_2 samples sintered at 2240-2300°C

The 3 wt% C, 32 nm TiO_2 samples showed sintered relative densities in the range of 91.91-96.57%, which was observably higher than the ranges measured for the 0 and 1 wt% C samples. The samples sintered at 2300°C showed relative densities in the range of 91.91-94.38%. The density values followed a trend of decreasing density as Ti

content increased from 0.5 to 3 wt%, but the sintered relative density then increased as the Ti content reached 5 wt%. The 2280°C samples showed relative density values in the range of 93.57-95.62%, and these values exhibited an oscillatory trend in which the densities alternately decreased and increased with incremental raises in the Ti content. The 2260°C samples had sintered relative density values in the range of 94.35-96.57%, which was the highest range observed for the 3 wt% C 32 nm TiO_2 samples. These samples exhibited steadily decreasing sintered relative densities with increasing Ti content. The 2240°C samples achieved sintered relative densities in the range of 93.34-95.25%, and these values followed a similar trend as observed for the 2260°C series.

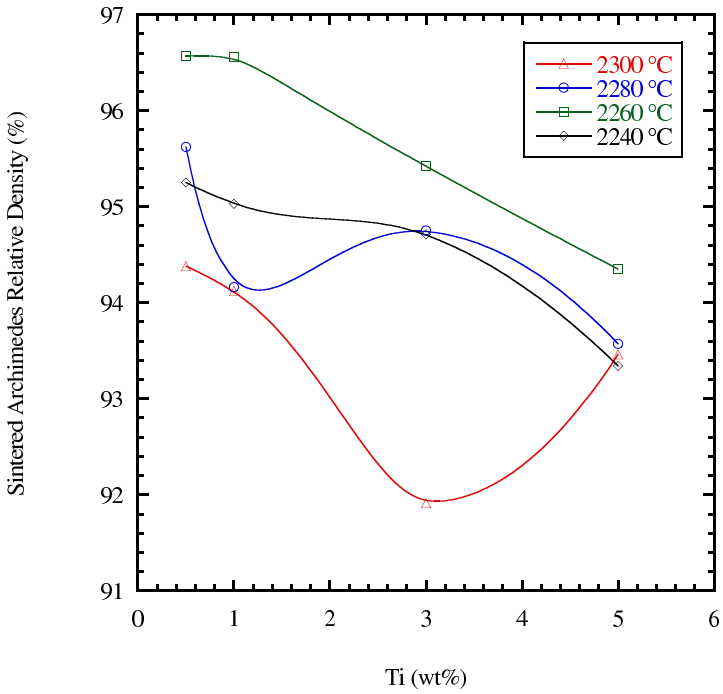

Figure 57: Sintered densities for all 3 wt% carbon 32 nm TiO_2 samples sintered at 2240-2300°C

The multitude of data points collected for the 0-3 wt% carbon, 32 nm TiO_2 series necessitated visualization in multiple dimensions in order to illustrate the effect of Ti and C composition on sintered relative density. Three-dimensional surface plots of the sintered density data for all of the 32 nm TiO_2 samples sintered at 2240°C to 2300°C are provided in Figures 58 through 61. For these 2300°C samples, the highest relative density (94.38%) was observed for the sample containing the lowest amount of Ti (0.5 wt%) and the highest carbon content (3 wt%). At this high temperature, the the relative density surface plot exhibits a saddle-type shape over the compositional space. The lowest sintered relative density was observed for the sample containing 1 wt% Ti and 0 wt% C.

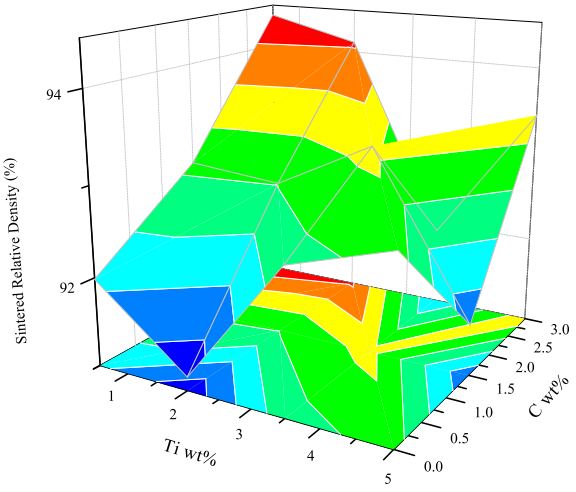

Figure 58: Relative densities for all 32 nm TiO_2 samples sintered at 2300°C

The surface plot for the sintered relative densities of the 2280°C samples is less irregular than that of the 2300°C series; it shows the lowest densities for compositions containing high Ti and low C content, and exhibits the highest density (95.62%) for the composition with the lowest amount of Ti (0.5 wt%) and the highest amount of carbon (3 wt%). From these observations, increasing carbon content appears to improve the sintered relative density, while the presence of 32 nm TiO_2 in increasing

amounts appears to have a deleterious effect.

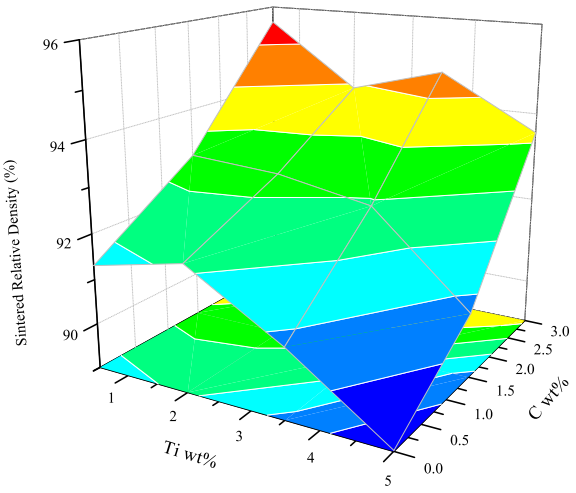

Figure 59: Relative densities for all 32 nm TiO_2 samples sintered at 2280°C

The surface plot of the sintered relative densities for the 32 nm TiO_2 samples sintered at 2260°C follows a similar trend as that observed for the 2280°C samples; however, the relative densities were higher overall. The highest density in this series (96.57%) was observed for the 0.5 wt% Ti, 3 wt% C sample.

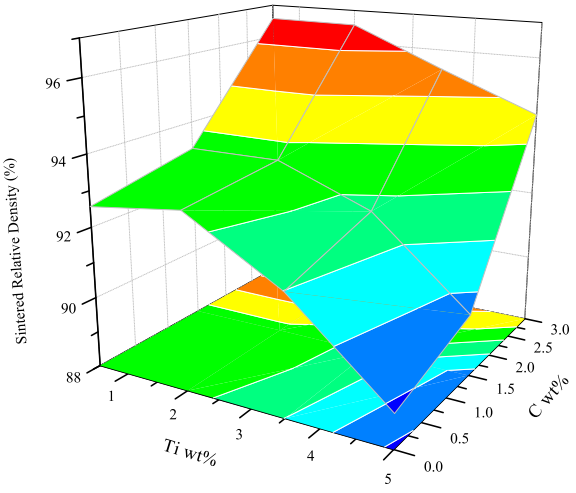

Figure 60: Relative densities for all 32 nm TiO_2 samples sintered at 2260°C

The surface plot of the sintered relative densities for the 32 nm TiO_2 samples

sintered at 2240°C exhibits a similar trend as that for the 2260°C and 2280°C series. However, it should be noted that the reduction in temperature resulted in a shift of the relative densities to lower values.

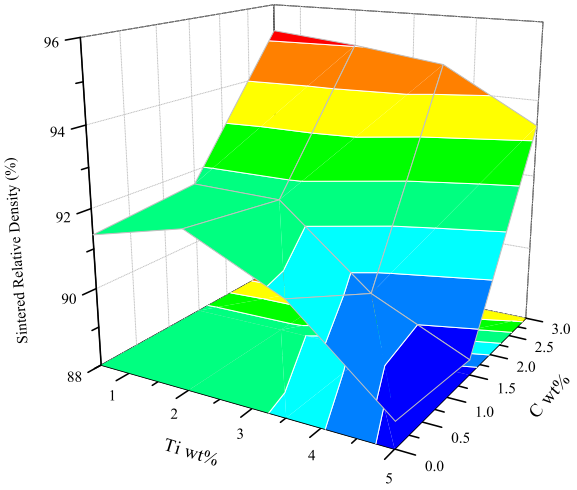

Figure 61: Relative densities for all 32 nm TiO_2 samples sintered at 2240°C

The sintered density data for the 0, 1, and 3 wt% carbon 0.9 μm TiO_2 samples sintered at 2240°C to 2300°C are provided in Figures 62 to 64. The 0 wt% C, 0.9 μm TiO_2 samples showed sintered relative densities in range of 87.29-93.93%. The samples sintered at 2300°C displayed a very similar trend as the 0 wt% C, 32 nm TiO_2 samples sintered at the same temperature, whereby an initial decrease in relative density for the lower Ti contents was followed by an increase with higher Ti contents. These samples displayed the highest densities overall in the temperature series and also showed higher density values than the 32 nm TiO_2 samples with the same composition and sintering temperature. The highest relative density measured for this 0 wt% C series (93.93%) was the composition containing 3 wt% Ti. The 2280°C samples showed relative densities in the range of 89.4-92.22%, and these values decreased with increasing Ti content. The 2260°C samples had relative densities in the range of 88.65-92.91%, and these values followed a similar trend of decreasing density with increasing Ti content as the 2280°C series. The 2240°C samples had sintered relative densities in the range of 87.29-92.12%. The sintered densities for these lower temperature samples exhibited a sharp decrease as the Ti content increased from 0.5 to 1 wt%. Further increases in the Ti content also resulted in decreased sintered relative density.

The 1 wt% C, 0.9 μm TiO_2 samples displayed sintered relative densities in the range of 87.73-93.81%, which was a broader range than observed for the 0 wt% C, 0.9 μm TiO_2 series. The samples sintered at 2300°C displayed relative densities in the range of 92.48-93.81%. The relative density of these samples increased with increasing Ti content, which is a different behavior than observed for the 0 wt% C, 0.9 μm TiO_2 and 0 wt% C, 32 nm TiO_2 samples sintered at the same temperature. The 2280°C samples showed sintered relative densities in the range of 91.81-92.44%. These samples exhibited a subtle decrease in relative density with increasing Ti content up to 3 wt% Ti; upon increasing to 5 wt% Ti, the relative density increased marginally. The 2260°C samples followed a trend of decreasing relative density with increasing

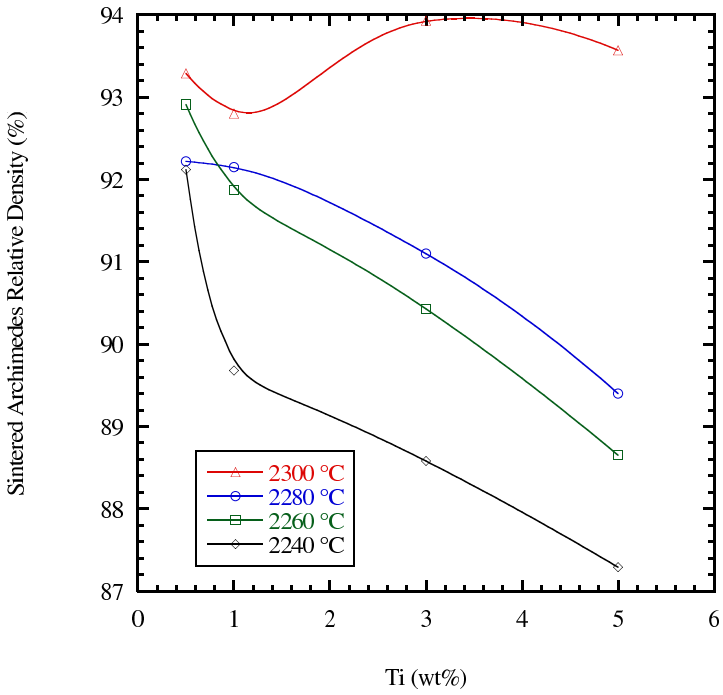

Figure 62: Sintered densities for all 0 wt% carbon 0.9 μm TiO_2 samples sintered at 2240-2300°C

Ti content and had relative densities in the range of 90.96-92.7%. The 2240°C series showed density values in the range of 87.73-91.84%. These samples exhibited the lowest relative densities out of the 1 wt% C series and followed a nearly identical behavior as the 0 wt% C, 0.9 μm TiO_2 samples also sintered at 2240°C (i.e., density decreased steadily with increasing Ti content).

The 3 wt% C, 0.9 μm TiO_2 samples showed sintered relative densities in the range of 92.66-96.91%, which was noticeably higher than the ranges measured for the 0 and 1 wt% C samples. The samples sintered at 2300°C showed relative densities in the range of 92.66-94.82%. The density values followed a trend of initially decreasing density as Ti content increased from 0.5 to 3 wt%, but the sintered relative density then increased as the Ti content reached 5 wt%. This behavior is similar to that observed for the 3 wt% C, 32 nm TiO_2 samples sintered at the same temperature. The 2280°C samples showed relative density values in the range of 94.86-95.77%, and these values exhibited behavior similar to the 2300°C samples; however, the initial decrease and subsequent increase in density with increasing Ti content were of smaller magnitude. The 2260°C samples had sintered relative density values in the range of

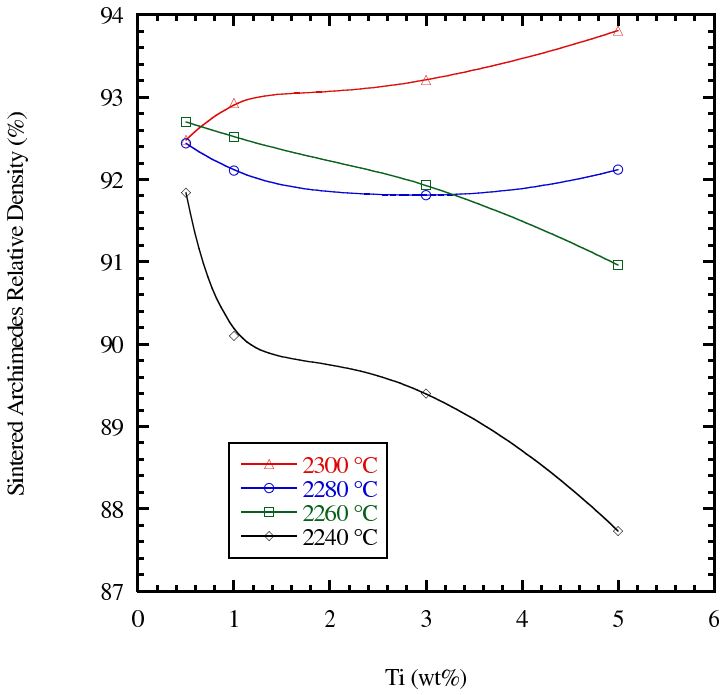

Figure 63: Sintered densities for all 1 wt% carbon 0.9 μm TiO_2 samples sintered at 2240-2300°C

95.55-96.91%, which was the highest range observed for the 3 wt% C 0.9 μm TiO_2 samples. Like the 3 wt% C, 32 nm TiO_2 samples sintered at the same temperature, these 0.9 μm TiO_2 samples exhibited steadily decreasing sintered relative densities with increasing Ti content. The 2240°C samples had sintered relative densities in the range of 93.18-95.84%, and these values decreased with increasing Ti content.

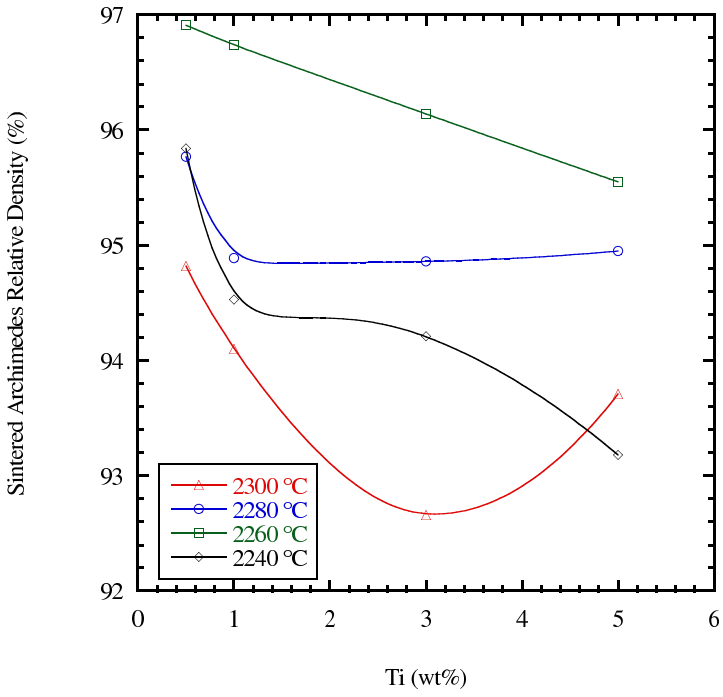

Figure 64: Sintered densities for all 3 wt% carbon 0.9 μm TiO_2 samples sintered at 2240-2300°C

Three-dimensional surface plots of the sintered density data for all of the 0.9 μm TiO_2 samples sintered at 2240°C to 2300°C are provided in Figures 65 through 68. The surface plot for the 0.9 μm TiO_2 samples sintered at 2300°C shows a similar irregular shape as the sintered density surface plot for the 32 nm TiO_2 samples sintered at the same temperature. The surface indicates that the highest density (94.82%) at this sintering temperature was observed for the lowest Ti content (0.5 wt%) and highest carbon content (3 wt%) composition, which is consistent with the behavior of the 32 nm TiO_2 samples examined above. The lowest sintered relative density (92.48%) was observed for the sample containing 0.5 wt% Ti and 1 wt% C.

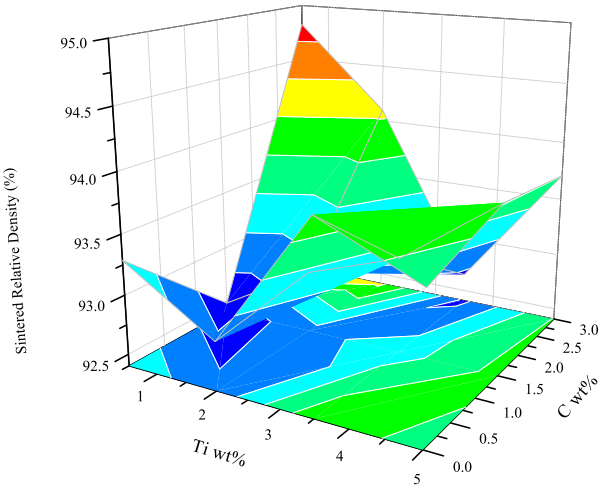

Figure 65: Relative densities for all 0.9 μm TiO_2 samples sintered at 2300°C

The surface plot for the sintered relative densities of the 2280°C samples lacks the irregularity of the surface plot for the 2300°C series. This plot shows the lowest densities for compositions containing high Ti and low C content. However, while the highest density (95.77%) was observed for the lowest Ti content (0.5 wt%) and highest carbon content (3 wt%) composition, other compositions containing increasing Ti content and containing 3 wt% C did not exhibit the reduction in density with increasing Ti content observed in the 32 nm TiO_2 samples with identical compositions and

sintering temperature. This difference between the two TiO_2 sources is noteworthy.

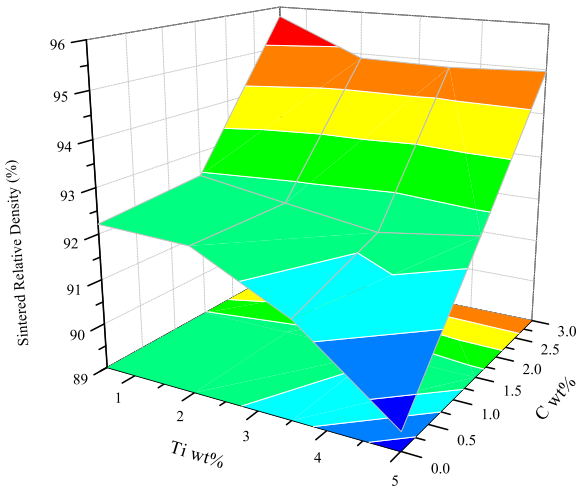

Figure 66: Relative densities for all 0.9 μm TiO_2 samples sintered at 2280°C

The surface plot of the sintered relative densities for the 0.9 μm TiO_2 samples sintered at 2260°C follows a similar trend as that observed for the 2280°C samples; however, the relative densities of the 2260°C samples were higher overall. As in the two higher temperature series, the highest relative density (96.91%) was observed for the 0.5 wt% Ti, 3 wt% C sample. It should be noted that with the reduction in temperature from 2280°C to 2260°C, the high carbon content samples exhibited a reduction in density with increasing Ti content.

The surface plot of the sintered relative densities for the 0.9 μm TiO_2 samples sintered at 2240°C exhibits a similar trend as that for the 2260°C and 2280°C series, with the highest relative density (95.84%) also being observed for the 0.5 wt% Ti, 3 wt% C composition. The reduction in temperature resulted in the samples achieving overall lower relative densities compared to the higher temperature sintering series.

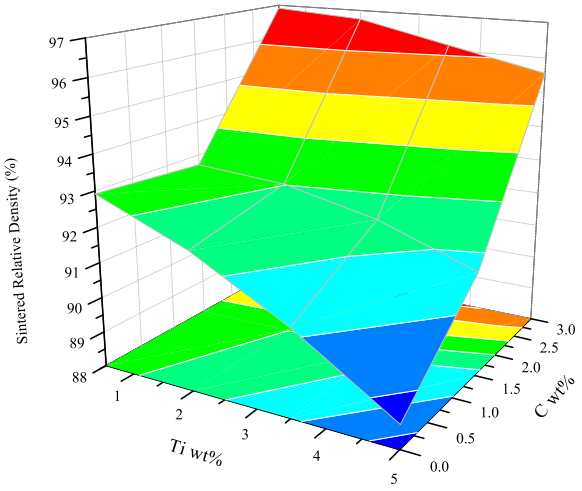

Figure 67: Relative densities for all 0.9 μm TiO_2 samples sintered at 2260°C

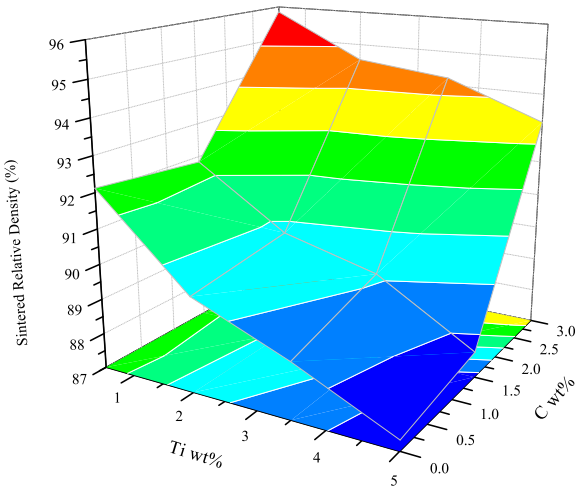

Figure 68: Relative densities for all 0.9 μm TiO_2 samples sintered at 2240°C

The sintering weight loss data for the 0, 1, and 3% carbon 32 nm TiO_2 samples sintered at 2240°C to 2300°C are provided in Figures 69 to 71. In general, for sintering temperatures below 2300°C, the sintering weight loss increased with increasing Ti content. For each carbon content series, the samples showed increasing weight loss as the sintering temperature increased from 2240°C to 2280°C. However, as the sintering temperature increased further to 2300°C, the weight loss of the higher Ti content samples began to demonstrate differing weight loss behavior that changed with carbon content. For the 0 wt% C samples, the higher Ti content compositions showed decreased weight loss at 2300°C compared to that measured for the samples sintered at 2280°C. For the 1 wt% C samples sintered at 2300°C, the weight loss values increased sharply with increasing Ti content, with the 5 wt% Ti sample exhibiting a high sintering weight loss value of 7.88 wt%. The 3 wt% C samples sintered at 2300°C exhibited sintering weight loss behavior similar to the 1 wt% C samples; however, the 3 wt% Ti sample showed the highest weight loss instead of the 5 wt% Ti sample. The differing behavior of the higher Ti content samples and the effect of carbon content resulted in broadened sintering weight loss ranges with varying carbon concentration; the sintering weight loss ranges for the 0, 1, and 3 wt% C 32 nm TiO_2 samples were 1.37-2.68 wt%, 1.37-7.88 wt%, and 1.72-6.84 wt%, respectively.

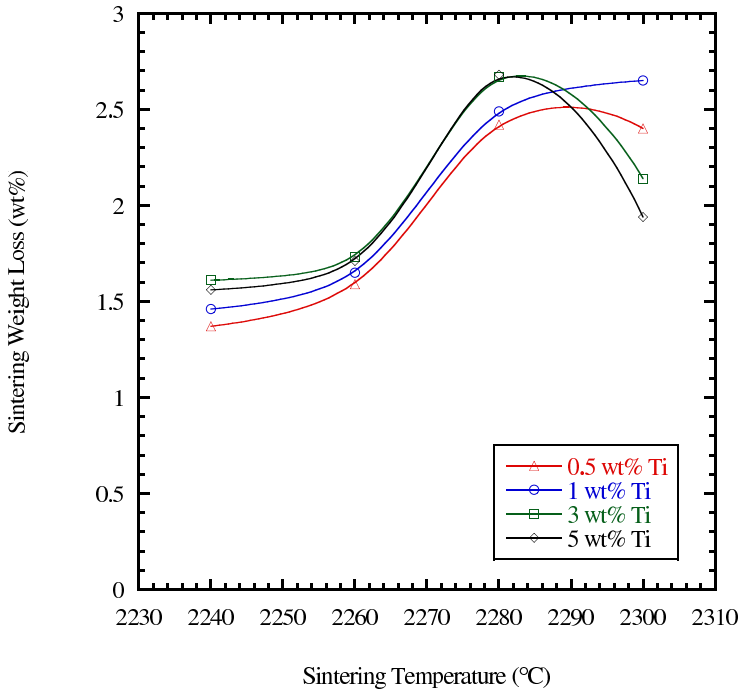

Figure 69: Sintering weight loss data for all 0% carbon 32 nm TiO_2 samples sintered at 2240-2300°C

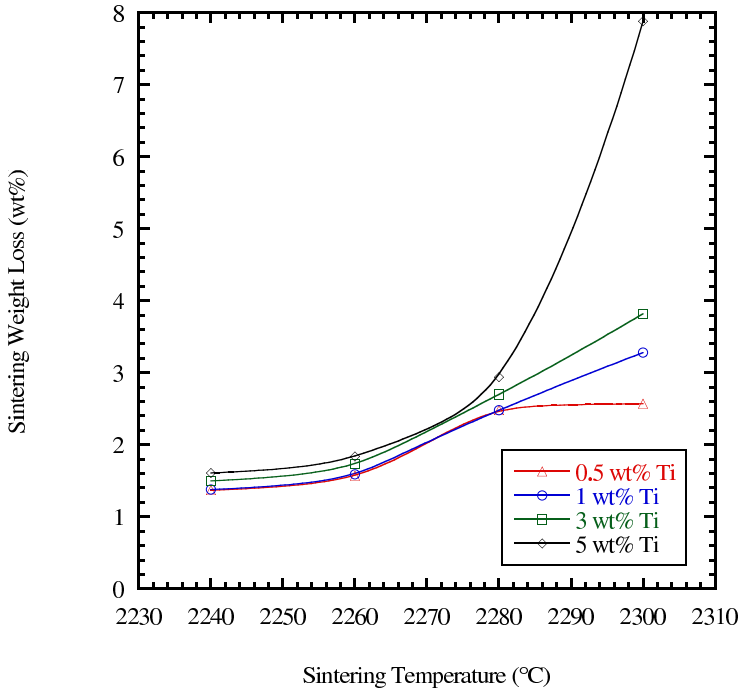

Figure 70: Sintering weight loss data for all 1% carbon 32 nm TiO_2 samples sintered at 2240-2300°C

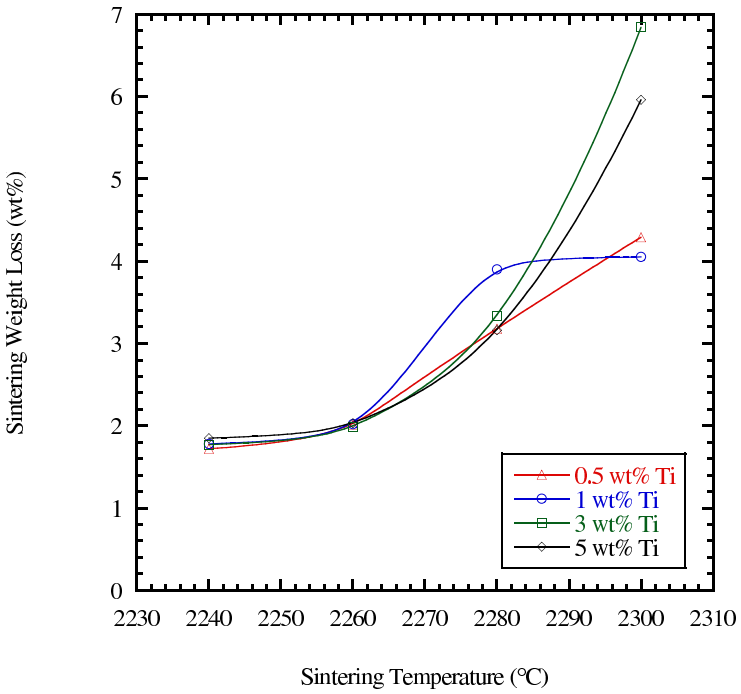

Figure 71: Sintering weight loss data for all 3% carbon 32 nm TiO_2 samples sintered at 2240-2300°C

The sintering weight loss data for the 0, 1, and 3% carbon 0.9 μm TiO_2 samples sintered at 2240°C to 2300°C are provided in Figures 72 to 74. The sintering weight loss data for the 0, 1, and 3 wt% 0.9 μm TiO_2 samples followed trends nearly identical to those observed for the 32 nm TiO_2 compositions. For each carbon content series, sintering weight loss for these samples increased with increasing sintering temperature up to 2280°C and increasing Ti content up to 3 wt%. For the 0 wt% C samples, the higher Ti content compositions showed lower weight loss at 2300°C compared to that measured for the samples sintered at 2280°C. For the 1 wt% C samples sintered at 2300°C, the weight loss values increased noticeably with increasing Ti content; the 5 wt% Ti sample exhibited the highest sintering weight loss value of 6.05 wt%. The 3 wt% C samples sintered at 2300°C showed sintering weight loss behavior similar to the 1 wt% C samples; the 5 wt% Ti sample also showed the highest sintering weight loss of 7.87 wt%. As observed in the 32 nm TiO_2 samples, the sintering weight loss ranges broadened with increasing carbon content; the sintering weight loss ranges for the 0, 1, and 3 wt% C, 0.9 μm TiO_2 samples were 1.40-2.81 wt%, 1.40-6.05 wt%, and 1.75-7.87 wt%, respectively.

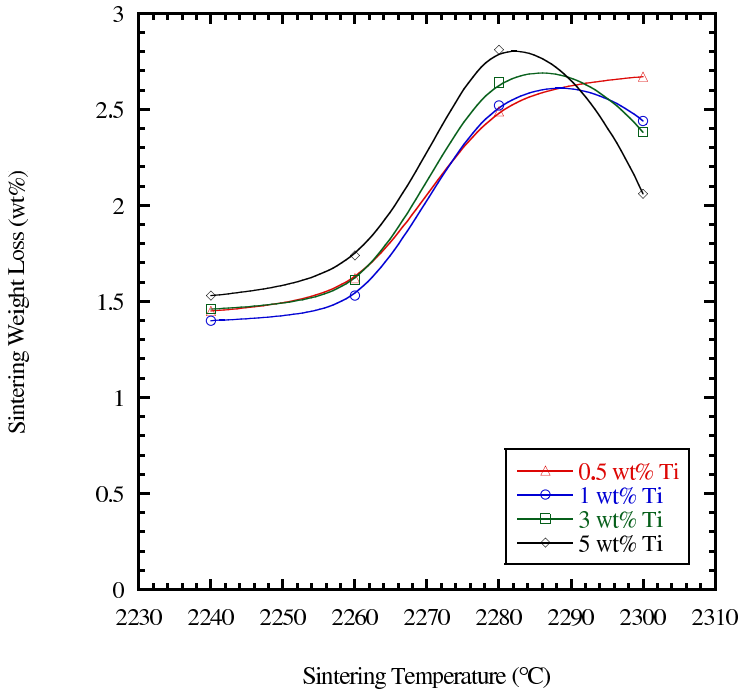

Figure 72: Sintering weight loss data for all 0% carbon 0.9 μm TiO_2 samples sintered at 2240-2300°C

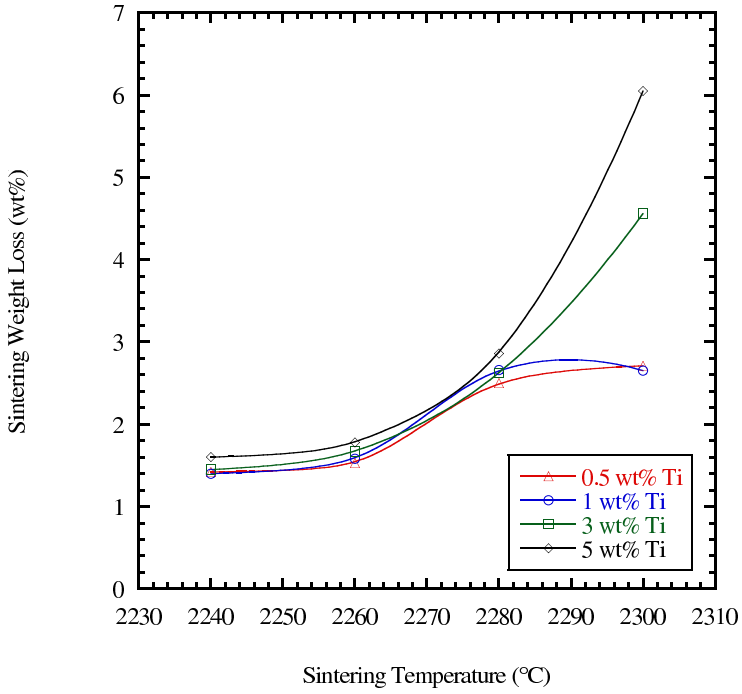

Figure 73: Sintering weight loss data for all 1% carbon 0.9 μm TiO_2 samples sintered at 2240-2300°C

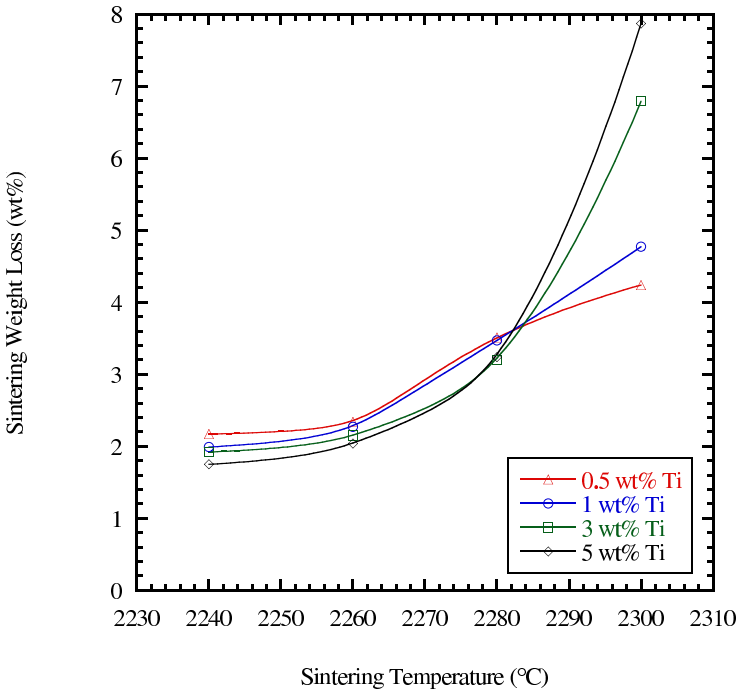

Figure 74: Sintering weight loss data for all 3% carbon 0.9 μm TiO_2 samples sintered at 2240-2300°C

The HIPed density data for the 0, 1, and 3 wt% carbon 32 nm TiO_2 samples sintered at 2240°C to 2300°C are provided in Figures 75 to 77. Post-HIPing after sintering resulted in increases in relative density for all of the 32 nm TiO_2 samples. For the 0 wt% C samples, the post-HIPed relative density of the samples followed a trend similar to that observed for the sintered relative densities. The samples sintered at 2300°C and post-HIPed exhibited an initially decreasing density followed by an increase in density for the 3-5 wt% Ti range, while the samples sintered at the remaining temperatures showed an initial increase in post-HIPed relative density for the 0.5-1 wt% Ti range followed by a sharp decrease with further increases in Ti content. Compared to the higher carbon content compositions, the 0 wt% C samples showed post-HIPed relative densities with a wide distribution and also the lowest values, having values in the range of 89.6-96.32%. The 1 wt% C samples followed the general trend of decreasing post-HIPed densities with increasing Ti content, which was similar to the behavior observed for the sintered relative densities of these samples. With increasing carbon content to 1 wt%, the post-HIPed relative densities showed higher values in a slightly broadened range of 90-98.23%. The post-HIPed relative densities of the 3 wt% C samples showed different behavior than the lower carbon content compositions; the samples sintered at 2240°C and 2260°C showed closely matched post-HIPed relative densities that were within a narrow range, exhibited limited variation with Ti content, and had values noticeably higher than the samples sintered at higher temperatures. The 2240°C and 2260°C samples had post-HIPed relative densities in the ranges of 98.66-99.25% and 98.76-99.36%, respectively. Overall, the post-HIPed relative densities of the 32 nm TiO_2 samples sintered at 2240-2300°C increased with increasing carbon content.

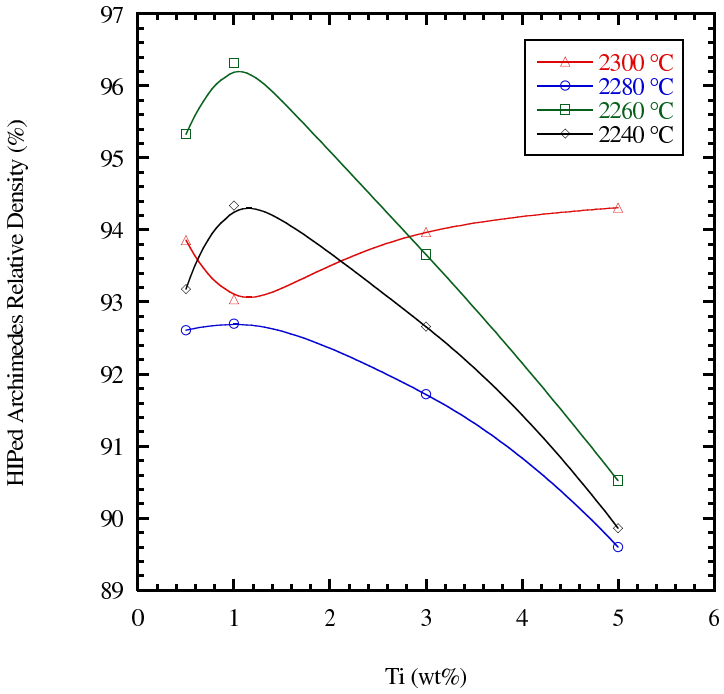

Figure 75: HIPed densities for all 0 wt% carbon 32 nm TiO_2 samples sintered at 2240-2300°C

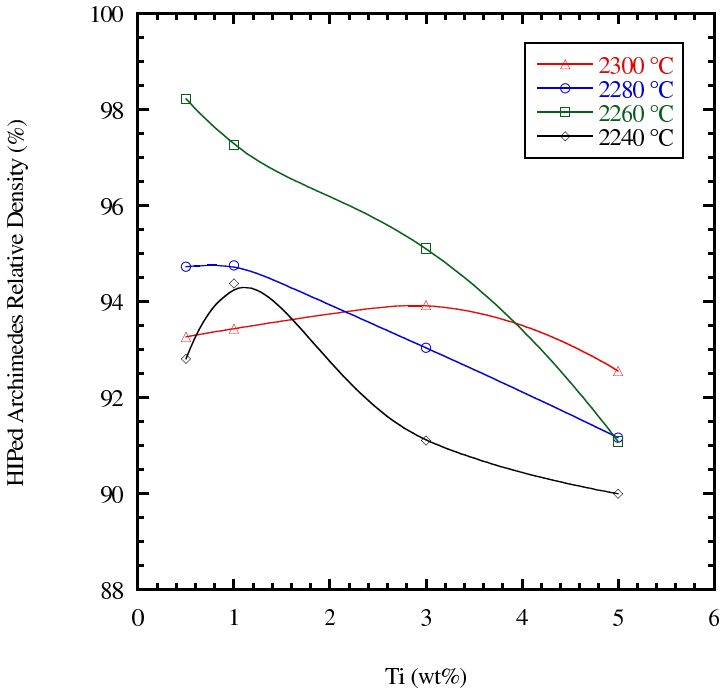

Figure 76: HIPed densities for all 1 wt% carbon 32 nm TiO_2 samples sintered at 2240-2300°C

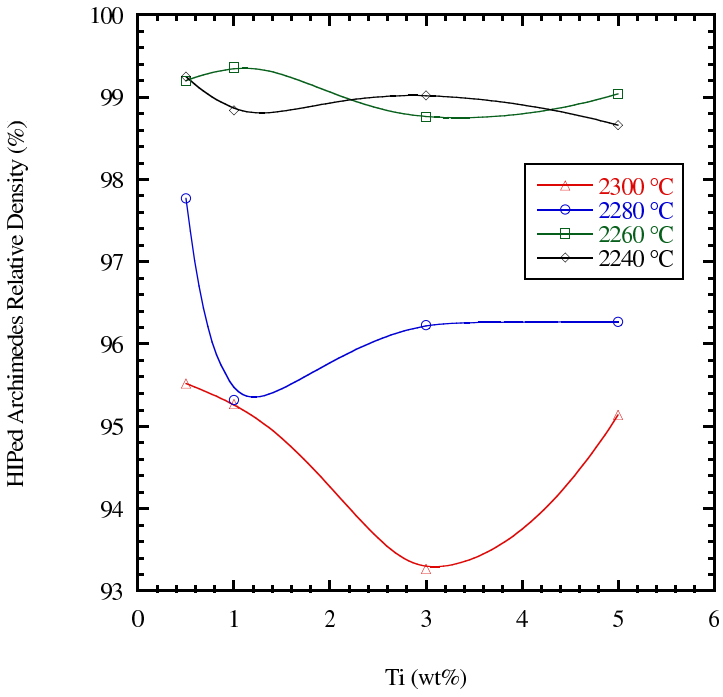

Figure 77: HIPed densities for all 3 wt% carbon 32 nm TiO_2 samples sintered at 2240-2300°C

Three-dimensional surface plots of the HIPed density data for all of the 32 nm TiO_2 samples sintered at 2240°C to 2300°C are provided in Figures 78 through 81. The surface plot for the 32 nm TiO_2 samples sintered at 2300°C and post-HIPed shows a shape similar to that observed for the sintered relative densities of the same specimens, although the post-HIPed values are higher. For these 2300°C samples, the highest relative density (95.52%) was observed for the sample containing the lowest amount of Ti (0.5 wt%) and the highest carbon content (3 wt%). The lowest post-HIPed relative density (92.56%) was observed for the sample containing 5 wt% Ti and 1 wt% C.

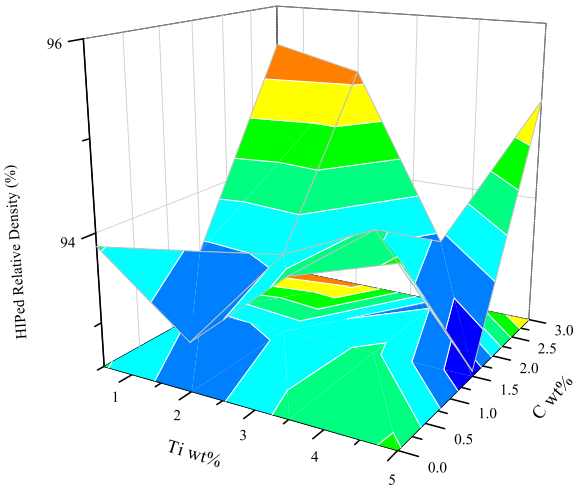

Figure 78: HIPed densities for all 32 nm TiO_2 samples sintered at 2300°C

The surface plot for the 32 nm TiO_2 samples sintered at 2280°C and post-HIPed does not exhibit the irregular topology noted for the 2300°C samples. The highest post-HIPed relative density (97.77%) was measured for the sample with low Ti content (0.5 wt%) and high carbon content (3 wt%), while the lowest density (89.6%) was measured for the high Ti content (5 wt%) and low carbon content (0 wt%) sample. The overall trend of the surface indicates that the presence of the 32 nm TiO_2 effected reduced densification.

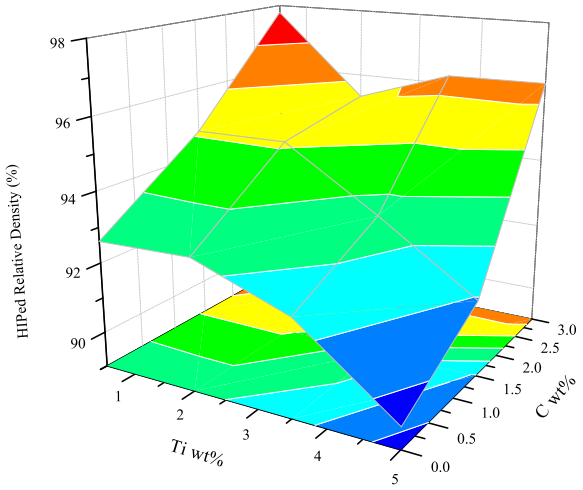

Figure 79: HIPed densities for all 32 nm TiO_2 samples sintered at 2280°C

The surface plot for the 32 nm TiO_2 samples sintered at 2260°C and post-HIPed exhibits a more convex topology than the surface plot for the 2280°C samples, indicating greater densification for compositions containing intermediate Ti and C amounts. Overall, the reduction in sintering temperature resulted in an increase in the post-HIPed relative densities. The highest post-HIPed relative density (99.36%) was measured for the sample with an intermediate Ti content (1 wt%) and high carbon content (3 wt%), while the lowest density (90.52%) was measured for the sample with high Ti content (5 wt%) and low carbon content (0 wt%). The trend of the surface indicates that the presence of the 32 nm TiO_2 reduced overall densification for low carbon content compositions; however, higher carbon contents appeared to substantially improve densification even in compositions containing high amounts of 32 nm TiO_2.

The surface plot for the 32 nm TiO_2 samples sintered at 2240°C and post-HIPed exhibits a steeper topology than the surface plot for the 2260°C samples. This trend is indicative of limited densification for compositions containing intermediate Ti and C amounts, which is a change from the samples sintered at 2260°C. The reduction in sintering temperature to 2240°C resulted in a slight decrease in the post-HIPed

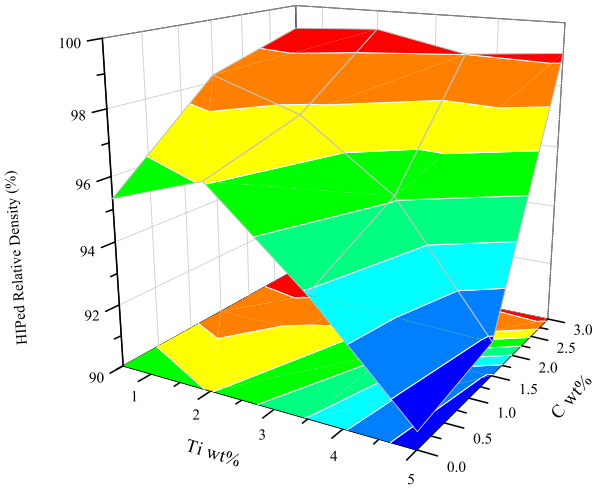

Figure 80: HIPed densities for all 32 nm TiO_2 samples sintered at 2260°C

relative densities compared to the 2260°C samples. The highest post-HIPed relative density (99.25%) was measured for the sample with low Ti content (0.5 wt%) and high carbon content (3 wt%), while the lowest density (89.86%) was measured for the sample with high Ti content (5 wt%) and low carbon content (0 wt%). The trend of the surface indicates that the presence of the 32 nm TiO_2 reduced overall densification for low carbon content compositions; however, like the 2260°C samples, the detrimental effect of the 32 nm TiO_2 is reduced in compositions containing high amounts of carbon.

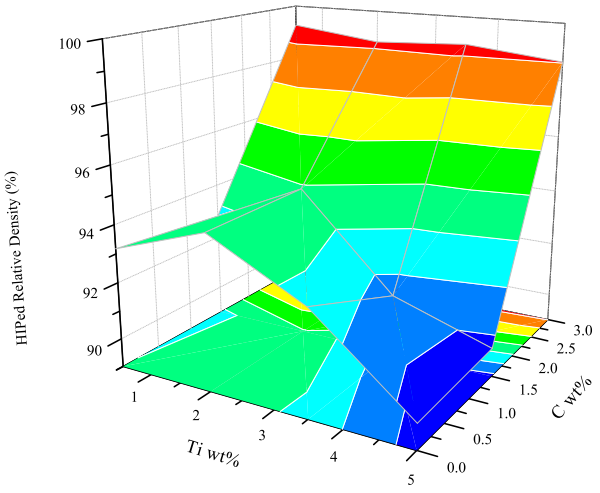

Figure 81: HIPed densities for all 32 nm TiO_2 samples sintered at 2240°C

The HIPed density data for the 0, 1, and 3% carbon 0.9 μm TiO_2 samples sintered at 2240°C to 2300°C are provided in Figures 82 to 84. Post-HIPing after sintering resulted in increases in relative density for all of the 0.9 μm TiO_2 samples. For the 0 wt% C samples, the post-HIPed relative density of the samples followed a trend similar to that observed for the sintered relative densities. The samples sintered at 2300°C and post-HIPed exhibited an initially decreasing density followed by an increase to higher relative densities for the higher Ti compositions. The samples sintered at the lower three temperatures exhibited decreases in post-HIPed relative density with increasing Ti content. Compared to the higher carbon content compositions, the 0 wt% C samples showed post-HIPed relative densities with a wide distribution and also the lowest values, having values in the range of 87.96-95.45%. The 1 wt% C samples sintered at 2240°C and 2260°C followed the trend of decreasing post-HIPed densities with increasing Ti content, while the 2280°C samples exhibited minimal variation in density with Ti content, and the 2300°C samples displayed increasing relative density with increasing Ti content. For the 1 wt% C samples, the post-HIPed relative densities showed higher values in the range of 88.84-96.64%. The 3 wt% C samples sintered at 2240°C and 2260°C showed the highest post-HIPed relative densities. The 2260°C samples exhibited limited variation with Ti content, while the 2240°C samples showed decreasing relative densities with increasing Ti content. The 2240°C and 2260°C samples had post-HIPed relative densities in the ranges of 97.55-99.59% and 99.39-99.96%, respectively. Overall, the post-HIPed relative densities of the 0.9 μm TiO_2 samples sintered at 2240-2300°C increased with increasing carbon content.

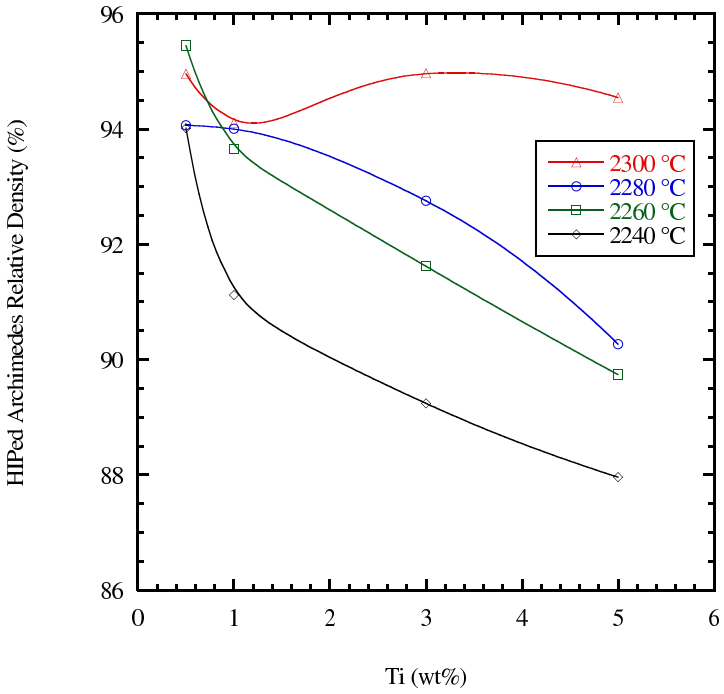

Figure 82: HIPed densities for all 0 wt% carbon 0.9 μm TiO_2 samples sintered at 2240-2300°C

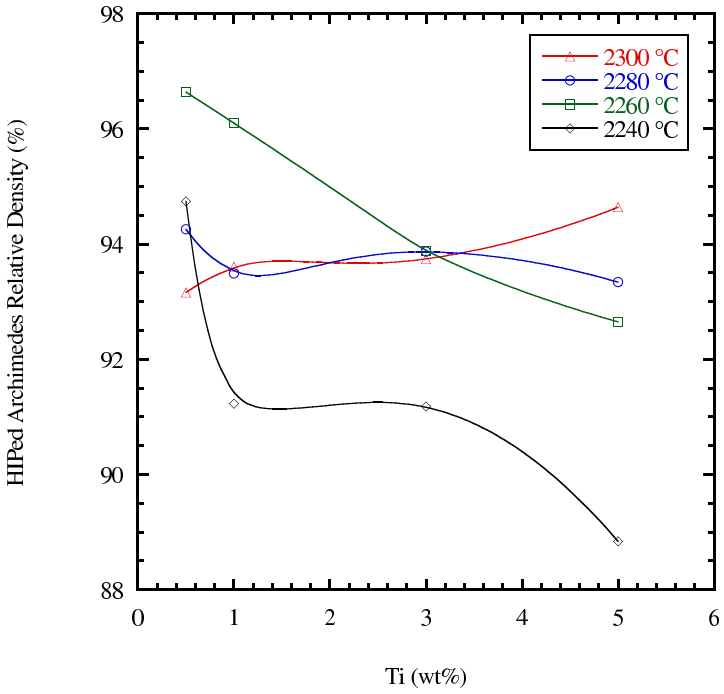

Figure 83: HIPed densities for all 1 wt% carbon 0.9 μm TiO_2 samples sintered at 2240-2300°C

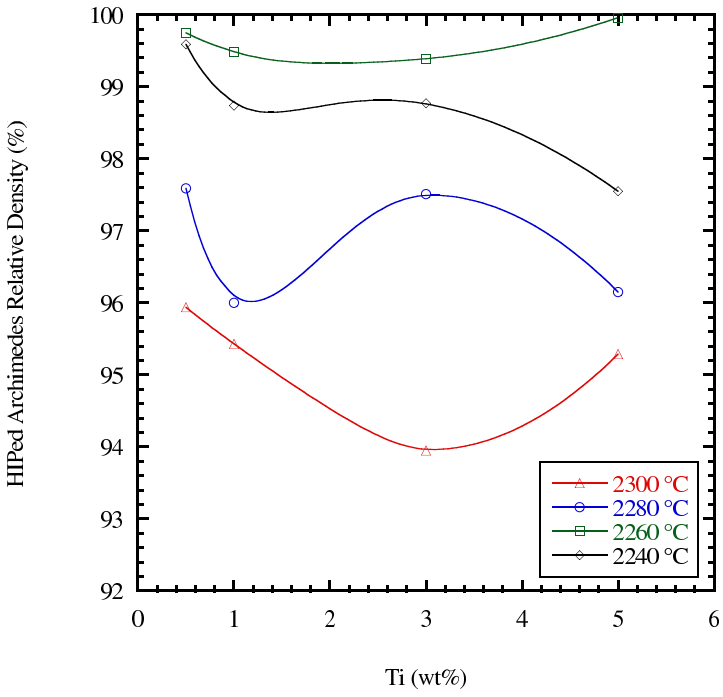

Figure 84: HIPed densities for all 3 wt% carbon 0.9 μm TiO_2 samples sintered at 2240-2300°C

Three-dimensional surface plots of the HIPed density data for all of the 0.9 μm TiO_2 samples sintered at 2240°C to 2300°C are provided in Figures 85 through 88. The surface plot for the 0.9 μm TiO_2 samples sintered at 2300°C and post-HIPed shows an irregular topology similar to that observed for the sintered relative densities of the same specimens; however, post-HIPing resulted in higher relative density values. For these 2300°C samples, the highest relative density (95.94%) was observed for the sample containing the lowest amount of Ti (0.5 wt%) and the highest carbon content (3 wt%). The lowest post-HIPed relative density (93.16%) was observed for the sample containing 0.5 wt% Ti and 1 wt% C.

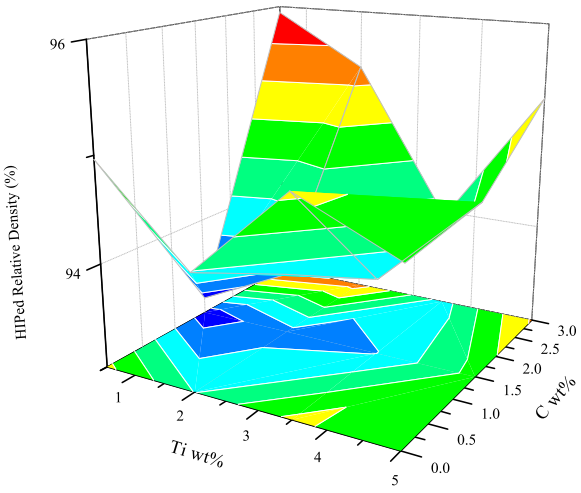

Figure 85: HIPed densities for all 0.9 μm TiO_2 samples sintered at 2300°C

The surface plot for the 0.9 μm TiO_2 samples sintered at 2280°C and post-HIPed exhibits a more regular topology that shows decreasing relative density with increasing Ti content and decreasing carbon content. The highest post-HIPed relative density (97.59%) was measured for the sample with low Ti content (0.5 wt%) and high carbon content (3 wt%), while the lowest density (90.27%) was measured for the high Ti content (5 wt%) and low carbon content (0 wt%) sample. As observed in the 32 nm TiO_2 compositions, the presence of the 0.9 μm TiO_2 reduced densification.

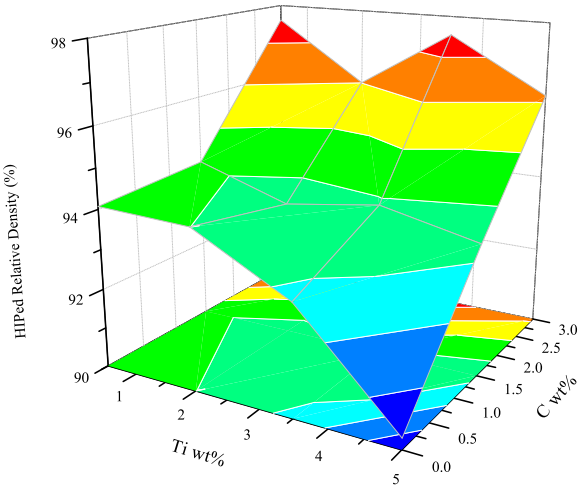

Figure 86: HIPed densities for all 0.9 μm TiO_2 samples sintered at 2280°C

The surface plot for the 0.9 μm TiO_2 samples sintered at 2260°C and post-HIPed exhibits a broader topology than the surface plot for the 2280°C samples, indicating greater densification for compositions with intermediate Ti and C amounts. The reduction in sintering temperature to 2260°C resulted in an increase in the post-HIPed relative densities. The highest post-HIPed relative density (99.96%) was measured for the sample with a high Ti content (5 wt%) and high carbon content (3 wt%), while the lowest density (89.74%) was measured for the sample with high Ti content (5 wt%) and low carbon content (0 wt%). The trend of the surface indicates that the presence of the 0.9 μm TiO_2 substantially reduced overall densification for low carbon content compositions, while compositions with higher carbon contents exhibited minimal variation in post-HIPed relative density with increasing Ti content.

The surface plot for the 0.9 μm TiO_2 samples sintered at 2240°C and post-HIPed exhibits a steeper topology than the surface plot for the 2260°C samples, which is similar to the behavior of the 32 nm TiO_2 samples sintered at 2240°C. The reduction in sintering temperature to 2240°C resulted in small decreases in the post-HIPed relative densities compared to the 2260°C samples. The highest post-HIPed relative

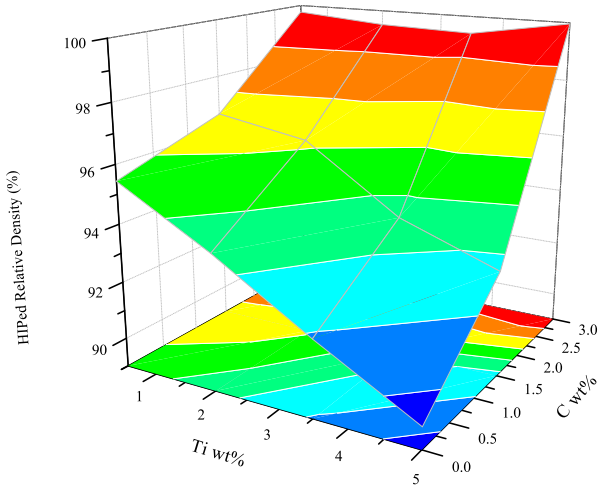

Figure 87: HIPed densities for all 0.9 μm TiO_2 samples sintered at 2260°C

density (99.59%) was measured for the sample with low Ti content (0.5 wt%) and high carbon content (3 wt%), while the lowest density (87.96%) was measured for the sample with high Ti content (5 wt%) and low carbon content (0 wt%). The trend of the surface indicates that the presence of the 0.9 μm TiO_2 reduced densification for low to high carbon content compositions.

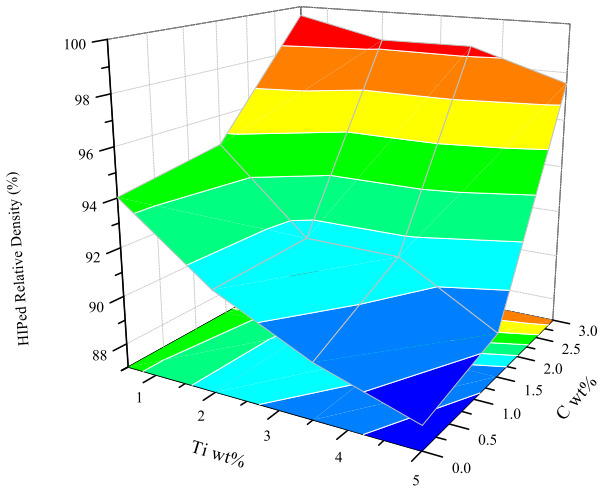

Figure 88: HIPed densities for all 0.9 μm TiO_2 samples sintered at 2240°C

4.3.3 Optical Microscopy

Low and high magnification optical microscopy images of the 0, 1, and 3% carbon 32 nm TiO_2 samples sintered at 2260°C and post-HIPed are provided in Figures 89 through 91. The 0 wt% C, 32 nm TiO_2 samples sintered at 2260°C and post-HIPed show improved densification as the Ti content increased from 0.5 wt% to 1 wt%; however, further increases in Ti content resulted in substantial degradation of the microstructure. According to the micrographs in Figure 89, increasing Ti content initially resulted in reductions in pore size and their apparent volume fraction, but increases up to 5 wt% Ti resulted in pore coalescence and the opening of fissures approximately 50 μm in size. As anticipated, the volume fractions of white TiB_2 particles increased with increasing Ti addition. The grain size also appeared to show slight refinement with increasing Ti content. As observed in Figure 90, increasing the carbon content to 1 wt% C resulted in increasing porosity and greater graphite clustering with increasing Ti content. Based on qualitative observation of the micrographs, the grain size did not appreciably change with increasing Ti content. As observed in Figure 91, the 3 wt% C, 32 nm TiO_2 samples showed roughly equivalent porosity and apparent grain sizes with increasing Ti content. However, the degree of graphite clustering reduced noticeably with increasing Ti content. Large TiB_2 inclusions were observed in the 3 wt% C samples containing 3-5 wt% Ti, with sizes approaching 10 μm in the longest direction.

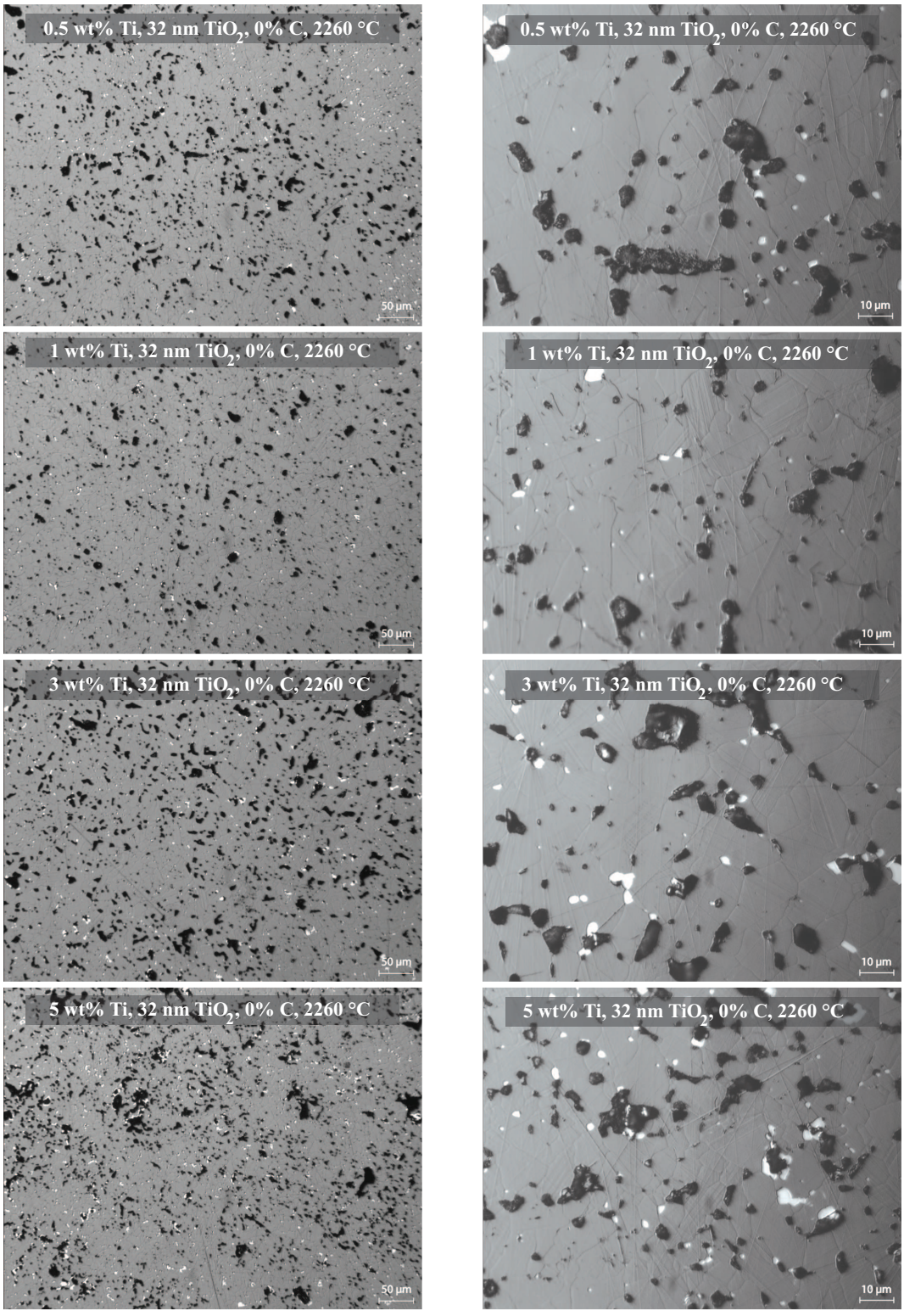

Figure 89: Optical microscopy images of all 0 wt% carbon 32 nm TiO_2 samples sintered at 2260°C and post-HIPed

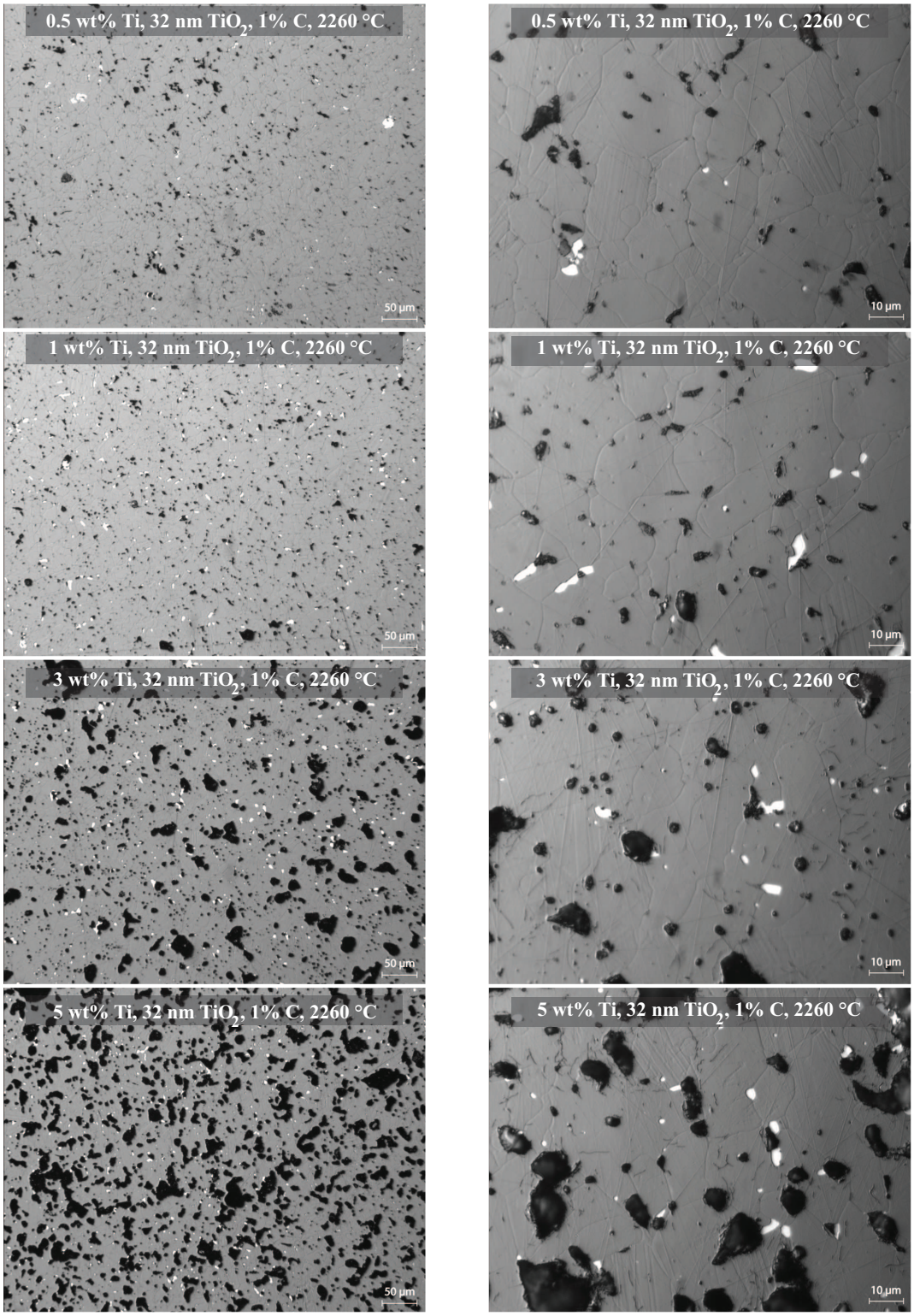

Figure 90: Optical microscopy images of all 1 wt% carbon 32 nm TiO_2 samples sintered at 2260°C and post-HIPed

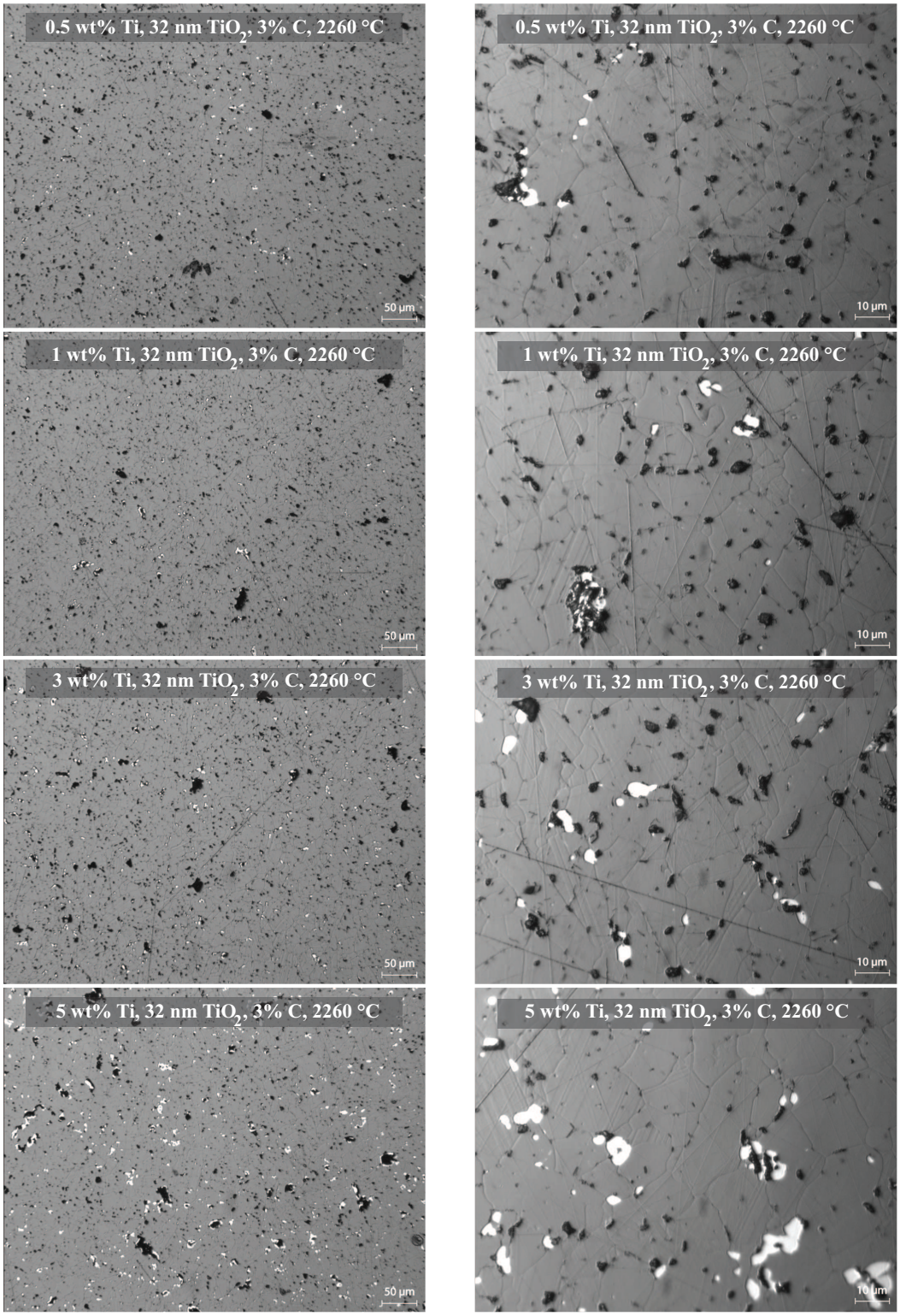

Figure 91: Optical microscopy images of all 3 wt% carbon 32 nm TiO_2 samples sintered at 2260°C and post-HIPed

Low and high magnification optical microscopy images of the 0, 1, and 3% carbon 0.9 μm TiO_2 samples sintered at 2260°C and post-HIPed are provided in Figures 92 through 94. The 0 wt% C, 0.9 μm TiO_2 samples sintered at 2260°C and post-HIPed show decreased densification (i.e., greater porosity) as the Ti content increased; however, the distribution and size of the porosity transitioned from large ($\sim$50 μm or larger) and widely dispersed to much finer ($\sim$5 μm or less) and more uniformly dispersed with increasing Ti content. Based on qualitative observation, the grain size appeared to increase with increasing Ti content up to 3 wt% and then decrease as the Ti content increased further to 5 wt%. As expected, increased volume fractions of white TiB_2 particles were observed with increasing Ti addition. As observed in Figure 93, the 1 wt% C samples displayed increasing porosity and decreasing graphite clustering with increasing Ti content. Based on qualitative observation of the micrographs, the grain size appeared to increase as Ti content increased to 3 wt% but decrease as the Ti content increased further to 5 wt%. As observed in Figure 94, the 3 wt% C, 0.9 μm TiO_2 samples showed substantially reduced porosity and improved microstructures compared to the 0-1 wt% C samples. The sample containing 0.5 wt% Ti displayed the finest grain size and finest distribution of graphite. Grain size appeared to increase with increasing Ti content up to 3 wt% Ti and decrease as the Ti content then increased to 5 wt%. Additionally, the amount of optically detectable graphite increased with increasing Ti content, which is a reversal of the trend observed for the 32 nm TiO_2 samples also containing 3 wt% C. It should also be noted that the 0.9 μm TiO_2 samples exhibited TiB_2 inclusions that were finer and more dispersed than equivalent compositions containing 32 nm TiO_2 as the Ti source.

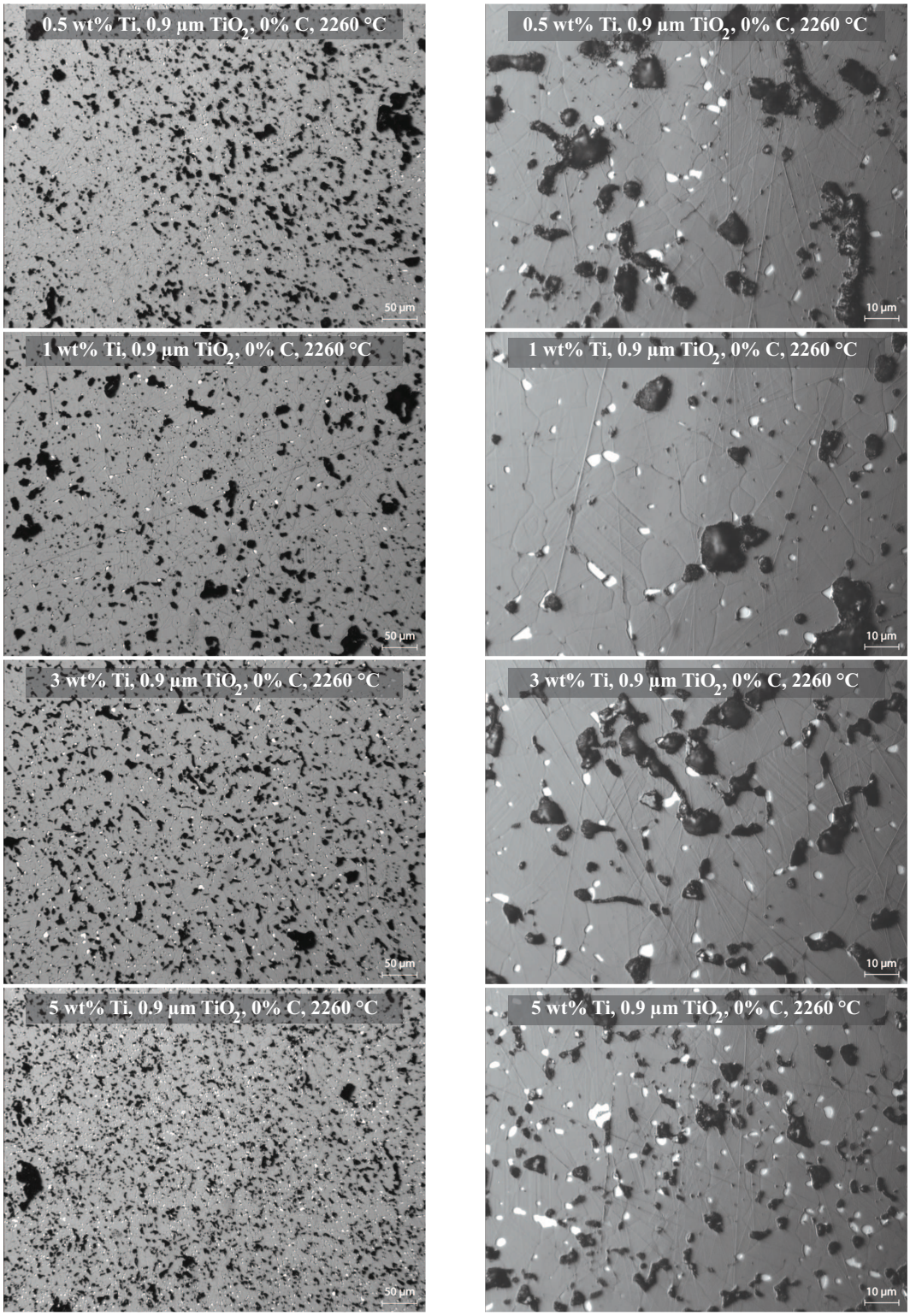

Figure 92: Optical microscopy images of all 0 wt% carbon 0.9 μm TiO_2 samples sintered at 2260°C and post-HIPed

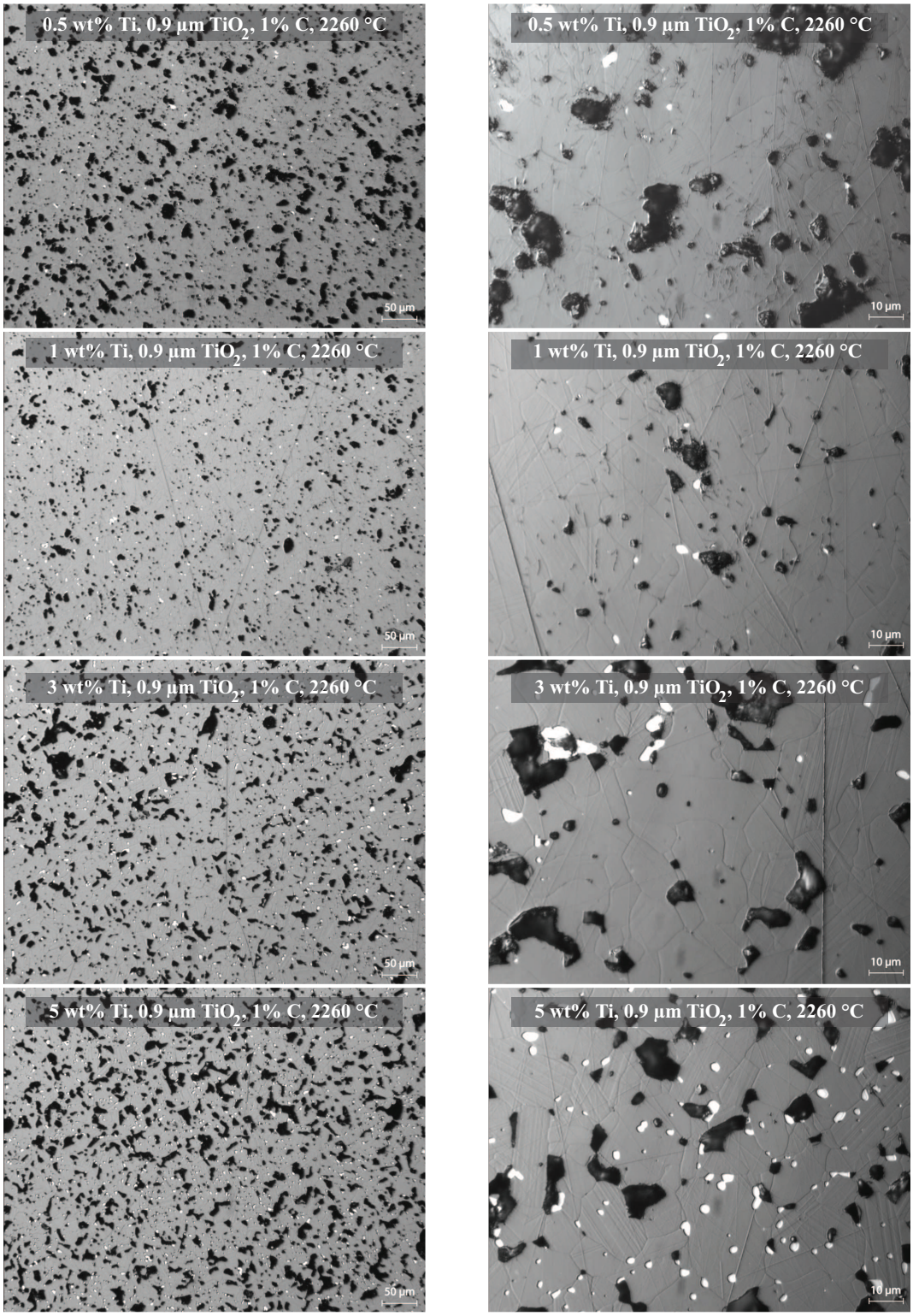

Figure 93: Optical microscopy images of all 1 wt% carbon 0.9 μm TiO_2 samples sintered at 2260°C and post-HIPed

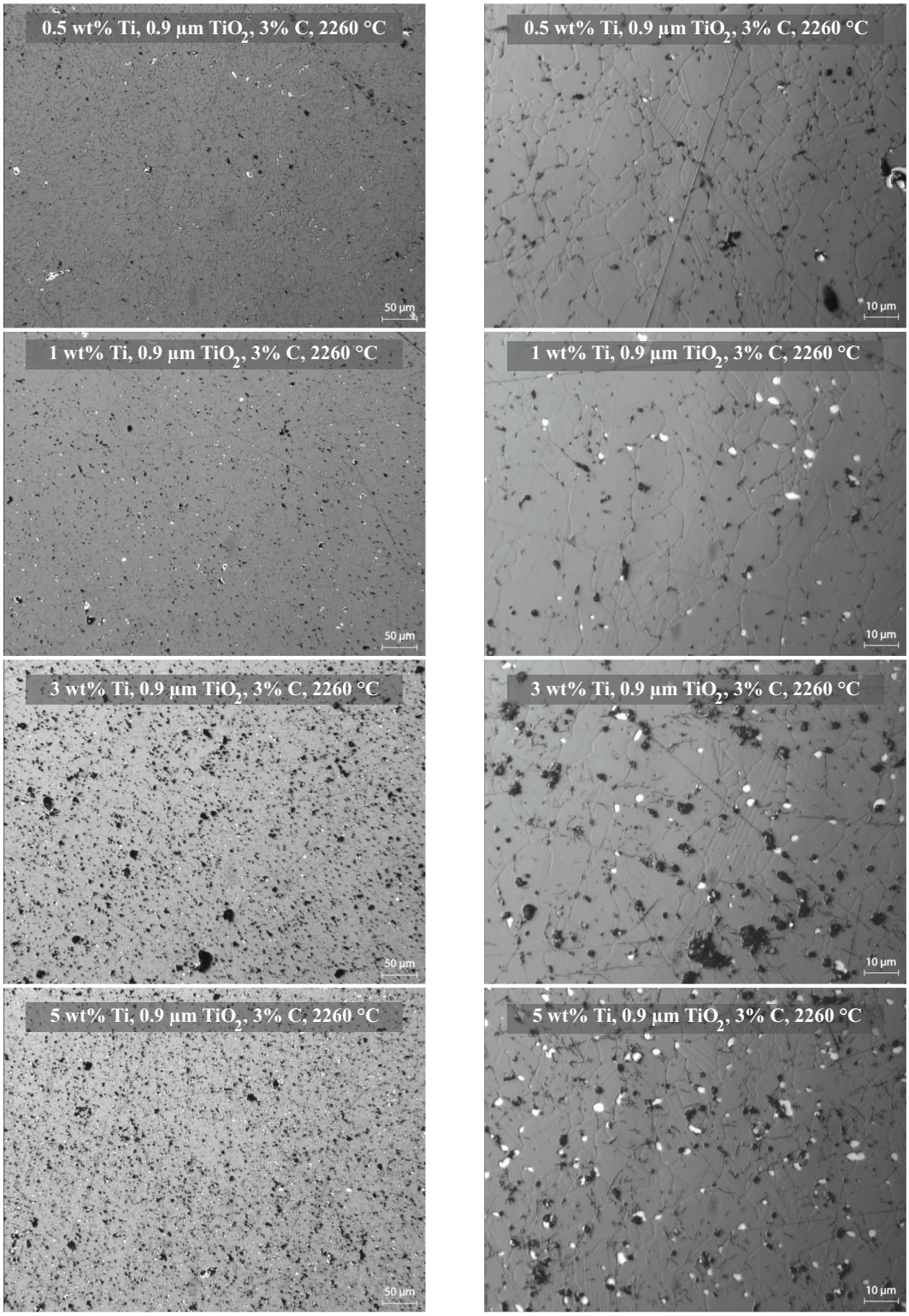

Figure 94: Optical microscopy images of all 3 wt% carbon 0.9 μm TiO_2 samples sintered at 2260°C and post-HIPed

According to the previously discussed relative density data, the 3 wt% C compositions for both the 32 nm TiO_2 and 0.9 μm TiO_2 samples yielded the best overall densification behavior, while the 0 wt% C compositions exhibited increasingly poor densification with increasing Ti content. These observations indicate that carbon may be a required chemical component for the sintering of these compositions. The effect of this carbon addition and its morphology within the microstructure appeared to be strongly dependent upon the amount of added TiO_2. Additionally, the sintering temperature selected for the various specimens resulted in significant changes in the microstructures of the samples. In order to illustrate the effect of both low (0.5 wt% Ti) and high Ti (5 wt% Ti) concentrations as well as sintering temperature on the microstructure of the sintered and HIPed samples containing a high concentration (3 wt% C) of carbon, optical micrographs of polished sections were produced. Optical micrographs of the 3 wt% C, 32 nm and 0.9 μm TiO_2 samples containing 0.5 and 5 wt% Ti and sintered at 2240-2300°C are provided in Figures 95 through 96.

As observed in the following micrographs, the 32 nm and 0.9 μm TiO_2 samples containing 3 wt% C displayed similar microstructural evolutions with changing Ti content and sintering temperature. In general, the samples sintered at 2300°C exhibited a higher number of very small pores ($\sim$5 μm or less in size) in the low Ti content samples compared to the high Ti content specimens sintered at the same temperature. However, according to the relative density measurements discussed earlier, the low Ti content samples showed the highest relative density for a given carbon content and sintering temperature, indicating that the porosity within the high Ti content compositions was contained within large pores $\sim$40 μm in size. As sintering temperature was reduced, pore entrapment was largely eliminated and the pore size transitioned from bimodal to increasingly uniform. In addition to affecting pore size distribution, the effect of Ti content also appeared to change the distribution of graphite within the microstructure; compositions with increasing Ti content displayed

increasing graphite clustering, resulting in the formation of distinct nodular graphitic inclusions for high Ti concentration (5 wt% Ti) compositions. For both Ti concentrations, sintering at 2300°C resulted in dramatic pore coalescence as well as pore entrapment within grains. Additionally, entire TiB_2 grains are observed within the interiors of boron carbide grains exposed to this high process temperature. These observations support the conclusion that severe grain growth occurred during this heat treatment. As the sintering temperature was reduced to 2260°C, the overall scale of the microstructures appeared to decrease; pore size and overall porosity reduced noticeably, the TiB_2 inclusions transitioned to smaller, more equiaxed morphologies, and the clustering of graphite into nodular structures generally decreased to produce a fine dispersion of ∼2-5 μm inclusions at 2260°C. It should be noted that lowering the sintering temperature to 2240°C resulted in a return to increased graphite clustering, causing the formation of segregated microstructures composed of graphite-rich nodules surrounded by largely graphite-free regions.

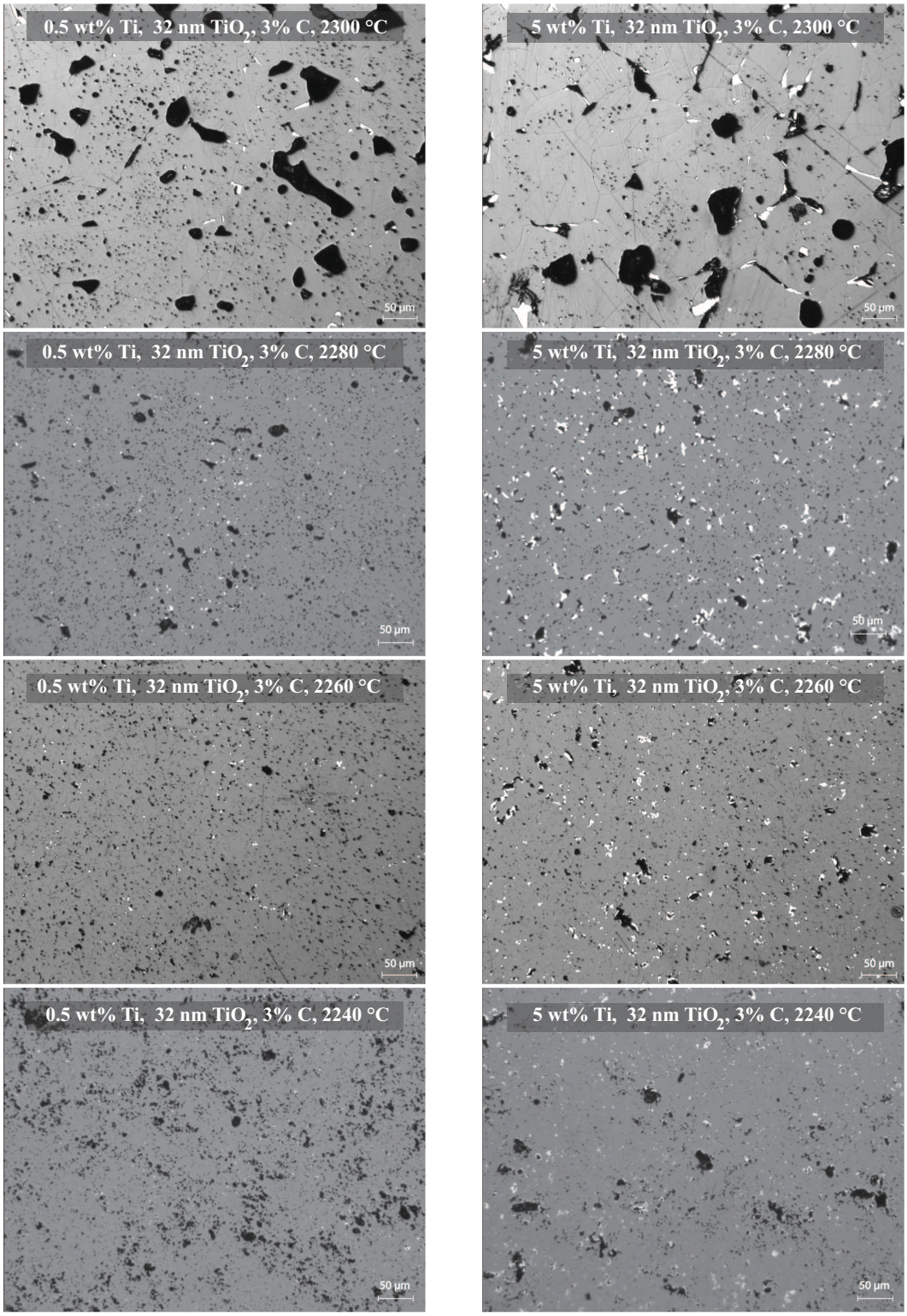

Figure 95: Optical microscopy images of 3 wt% carbon, 32 nm TiO_2 samples containing 0.5 and 5 wt% Ti and sintered at 2240-2300°C and post-HIPed

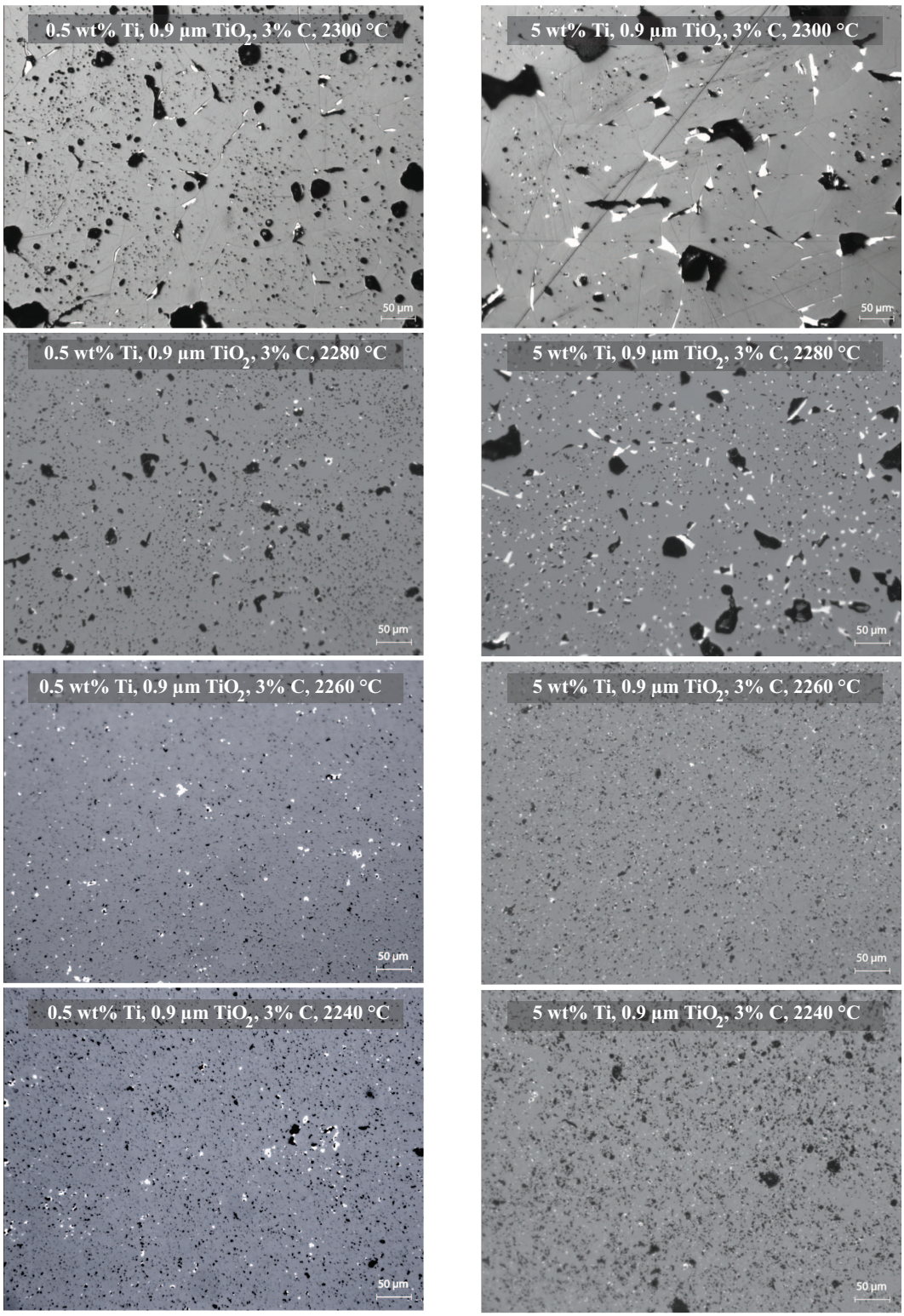

Figure 96: Optical microscopy images of 3 wt% carbon, 0.9 μm TiO_2 samples containing 0.5 and 5 wt% Ti and sintered at 2240-2300°C and post-HIPed

Samples containing large amounts of the respective TiO_2 sources and sintered at high temperatures (i.e., 2300°C) displayed coarse crystalline surfaces on the exterior of the sintered disks upon removal from the furnace, and this observation was suggestive of a transition in sintering behavior. In order to illustrate the effect of both high Ti content and high sintering temperature on microstructural features, low magnification optical microscopy images of the high Ti content 32 nm TiO_2 and 0.9 μm TiO_2 samples containing 0 and 3 wt% carbon sintered at 2300°C and post-HIPed are provided in Figures 97 through 98. Qualitative analysis of these images indicates extremely large grains with sizes in the range of ∼50-150 μm and a segregation of the white TiB_2 phase along the grain boundaries of the boron carbide grains. The size and morphology of the TiB_2 grains for these high sintering temperature samples differed noticeably from samples sintered at lower temperatures. For a given sample composition, the TiB_2 inclusions increased in grain size, and their geometry became increasingly lengthened in one direction along the boron carbide grain boundaries with increasing sintering temperature. These high aspect ratio TiB_2 grains preferentially curving along grain boundaries is indicative of liquid-phase sintering behavior. Each of the micrographs displays the presence of numerous pores with approximately spherical geometries entrapped within the large grains for each composition. Large aspheric pores approximately 40-50 μm in size are visible between grains for both the 32 nm and 0.9 μm TiO_2 samples. It should also be noted that the boron carbide grains within the micrographs exhibit curved grain boundaries as well as grain growth toward convex surfaces, which are additional indications of a liquid-phase sintering mechanism.

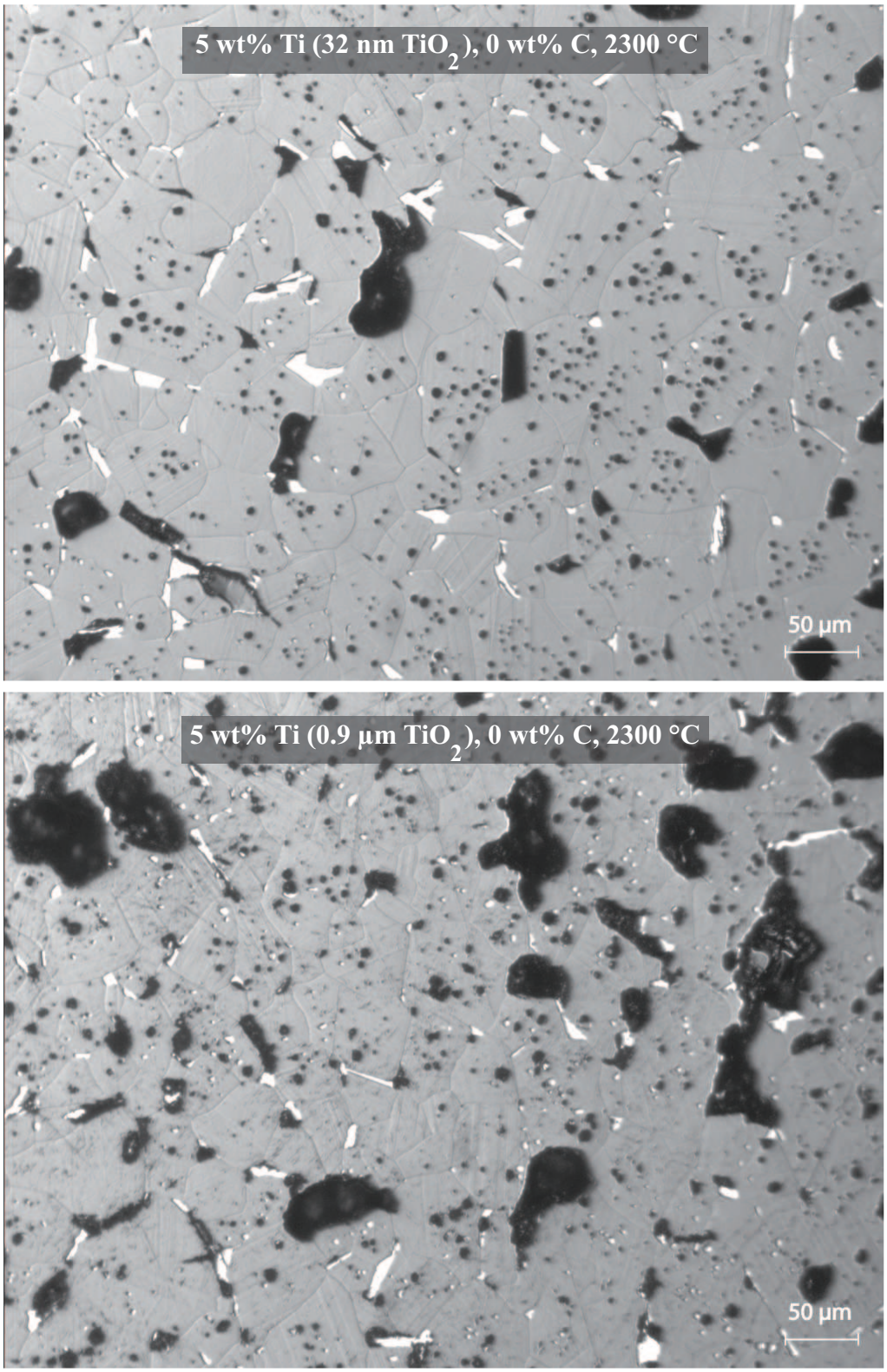

Figure 97: Optical microscopy images of the high Ti content 32 nm TiO_2 and 0.9 μm TiO_2 samples containing 0 wt% carbon sintered at 2300°C and post-HIPed

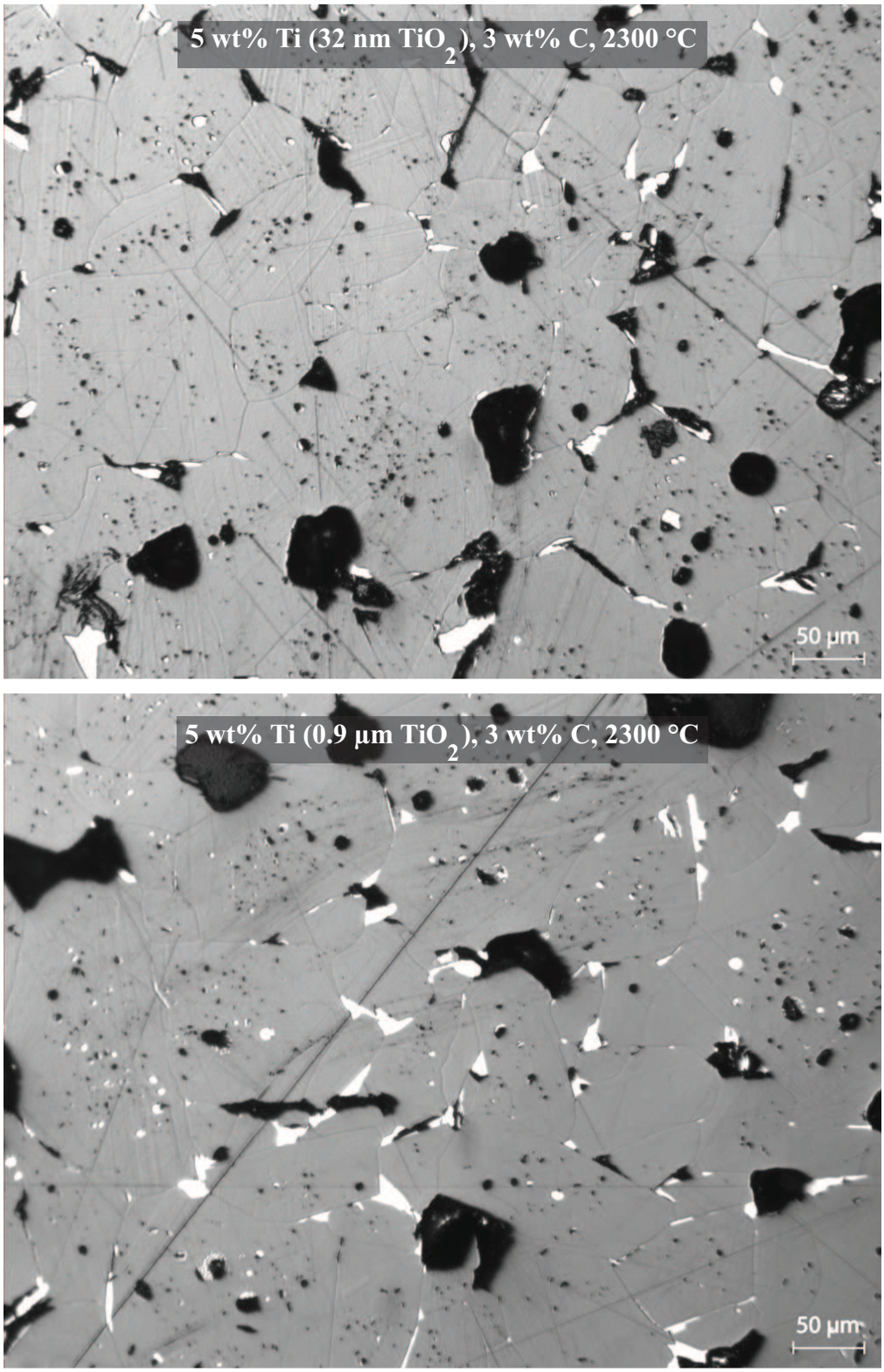

Figure 98: Optical microscopy images of the high Ti content 32 nm TiO_2 and 0.9 μm TiO_2 samples containing 3 wt% carbon sintered at 2300°C and post-HIPed

In order to illustrate the effect of the various additives as well as a lower sintering temperature on the microstructure of the prepared compositions, low magnification optical microscopy images of the 32 nm TiO_2 and 0.9 μm TiO_2 samples containing 0 wt% C sintered at 2240°C and post-HIPed are provided in Figures 99 through 100. The 0 wt% C, 32 nm TiO_2 samples sintered at 2240°C showed moderate pore coalescence but otherwise no significant change in microstructure until the Ti content reached 5 wt%. This high Ti content 32 nm TiO_2 sample exhibited large microstructural fissures with geometries reminiscent of a tearing action. The post-HIPed densities agreed with the overall trend of negative microstructure developments with increasing Ti content, with the 0.5, 1, 3, and 5 wt% Ti samples having post-HIPed relative densities of 93.18%, 94.34%, 92.66%, and 89.86%, respectively. The 0.9 μm TiO_2 samples containing 0 wt% C displayed clearly observable degradation in the microstructures with increasing Ti content. The samples showed pore coalescence and poor overall sintering behavior as the Ti content increased from 0.5 to 5 wt%. The post-HIPed relative densities of the 0.9 μm TiO_2 samples were in agreement with these qualitative observations of the microstructures; the 0.5, 1, 3, and 5 wt% Ti samples had post-HIPed relative densities of 94.02%, 91.12%, 89.24%, and 87.96%, respectively. For this lower temperature and low carbon content series, no improvement in the sintering characteristics of boron carbide were observed with increasing Ti content.

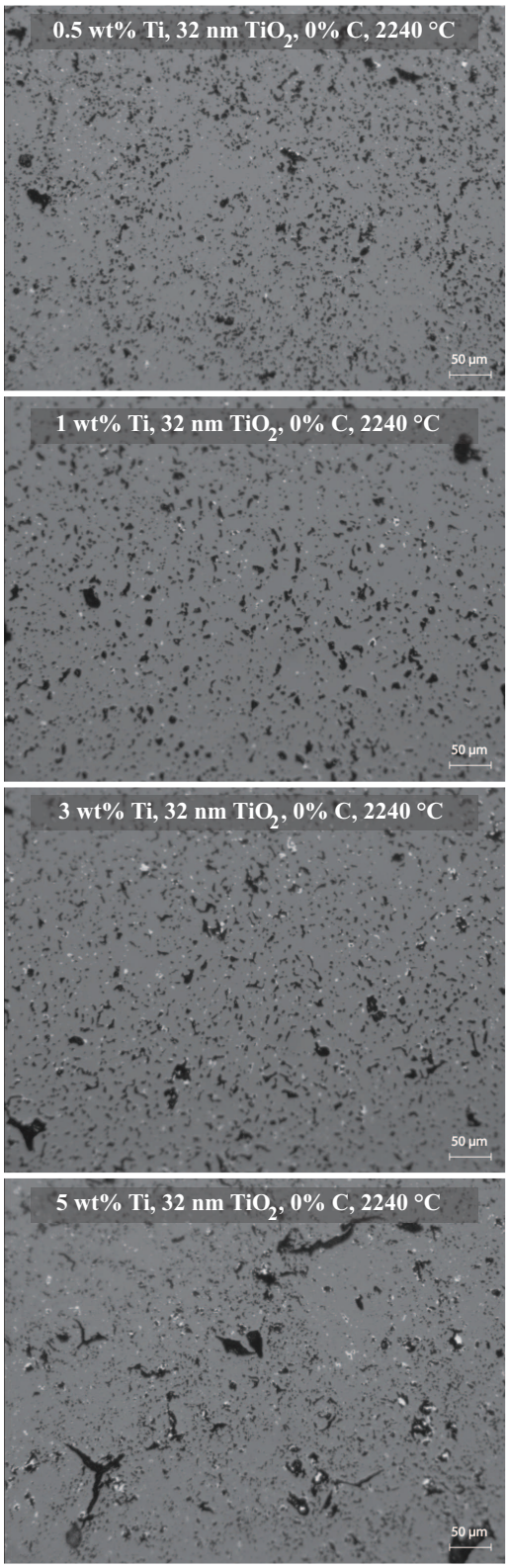

Figure 99: Optical microscopy images of the 32 nm TiO_2 samples containing 0 wt% carbon sintered at 2240°C and post-HIPed

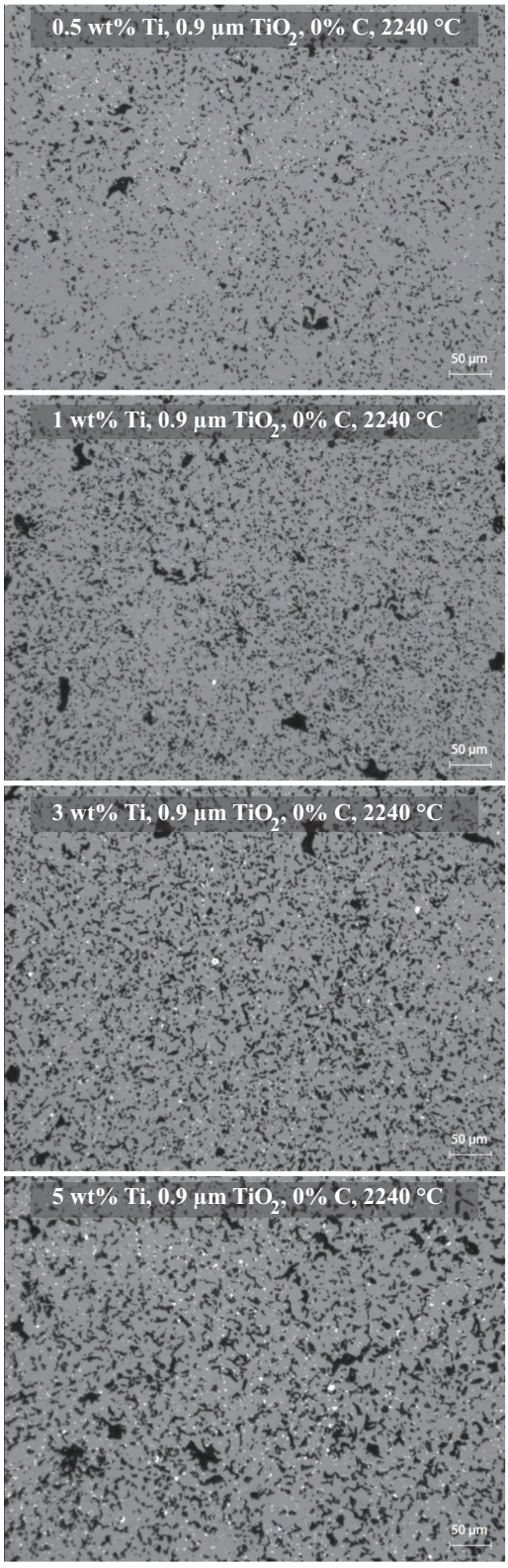

Figure 100: Optical microscopy images of the 0.9 μm TiO_2 samples containing 0 wt% carbon sintered at 2240°C and post-HIPed

Table 16: EDS Data - 5 wt% Ti, 3 wt% C 0.9 μm TiO_2 Sample Sintered at 2260°C

Location	B (at%)	C (at%)	O (at%)	Si (at%)	Ti (at%)
1	65.24				34.76
2	44.57	54.28	1.02	0.12	
3	75.39	24.61			
4	83.39	16.61			

4.3.4 Electron Microscopy and Energy-Dispersive X-ray Spectroscopy

Scanning electron microscopy (SEM) was performed on the sample exhibiting the best overall microstructure (i.e., the 0.9 μm TiO_2 sample containing 5 wt% Ti and 3 wt% C, and sintered at 2260°C) in order to view features such as grain boundaries. High resolution SEM images of the sample are provided in Figure 101. The results of energy-dispersive X-ray spectroscopy (EDS) performed during SEM are provided in Figure 102. In these images, graphite appears as dark regions measuring ∼1-4 μm and is typically clustered near faceted white ∼1-2 μm TiB_2 inclusions that are distributed throughout the microstructure. The gray matrix is confirmed as boron carbide; however, the atomic percentages from the EDS data indicate that the boron carbide matrix material varies in composition from carbon-rich to boron-rich. This result disagrees with X-ray diffraction data in the following section; however, this discrepancy may be the result of sampling a greater volume than anticipated, whereby statistical averaging of the large electron beam interaction volume caused the characteristic X-rays of boron-rich boron carbide to be convoluted with those of dispersed graphite located beneath the surface. The elemental components detected via EDS at the various indicated locations on the sample are provided in Table 16. The presence of a small amount of silicon and oxygen in the dark carbon-rich region (i.e., graphite) at location #2 in the EDS image (Figure 102) could be explained by a small contamination from the silica glass slide used to level the sample surface during optical microscopy.

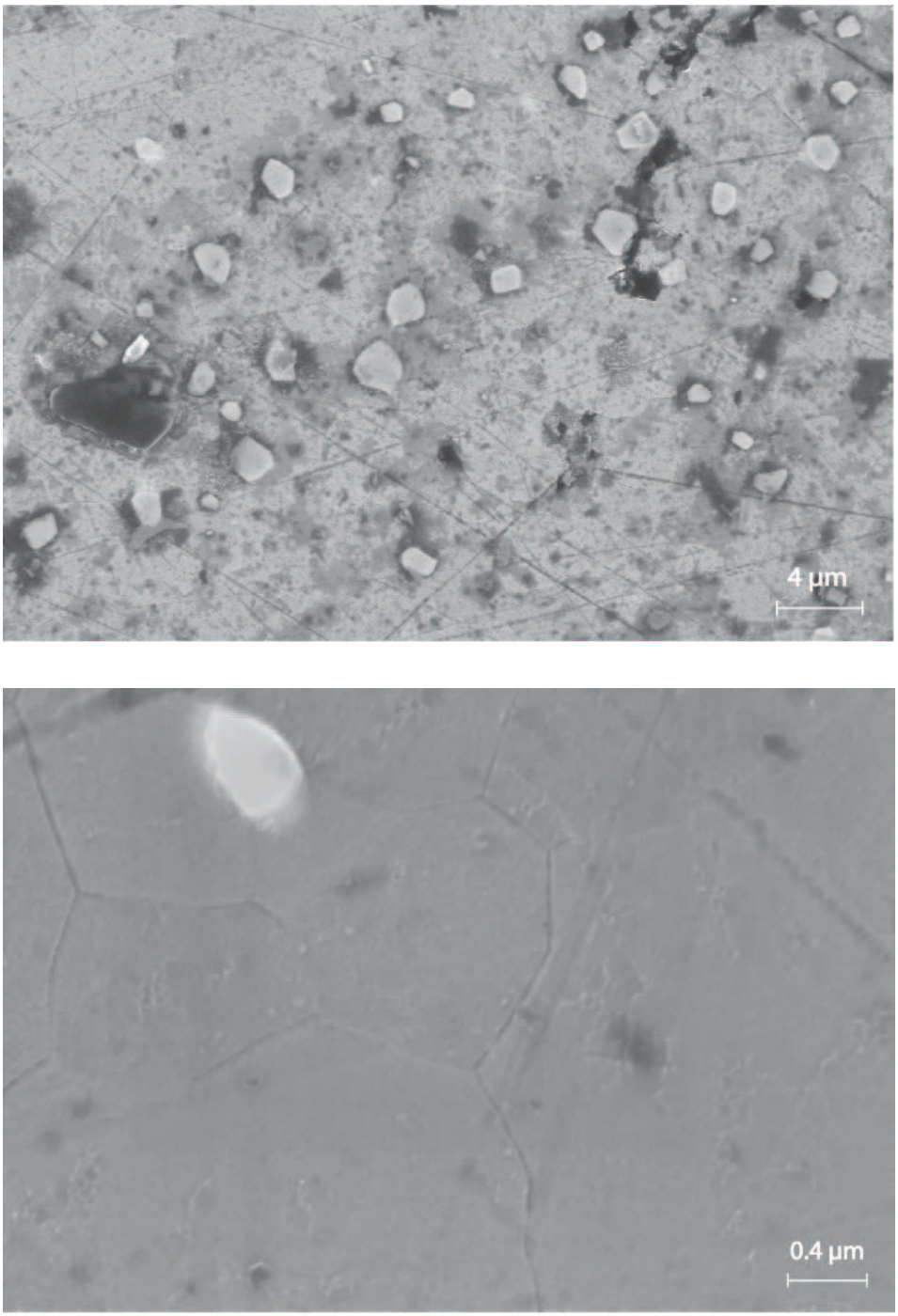

Figure 101: High resolution scanning electron microscopy images of the 5 wt% Ti, 3 wt% C, 0.9 μm TiO_2 Sample Sintered at 2260°C and post-HIPed

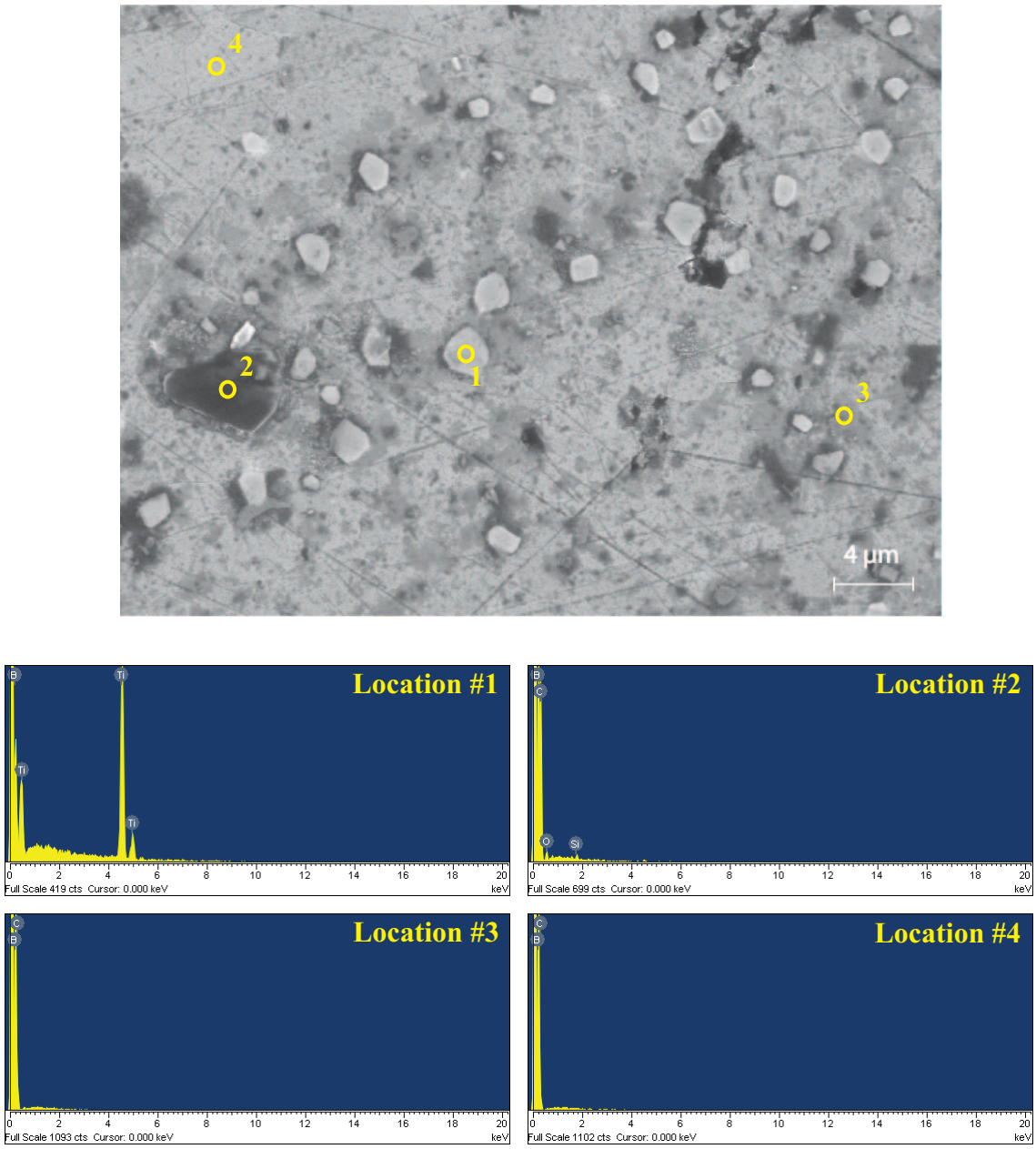

Figure 102: Energy-dispersive X-ray spectroscopy (EDS) of the 5 wt% Ti, 3 wt% C, 0.9 μm TiO_2 Sample Sintered at 2260°C and post-HIPed

4.3.5 Phase Identification via X-ray Diffraction

XRD was performed on all compositions sintered at 2260°C (the sintering temperature yielding, on average, the highest post-HIPed relative densities) in order to determine the phases present following sintering and HIPing. The XRD traces of the 32 nm TiO_2 and 0.9 μm TiO_2 samples are provided in Figures 103 and 104, respectively. In general, the integrated intensity of the most intense TiB_2 peak at 44.416° 2θ increases with added Ti content. However, for some samples, the integrated intensity of the most intense TiB_2 peak appears to be independent of the amount of added Ti. For example, the 0.5 wt% Ti samples for both the 32 nm and 0.9 μm TiO_2, 0% C compositions show a higher TiB_2 integrated intensity compared to the subsequent 1 wt% Ti compositions of the same carbon content, which is non-intuitive. This anomaly could be explained by the contamination of higher-concentration TiO_2 spray dried particles making their way into the powders prepared for the lower Ti content compositions. The integrated intensity of the most intense diffraction peak of graphite at 26.426° 2θ follows the general trend of increasing with the amount of added carbon; however, for a given carbon content, the graphite intensity decreases with increasing Ti content. This decreasing graphite content with increasing Ti content could be explained by the removal of carbon via the carbothermal reduction of TiO_2 or a sub-oxide of TiO_2.

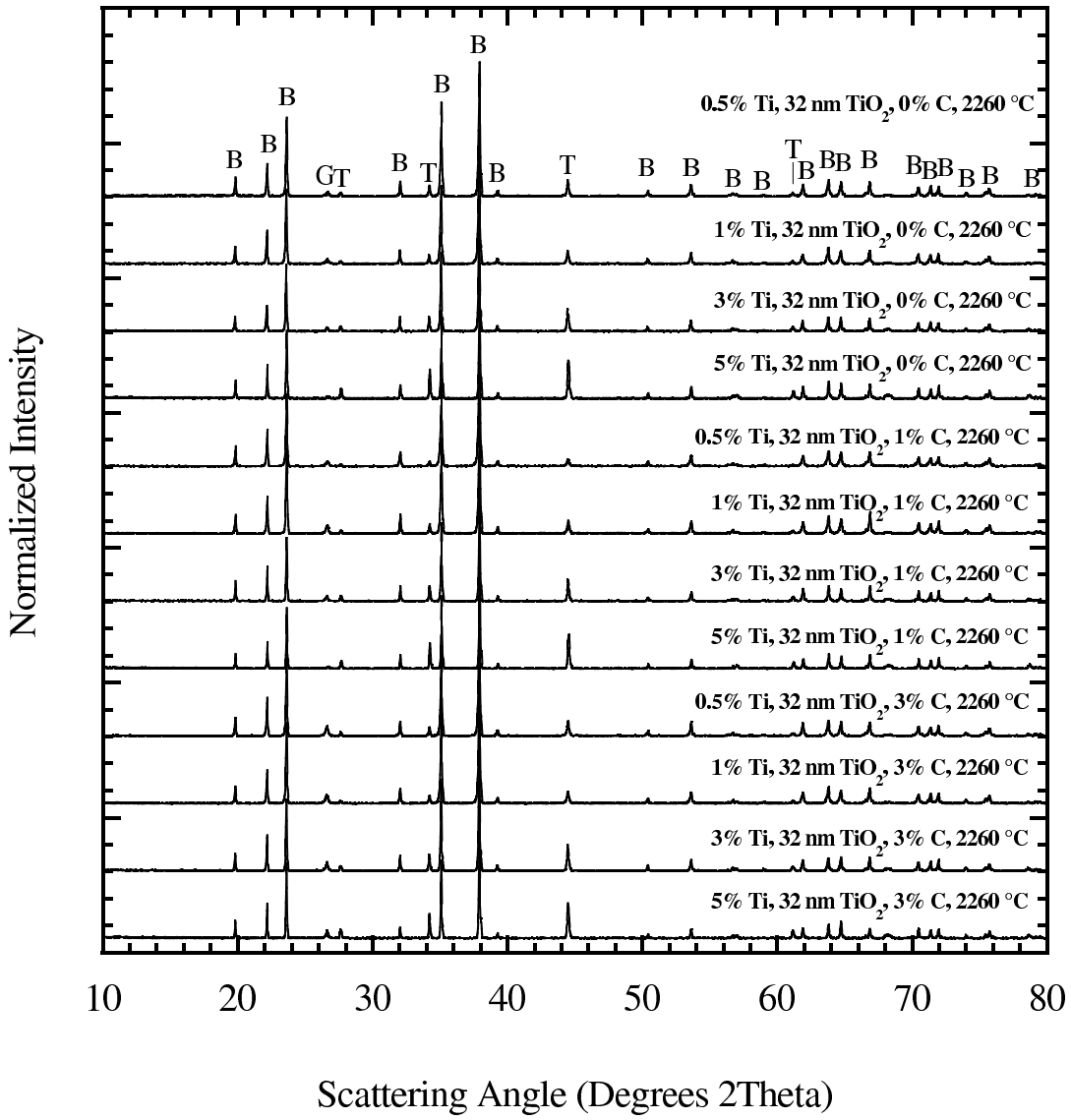

Figure 103: XRD traces of all 32 nm TiO_2-added compositions pressed into small disks, sintered at 2260°C, and post-HIPed. The diffraction patterns were normalized based upon the most intense peak in each scan. Labeling corresponds to the following: B($B_{13.43}C_{1.71}$ and $B_{13}C_2$), G(graphite), and T(TiB_2).

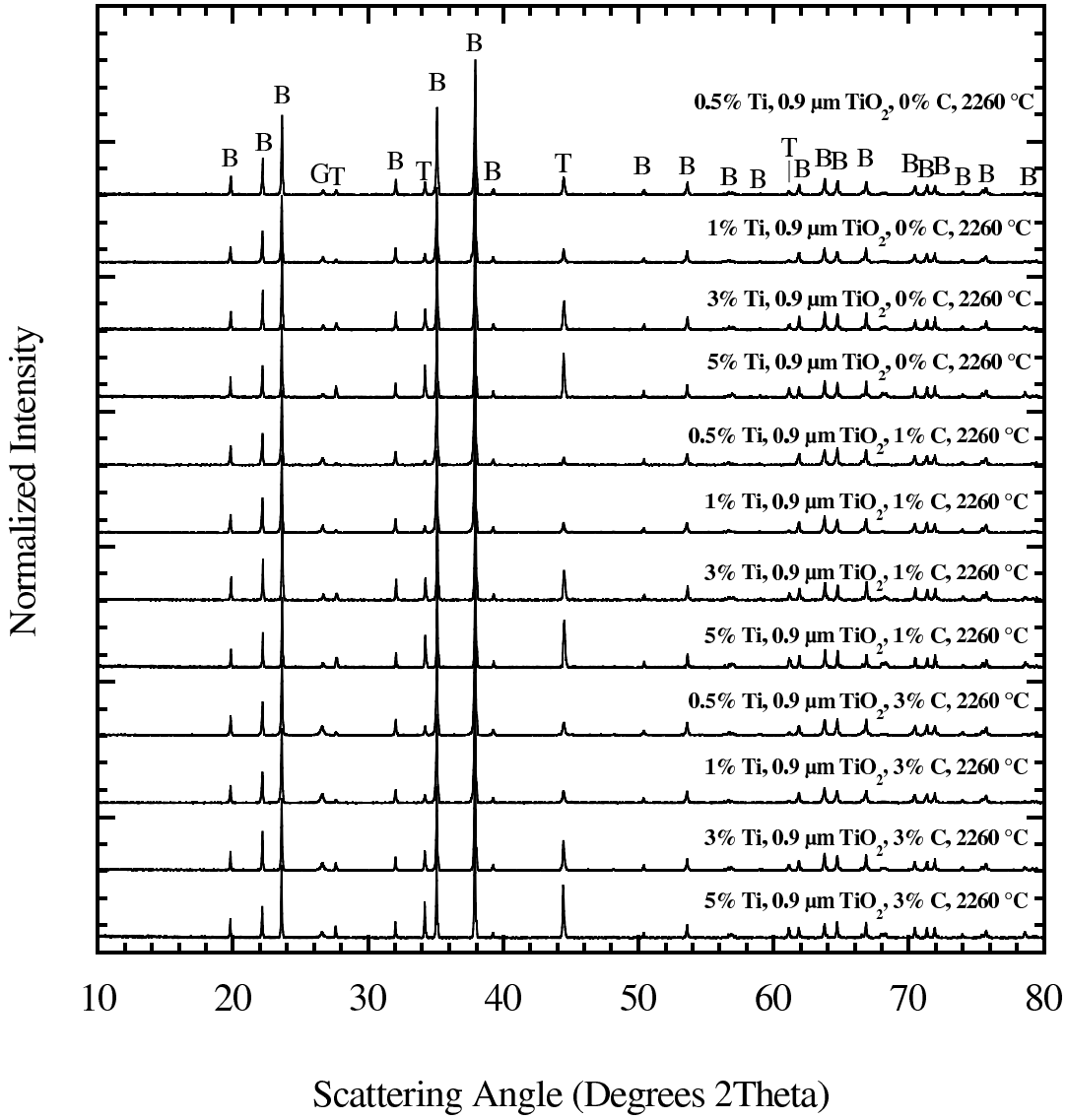

Figure 104: XRD traces of all 0.9 μm TiO_2-added compositions pressed into small disks, sintered at 2260°C, and post-HIPed. The diffraction patterns were normalized based upon the most intense peak in each scan. Labeling corresponds to the following: B($B_{13.43}C_{1.71}$ and $B_{13}C_2$), G(graphite), and T(TiB_2).

4.3.6 Grain Size Measurement

Cumulative percent finer plots based on grain size measurements of the 0, 1, and 3 wt% carbon, 32 nm TiO_2 samples sintered at 2260°C and post-HIPed are provided in Figures 105 through 107. For the 32 nm TiO_2 samples containing 0 wt% C, the grain size distributions followed an irregular order, with the 5 wt% Ti sample displaying the finest grain distribution followed by the 0.5, 1, and 3 wt% Ti samples. The grain size distributions of the samples containing 1 and 3 wt% Ti intersect, with the 3 wt% Ti sample exhibiting a shift to grains smaller than those measured in the 1 wt% Ti sample. These observations are confirmed by the d_{90} grain size data; the 0.5, 1, 3, and 5 wt% Ti samples containing 0 wt% C displayed d_{90} grain size values of 14.11, 19.57, 15.59, and 10.56 μm, respectively.

For the 32 nm TiO_2 samples containing 1 wt% C, the 0.5 wt% Ti sample displayed the finest grain distribution followed by the 1, 5, and 3 wt% Ti samples. It should be noted that the grain size distributions for the 0.5, 1, and 5 wt% Ti samples intersected; the 0.5 wt% Ti sample shifted to higher grain sizes than the 1 and 5 wt% Ti samples beginning at $\sim$20 μm, while the grain size distribution for the 5 wt% Ti sample shifted to smaller grain sizes. The grain size distribution for the 1 wt% Ti sample oscillated between the 0.5 and 5 wt% Ti samples with increasing grain size and eventually terminated with a smaller maximum grain size than the 0.5 wt% Ti sample. The 3 wt% Ti sample possessed a grain size distribution that was substantially larger than the other samples, showing very few grains less than 10 μm. These observations are supported by the d_{90} grain size data; the 0.5, 1, 3, and 5 wt% Ti samples containing 1 wt% C displayed d_{90} grain size values of 24.01, 21.38, 34.55, and 21.69 μm, respectively.

For the 32 nm TiO_2 samples containing 3 wt% C, the grain size distributions followed tight grouping, with the 0.5 wt% Ti sample displaying the only outlying larger grain size distribution. Of the the remaining samples, the 1 wt% Ti sample

exhibited the finest grain size distribution followed by the 5 and 3 wt% Ti samples. The order of the distributions is supported by the d_{90} grain size data; the 0.5, 1, 3, and 5 wt% Ti samples containing 3 wt% C showed d_{90} grain size values of 22.27, 20.05, 21.59, and 20.27 μm, respectively.

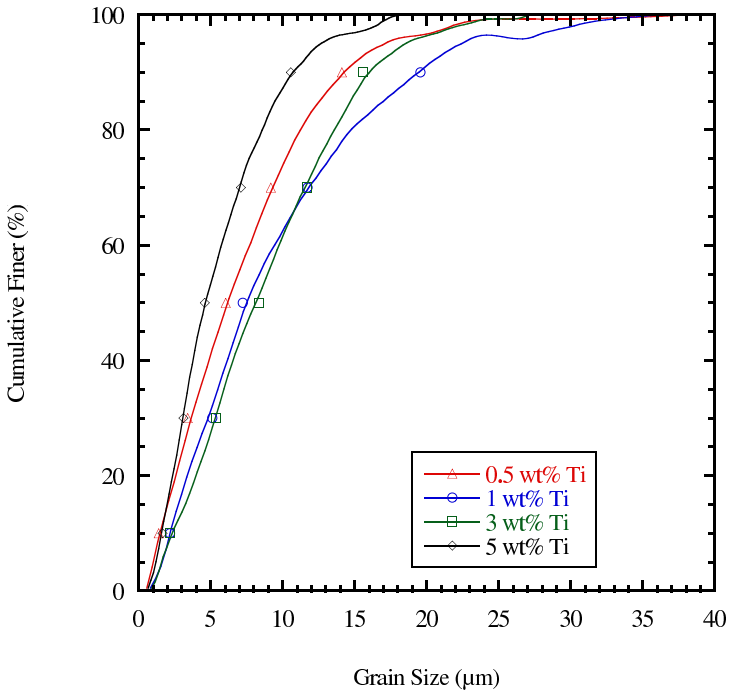

Figure 105: Cumulative percent finer grain size plots of all 0 wt% carbon, 32 nm TiO_2 samples sintered at 2260°C and post-HIPed

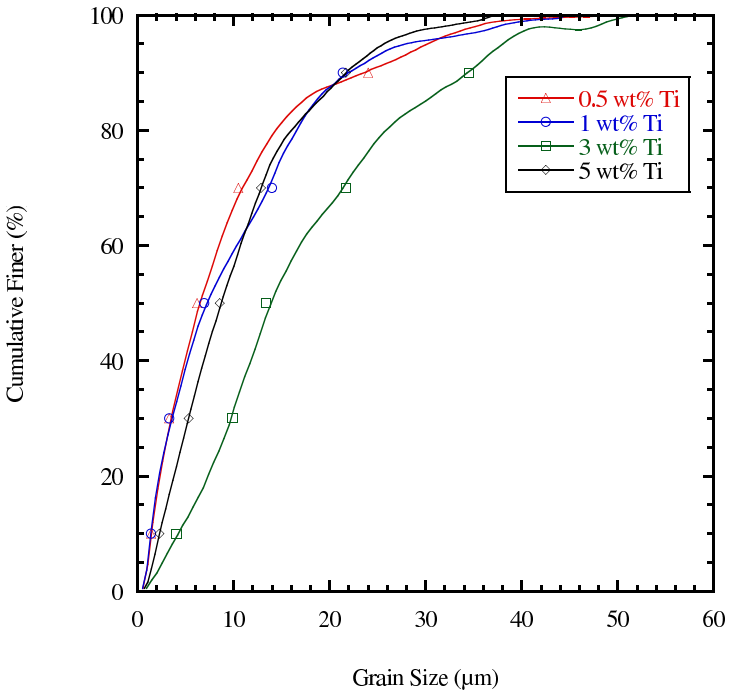

Figure 106: Cumulative percent finer grain size plots of all 1 wt% carbon, 32 nm TiO_2 samples sintered at 2260°C and post-HIPed

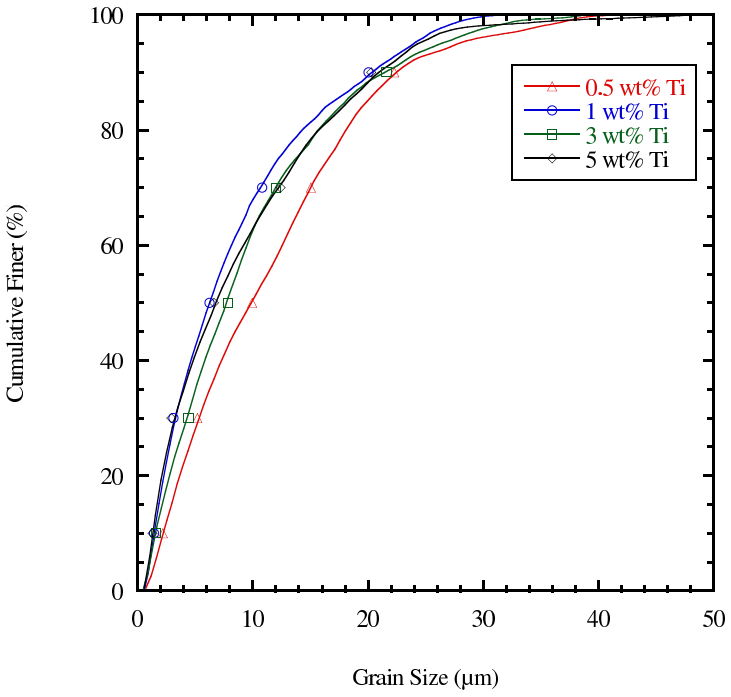

Figure 107: Cumulative percent finer grain size plots of all 3 wt% carbon, 32 nm TiO_2 samples sintered at 2260°C and post-HIPed

Cumulative percent finer plots based on grain size measurements of the 0, 1, and 3 wt% carbon, 0.9 μm TiO_2 samples sintered at 2260°C and post-HIPed are provided in Figures 108 through 110. For the 0.9 μm TiO_2 samples containing 0 wt% C, the 5 wt% Ti sample displayed the finest grain size distribution followed by the 0.5, 3, and 1 wt% Ti samples. These observations are confirmed by the d_{90} grain size data; the 0.5, 1, 3, and 5 wt% Ti samples containing 0 wt% C displayed d_{90} grain size values of 15.16, 22.78, 16.35, and 12.84 μm, respectively.

For the 0.9 μm TiO_2 samples containing 1 wt% C, each of the compositions displayed closely grouped grain size distributions. The perceived similarity between these samples is supported by the d_{90} grain size data; the 0.5, 1, 3, and 5 wt% Ti samples containing 1 wt% C displayed d_{90} grain size values of 17.33, 20.74, 22.08, and 18.85 μm, respectively.

For the 0.9 μm TiO_2 samples containing 3 wt% C, the 0.5 and 5 wt% Ti samples displayed nearly identical grain size distributions that were the finest out of the four samples. The 3 wt% Ti sample possessed the largest grain size distribution, and the 1 wt% Ti sample exhibited an intermediate distribution between the other samples. These observations are supported by the d_{90} grain size data; the 0.5, 1, 3, and 5 wt% Ti samples containing 3 wt% C showed d_{90} grain size values of 9.35, 16.1, 20.74, and 10.03 μm, respectively.

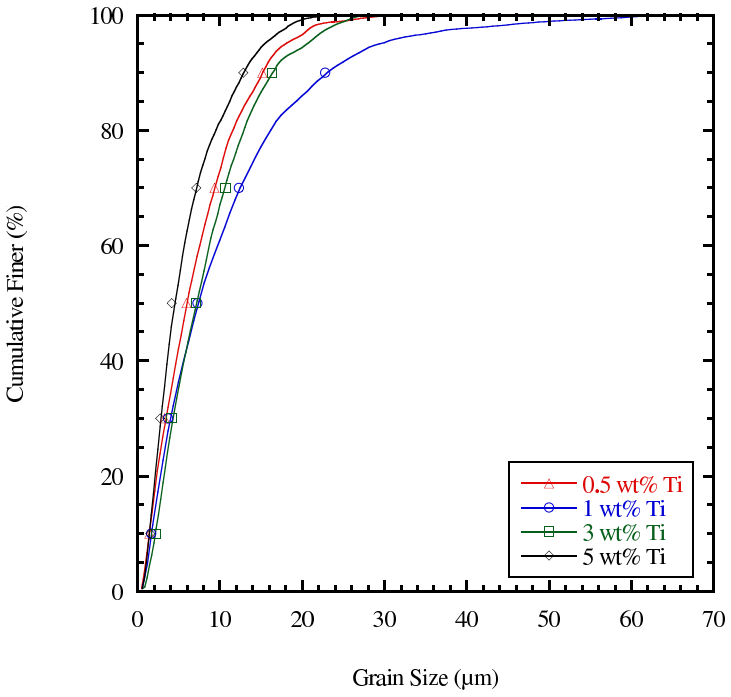

Figure 108: Cumulative percent finer grain size plots of all 0 wt% carbon, 0.9 μm TiO_2 samples sintered at 2260°C and post-HIPed

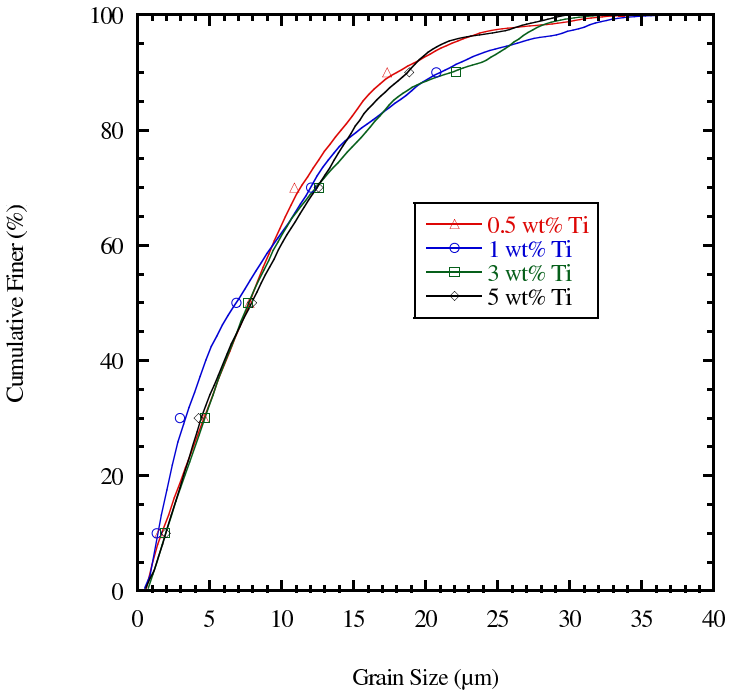

Figure 109: Cumulative percent finer grain size plots of all 1 wt% carbon, 0.9 μm TiO_2 samples sintered at 2260°C and post-HIPed

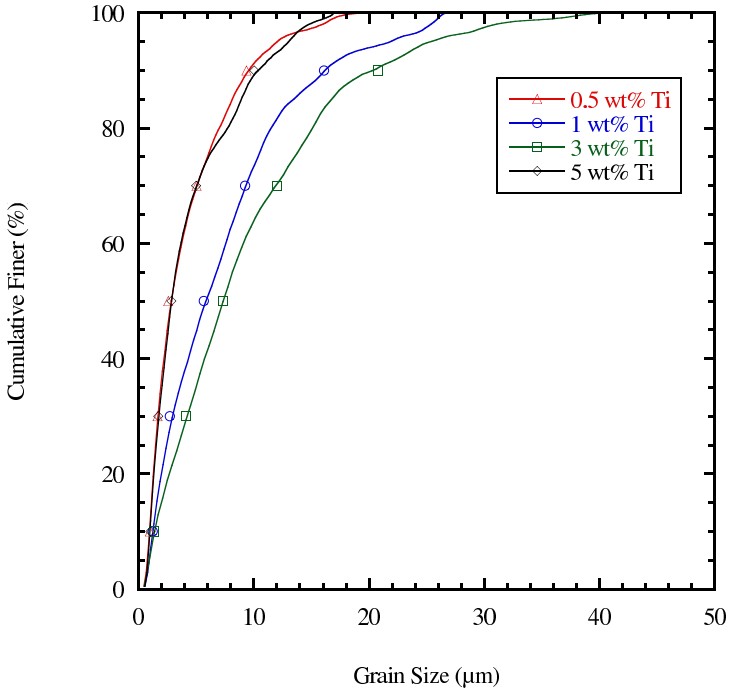

Figure 110: Cumulative percent finer grain size plots of all 3 wt% carbon, 0.9 μm TiO_2 samples sintered at 2260°C and post-HIPed

The d_{50} grain size (i.e., the median grain size) was calculated based on the grain size data obtained via quantitative characterization of the optical micrographs for each specimen. Plots of the d_{50} grain size (in μm) for the 0, 1, and 3 wt% carbon, 32 nm TiO_2 samples sintered at 2260°C and post-HIPed are provided in Figure 111. The 32 nm TiO_2 samples containing 0 wt% C and sintered at 2260°C displayed an initial increase in d_{50} grain size from 6.05 μm up to 8.4 μm as the Ti content increased from 0.5 wt% to 3 wt%. The d_{50} grain size then decreased to 4.6 μm as the Ti content increased to 5 wt%. The 1 wt% C samples showed grain size behavior similar to the 0 wt% C samples, although the values were ultimately larger. For the 1 wt% C specimens, the grain size increased from 6.19 μm up to 13.34 μm as the Ti content increased up to 3 wt% and then decreased substantially back to 8.66 μm as the Ti content increased up to 5 wt%. The 32 nm TiO_2 samples containing 3 wt% C exhibited an oscillatory trend in which the grain size initially decreased from 9.96 μm to 6.26 μm as the Ti content increased up to 1 wt%. The median grain size then increased marginally up to 7.85 μm and subsequently decreased slightly to 6.66 μm as the Ti content increased to 3 and 5 wt%, respectively. The smallest grain size value for the 32 nm TiO_2 samples sintered at 2260°C and post-HIPed was observed for the composition containing high Ti content (5 wt%) and 0 wt% C.

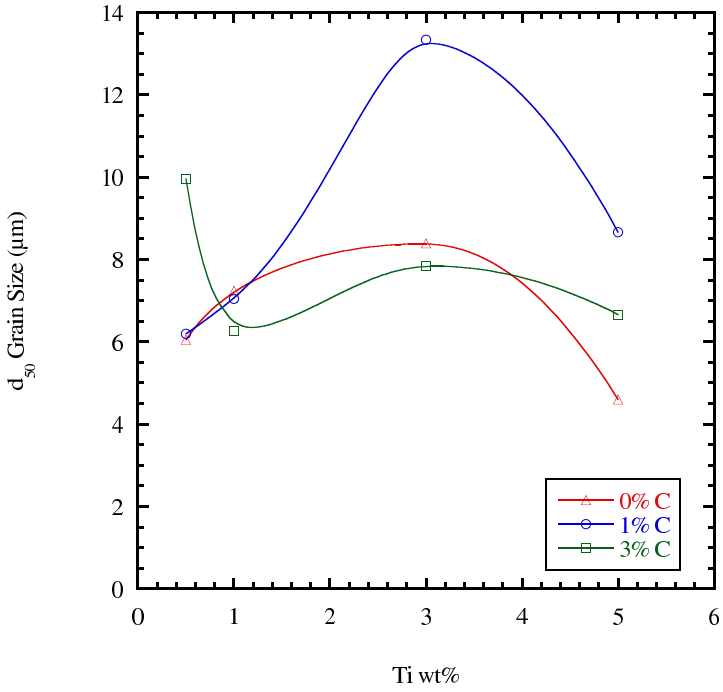

Figure 111: d_{50} grain size plots for all 0, 1, and 3 wt% carbon, 32 nm TiO_2 samples sintered at 2260°C and post-HIPed

Plots of the d_{50} grain size (in μm) for the 0, 1, and 3 wt% carbon, 0.9 μm TiO_2 samples sintered at 2260°C and post-HIPed are provided in Figure 112. The 0.9 μm TiO_2 samples containing 0 wt% C and sintered at 2260°C displayed an initial increase in d_{50} grain size followed by a plateau and subsequent decrease. As the Ti content increased from 0.5 wt% to 1 wt%, the median grain size increased from 5.99 μm up to 7.27 μm. The d_{50} grain size decreased marginally to 7.16 μm as the Ti content increased to 3 wt% and then decreased sharply to 4.3 μm as the Ti content increased further to 5 wt%. The 1 wt% C samples showed grain size behavior that was relatively invariant with Ti content, displaying d_{50} grain size values in the range of 7.05-7.99 μm. The 0.9 μm TiO_2 samples containing 3 wt% C exhibited a median grain size trend similar to the 0 wt% C, 0.9 μm TiO_2 specimens; the d_{50} grain size initially increased from 2.57 μm up to 7.37 μm as the Ti content increased to 3 wt% and then decreased to 2.86 μm as the Ti content increased to 5 wt%. The smallest median grain size values for the 0.9 μm TiO_2 samples sintered at 2260°C and post-HIPed were observed for compositions containing low (0.5 wt%) and high (5 wt%) Ti content and 3 wt% C.

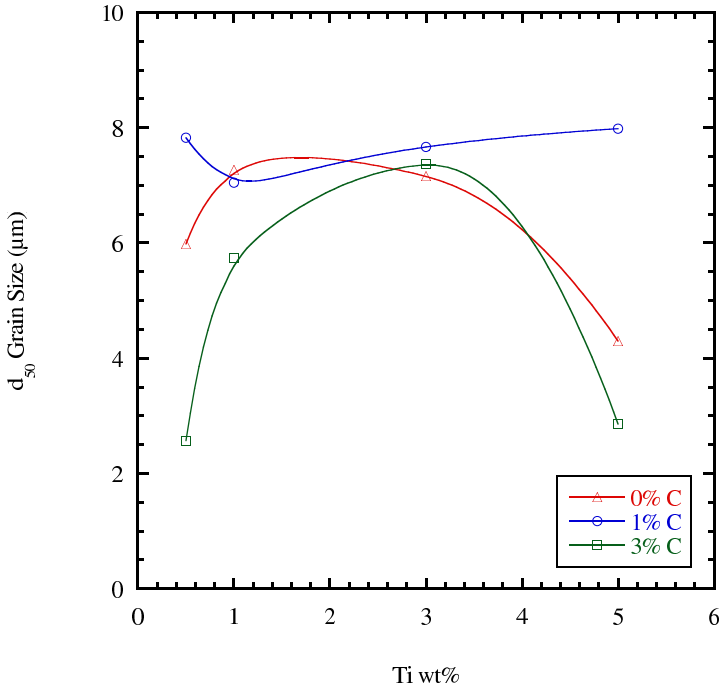

Figure 112: d_{50} grain size plots for all 0, 1, and 3 wt% carbon, 0.9 μm TiO_2 samples sintered at 2260°C and post-HIPed

4.3.7 Hardness and Fracture Toughness Measurement

The microindentation hardness was measured on the diamond-polished surface of each specimen using a certified Vickers diamond indenter under a 1 kg load (HV1). In addition to measuring hardness, the lengths of the cracks emanating from the corners of the indent were measured and used to calculate fracture toughness. Ten acceptable indentations and the associated set of crack lengths were measured for each sample. Plots of the HV1 hardness (in kg/mm^2) and indentation fracture toughness (in $MPa{\cdot}m^{1/2}$) for the 0, 1, and 3% carbon 32 nm TiO_2 samples sintered at 2260°C and post-HIPed are provided in Figures 113 through 115. The hardness values of the 32 nm TiO_2 samples exhibited the general trend of decreasing with increasing Ti content, although a marginal increase from 2590.2 kg/mm^2 to 2633.7 kg/mm^2 was observed as the Ti content increased from 0.5 wt% to 1 wt%. The 1 wt% C, 32 nm TiO_2 samples also exhibited a similar trend of substantially decreasing hardness with increasing Ti content. The lowest hardness of the 32 nm TiO_2 series (1752.8 kg/mm^2) was observed for the composition containing 5 wt% Ti and 1 wt% C. The 3 wt% C, 32 nm TiO_2 samples displayed the opposite trend observed for the 0 and 1 wt% C compositions; hardness increased incrementally with increasing Ti content. The highest hardness (2846 kg/mm^2) for the 32 nm TiO_2 series was measured for the sample containing 5 wt% Ti and 3 wt% C.

The fracture toughness of the 0 and 1 wt% C, 32 nm TiO_2 samples followed the trend of increasing with increasing Ti content. The fracture toughness of the 3 wt% C samples initially decreased as the Ti content increased from 0.5 wt% to 1 wt% and then increased with further increasing Ti content up to 5 wt%. The highest fracture toughness for the 2260°C 32 nm TiO_2 series (4.58 $MPa{\cdot}m^{1/2}$) was measured for the composition containing 5 wt% Ti and 1 wt% C, which—as stated above—also displayed the lowest hardness.

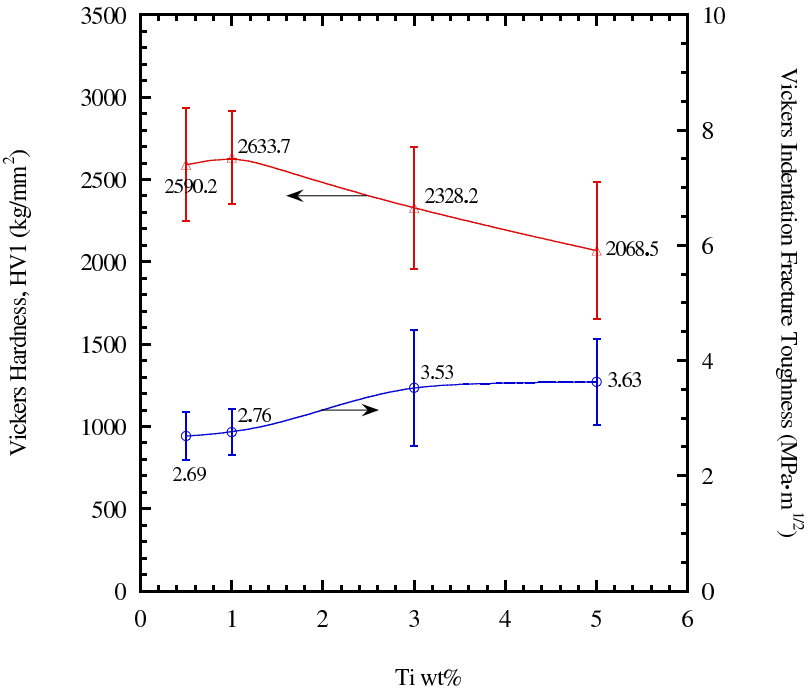

Figure 113: Vickers hardness and indentation fracture toughness plots for all 0% carbon, 32 nm TiO_2 samples sintered at 2260°C and post-HIPed

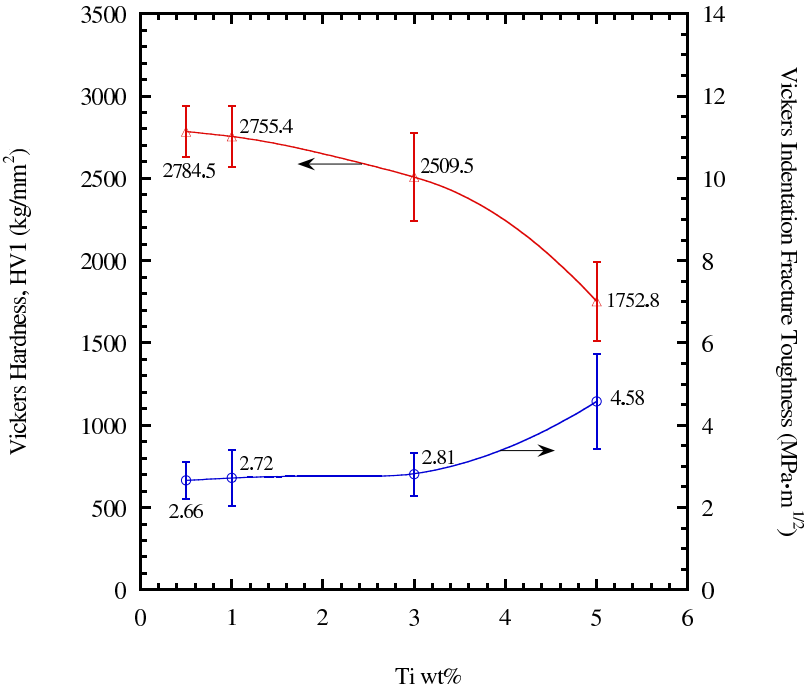

Figure 114: Vickers hardness and indentation fracture toughness plots for all 1% carbon, 32 nm TiO_2 samples sintered at 2260°C and post-HIPed

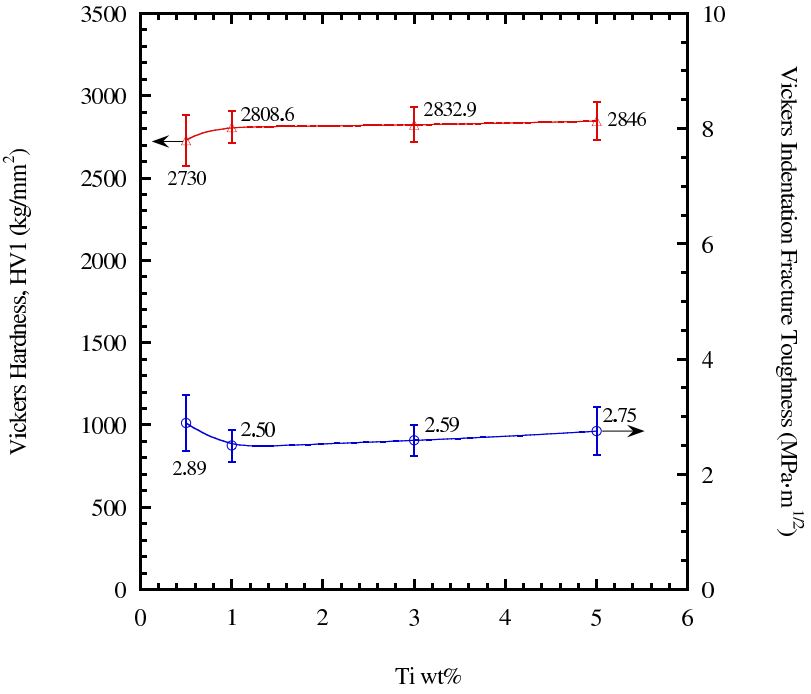

Figure 115: Vickers hardness and indentation fracture toughness plots for all 3% carbon, 32 nm TiO_2 samples sintered at 2260°C and post-HIPed

As the sintering temperature was lowered to 2240°C, only the 3% carbon, 32 nm TiO_2 samples sintered and then HIPed to acceptable relative densities (for reference, see Figures 75 through 77). Consequently, Vickers hardness and indentation fracture toughness were only measured for the 3%C, 32 nm TiO_2 samples sintered at 2240°C. A plot of the HV1 hardness (in kg/mm^2) and indentation fracture toughness (in $MPa \cdot m^{1/2}$) for the 3% carbon, 32 nm TiO_2 samples sintered at 2240°C and post-HIPed is provided in Figure 116. These lower sintering temperature 32 nm TiO_2 samples exhibited the general trend of increasing hardness with increasing Ti content; however, the hardness values were substantially below those measured for the 3 wt% C, 32 nm TiO_2 samples sintered at 2260°C. For these lower sintering temperature 3 wt% C, 32 nm TiO_2 samples, the highest hardness value (2786.8 kg/mm^2) was measured for the composition containing 5 wt% Ti.

The fracture toughness of the 3 wt% C, 32 nm TiO_2 samples sintered at 2240°C decreased with increasing Ti content, which is the opposite trend observed for the 2260°C samples of the same composition. Overall, these lower sintering temperature 3 wt% C samples exhibited higher fracture toughness values than the 2260°C samples containing the same carbon content.

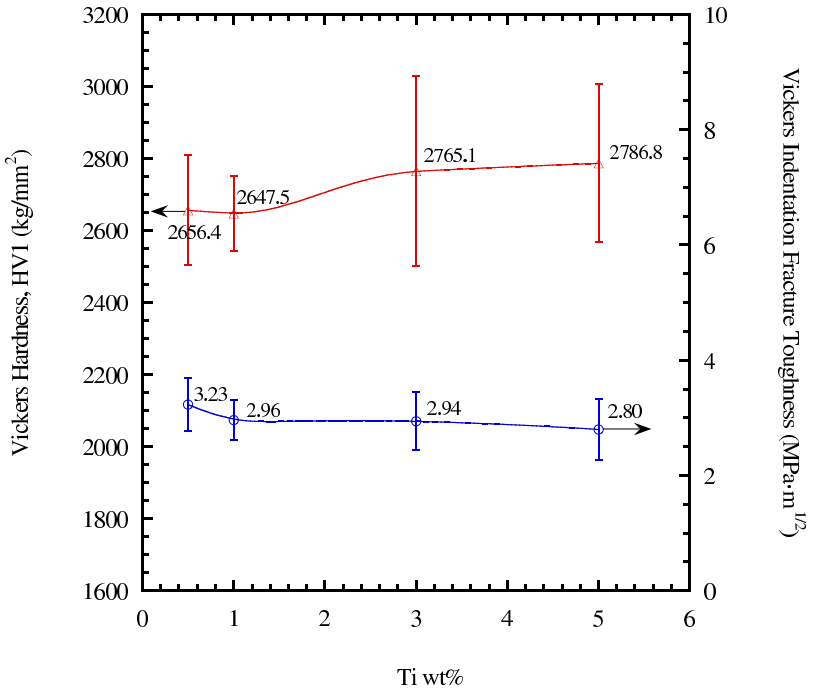

Figure 116: Vickers hardness and indentation fracture toughness plots for all 3% carbon, 32 nm TiO_2 samples sintered at 2240°C and post-HIPed

Three-dimensional surface plots of the HV1 hardness (in kg/mm^2) and indentation fracture toughness (in MPa·m$^{1/2}$) for all of the 32 nm TiO_2 samples sintered at 2260°C and post-HIPed are provided in Figures 117 through 118. The hardness surface plot for the 2260°C 32 nm TiO_2 samples indicates that the highest hardness range occurs in compositions with moderate to high Ti content (1-5 wt% Ti) and high C content (3 wt% C). The surface plot also indicates that the lowest hardness values are observed for compositions containing high Ti (5 wt% Ti) and intermediate C (1 wt% C) amounts.

The fracture toughness surface plot for the 2260°C 32 nm TiO_2 samples indicates that the composition with the highest fracture toughness contains high Ti (5 wt% Ti) and intermediate C (1 wt% C) amounts, which is also the composition range exhibiting the lowest hardness. The composition range exhibiting the lowest fracture toughness contains a moderate Ti concentration (1-3 wt% Ti) and high C concentration (3 wt% C).

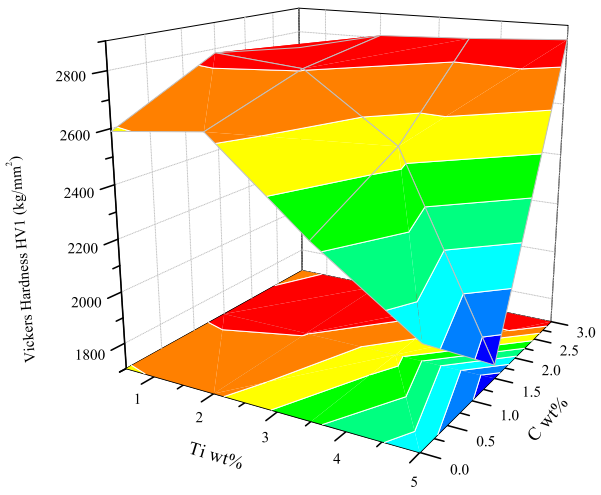

Figure 117: Vickers hardness for all 32 nm TiO_2 samples sintered at 2260°C and post-HIPed

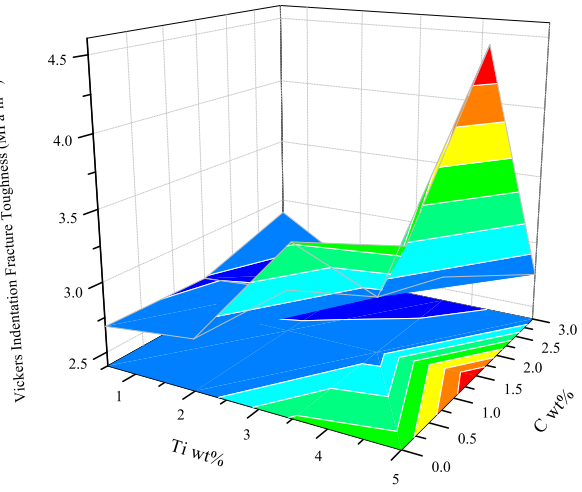

Figure 118: Vickers indentation fracture toughness for all 32 nm TiO_2 samples sintered at 2260°C and post-HIPed

Plots of the HV1 hardness (in kg/mm^2) and indentation fracture toughness (in MPa·m$^{1/2}$) for the 0, 1, and 3% carbon 0.9 μm TiO_2 samples sintered at 2260°C and post-HIPed are provided in Figures 119 through 121. The 0.9 μm TiO_2 samples exhibited hardness values that followed general trends very similar to those of the 32 nm TiO_2 samples sintered at the same temperature. The 0 wt% C samples displayed decreasing hardness values with increasing Ti content, while the 1 wt% C samples showed an initial increase in the Ti range of 0.5-1 wt% followed by steadily decreasing hardness values with continued increases in Ti content. The 3 wt% C samples followed the same trend as the 32 nm TiO_2 samples containing the same amount of carbon; hardness increased with increasing Ti content. The highest hardness value for these 2260°C 0.9 μm TiO_2 samples (2884.5 kg/mm^2) was measured for the composition containing 5 wt% Ti and 3 wt% C. It should be noted that half of the indents measured for the hardness testing of the 5 wt% Ti, 3 wt% C sample exceeded 3000 kg/mm^2 hardness values, while the other indents were significantly lower ($\sim$2500-2700 kg/mm^2). The low hardness indents were typically observed in areas of high graphite concentration within the microstructure. It should be noted that the average hardness is approaching that of the phase-pure, theoretically-dense, sintered and post-HIPed boron carbide produced in our lab.

The fracture toughness values of the 0, 1, and 3 wt% C, 0.9 μm TiO_2 samples each exhibited the same trend of initially decreasing in the Ti content range of 0.5-1 wt% and then increasing with further increases in Ti content. The highest fracture toughness for these 2260°C 0.9 μm TiO_2 samples (4.79 MPa·m$^{1/2}$) was measured for the composition containing 5 wt% Ti and 0 wt% C.

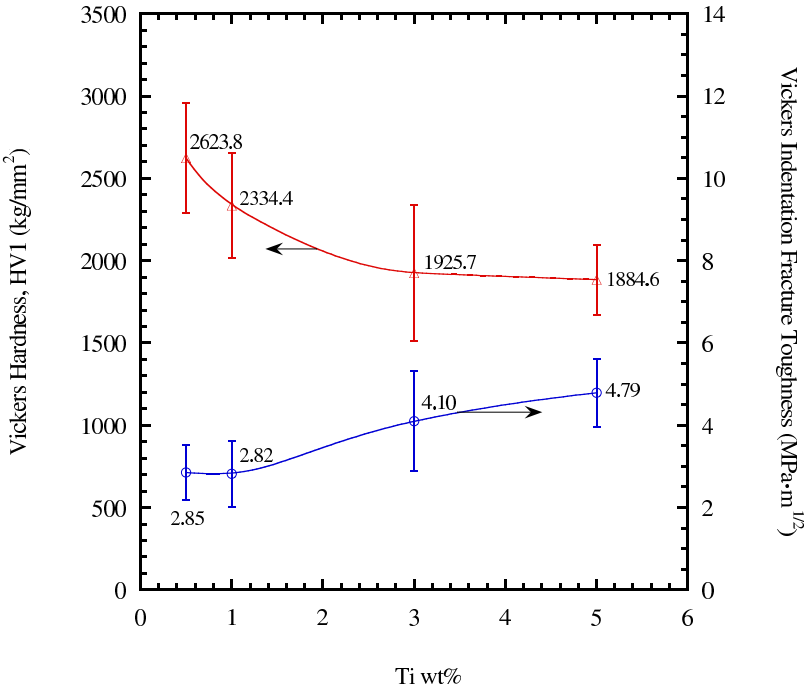

Figure 119: Vickers hardness and indentation fracture toughness plots for all 0 wt% carbon, 0.9 μm TiO_2 samples sintered at 2260°C and post-HIPed

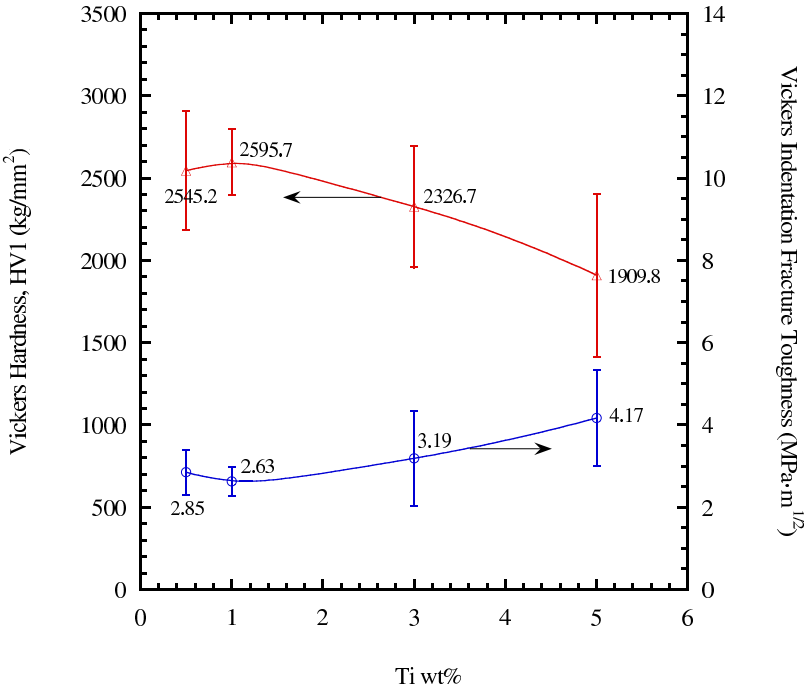

Figure 120: Vickers hardness and indentation fracture toughness plots for all 1 wt% carbon, 0.9 μm TiO_2 samples sintered at 2260°C and post-HIPed

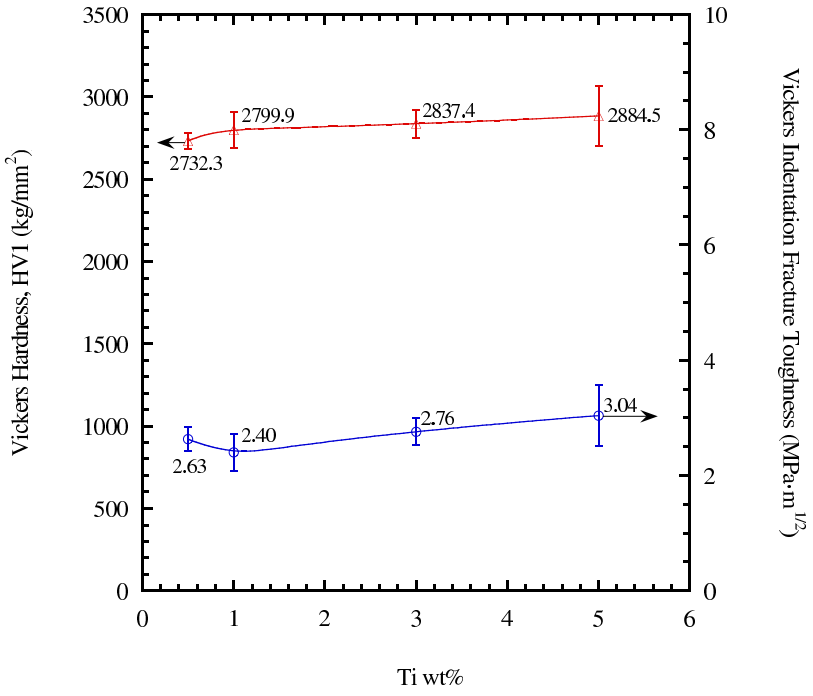

Figure 121: Vickers hardness and indentation fracture toughness plots for all 3 wt% carbon, 0.9 μm TiO_2 samples sintered at 2260°C and post-HIPed

As the sintering temperature was lowered to 2240°C, only the 3% carbon, 0.9 μm TiO_2 samples sintered and then HIPed to acceptable relative densities (for reference, see Figures 82 through 84). As a result, Vickers hardness and indentation fracture toughness were only measured for the 3%C, 0.9 μm TiO_2 samples sintered at 2240°C. A plot of the HV1 hardness (in kg/mm^2) and indentation fracture toughness (in MPa·m$^{1/2}$) for the 3% carbon, 0.9 μm TiO_2 samples sintered at 2240°C and post-HIPed is provided in Figure 122. The hardness values of the lower sintering temperature 0.9 μm TiO_2 samples exhibited an oscillatory trend in which the hardness alternately increased and decreased with incremental increases in Ti content. This behavior was not observed in the 32 nm TiO_2 specimens containing the same carbon content and sintered at the same temperature. The highest hardness value for these 3 wt% C, 0.9 μm TiO_2 samples (2830.9 kg/mm^2) was measured for the composition containing 1 wt% Ti.

The fracture toughness values for these samples exhibited the same oscillatory behavior with increasing Ti content; however, the fracture toughness generally followed an inverse relationship with the hardness. The fracture toughness values initially increased as the Ti content increased up to 3 wt% and then decreased as the Ti content further increased to 5 wt%. The highest fracture toughness value (4.02 MPa·m$^{1/2}$) was measured for the 3 wt% C, 0.9 μm TiO_2 sample containing 3 wt% Ti, which was also the composition exhibiting the lowest hardness.

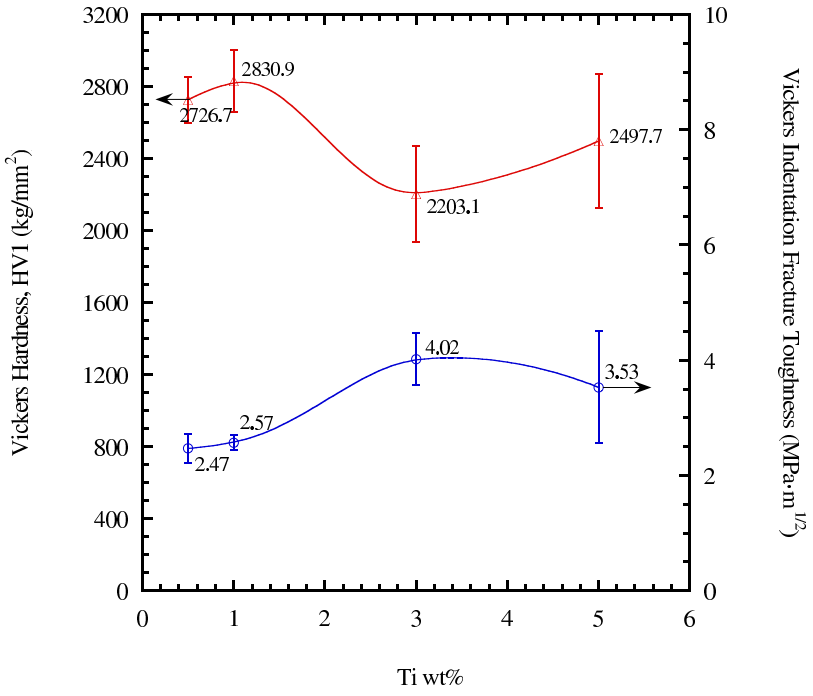

Figure 122: Vickers hardness and indentation fracture toughness plots for all 3 wt% carbon, 0.9 μm TiO_2 samples sintered at 2240°C and post-HIPed

Three-dimensional surface plots of the HV1 hardness (in kg/mm^2) and indentation fracture toughness (in $MPa \cdot m^{1/2}$) for all of the 0.9 μm TiO_2 samples sintered at 2260°C and post-HIPed are provided in Figures 123 through 124. The hardness surface plot for the 2260°C 0.9 μm TiO_2 samples indicates that the highest hardness values are observed in compositions containing moderate to high Ti concentrations (1-5 wt% Ti) and high C concentrations (3 wt% C). This optimal composition range is similar to that observed for the 32 nm TiO_2 samples sintered at the same temperature. The surface plot also indicates that the lowest hardness values are manifested in compositions containing high Ti (5 wt% Ti) and low C (0 wt% C) amounts. This is a shift from the 32 nm TiO_2 samples, which displayed the lowest hardness value at the same high Ti content but at an intermediate C concentration (1 wt% C).

The fracture toughness surface plot for the 2260°C 0.9 μm TiO_2 samples indicates that the composition with the highest fracture toughness contains high Ti (5 wt% Ti) and low C (0 wt% C) concentrations, which is also the composition exhibiting the lowest hardness. The surface plot suggests that the composition range manifesting the lowest fracture toughness contains a moderate Ti concentration (1-3 wt% Ti) and high C (3 wt% C) concentration.

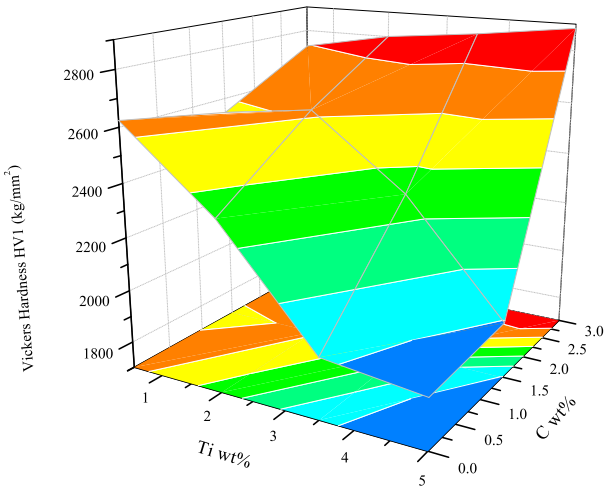

Figure 123: Vickers hardness for all 0.9 μm TiO_2 samples sintered at 2260°C and post-HIPed

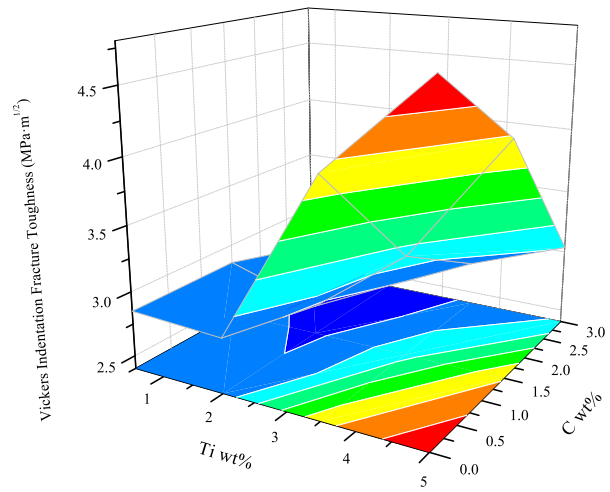

Figure 124: Vickers indentation fracture toughness for all 0.9 μm TiO_2 samples sintered at 2260°C and post-HIPed

CHAPTER V

DISCUSSION

Based on dilatometry analysis of the samples containing 32 nm and 0.9 μm TiO_2, the dramatic slowing of the sintering rate with added TiO_2 for compositions containing low (0 wt% C) to intermediate (1 wt% C) carbon concentrations could be the result of a previously undocumented liquid-phase assisted coarsening mechanism. At higher temperatures, this liquid-phase coarsening may have then transitioned into a solid-state sintering mechanism (upon the complete reduction of TiO_2 into TiB_2) that was insufficient to fully densify the specimens due to pre-coarsening of the particles at lower temperatures. TiO_2 melts at ~1840°C, which corresponds very closely to the onset temperature of the initial sintering rate deceleration for the 0 and 1 wt% carbon samples containing 5 wt% Ti in the form of TiO_2.

The onset of sintering rate deceleration was observed to shift toward lower temperatures with increasing concentrations of Ti, and this observation is indicative of an increasing coarsening effect with increasing volume fraction of liquid TiO_2 progressing through the microstructure. The increasing liquid volume fraction with increasing TiO_2 content could facilitate surface diffusion or the preferential dissolution of sufficiently small boron carbide particles and provide a transport medium for the redeposition of this dissolved material onto the higher energy concave surfaces of the necks between partially sintered particles, thereby dramatically reducing the overall densification rate and lowering the terminal relative density of the specimen. Dilatometry analysis indicated that the 32 nm TiO_2 specimens containing 0 wt% C exhibited generally decreasing sintering rate deceleration onset temperatures of 1923, 1934, 1872, and 1869°C for the 0.5, 1, 3, and 5 wt% Ti compositions, respectively.

Additionally, the samples displayed decreasing end temperatures (2077, 2076, 2034, and 1962°C for the 0.5, 1, 3, and 5 wt% Ti samples, respectively) for the deceleration behavior with increasing amounts of added TiO_2, indicating that the proposed coarsening process occurred more quickly with increasing liquid volume.

The 0.9 μm TiO_2 samples containing 0 wt% C displayed deceleration onset temperatures of 1924, 1930, 1910, and 1884°C for the 0.5, 1, 3, and 5 wt% Ti compositions, respectively. The same decrease in the end temperature of the sintering rate deceleration noted for the 32 nm TiO_2 samples was observed for the 0.9 μm TiO_2 specimens; end temperatures of 2066, 2076, 2009, and 1991°C were detected for the 0.5, 1, 3, and 5 wt% Ti samples, respectively. The slightly lower deceleration onset temperatures noted for the higher Ti content 32 nm TiO_2 samples could be the result of slight melting point depression resulting from the higher surface energy of the nano-sized particles. The decrease in the end temperatures for sintering rate deceleration for both the 32 nm and 0.9 μm TiO_2 sources implies that sample contraction began re-accelerating at reduced temperatures with increasing Ti content.

This phenomenon suggests that the liquid within these samples may have permitted the liquid-phase sintering of the already-coarsened boron carbide particles at elevated temperatures approaching 2000°C by allowing some particle rearrangement to occur. In order to illustrate the phenomena discussed above, the previously discussed dilatometry dimension change rate plot for the 0.9 μm TiO_2 samples containing 0 wt% C and sintered at 2300°C is reprinted in Figure 125.

The dilatometry data show decreases in overall sintering contraction and associated reductions in relative density with increasing Ti content. Intuitively, this agrees with the proposed coarsening mechanism, whereby samples containing more liquid incurred greater coarsening and thus exhibited reduced sintering shrinkage. The decrease in sintered and post-HIPed densities as well as Vickers hardness with increasing

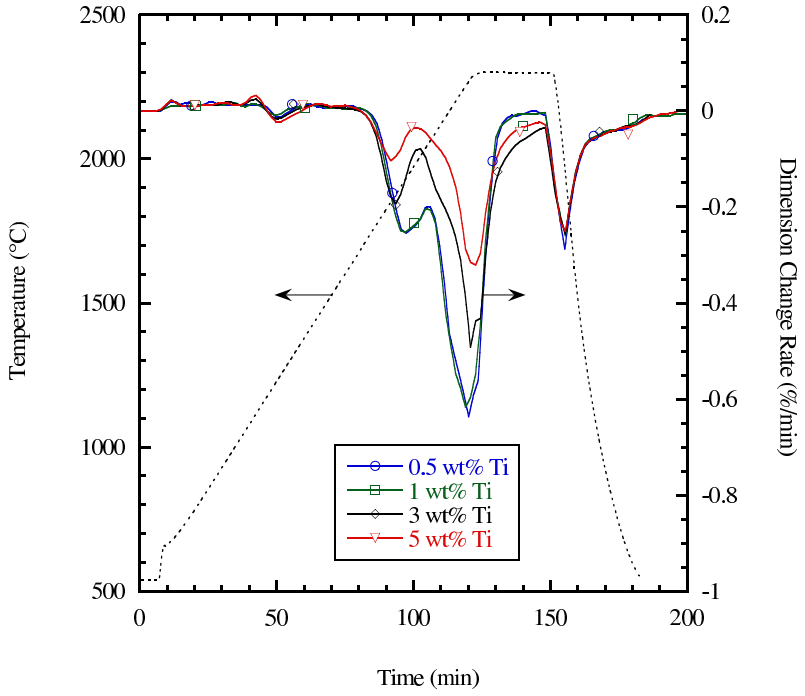

Figure 125: Dilatometry dimension change rate plot for all 0 wt% carbon, 0.9 μm TiO_2 samples sintered at 2300°C

TiO_2 content for the larger disks produced from the 32 nm and 0.9 μm TiO_2 compositions containing 0 wt% C support this conclusion.

It should also be noted that these results initially appear to disagree with the conclusions of Levin *et al.*, who stated that large quantities of TiO_2 enhanced the sintering of boron carbide at a sintering temperature of ~2160°C [48]. For this current study, the lower sintering temperature examined during dilatometry (2200°C) and the lower temperature explored during the larger disk sintering parametric study (2240°C) yielded very low relative densities in the range of 61-77% and 87-92%, respectively. However, these discrepancies between the work of Levin *et al.* (in which a low sintering temperature produced densities as high as ~95%) and the current study (in which a higher sintering temperature produced lower densities) may be the result of differences in experimental procedure that affected the preferred sintering path. Levin *et al.* researched the addition of large amounts of TiO_2 (5-40 wt%) to boron carbide powders and observed greater sintered relative densities with increasing TiO_2 addition. It

should be noted that 5 to 40 wt% TiO_2 corresponds to 3.01 to 28.21 vol% solid TiO_2 in the mixture, respectively, assuming the TiO_2 crystal structure (and therefore the density) is that corresponding to rutile, which is the polytype stable at high temperatures. According to published literature, the estimated volume fraction of second-phase liquid required for liquid-phase sintering is approximately 35 vol% [13]. In the work of Levin, the ∼28 vol% TiO_2 within the mixture would have substantially increased with the associated volumetric expansion occurring upon melting, yielding a suitable volume for liquid-phase sintering, which could occur at lower temperatures (i.e., 2160°C). The maximum concentration of TiO_2 in the compositions prepared for this study was 8.08 wt%, which corresponds to 4.93 vol%. This lower additive amount may have produced a hybrid combination of liquid-phase and solid-state sintering, which required higher temperatures to compensate for the insufficient liquid volume necessary for true liquid-phase sintering. The large difference in the range of added TiO_2 amounts between this current study and the work of Levin *et al.* explains the disagreement on the effect of TiO_2 concentration on the sintering behavior of boron carbide.

Despite the differences in the observed effect of TiO_2 additions, these results do confirm the findings of Levin *et al.* that increasing quantities of TiO_2 addition result in the formation of increasing amounts of TiB_2 upon sintering at high temperatures. Both Levin *et al.* and Kakazey *et al.* investigated the formation of TiB_2 via the borothermal reduction of TiO_2, where boron carbide was used as the boron source. Kakazey *et al.* proposed the following reaction [50]:

$$B_4C + 5TiO_2 \rightarrow 5TiB_2 + 4CO_{(g)} + 6BO_{(g)} \tag{34}$$

In experimentation, Kakazey *et al.* observed that the reaction did not produce TiB_2 until temperatures approached 1700°C. Additionally, Kakazey cited the formation of the Ti_2O_3 suboxide of TiO_2, indicating the gradual reduction of TiO_2 to form

Table 17: Melting Temperatures of Various Ti-O Compounds [73][74]

Compound	Melting Temperature (°C)
TiO_2	1840±10
Ti_4O_7	1687
Ti_3O_5	1800
Ti_2O_3	2130
TiO	1700

increasingly Ti-rich compounds. The formation of lower melting temperature sub-oxides of TiO_2 and potentially sluggish reaction kinetics with respect to the heating rate of the furnace for this current study (15°C/min) could explain the presence of the coarsening-inducing liquid at temperatures above 1700°C. In order to illustrate the effect of the continual reduction of TiO_2, a list of melting temperatures of various Ti-O compounds in order of decreasing oxygen content are provided in Table 17.

The samples in this study containing added carbon in the form of phenolic resin as well as TiO_2 exhibited dramatically different sintering behavior than the compositions to which only TiO_2 had been added. For samples containing both TiO_2 and added carbon, the reaction may follow the equation proposed by Skorokhod *et al.* [46]:

$$B_4C + 2TiO_2 + 3C \rightarrow 2TiB_2 + 4CO_{(g)} \tag{35}$$

Based on calculations by Koc *et al.*, the equilibrium temperature (T_{eq}) of this reaction is 991°C [75]. Levin observed the evolution of gaseous species (indicated by an increase in pressure) during heating of TiO_2 and B_4C powders after protracted heating in a vacuum furnace at 1300°C [48]. It should be noted that Levin did not indicate the free carbon contents of the boron carbide powder used in the experiment, implying that some carbon not originating from boron carbide may have assisted in the reduction of the added TiO_2.

Reaction progression analysis was performed on several compositions examined in this study via XRD of loose powder samples (5 wt% Ti, 0.9 μm TiO_2 compositions containing 0 and 3 wt% C) that had been heated at 50°C/min to 1000, 1300, 1600, and 1900°C in flowing He, and then immediately cooled at 100°C/min to prevent further reaction. It should be noted that these studies were performed on loose powder samples open to the furnace environment of flowing He gas. Given the reaction proposed by Kakazey *et al.*, the BO and CO gas reaction products imply that the progression of these reactions is greatly dependent upon the degree to which gas is liberated from the system. A compacted ceramic preform would present a tortuous pore network that could slow gas escape and delay reaction to higher temperatures.

The XRD traces of these samples in Figures 35 and 36 indicate that the 0 wt% C samples showed decreasing residual graphite content with increasing temperature beyond 1300°C. Additionally, the 0 wt% C composition heat-treated at 1900°C displayed no residual carbon, implying that the graphite observed in the 1600°C sample was consumed via reaction at temperatures above 1600°C. This behavior was not observed for the 3 wt% C samples containing the same concentration of added TiO_2.

Relative measurements of particle size via XRD peak broadening measurements (i.e., FWHM measurements) can be used to illustrate the progressive conversion of TiO_2 into TiB_2. The XRD scan for the 0 wt% C samples heat-treated at 1000°C (Figure 35) exhibits substantial broadening (FWHM=0.653 °2θ) for the most intense peak of TiB_2, implying a small particle size. Assuming the continual reduction of TiO_2 particles would result in the continual increase in TiB_2 inclusion size, the XRD peaks of the formed TiB_2 should have continually decreased in width as the reduction reaction progressed until all of the TiO_2 was consumed. This behavior in the heat-treated samples is illustrated by the plots of the FWHM data in Figure 126.

Comparing the FWHM data from the XRD scans of the heat-treated 0 and 3 wt%

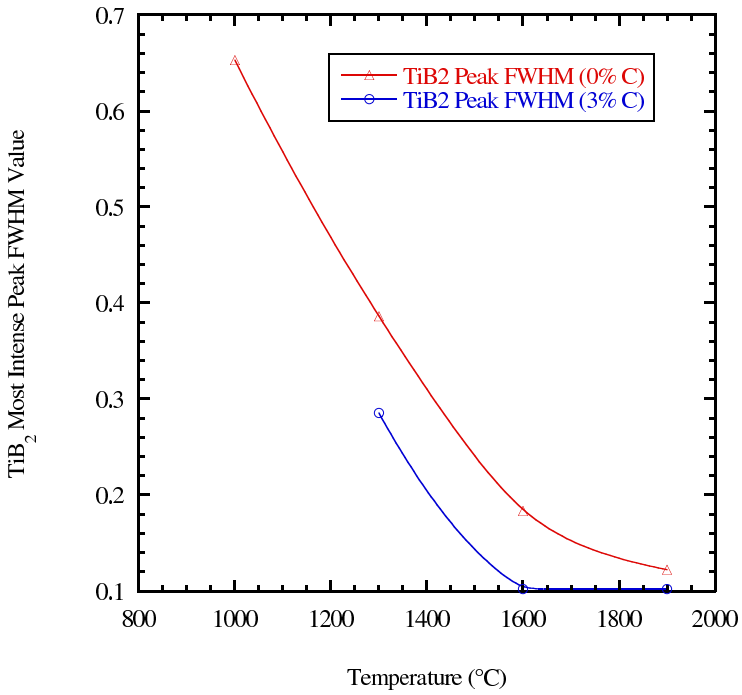

Figure 126: Plots of the full-width half-maximum (FWHM) values of the most intense peak of TiB_2 at 44.393 °2θ for the 0 and 3 wt% C powder samples of the 5 wt% Ti, 0.9 μm TiO_2 composition heated to 1000, 1300, 1600, and 1900°C.

C samples implies that residual TiO_2 may have still remained in the 0 wt% C composition heated to 1900°C. The same comparison indicates that the 3 wt% C sample may have completed the conversion of TiO_2 to TiB_2 prior to 1600°C. These observations support the conclusion that liquid TiO_2 existed at sufficiently high temperatures to facilitate coarsening inducing mass-transport in boron carbide. Additionally, the apparent completion of TiB_2 formation in the 3 wt% C specimen by 1600°C (i.e., below the melting temperature of TiO_2) is consistent with the substantially higher sintered densities observed in high carbon (3 wt% C) content compositions.

These results are further supported by previously published literature on the activity data for the elemental components boron carbide. According to Levin *et al.*, the activity of carbon in boron carbide decreases substantially with decreasing carbon content. Based upon this activity model, the activity of carbon in boron carbide decreases by ~97% as the composition shifts from stoichiometric boron carbide (B_4C) to boron-rich boron carbide ($B_{13}C_2$) [48]. The implication of this activity information is that carbothermal reduction reactions in boron carbide systems may proceed very

slowly if no excess free carbon is added. Taking the converse view indicates that the addition of free carbon, which has an activity equal to unity, would result in greatly improved reaction thermodynamics. This information appears to agree with the differences in behavior observed in the compositions containing various amounts of added carbon.

Dilatometry analysis of samples to which carbon had been added showed substantially higher sintering shrinkage with increasing carbon content. The 1 wt% C samples showed moderate improvement in the sintering shrinkage and sintered relative densities compared to that observed in the 0 wt% C samples. However, the sintered relative densities still decreased noticeably with increasing TiO_2 content, indicating that high Ti content compositions contained insufficient carbon content required to reduce the added TiO_2 entirely before melting-induced coarsening. The compositions containing 3 wt% C did not exhibit the substantial sintering rate deceleration observed in the temperature range of ~1860-2090°C for the lower carbon concentration samples, and also exhibited noticeably higher sintered relative densities. These differences suggest that 3 wt% carbon was a sufficient concentration for the effective carbothermal reduction of TiO_2 throughout the specimen. As a result, boron carbide particle coarsening was minimized in the early stages of sintering, permitting enhanced solid-state sintering and densification. The reduced overall porosity in these higher relative density 3 wt% C samples permitted post-HIPing to near theoretical densities. Based on stoichiometry calculations, all of the 32 nm and 0.9 μm TiO_2 compositions containing 3 wt% C should have contained excess carbon; compositions containing 1 wt% C should have only possessed excess carbon for lower (0.5 and 1 wt% Ti) Ti concentrations. These observations support the conclusion that the effective sintering of B_4C-TiO_2 mixtures requires sufficient carbon to reduce the TiO_2 species at lower temperatures prior to incipient melting of the oxide.

The highest sintered relative densities were obtained with compositions containing high carbon concentrations. These samples followed a solid-state process. The proposed steps in this sintering process are the following:

1. Carbothermal reduction of TiO_2 prior to the melting of TiO_2.
2. Solid-state sintering upon formation of intergranular TiB_2 inclusions.

The highest post-HIPed relative densities for these samples occurred at a sintering temperature of 2260°C, which was well below the eutectic temperature of the B_4C-TiB_2 system. This temperature being below the eutectic temperature implies that sintering occurred via non-liquid dominated mass transport mechanisms (i.e., evaporation/condensation and vacancy diffusion). Interestingly, a different mechanism was observed for samples containing no added carbon that were sintered at a higher temperature. For samples containing 0 wt% C, the observed increase in density as the Ti content increased to 3 and 5 wt% for samples sintered at the highest temperature in the study (2300°C) could be the result of a three-stage sintering process. For compositions containing a sufficiently high volume percentage of second-phase additive, this three-stage sintering process would involve the following:

1. Initial liquid-phase coarsening due to melting and redistribution of liquid TiO_2.
2. Solid-state sintering upon formation of intergranular TiB_2 inclusions.
3. Liquid-phase sintering due to formation of TiB_2-rich liquid at eutectic temperature.

The high-temperature eutectic liquid-phase sintering mechanism (i.e., #3 in the above list) is evidenced by the microstructural evolution of the samples at higher temperatures. Based on analysis of optical micrographs of the sample microstructures (Figures 97 and 98), clustering of graphite and TiB_2 was observed to increase

with increasing sintering temperature and increasing TiO_2 content. The formation of nodular graphitic regions with increasing sintering temperature could be explained by the increasing vacancy concentration with increasing temperature as well as the concomitant melting of TiB_2 beginning at ~2280°C (literature cites the eutectic temperature at ~2272-2310°C) [69][61]. The melting of TiB_2 is evidenced by the increase in the aspect ratios of TiB_2 inclusions and their preferential locations along boron carbide grain boundaries. The formation of a small fraction of intergranular TiB_2-rich liquid would significantly increase grain growth and simultaneously provide a kinetically favorable transport medium for the redistribution of pores and graphite located at the grain boundary to the energetically favorable triple point locations between grains. Based on comparison of the microstructures, the high Ti (5 wt% Ti) and low C (0 wt% C) content compositions sintered at 2300°C show a higher degree of pore and graphite inclusion coalescence as well as fewer small intra-granular pores (i.e., pores enveloped during grain growth) near grain boundaries containing TiB_2. The ternary Ti-B-C phase diagram produced by Gusev indicates that boron carbide dissolves 1.5 mol% TiB_2 at the eutectic temperature [69]. Assuming no loss of Ti during the sintering process, the molar percentages of TiB_2 formed for the 0.5, 1, 3, and 5 wt% Ti compositions in the current study amount to 0.58, 1.15, 3.45, and 5.73 mol%, respectively. Accordingly, the additional vacancies produced within the boron carbide due to this dissolution would accelerate the kinetics of diffusion-controlled processes at the grain boundaries. It should be noted that this same phenomenon of dissolution-initiated vacancy formation may explain the increase in graphite clustering with increasing Ti content observed in samples sintered at temperatures below the eutectic temperature. Higher Ti contents produced a more widely distributed quantity of TiB_2, resulting in increased diffusion rates along the grain boundaries with increasing Ti content.

For sintering temperatures sufficiently below the eutectic temperature, the microstructural features appear to be also controlled by the additive type. Interestingly, based on comparison of micrographs produced from specimens sintered at 2260°C (Figures 89 to 94), the 0.9 μm TiO_2 samples exhibited TiB_2 inclusions and graphite regions that were smaller and more finely distributed across the polished microstructure than identical compositions containing 32 nm TiO_2 as the Ti source. This result is seemingly non-intuitive, because one would anticipate smaller TiO_2 particles to produce similarly fine TiB_2 particles upon reaction with boron carbide. This observation could be explained by a larger degree of agglomeration in the nanoscale TiO_2 powder during batch preparation for spray drying; these larger TiO_2 agglomerates could have presented more localized reaction regions that did not migrate significantly through the microstructure prior to reaction with the surrounding carbon or boron carbide.

The grain size of the boron carbide microstructures following sintering and HIPing was also influenced by the additive amount. The d_{50} grain size data for the 32 nm and 0.9 μm TiO_2 samples appears to be dependent on multiple interrelated variables, such as the amount of residual porosity, TiB_2 content, as well as carbon content. Porosity serves as a hindrance to grain growth, and TiB_2 and graphite inclusions also impede grain boundary motion. However, porosity is an undesirable entity in the microstructure. Consequently, the finest microstructures that also displayed positive mechanical properties were generally those containing high amounts of TiB_2 and graphite. It should be noted that the smallest median grain size measured in this study (2.86 μm) corresponds to the sample yielding the highest hardness.

In addition to influencing the sintering characteristics of boron carbide, TiO_2 additions also altered the chemical composition of the boron carbide. Energy dispersive x-ray spectroscopy (EDS) indicated the presence of both stoichiometric and boron-rich boron carbide analyzed during scanning electron microscopy. These findings are in agreement with the previously cited work of Levin *et al.*, who proposed that the

reaction between stoichiometric boron carbide and an oxygen-containing Ti source would result in the formation of boron-rich boron carbide [48]. X-ray diffraction of the samples sintered at 2260°C and post-HIPed confirmed the presence of boron-rich boron carbide ($B_{13}C_2$ and $B_{13.43}C_{1.71}$). According to Suematsu *et al.*, boron carbide exhibits increasing electrical conductivity with increasing boron content; as the composition shifts from stoichiometric boron carbide (B_4C) to more boron-rich boron carbide ($B_{13}C_2$), the electrical conductivity increases from $\sim 5 \times 10^2$ $\frac{1}{\Omega m}$ to $\sim 8 \times 10^3$ $\frac{1}{\Omega m}$, respectively, which represents an increase by over an order of magnitude [76]. The higher conductivity of boron-rich boron carbide suggests that the samples produced from this work may be machined via electrical discharge machining (EDM) techniques.

The change in microstructure with additive content significantly influenced the mechanical properties of the post-HIPed samples. Mechanical characterization was performed almost entirely on the samples sintered at 2260°C, because this sintering temperature resulted in the highest post-HIPed densities. For the compositions examined in this study containing 0 and 1 wt% C, hardness generally decreased with increasing TiO_2 content. This observation is in agreement with the dilatometry results and sintered/post-HIPed density data, which indicate substantial reduction in sintering contraction/densification with higher Ti content; one would expect a higher porosity sample to yield lower hardness values. These same samples exhibited increasing fracture toughness with increasing Ti content; the porosity resulting from increasing Ti content may have reduced crack propagation by blunting the crack tips emanating from the indent corners. The highest Vickers hardness values were measured for compositions containing 3 wt% C, and these high carbon content samples also displayed the highest sintered and post-HIPed relative densities, supporting the conclusion that porosity is the primary determinant of hardness. These samples also exhibited increasing fracture toughness with increasing Ti content. This observation

could be the result of increasing numbers of TiB_2 inclusions as well as marginal increases in graphite clustering with increasing Ti content as mentioned above. The TiB_2 inclusions served to deflect cracks and their occasional location amid graphite regions served to arrest cracks via crack tip blunting due to the weak interface between the boron carbide and soft graphite. The confluence of these phenomena resulted in the optimal sample (i.e., the 0.9 μm TiO_2, 5 wt% Ti, 3 wt% C composition sintered at 2260°C) from this study having both a high hardness (2884.5 kg/mm^2) as well as a high fracture toughness (3.04 MPa·m$^{1/2}$). It should be noted that the hardness value is approaching that of phase-pure and theoretically-dense boron carbide (2939 kg/mm^2), while the fracture toughness value is notably improved over that of the phase-pure sample (2.42 MPa·m$^{1/2}$), or a 25.6% improvement.

CHAPTER VI

CONCLUSION

The primary objective of this research was to study the effect titanium and carbon additives on the sintering and mechanical properties of inexpensive B_4C powders. Dilatometric measurements of the *in-situ* sample contraction during sintering permitted the investigation of the effects of small amounts of TiO_2 and carbon additives on the sintering behavior of boron carbide. These findings suggested the previously unexplored phenomenon of liquid-phase assisted coarsening in this system. Samples containing no added carbon showed clear indications of reduced sintering shrinkage with increasing amounts of added TiO_2. The introduction of carbon greatly enhanced the sintering of the compositions containing TiO_2 powders by providing a lower-temperature reduction reaction for the formation of TiB_2, which obviated the high-temperature melting of TiO_2. The addition of increasing carbon amounts up to 3 wt% greatly enhanced overall sintering contraction and permitted post-HIPing to near theoretical density. Vickers hardness measurements indicated that samples containing high concentrations of carbon also manifested the highest hardness values. The highest microindentation fracture toughness values were measured for specimens with high porosity (i.e., low relative densities). However, high carbon content compositions displayed the unique trend of increasing hardness as well as fracture toughness with increasing Ti content.

The introduction of these second phases caused a substantial increase in hardness; the highest hardness specimen yielded a hardness value (2884.5 kg/mm^2) approaching that of phase-pure and theoretically-dense boron carbide (2939 kg/mm^2). Additionally, the same high-hardness composition exhibited a noticeably higher fracture

toughness (3.04 MPa·$m^{1/2}$) compared to phase-pure boron carbide (2.42 MPa·$m^{1/2}$), representing a 25.6% improvement. A potential consequence of this study would be the development of a superior armor material that is sufficiently affordable, allowing it to be incorporated into the general soldier's armor chassis.

REFERENCES

[1] H. Lee, R. F. Speyer, and W. S. Hackenberger, "Sintering of Boron Carbide Heat-Treated with Hydrogen," *J. Am. Ceram. Soc.*, **85**[8] 2131-2133 (2002).

[2] R. F. Speyer, N. Cho, and Z. Bao, "Density- and Hardness Optimized Pressureless Sintered and Post-HIPed B_4C," *J. Mat. Res.,* **20**[8] 2110-2116 (2005).

[3] R. R. Rigdway, "Boron Carbide: A New Crystalline Abrasive and Wear-Resisting Product," *Trans. Am. Electrochem. Soc.*, **66** 117-133 (1934).

[4] F. Theveonot, "Boron Carbide - A Comprehensive Review," *J. Euro. Ceram. Soc.,* **6** [4] 205-225 (1990).

[5] H. O. Pierson, *Handbook of Refractory Carbides and Nitrides,* John Wiley & Sons, New York, 1996.

[6] A. W. Weimer, *Carbide, Nitride and Boride Materials Synthesis and Processing*, Chapman and Hall, New York, 1997.

[7] P. Rentzepis, D. White and P. N. Walsh, "Heat of Formation of $B_2O_{2(g)}$," *J. Phys. Chem.*, **64**, 1784 (1960).

[8] D. Emin, "Structure and Single-Phase Regime of Boron Carbides," *Phys. Rev. B*, **38** 6041-6055 (1988).

[9] T. L. Aselage and R. G. Tissot, "Lattice Constants of Boron Carbide," *J. Am. Ceram. Soc.*, **75**[8] 2207-2212 (1992).

[10] K. Niihara, A. Nakahira, and T. Hirai, "The Effect of Stoichiometry on Mechanical Properties of Boron Carbide," *J. Am. Ceram. Soc.,* **67** C13-C14 (1984).

[11] J. S. Reed, *Principles of Ceramic Processing,* John Wiley & Sons, New York, 1995.

[12] S.-J. L. Kang, *Sintering*, Elsevier Butterworth-Heinemann, Boston, 2005.

[13] R. M. German, *Sintering Theory and Practice*, John Wiley & Sons, New York, 1996.

[14] W. D. Kingery, H. K. Bowen, and D. R. Uhlmann, *Introduction to Ceramics*, 2nd Edition, John Wiley & Sons, New York, 1976.

[15] H. S. Cannon and F. V. Lenel, "Some Observations on the Mechanism of Liquid Phase Sintering," in *Plansee Proceedings*, 1952, F. Benesovsky (Ed.), Metalwerk Plansee, Reutte, p. 106 (1953).

[16] W. D. Kingery, "Sintering in the Presence of a Liquid Phase," in *Ceramic Fabrication Processes*, 2nd Edition, MIT Press and John Wiley & Sons, New York, 1960.

[17] S.-M. Lee and S.-J. L. Kang, "Evaluation of Densification Mechanisms of Liquid Phase Sintering," *Z. Metallkd.*, **92** 669-674 (2001).

[18] O. J. Kwon and and D. N. Yoon, "The Liquid Phase Sintering of W-Ni," *Sintering Processes (Proc. 5th Inter. Conf. on Sintering and Related Phenomena)*, G. C. Kuczynski(ed.), Plenum Press, New York, 208-218 (1980).

[19] O. J. Kwon and and D. N. Yoon, "Closure of Isolated Pores in Liquid Phase Sintering of W-Ni," *Inter. J. Powder Metall. Powder Tech.*, **17** 127-133 (1981).

[20] Y.-S. Yoo, J.-J. Kim and D.-Y. Kim, "Effect of Heating Rate on the Microstructural Evolution During Sintering of $BaTiO_3$ Ceramics," *J. Am. Ceram. Soc.*, **70** C322-C324 (1987).

[21] H.-H. Park, O.-J. Kwon and D. N. Yoon, "The Critical Grain Size for Liquid Flow Into Pores During Liquid Phase Sintering," *Metall. Trans. A*, **17A** 1915-1919 (1986).

[22] H.-H. Park, S.-J. Cho and D. N. Yoon, "Pore Filling Process in Liquid Phase Sintering," *Metall. Trans. A*, **15A** 1075-1080 (1984).

[23] S.-J. L. Kang, K.-H. Kim, D. N. Yoon, "Densification and Shrinkage During Liquid Phase Sintering," *J. Am. Ceram. Soc.*, **74** 425-427 (1991).

[24] J. K. Park, S.-J. L. Kang, K. Y. Eun and D. Y. Yoon, "The Microstructural Change During Liquid Phase Sintering," *Metall. Trans. A*, **20A** 837-845 (1989).

[25] J.-C. Baung, Y.-G. Choi, E.-S. Kang, Y.-K Baek, S.-W. Jung, and S.-J. L. Kang, "Effects of Sintering Atmosphere and Ni Content on the Liquid Phase Sintering of TiB_2-Ni," *J. Kor. Ceram. Soc.*, **38** 207-211 (2001).

[26] R. Angers and M. Beauvy, "Hot Pressing of Boron Carbide," *Ceram. Int.*, **10**[2] 49-55 (1984).

[27] T. Vasilos and S. K. Dutta, "Low Temperature Hot Pressing of Boron Carbide and its Properties," *Am. Ceram. Soc. Bull.*, **53**[5] 453-454 (1974).

[28] S. L. Dole, S. Prochazka and R. H. Doremus, "Microstructural Coarsening During Sintering of Boron Carbide," *J. Am. Ceram. Soc.*, **72**[6] 958-966 (1989).

[29] S. L. Dole and S. Prochazka, "Densification and Microstructure Development in Boron Carbide," *Ceram. Eng. Sci. Proc.*, **6**[7-8] 1151-1160 (1985).

[30] S. Prochazka, S. L. Dole and C. I. Hejna, "Abnormal Grain Growth and Microcracking in Boron Carbide," *J. Am. Ceram. Soc.*, **68**[9] c235-c236 (1985).

[31] K. Schwetz and G. Vogt, "Process for the Production of Dense Sintered Articles of Boron Carbide," *U.S. Patent 4,195,066,* (1980).

[32] H. Lee and R. F. Speyer, "Pressureless Sintering of Boron Carbide," *J. Am. Ceram. Soc.*, **86**[9] 1468-1473 (2003).

[33] J. Beauvy, "System B-C, Solid State Phase Equilibria," *J. Less-Common Mat.*, **90** 169-175 (1983).

[34] N. Cho, Georgia Institute of Technology, Atlanta, GA, private communication, May 2008.

[35] L. R. Vargas, Georgia Institute of Technology, Atlanta, GA, private communication, May 2008.

[36] Y. Kanno, K. Kawase and K. Nakano, "Additive Effect of Sintering Boron Carbide," *J. Ceram. Soc. Jap.*, **95**[11] 1137-1140 (1987).

[37] L. B. Ekbom and C. O. Amundin, "The Microstructure of Hot-Press Sintered Boron Carbide of Various Compositions," *Proc. 10th Int. Conf. on Science of Ceramics*, H. Hausner(ed.), Deutsche Keramische Gesellschaft, 303 (1980).

[38] R. Telle. and G. Petzow, "Structure and Properties of Si-Doped Boron Carbide," *High Tech Ceramics, Proc. 6th Int. Conf. on High Technology Ceramics, Milan*, P. Vincenzini(ed.), Elsevier, Amsterdam, 961 (1987).

[39] R. Lorcher, K. Strecker, R. Riedel, R. Telle and R. Petzow, "Microstructure and Oxidation Behaviour of Boron Carbide Based Ceramics Doped with Polysilane Derived Silicon Carbide," *Diffusion and Defect Data - Solid State Data, Part B (Solid State Phenomena)*, **B8-9** 479-491 (1990).

[40] G. Sasaki, T. Suga, T. Yanai, K. Suganuma and K. Niihara, " Microstructure of B_4C/TiB_2 Composite Fabricated by Reaction Sintering of B_4C and TiC," *Journal of the Ceramic Society of Japan*, **102**[4] 321-325 (1994).

[41] R. Telle, G. Petzow, J. Alderborn and K. Weiss, *Proc. 9th Int. Symp. on Boron, Borides and Related Compounds*, H. Wertheim(ed.), Duisburg, 453 (1987).

[42] V. V. Skorokhod and V. D. Krstic, "Processing, Microstructure and Mechanical Properties of B_4C-TiB_2 Particulate Sintered Composites: Fracture and Mechanical Properties," *Por. Metall.*, **9-10** 96-107 (2000).

[43] L. S. Sigl and H.-J. Kleebe, "Microcracking in B_4C-TiB_2 Composites," *Journal of the American Ceramic Society*, **78**[9] 2374-2380 (1995).

[44] G. Wen, S. B. Li, B. S. Zhang and Z. X. Guo, "Processing of *In-Situ* Toughened B-W-C Composites By Reaction Hot Pressing of B_4C and WC," *Scripta Mater.*, **43** 853-857 (2000).

[45] R. Telle and G. Petzow, "Strengthening and Toughening of Boride and Carbide Hard Material Composites," *Materials Science and Engineering A (Structural Materials: Properties, Microstructure and Processing)*, **A105-106** 97-104 (1988).

[46] V. Skorokhod, M. D. Vlasjic and V. D. Krstic, "Mechanical Properties of Pressureless Sintered Boron Carbide Containing TiB_2 Phase," *Journal of Materials Science Letters*, **15**[15] 1337-1339 (1996).

[47] V. V. Skorokhod and V. D. Krstic, "Processing, Microstructure and Mechanical Properties of B_4C-TiB_2 Particulate Sintered Composites. I. Pressureless Sintering and Microstructure Evolution," *Por. Metall.*, **7-8** 111-121 (2000).

[48] L. Levin, N. Frage and M. P. Daniel, "The Effect of Ti and TiO_2 Additions on the Pressureless Sintering of B_4C," *Metall. Mater. Trans.*, **A30A**[12] 3201-3210 (1999).

[49] A. Goldstein, Y. Yeshurun and A. Goldenberg, "B_4C/Metal Boride Composites Derived from B_4C/Metal Oxide Mixtures," *J. Eur. Ceram. Soc.*, **27** 695-700 (2007).

[50] M. Kakazey, M. Vlasova, J.G. Gonzalez-Rodriguez, M. Dominguez-Patino, and R. Leder, "X-ray and EPR Study of Reactions Between B_4C and TiO_2," *Mat. Sci. & Eng. A*, **418** 111-114 (2006).

[51] D. D. Radev and Z. Zakhariev, "Structural and Mechanical Properties of Activated Sintered Boron Carbide-Based Materials," *J. Solid State Chem.*, **137** 1-5 (1998).

[52] K. I. Portnoy, G. V. Samsonov, K. I. Frolova and J. Prikladnoj, *Himii*, **33** 577 (1960).

[53] A. Lipp and M. Roder, "On the Subject of Aluminum Containing Boron Carbides," *Z. Anorg. Allg. Chem.*, **343** 1 (1966).

[54] D. D. Radev, B. Mihailova and L. Konstantinov, "Raman Spectroscopy Study of Metal-Containing Boron Carbide-Based Ceramics," *Solid State Sciences*, **4** 37-41 (2002).

[55] G. Fanchini, J. W. McCauley and M. Chhowalla, "Behavior of Disordered Boron Carbide Under Stress," *Phys. Rev. Letters*, **97** 035502 (2006).

[56] M. Chen, J. W. McCauley and K. J. Hemker, "Shock-Induced Localized Amorphization in Boron Carbide," *Science*, **299** 1563-1566 (2003).

[57] G. Fanchini, D. E. Niesz, R. A. Haber, J. W. McCauley and M. Chhowalla, "Root Causes of the Performance of Boron Carbide Under Stress," *Cer. Eng. and Sci. Pro.*, **27** 179-188 (2006).

[58] C. H. Lee and C. H. Kim, "Pressureless Sintering and Related Reaction Phenomena of Al_2O_3-doped B_4C," *J. Mater. Sci.*, **27** [23] 6335-6340 (1992).

[59] R. G. Lange, Z. A. Munir and J. R. Holt, "Sintering Kinetics of Pure and Doped Boron Carbide," *Proc. 5th Int. Conf. on Sintering and Related Phenomena*, G. C. Kuczynski(ed.), Plenum Press, New York, 311 (1979).

[60] S. Yamada, K. Hirao, Y. Yamauchi and S. Kanzaki, "Densification Behaviour and Mechanical Properties of Pressureless-Sintered B_4C-CrB_2 Ceramics," *J. Mat. Sci.*, **37** 5007-5012 (2002).

[61] M. C. Schouler, M. Ducarroir, and C. Bernard, "Mise au point sur la topographie et les proprietes des systemes metal-carbone-azote (M-C-N) et metal-carbone-bore (M-C-B)," *Rev. Int. Hautes Temp. Refract. Fr.*, **20** 261-311 (1983).

[62] B. L. Grabchuk and P. S. Kislyi, "Sintering of Technical Boron Carbide," *Porosh. Metall.*, **7** 27-31 (1975).

[63] P. Rogl and H. Bitterman, "Ternary Metal Boron Carbides," *Int. J. Ref. Met. & Hard Met.*, **17** 27-32 (1999).

[64] Patent Rep. Bulgaria 73313, 30.01.(1986)

[65] Patent Rep. Bulgaria 49099, 19.09. (1989)

[66] R. G. Munro, "Material Properties of Titanium Diboride," *J. Res. Natl. Inst. Stand. Technol.*, **105** [5] 709-720 (2000).

[67] H. Holleck, "Material Selection for Hard Coatings," *Journal of Vacuum Science and Technology A*, **4** [6] 2661-2669 (1986).

[68] N. Frage, S. Hayun, S. Kalabukhov, and M. P. Dariel, "The Effect of Fe Addition on the Densification of B_4C Powder by Spark Plasma Sintering," *Powder Metallurgy and Metal Ceramics*, **46** [11-12] 533-538 (2007).

[69] A. I. Gusev, "Phase Diagram of the Ti-B-C System in the Temperature Range 300-3500 K," *Doklady Physical Chemistry*, **350** [1-3] 230-233 (1996).

[70] R. E. Taylor, H. Groot, "Thermophysical Properties of POCO Graphite," *High Temp. High Press.*, **12** 147-160 (1980).

[71] *CRC Handbook of Chemistry and Physics*, 81st Edition, CRC Press, Boca Raton, 2000.

[72] G. D. Quinn, J. Salem, I. Bar-on, K. Cho, M. Foley, and H. Fang, "Fracture Toughness of Advanced Ceramics at Room Temperature," *J. Res. Natl. Inst. Stand. Technol.*, **97** [5] 579-607 (1992).

[73] Alfa Aesar. http://www.alfa.com (accessed November 29, 2010).

[74] G. K. Moiseev, and A. L. Ivanovskii, "Composition and Aggregate State of Products of Titanium Dioxide Heated in Argon Medium," *Glass and Ceramics*, **63** [3-4] 116-118 (2006).

[75] R. Koc, and D. B. Hodge, "Production of TiB_2 from a Precursor Containing Carbon Coated TiO_2 and B_4C," *J. Mat. Sci. Let.*, **19** 667-669 (2000).

[76] H. Suematsu, K. Kitajima, I. Ruiz, K. Kobayashi, M. Takedaa, D. Shimbo, T. Suzuki, W. Jiang, and K. Yatsui, "Thermoelectric Properties of Crystallized Boron Carbide Thin Films Prepared by Ion-Beam Evaporation," *Thin Solid Films*, **407** 132-135 (2002).